PARKINSON'S DISEASE: INSIGHTS INTO NOVEL ASTROCYTE-MEDIATED MECHANISMS OF DOPAMINERGIC NEURODEGENERATION

A Dissertation

by

ERIC ANDREW BANCROFT

Submitted to the Graduate and Professional School of
Texas A&M University
in partial fulfillment of the requirements for the degree of

DOCTOR OF PHILOSOPHY

Chair of Committee,	Rahul Srinivasan
Committee Members,	William Griffith III
	David Earnest
	Jianrong Li
Head of Program,	Carol Vargas Bautista

December 2022

Major Subject: Medical Sciences

ABSTRACT

Parkinson’s Disease (PD) is the second most common neurodegenerative disorder worldwide, with no known cure. The main pathological hallmark of PD is the loss of DA neurons within the substantia nigra pars compacta (SNc). The neurocentric approach to PD research has given us insight into intrinsic mechanisms by which DA neurons degenerate, however, considering the lack of therapeutic breakthroughs, it is imperative to consider the role that glia, particularly astrocytes, play in PD pathogenesis.

Astrocytes are the most prominent cell type within the central nervous system (CNS) and were originally thought to only provide passive support for neurons. Emerging evidence has implicated astrocytes as an active contributor to CNS physiology via numerous mechanisms. One method by which astrocytes regulate brain activity is via the secretion of a plethora of molecules. While many of these molecules such as glutamate and ATP have known targets and cellular effects, it is important to consider the entirety of the astrocyte secretome and novel targets by which these molecules may modulate DA neuron physiology in the context of PD.

Additionally, developing specific, targeted therapies for PD has been challenging because of the difficulty of drug delivery. Effective drug-delivery to the brain has been challenging due to the high selectivity of the blood-brain barrier (BBB), therefore it is also essential to develop novel methods, such as nanoparticles, to deliver therapeutic molecules across the BBB.

In this dissertation, I focus on these barriers for developing novel PD treatments by understanding how pathological astrocyte-neuron interactions affect neurodegeneration and developing optimized drug delivery systems for targeted brain-region specific drug delivery. I specifically address these issues by: (i) Developing a primary midbrain astrocyte-neuron co-

culture system to investigate astrocyte-neuron communication, (ii) Determine the effects of gold-coated superparamagnetic iron-oxide nanoparticles on DA neuron activity, (iii) Discover a novel mechanism by which extracellular astrocytic S100B modulates DA neuron physiology via voltage-gated ion channel activity, (iv) review evidence suggesting that calcium signals in astrocytes are an upstream regulator of their function, and (v) Show that MIF treatment following TBI contributes to increased CA1 hippocampal neuron activity and the sensitivity to glutamatergic astrocytes.

DEDICATION

I would like to dedicate this work to my parents Pat and Deborah Bancroft, my late grandparents Jim and Annette Sharp, Harry Bancroft, and my remaining grandmother Ann (Peggy) Bancroft. Their unconditional love and support throughout the course of my life has been instrumental in my success and has been greatly responsible for fostering my desire to pursue knowledge. I can still hear the echoes of my parents sternly enforcing the completion of my homework.

I also dedicate this work to my younger brother Alan Bancroft. While we have both become very busy and grown physically distant in recent years, he has always been there for emotional support. I can always count on Alan for comedic relief in times of stress and frustration, which I am incredibly grateful for.

In addition, I dedicate this work to all other members of my extended family who have shown interest in my pursuits over the years. Their continued support has helped motivate me to be where I am today.

Finally, I would also like to dedicate this work to all former and current patients suffering from Parkinson’s disease, including my grandfather Jim.

ACKNOWLEDGEMENTS

I would like to thank my committee chair, Dr. Srinivasan, and my committee members, Dr. Griffith, Dr. Earnest, and Dr. Li, for their patient guidance and support throughout the course of this research.

Special thanks go to Dr. Michelle Hook and Dr. William Griffith III for allowing me into their laboratories as a naïve undergraduate student and by doing so, nurturing my interest in scientific research.

Thanks also go to all members of the Srinivasan lab over the years, particularly Gauri Pandey, Sara Zarate and Taylor Huntington. Additionally, thanks to my friends and colleagues here at Texas A&M, including the department faculty and staff, for instilling an inclusive and collaborative environment which made the stress of graduate school all that much easier to manage. I am also thankful for the help of numerous undergraduate students throughout the course of my research, specifically Martha De La Mora and Ramlah Khan.

Last but certainly not least, a huge thank you to my two best friends Benjamin Reeves and Arseniy Kolonin. Having known them for over decade, there are too many memories, both good and bad, to recollect here. These two helped me through some of the most difficult times in my life, and for that, I am forever indebted.

CONTRIBUTORS AND FUNDING SOURCES

Contributors

This work was supervised by a dissertation committee consisting of Professor Srinivasan [Chair], Professor Griffith, and Professor Earnest of the Department of Neuroscience and Experimental Therapeutics and Professor Li of the Department of Veterinary Integrative Biosciences.

Much of the data generated and analyzed for Chapter III and featured in Figures 4-5, 9-11 and 13-16 was in collaboration with Professor Ya Wang of the Department of Mechanical Engineering and were published in 2022.

The data generated and analyzed for Chapter VI was in collaboration with Professor Lee Shapiro of the Department of Neuroscience and Experimental Therapeutics and were published in 2019.

All other work conducted for the dissertation was completed by the student independently.

Funding Sources

Graduate study was supported by a fellowship from Texas A&M University.

This work was also made possible in part by a research grant from the American Parkinson Disease Association (APDA), the National Science Foundation (NSF) GCR under grant number 3032082 and the National Institutes of Health (NIH) under grant number R01NS115809. Its contents are solely the responsibility of the authors and do not necessarily represent the official views of the APDA, NSF or NIH.

NOMENCLATURE

α-syn	α-synuclein
4-AP	4-amminopyridine
6-OHDA	6-hydroxydopamine
AAV	Adeno-associated virus
AD	Alzheimer’s disease
ALS	Amyotrophic lateral sclerosis
AP	Action potential
ApoE	Apolipoprotein E
AQP4	Aquaporin 4
Au-SPIO	Gold-coated superparamagnetic iron oxide
BBB	Blood brain barrier
BDNF	Brain-derived neurotrophic factor
BSA	Bovine serum albumin
CNS	Central nervous system
DA	Dopaminergic
DAMP	Damage associated molecular pattern
DIV	Days in vitro
DNase	Deoxyribonuclease
DRG	Dorsal root ganglion
ED	Embryonic day
ENS	Enteric nervous system

ER	Endoplasmic reticulum
FFT	Fast Fourier transform
FOV	Field of view
GDNF	Glial cell-derived neurotrophic factor
GECI	Genetically encoded calcium indicator
GFS	Global field synchronization
GI	Gastrointestinal
GLP1R	Glucagon-like peptide 1 receptor
HBSS	Hank’s balanced salt solution
HD	Huntington’s disease
hSyn	Human synapsin promoter
IL1β	Interleukin 1β
iPSC	Induced pluripotent stem cell
KO	Knockout
LB	Lewy body
LRRK2	Leucine rich repeat kinase 2
MCU	Mitochondrial uniporter
MGV	Mean gray value
MIF	Macrophage migration inhibitory factor
MPTP	1-methyl-4-phenyl-1,2,3,6-tetrahydropyridine
MS	Pulsed magnetic stimulation
NA	Numerical aperture
NGS	Normal goat serum

NLR	Nucleotide-binding oligomerization domain-like receptor
NP	Nanoparticle
PAMP	Pathogen associated molecular pattern
PBS	Phosphate buffered saline
PD	Parkinson’s disease
PNS	Peripheral nervous system
PRR	Pattern recognition receptors
PSD	Power spectral density
RAGE	Receptor for advanced glycation end products
ROI	Region of interest
SMS	Static magnetic stimulation
SNc	Substantia nigra pars compacta
SNr	Substantia nigra pars reticulata
TBI	Traumatic brain injury
TEM	Transmission electron microscopy
TH	Tyrosine hydroxylase
TJP	Tight junction protein
TLR	Toll-like receptor
TNFα	Tumor necrosis factor α
TRP	Transient receptor potential
TTX	Tetrodotoxin
VGC	Voltage-gated channel
VGCC	Voltage-gated calcium channel

VGKC	Voltage-gated potassium channel
VM	Ventral mesencephalon
VTA	Ventral tegmental area

TABLE OF CONTENTS

LIST OF FIGURES

Page

LIST OF TABLES

Page

CHAPTER I

INTRODUCTION

Parkinson's disease (PD) incidence and sex differences

Parkinson's disease (PD) is the second most common neurodegenerative disorder worldwide, with no known cure. Some estimates suggest that PD prevalence will continue to increase and is projected to surpass 1 million diagnoses by the year 2030 in the United States alone [1, 2]. Multiple lines of evidence have identified biological sex as a factor in the presentation and phenotypic expression of PD. Epidemiological studies have found that PD diagnosis is twice as common in men as compared to women [3, 4]. Further, women experience faster progression, increased mortality rates, distinct symptoms, and different responses to currently available PD therapies [5, 6]. In addition to sex-based clinical disparities of PD, recent studies are beginning to uncover sex-based differences in PD pathology. While sex-based differences in PD pathophysiology are still understudied, it is becoming clear that estrogens play an important role by conferring neuroprotection via numerous mechanisms such as regulating endoplasmic reticulum (ER) stress, oxidative stress and iron accumulation [7-11]. These studies add yet another layer of complexity to studying PD. Despite the intricacies of PD, the main hallmark of pathology conserved across different forms of the disease is the loss of midbrain dopaminergic (DA) neurons and depletion of striatal DA levels [12-15]. By the time PD is diagnosed clinically, around 50% of substantia nigra pars compacta (SNc) DA neurons have been lost [16, 17]. As such, it is imperative to discover the precise mechanisms leading DA neuron loss, and generate truly neuroprotective therapies for PD.

Clinical symptoms of PD

Motor symptoms of PD

PD has traditionally been classified as a motor disorder, as the disease is typically diagnosed upon development of motor deficits. Clinical diagnosis is defined by a set of criteria with bradykinesia and an additional symptom such as muscle rigidity, resting tremor, or postural instability being prerequisite symptoms [18, 19]. Other supporting diagnostic criteria for PD is the unilateral onset of symptoms, response to dopamine replacement therapies, such as levodopa treatment, and induction of dyskinesia due to dopaminergic treatment [18-20]. Additional motor symptoms as the disease progresses include stooped body posture, limb rigidity, and shuffling gait [21]. As other parkinsonian diseases have similar clinical symptoms accurately diagnosing PD can be tricky, and many patients initially diagnosed with PD are eventually reclassified [22]. The motor deficits used to diagnose PD are associated with the loss of DA neurons in the SNc [16, 17, 23], however, PD pathology and symptomatology extends far beyond the clinical motor symptoms.

Non-motor symptoms of PD

Since a large portion of DA neurons are lost before diagnosis of PD, recent efforts have focused on studying the early, non-motor symptoms of PD, in hope to discover novel biomarkers or more effective diagnostic criteria to catch the disease earlier in its pathogenesis. Multiple studies have identified a number of non-motor prodromal symptoms which can precede PD diagnosis by up to 10 years [24, 25]. These symptoms include neuropsychiatric abnormalities such as apathy, anhedonia, depression and anxiety [24-27]. Additionally, sleep disturbances including excessive daytime drowsiness, REM sleep disorder and autonomic disruptions such as constipation occur prior to PD diagnosis [20, 24, 25, 27-29]. Further, non-motor symptoms continue to develop alongside motor symptoms, and for many patients become more problematic than the motor symptoms themselves. This evidence suggests that PD is a complex multi-system disease consisting of bi-directional communication between the brain, the immune system and other organ systems, such as the gut. Similarly, the occurrence of these non-motor symptoms likely involve communication between multiple cell types, particularly interactions between glia and neurons. Therefore, effective pre-clinical modeling of PD is challenging and currently no singular model captures the entirety of PD phenotypes.

Complex multi-system and multi-cellular pathology of PD

Based on the complex clinical presentation of PD that includes prodromal, motor and non-motor symptoms, recent evidence has shed light on the vast complexity of PD-associated mechanisms and is beginning to shift the neurocentric focus of PD research. The involvement of multiple organ systems and cell types has now been implicated in PD pathology. Understanding how each of these mechanisms contribute to DA neuron loss is vital for generating novel strategies to prevent neurodegeneration and for developing more effective PD treatments. In the following sections, I consider multisystem, intercellular and neuron-specific dysfunctions that can lead to the pathogenesis of PD.

The gut-brain axis in PD

PD associated gastrointestinal (GI) dysfunctions were reported in the first clinical descriptions of the disease by James Parkinson [30]. Yet, until recent years research into GI dysfunction associated with PD was largely absent [30, 31]. Early theories of how the gut contributes to PD pathology were spurred by the discovery of α-synuclein deposits within the enteric nervous system (ENS) of PD patients [32]. Soon after, based on autopsy studies, Braak et al. proposed a theory of ascending propagation of α-synuclein pathology, classifying the spread in stages [33]. It is thought that insults to the gut microbiome initiate misfolding and aggregation of α-synuclein which leads to prion-like cell-cell spread, ultimately propagating to the brain [30, 34, 35]. There is no clear consensus on if gut-brain spread of α-synuclein is a causal factor of PD, as there is substantial evidence arguing both for and against this idea [32, 36-39]. Additionally, evidence suggests that intestinal permeability, a common hallmark of PD, contributes to increased brain inflammation and α-synuclein propagation. Increased intestinal permeability allows microbes to cross the intestinal epithelium [40-42], and activate Toll-like receptors expressed on epithelial, immune and enteric glial cells [43, 44]. This likely leads to brain effects via systemic mechanisms such as increased cytokine production, blood brain barrier (BBB) disruption, and glial reactivity eventually leading to neuronal dysfunction [45, 46].

The immune-brain axis in PD

While it is generally accepted that the immune system contributes to PD pathology, the exact nature of this relationship is yet to be defined. Mechanisms by which the immune system contributes to neurodegeneration have been elusive, however, multiple lines of evidence implicate the involvement of immune related processes. For example, patients with autoimmune disorders have an increased risk of PD [47, 48]. Furthermore, autoantibodies against α-synuclein have been found in patients with PD, however the results are inconsistent, and it is not clear if the presence of the autoantibodies is beneficial or detrimental [49, 50]. In early PD pathology, microglia, the innate immune cell of the central nervous system (CNS), help clear aggregations of α-synuclein, yet microglial overactivation can lead to increased brain inflammation and DA neuron damage [51-53]. Microglia are also responsible for recruitment of T cells, via presentation of autoantigens like α-synuclein, which infiltrate the brain and release proinflammatory cytokines and contributes to neurodegeneration [54, 55]. Activated microglia have also been shown to convert astrocytes into a neurotoxic form. Astrocytes expressing the D2 Dopamine receptor can protect neurons against innate immune responses but when exposed to proinflammatory cytokines such as IL-1 and TNF they lose their neuroprotective effect [56]. This conversion of astrocytes into a neurotoxic form can be blocked by treatment with a glucagon-like peptide 1 receptor (GLP1R) agonist promotes neuroprotection, suggesting astrocytes may be an effective therapeutic target for PD therapies [57, 58].

Abnormal DA physiology

When considering pathologic processes leading to neurodegeneration, it is important to remember the distinct nature of DA neuron physiology. Midbrain DA neurons display pacemaking activity, with tonic, intrinsically driven action potentials [59, 60]. Much work has been done to understand why SNc DA neurons are more vulnerable to neurodegeneration than other midbrain neurons, such as ventral tegmental area (VTA) DA neurons, and this vulnerability can at least be partially explained by their physiologic properties. Action potentials of SNc DA neurons are slow (2-10 Hz) and broad which maximizes Ca^{2+} entry via Cav1 channels on the plasma membrane and Ca^{2+} release from ER stores [61-63]. SNc DA neurons have significantly lower expression of Ca^{2+} buffering proteins compared to their neighbors in the VTA and therefore are more vulnerable to dysfunction in response to changes in intracellular Ca^{2+} levels [64, 65]. Research addressing the mechanisms governing pacemaking activity in SNc DA neurons suggests that pacemaking activity is regulated by L-type voltage-gated Ca^{2+} channels (VGCCs) [63, 66, 67]. Recent work indicates that the pacemaking mechanism in adult SNc neurons shifts to depend on Cav1.3 subunits, which are enriched in SNc DA neurons [68]. Distinct ion-channel expression in SNc DA neurons partially explains their shifted activity range and differential response to dihydropyridine drugs when compared to VTA neurons and allows potential for specifically modulating SNc pacemaking activity via Cav1.3 [69, 70]. Interestingly, multiple lines of evidence suggest that this distinct L-type VGCC mediated pacemaking activity is compromised in PD, contributes to neurodegeneration via oxidative stress, and that treatment with L-type VGCC blockers decrease risk for PD in humans and is protective against neurodegeneration in pre-clinical models of PD [68, 71-75]. However, recent clinical trial data has shown that the L-type VGCC blocker isradipine did not slow the progression of PD [76]. Despite this recent setback, these findings suggest that further efforts targeting Cav channels specifically expressed on SNc DA neurons to modulate activity and downstream effects may prove useful to combat PD associated neurodegeneration. Another approach to circumvent issues with the failure of VGCC-targeted drugs is to better understand the complex interactions between VGCCs and other voltage-gated channels (VGCs) in DA neurons. In this regard, chapter IV of this dissertation considers the specific and complex interaction between VGKCs and VGCCs in DA neurons.

Astrocytes in PD

In addition to neuron intrinsic factors such as VGC function and dysfunction, intercellular interactions between CNS cells play a critical role in PD pathogenesis. Glia are an essential cell type that play significant roles in the pathogenesis of several neurodegenerative disorders such as PD, traumatic brain injury (TBI), Alzheimer's disease (AD), Huntington's disease (HD), and amyotrophic lateral sclerosis (ALS). This is unsurprising, given the fact that glia compose around 50% of brain cells, with astrocytes being the most common glial subtype [77, 78]. Astrocytes are responsible for a range of functions, including many that are responsible for maintaining neuronal health and function. Astrocytes have been shown to regulate synaptic function, provide metabolic support for neurons, release neurotrophic factors such as GDNF, contribute to the inflammatory response via cytokine release, help regulate the blood brain barrier (BBB) and uptake extracellular glutamate [78, 79]. Multiple genes implicated in PD have recently been demonstrated to help initiate astrocytic response to inflammation and disruption of these inflammatory signaling pathways leads to compromised astrocytic glutamate transport, water transport, and neurotrophic capacity [78, 80-83]. Recently, the concept that astrocytes can regulate neuronal physiology via secretory proteins such as S100B has gained traction. In PD, midbrain astrocytes become reactive and demonstrate a pathological increase in the expression levels of astrocyte-specific proteins such as glial fibrillary acid protein (GFAP) [84, 85] and S100B [86]. Multiple studies have implicated S100B in PD pathogenesis. For example, a single nucleotide polymorphism, rs9722, which is associated with increased levels of serum S100B results in an elevated risk for early onset PD [87, 88]. Ablation of S100B in mice protects against MPTP-induced DA loss [86]. Mice overexpressing S100B develop parkinsonian features [86, 89], and overnight S100B elevation correlates with increased PD severity and sleep disruption [90]. One mechanism through which extracellularly secreted astrocytic S100B accelerates neurodegeneration is by engaging receptor for advanced glycation endproducts (RAGE)-mediated pro-inflammatory pathways in astrocytes and microglia [91-93]. Additionally, more recent findings have demonstrated that extracellular S100B can alter neuronal activity in multiple brain regions via interactions with ion channels [94, 95]. Therefore, one can speculate that elevated levels of S100B in the midbrain may contribute to DA neuron dysfunction and eventual death. An understudied aspect of astrocyte biology is determining how they encode information to help facilitate cell-cell communication in health and disease. Recent evidence suggests that astrocytic Ca^{2+} signals are responsible for governing their function. Astrocytic Ca^{2+} signals are observed in distinct compartments of the cell and respond to numerous pharmacological and behavioral stimuli [96-98]. Abnormal astrocytic Ca^{2+} signals are now being linked to multiple disease pathologies, including PD, and is discussed more thoroughly in Chapter V.

Pre-clinical models of PD

As idiopathic PD is a complex disease, it has been challenging to produce cellular and animal models which encompass the entirety of the pathology seen in human patients [99, 100]. Both *in vitro* cellular and *in vivo* animal models each have their strengths and weaknesses and can help elucidate different aspects of PD. Cellular models can be preferential to animal models for multiple reasons: rapid development of pathology, low cost, easy and precise genetic or pharmacologic manipulation, ability to study specific cell types in isolation and preform high-resolution time-lapse imaging. In contrast, animal models are advantageous to study interactions between specific cell types, changes in synaptic and circuit properties, contribution of inflammatory processes, behavioral changes, and motor deficits. The advance of technological methods, such as multi-photon microscopy and fiber photometry, is allowing more intricate *in vivo* studies to be performed, yet still with limitations. Therefore, to fully understand PD pathogenesis both types of models will need to be used and further improved.

Cellular models of PD

Two main hallmarks of human PD patients are well represented by currently used cellular models of PD, these being the loss of DA neurons and formation of protein aggregates that contain α-synuclein. Cellular models of PD can utilize three types of cell lines, immortalized, induced pluripotent stem cells (iPSCs), or primary cultures. Immortalized cell lines such as, SH-SY5Y, PC12, LUHMES, etc., all display neuron like properties, are generally easy to maintain, are usually cultured in isolation, and allow for manipulation of gene expression and pharmacological intervention [99, 100]. However, these cells are quite distinct from primary neurons in their morphology, electrophysiological properties and ion channel expression profiles.

In recent years, iPSCs have become a popular tool for researching PD and other neurological diseases [101-103]. iPSCs provide the distinct advantage of being able to study dopaminergic neurons from PD patients. These patient-derived iPSCs have been shown to carry PD-associated genetic mutations (A53T, LRRK2, DJ-1, PARK2/PARKIN, PINK1), mitochondrial deficits, oxidative stress and lysosomal defects, and display increased α-synuclein aggregation, similar to the phenotypes seen in other cellular models of PD [104-109]. However, they are harder to acquire, difficult to maintain, expensive to culture, display significant variability among clones, and often do not completely mature to dopaminergic neurons found in native tissue [104]. More complex iPSC-co-cultures with astrocytes and other cell types do exist and may circumvent some of the issues with maturity of iPSC derived DA cells [110], but are nonetheless plagued with cost of maintenance and difficult culturing techniques.

As such, to explore acute changes in cellular processes which may contribute to downstream DA neuron dysfunction and neurodegeneration, primary midbrain cultures are more appropriate. Primary midbrain neurons display electrical properties and ion channel expression similar to what is seen *in vivo,* and additionally these cells can be co-cultured with glia to explore questions related to cellular interactions. While primary midbrain neurons mirror intrinsic electrophysiological properties of their *in vivo* equivalents, a major drawback is the formation of ectopic synaptic connections that do not reflect the circuitry of the whole brain [99, 100]. Primary midbrain culture models are a great tool for understanding basic interactions between glia, particularly astrocytes, and DA neurons in both healthy and pathologic conditions.

Animal models of PD

Like cellular models, animal models of PD can be separated into two main categories, toxin-induced models and genetic models of PD. Historically, toxin models of PD have been favored as, until the late 1990s, PD genes had not been identified [111, 112]. There are numerous toxin models of PD currently being used, with the most popular being 6-hydroxydopamine (6-ODHDA), 1-methyl-4-phenyl-1,2,3,6-tetrahydropyridine (MPTP), rotenone and paraquat [15, 100].

The use of 6-ODHA to generate DA neuron death in the substantia nigra pars compacta (SNc) was first demonstrated over 50 years ago [113]. While 6-OHDA-induced neurodegeneration fails to exactly replicate PD pathology, including the formation of Lewy bodies (LBs), it mirrors certain aspects of the disease quite nicely [100]. 6-OHDA treatment is relatively selective for monoamine neurons at lower doses and DA neurons of the ventral midbrain show a range of sensitivity to 6-OHDA treatment with the greatest cell loss occurring in the SNc, similar to what is seen in clinical PD [15, 114]. 6-OHDA injections must be given intracranially as it does not cross the blood brain barrier (BBB), and can be delivered to the SNc, striatum or medium forebrain bundle to initiate neurodegeneration [115]. Usually, 6-OHDA is unilaterally delivered to the striatum to generate retrograde neurodegeneration which occurs over 1-3 weeks [15, 116, 117]. Unilateral administration leads to asymmetric motor deficits, including rotational behavior where the extent of rotations can be correlated to the severity of the unilateral lesion [15, 117].

The MPTP model of PD was discovered in the early 1980s, when young intravenous drug users developed rapid parkinsonian like symptoms, where MPTP was identified as the contaminant leading to neurodegeneration [118, 119]. MPTP exposure in humans and primates leads to symptoms almost exactly like clinical PD, including tremor, rigidity, bradykinesia, and postural instability. Like 6-OHDA, midbrain neurons show a range of sensitivity to MPTP treatment with the ventral portion of the SNc displaying the greatest cell loss [120]. The phenotype of MPTP treatment differs from clinical PD in two key areas, MPTPs lack of effect on other non-DA monoaminergic neurons and the lack of classical LB formation. Despite this, the MPTP model continues to be the standard model for preclinical assessment of novel therapeutic strategies [121].

While both 6-OHDA and MPTP models of PD capture the intrinsic changes in cellular function associated PD pathogenesis, it is important to consider how rapidly these models drive neurodegeneration, which is not reflective of clinical PD, and may contribute to the lack of certain phenotypes of PD, such as LB formation. Therefore, it may be of use to administrate lower doses of these toxins to slow the rate of neurodegeneration, or in the case of MPTP using multiple small doses.

Another main approach for PD researchers employs animal models with genetic mutations in PD-associated genes such as, α-synuclein, LRRK2, PINK1/PARKIN, and DJ-1. While the etiology of genetic versus idiopathic forms of PD is unknown and likely distinct, each form shares common mechanisms of cellular dysfunction making genetic models of PD useful tools to study both forms of the disease [100]. In contrast to cellular and toxin-induced animal models, genetic models lack certain cellular and anatomical phenotypes of PD, such as altered striatal DA levels and SNc DA neuron loss, yet still produce Parkinsonian like behaviors in animals.

In the case of α-synuclein models of PD it has been reported that transgenic mice carrying the A30P or A53T mutations produced decreased striatal DA and behavioral alterations but failed to drive SNc DA neuron loss [122]. However, specific overexpression of α-synuclein in DA neurons via the Thy-1 promoter reduces striatal DA levels, promotes DA neurodegeneration, and development of motor deficits [123, 124]. Additionally, both AAV and fibril based α-synuclein models have demonstrated progressive, age-related DA neuron loss, intercellular α-synuclein transmission and impairment of motor functions, but unfortunately these approaches suffer from significant variability and require further development [125-128].

Another popular genetic model of PD involves mutations in the lucine rich repeat kinase 2 (LRRK2) gene. LRRK2 mutations are the most common cause of genetic PD, and while LRRK2 models of PD have given us insight to how LRRK2 function relates to neuropathology, few LRRK2 transgenic models have been able to establish DA neuron loss [129-132]. BAC transgenic mice with LRRK2 mutations specific to DA neurons demonstrate age- and kinase-dependent motor deficits that are associated with reduced striatal DA release [133, 134]. Additionally, there is evidence to suggest that LRRK2 mutations contribute to PD pathology via regulation of α-synuclein pathology [135, 136].

Considering both the complexity of PD pathology and the numerous sophisticated cellular and animal models of PD underscores the importance of picking an appropriate model for the research question of interest. Additionally, as no one pre-clinical model replicates PD pathology entirely, it may be of benefit to combine models, for example, genetic protein overexpression with toxin-induced neurodegeneration. Further, much of the work using these models have focused on intrinsic changes to neuronal function and can easily be repurposed to study changes in glial biology in the context of PD.

Nanoparticle based CNS drug delivery

Parallel with developing a better understanding of PD pathogenesis, it is imperative to begin developing drug delivery systems that can optimize the delivery of potential neuroprotective agents to the brain. Some pre-clinical studies have identified therapeutic molecules that confer neuroprotection but many of these are plagued by difficulties with precise drug delivery to the midbrain, one such example being glial cell-derived neurotrophic factor (GDNF) [137, 138]. The main barrier for delivery of drugs to the CNS is the existence of the BBB. The BBB serves to limit molecules and ions from entering the CNS and is composed of endothelial cells connected via tight junctions, pericytes, and astrocyte end feet [139]. Generally, the BBB can restrict the passage of molecules based on their size, hydrophobicity, and charge [140]. Nanoparticle based drug delivery approaches attempt to overcome these restrictions by packaging or caging of therapeutics to nanoparticles engineered with properties facilitating passage through the BBB [140, 141]. As these nanoparticles are typically made of metals, magnetic stimulation has been shown to increase the infiltration of nanoparticles to the brain [142-144]. However, it is important to identify toxicity of these nanoparticles and determine the extent to which, if at all, they alone modulate CNS biology. While the idea that nanoparticles will provide a very precise mechanism of drug delivery to the brain is promising, they are still in very early stages of research and will need to be validated thoroughly. Chapter III aims to develop a better understanding of how nanoparticles interact with DA neurons in terms of altering their physiology via interactions with VGCCs.

Summary

With PD incidence estimated to increase in the coming decades and because current available therapies have sub-optimal effectiveness, it is imperative that we generate novel therapeutics and drug-delivery mechanisms to directly combat PD-associated neurodegeneration. PD pathology is incredibly complex, multimodal disease involving multiple organ systems and cell types, and while there are numerous pre-clinical models available to researchers wanting to explore PD pathogenesis, none reflect the phenotypes of PD in its entirely. Therefore, advancing our knowledge of PD pathology will require the combination of multiple research models or completely novel systems in order to understand how distinct molecular changes in different cell types work together to drive PD pathogenesis. As the current neurocentric approach to PD research has left us with few effective therapies and more questions than answers it is imperative to understand the nature of cell-to-cell interactions in PD. In particular, improved understanding of astrocyte-neuron interactions in the context of PD, paired with more effective drug-delivery systems may be to key to truly neuroprotective PD therapies.

In this dissertation, I present work done to develop novel strategies to study astrocytic modulation of neuronal function via secreted factors, with a focus on astrocytic contribution to PD pathology, through which I discover a novel mechanism of astrocytic modulation of DA neuron physiology. In Chapter II, I review how astrocytic Ca^{2+} signals relate to their function and how these may change in the context of PD. In Chapter III, I generated a primary mouse midbrain co-culture system to study astrocyte-DA neuron interactions *in vitro* and demonstrate its utility in studying glutamate excitotoxicity. In Chapter IV, I used the primary mouse midbrain co-culture system generated in Chapter III to discover a novel mechanism by which astrocytes, via the secreted protein S100B, can regulate the firing properties of DA neurons, likely contributing to PD pathogenesis. In Chapter V, I demonstrate the utility of similar research strategies and tools used in Chapters III and IV to study other neurodegenerative processes and discover that the astrocytic protein macrophage migration inhibitory factor (MIF) alters functional properties of CA1 layer hippocampal neurons in TBI. In Chapter VI, I used the culture system generated in Chapter III to assess the effects of gold-plated silver nanoparticles, a novel strategy for precise CNS drug delivery, on DA neuron physiology.

References

1. Marras, C.; Beck, J. C.; Bower, J. H.; Roberts, E.; Ritz, B.; Ross, G. W.; Abbott, R. D.; Savica, R.; Van Den Eeden, S. K.; Willis, A. W.; Tanner, C. M.; Parkinson's Foundation, P. G., Prevalence of Parkinson's disease across North America. *NPJ Parkinsons Dis* **2018,** 4, 21.
2. Dorsey, E. R.; Bloem, B. R., The Parkinson Pandemic-A Call to Action. *JAMA Neurol* **2018,** 75, (1), 9-10.
3. Baldereschi, M.; Di Carlo, A.; Rocca, W. A.; Vanni, P.; Maggi, S.; Perissinotto, E.; Grigoletto, F.; Amaducci, L.; Inzitari, D., Parkinson's disease and parkinsonism in a longitudinal study: two-fold higher incidence in men. ILSA Working Group. Italian Longitudinal Study on Aging. *Neurology* **2000,** 55, (9), 1358-63.
4. Solla, P.; Cannas, A.; Ibba, F. C.; Loi, F.; Corona, M.; Orofino, G.; Marrosu, M. G.; Marrosu, F., Gender differences in motor and non-motor symptoms among Sardinian patients with Parkinson's disease. *J Neurol Sci* **2012,** 323, (1-2), 33-9.
5. Dahodwala, N.; Shah, K.; He, Y.; Wu, S. S.; Schmidt, P.; Cubillos, F.; Willis, A.

W., Sex disparities in access to caregiving in Parkinson disease. *Neurology* **2018,** 90, (1), e48-e54.

6. Georgiev, D.; Hamberg, K.; Hariz, M.; Forsgren, L.; Hariz, G. M., Gender differences in Parkinson's disease: A clinical perspective. *Acta Neurol Scand* **2017,** 136, (6), 570-584.

7. Zarate, S. M.; Pandey, G.; Chilukuri, S.; Garcia, J. A.; Cude, B.; Storey, S.; Salem, N. A.; Bancroft, E. A.; Hook, M.; Srinivasan, R., Cytisine is neuroprotective in female but not male 6-hydroxydopamine lesioned parkinsonian mice and acts in combination with 17-beta-estradiol to inhibit apoptotic endoplasmic reticulum stress in dopaminergic neurons. *Journal of neurochemistry* **2021,** 157, (3), 710-726.

8. Yazgan, Y.; Naziroglu, M., Ovariectomy-Induced Mitochondrial Oxidative Stress, Apoptosis, and Calcium Ion Influx Through TRPA1, TRPM2, and TRPV1 Are Prevented by 17beta-Estradiol, Tamoxifen, and Raloxifene in the Hippocampus and Dorsal Root Ganglion of Rats. *Molecular neurobiology* **2017,** 54, (10), 7620-7638.

9. Petrik, D.; Jiang, Y.; Birnbaum, S. G.; Powell, C. M.; Kim, M. S.; Hsieh, J.; Eisch, A. J., Functional and mechanistic exploration of an adult neurogenesis-promoting small molecule. *FASEB journal : official publication of the Federation of American Societies for Experimental Biology* **2012,** 26, (8), 3148-62.

10. Wang, L. F.; Yokoyama, K. K.; Chen, T. Y.; Hsiao, H. W.; Chiang, P. C.; Hsieh, Y. C.; Lo, S.; Hsu, C., Male-Specific Alleviation of Iron-Induced Striatal Injury

by Inhibition of Autophagy. *PloS one* **2015,** 10, (7), e0131224.

11. Chen, T. Y.; Lin, C. L.; Wang, L. F.; Tsai, K. L.; Lin, J. Y.; Hsu, C., Targeting GPER1 to suppress autophagy as a male-specific therapeutic strategy for iron-induced striatal injury. *Scientific reports* **2019,** 9, (1), 6661.
12. Poewe, W.; Seppi, K.; Tanner, C. M.; Halliday, G. M.; Brundin, P.; Volkmann, J.; Schrag, A. E.; Lang, A. E., Parkinson disease. *Nat Rev Dis Primers* **2017,** 3, 17013.
13. Braak, H.; Ghebremedhin, E.; Rub, U.; Bratzke, H.; Del Tredici, K., Stages in the development of Parkinson's disease-related pathology. *Cell Tissue Res* **2004,** 318, (1), 121-34.
14. Surmeier, D. J.; Obeso, J. A.; Halliday, G. M., Selective neuronal vulnerability in Parkinson disease. *Nat Rev Neurosci* **2017,** 18, (2), 101-113.
15. Dauer, W.; Przedborski, S., Parkinson's disease: mechanisms and models. *Neuron* **2003,** 39, (6), 889-909.
16. Sulzer, D.; Surmeier, D. J., Neuronal vulnerability, pathogenesis, and Parkinson's disease. *Mov Disord* **2013,** 28, (1), 41-50.
17. Hirsch, E.; Graybiel, A. M.; Agid, Y. A., Melanized dopaminergic neurons are differentially susceptible to degeneration in Parkinson's disease. *Nature* **1988,** 334, (6180), 345-8.
18. Hughes, A. J.; Daniel, S. E.; Kilford, L.; Lees, A. J., Accuracy of clinical diagnosis of idiopathic Parkinson's disease: a clinico-pathological study of 100 cases. *J Neurol Neurosurg Psychiatry* **1992,** 55, (3), 181-4.
19. Reichmann, H., Clinical criteria for the diagnosis of Parkinson's disease.

Neurodegener Dis **2010,** 7, (5), 284-90.

20. Sveinbjornsdottir, S., The clinical symptoms of Parkinson's disease. *Journal of neurochemistry* **2016,** 139 Suppl 1, 318-324.

21. Jankovic, J., Parkinson's disease: clinical features and diagnosis. *J Neurol Neurosurg Psychiatry* **2008,** 79, (4), 368-76.

22. Schrag, A.; Ben-Shlomo, Y.; Quinn, N., How valid is the clinical diagnosis of Parkinson's disease in the community? *J Neurol Neurosurg Psychiatry* **2002,** 73, (5), 529-34.

23. Chung, K. K.; Zhang, Y.; Lim, K. L.; Tanaka, Y.; Huang, H.; Gao, J.; Ross, C. A.; Dawson, V. L.; Dawson, T. M., Parkin ubiquitinates the alpha-synuclein-interacting protein, synphilin-1: implications for Lewy-body formation in Parkinson disease. *Nature medicine* **2001,** 7, (10), 1144-50.

24. Schrag, A.; Horsfall, L.; Walters, K.; Noyce, A.; Petersen, I., Prediagnostic presentations of Parkinson's disease in primary care: a case-control study. *Lancet Neurol* **2015,** 14, (1), 57-64.

25. Pont-Sunyer, C.; Hotter, A.; Gaig, C.; Seppi, K.; Compta, Y.; Katzenschlager, R.; Mas, N.; Hofeneder, D.; Brucke, T.; Bayes, A.; Wenzel, K.; Infante, J.; Zach, H.; Pirker, W.; Posada, I. J.; Alvarez, R.; Ispierto, L.; De Fabregues, O.; Callen, A.; Palasi, A.; Aguilar, M.; Marti, M. J.; Valldeoriola, F.; Salamero, M.; Poewe, W.; Tolosa, E., The onset of nonmotor symptoms in Parkinson's disease (the ONSET PD study). *Mov Disord* **2015,** 30, (2), 229-37.

26. Chen, H.; Burton, E. A.; Ross, G. W.; Huang, X.; Savica, R.; Abbott, R. D.;

Ascherio, A.; Caviness, J. N.; Gao, X.; Gray, K. A.; Hong, J. S.; Kamel, F.; Jennings, D.; Kirshner, A.; Lawler, C.; Liu, R.; Miller, G. W.; Nussbaum, R.; Peddada, S. D.; Rick, A. C.; Ritz, B.; Siderowf, A. D.; Tanner, C. M.; Troster, A. I.; Zhang, J., Research on the premotor symptoms of Parkinson's disease: clinical and etiological implications. *Environ Health Perspect* **2013,** 121, (11-12), 1245-52.

27. Schapira, A. H. V.; Chaudhuri, K. R.; Jenner, P., Non-motor features of Parkinson disease. *Nat Rev Neurosci* **2017,** 18, (7), 435-450.

28. Hickey, M. G.; Demaerschalk, B. M.; Caselli, R. J.; Parish, J. M.; Wingerchuk, D. M., "Idiopathic" rapid-eye-movement (REM) sleep behavior disorder is associated with future development of neurodegenerative diseases. *Neurologist* **2007,** 13, (2), 98-101.

29. Jost, W. H., Gastrointestinal dysfunction in Parkinson's Disease. *J Neurol Sci* **2010,** 289, (1-2), 69-73.

30. Tan, A. H.; Lim, S. Y.; Lang, A. E., The microbiome-gut-brain axis in Parkinson disease - from basic research to the clinic. *Nat Rev Neurol* **2022,** 18, (8), 476-495.

31. Pfeiffer, R. F., Gastrointestinal Dysfunction in Parkinson's Disease. *Curr Treat Options Neurol* **2018,** 20, (12), 54.

32. Wakabayashi, K.; Takahashi, H.; Takeda, S.; Ohama, E.; Ikuta, F., Parkinson's disease: the presence of Lewy bodies in Auerbach's and Meissner's plexuses. *Acta Neuropathol* **1988,** 76, (3), 217-221.

33. Braak, H.; Del Tredici, K.; Rub, U.; de Vos, R. A.; Jansen Steur, E. N.; Braak, E.,

Staging of brain pathology related to sporadic Parkinson's disease. *Neurobiology of aging* **2003,** 24, (2), 197-211.

34. Breen, D. P.; Halliday, G. M.; Lang, A. E., Gut-brain axis and the spread of alpha-synuclein pathology: Vagal highway or dead end? *Mov Disord* **2019,** 34, (3), 307-316.

35. Klingelhoefer, L.; Reichmann, H., Pathogenesis of Parkinson disease--the gut-brain axis and environmental factors. *Nat Rev Neurol* **2015,** 11, (11), 625-36.

36. Liu, B.; Fang, F.; Pedersen, N. L.; Tillander, A.; Ludvigsson, J. F.; Ekbom, A.; Svenningsson, P.; Chen, H.; Wirdefeldt, K., Vagotomy and Parkinson disease: A Swedish register-based matched-cohort study. *Neurology* **2017,** 88, (21), 1996-2002.

37. Tysnes, O. B.; Kenborg, L.; Herlofson, K.; Steding-Jessen, M.; Horn, A.; Olsen, J. H.; Reichmann, H., Does vagotomy reduce the risk of Parkinson's disease? *Annals of neurology* **2015,** 78, (6), 1011-2.

38. Hilton, D.; Stephens, M.; Kirk, L.; Edwards, P.; Potter, R.; Zajicek, J.; Broughton, E.; Hagan, H.; Carroll, C., Accumulation of alpha-synuclein in the bowel of patients in the pre-clinical phase of Parkinson's disease. *Acta Neuropathol* **2014,** 127, (2), 235-41.

39. Beach, T. G.; Adler, C. H.; Sue, L. I.; Shill, H. A.; Driver-Dunckley, E.; Mehta, S. H.; Intorcia, A. J.; Glass, M. J.; Walker, J. E.; Arce, R.; Nelson, C. M.; Serrano, G. E., Vagus Nerve and Stomach Synucleinopathy in Parkinson's Disease, Incidental Lewy Body Disease, and Normal Elderly Subjects: Evidence Against

the "Body-First" Hypothesis. *J Parkinsons Dis* **2021,** 11, (4), 1833-1843.

40. Forsyth, C. B.; Shannon, K. M.; Kordower, J. H.; Voigt, R. M.; Shaikh, M.; Jaglin, J. A.; Estes, J. D.; Dodiya, H. B.; Keshavarzian, A., Increased intestinal permeability correlates with sigmoid mucosa alpha-synuclein staining and endotoxin exposure markers in early Parkinson's disease. *PloS one* **2011,** 6, (12), e28032.

41. Kelly, L. P.; Carvey, P. M.; Keshavarzian, A.; Shannon, K. M.; Shaikh, M.; Bakay, R. A.; Kordower, J. H., Progression of intestinal permeability changes and alpha-synuclein expression in a mouse model of Parkinson's disease. *Mov Disord* **2014,** 29, (8), 999-1009.

42. Schwiertz, A.; Spiegel, J.; Dillmann, U.; Grundmann, D.; Burmann, J.; Fassbender, K.; Schafer, K. H.; Unger, M. M., Fecal markers of intestinal inflammation and intestinal permeability are elevated in Parkinson's disease. *Parkinsonism & related disorders* **2018,** 50, 104-107.

43. Burgueno, J. F.; Abreu, M. T., Epithelial Toll-like receptors and their role in gut homeostasis and disease. *Nat Rev Gastroenterol Hepatol* **2020,** 17, (5), 263-278.

44. Perez-Pardo, P.; Dodiya, H. B.; Engen, P. A.; Forsyth, C. B.; Huschens, A. M.; Shaikh, M.; Voigt, R. M.; Naqib, A.; Green, S. J.; Kordower, J. H.; Shannon, K. M.; Garssen, J.; Kraneveld, A. D.; Keshavarzian, A., Role of TLR4 in the gut-brain axis in Parkinson's disease: a translational study from men to mice. *Gut* **2019,** 68, (5), 829-843.

45. Tan, E. K.; Chao, Y. X.; West, A.; Chan, L. L.; Poewe, W.; Jankovic, J., Parkinson

disease and the immune system - associations, mechanisms and therapeutics. *Nat Rev Neurol* **2020,** 16, (6), 303-318.

46. Houser, M. C.; Tansey, M. G., The gut-brain axis: is intestinal inflammation a silent driver of Parkinson's disease pathogenesis? *NPJ Parkinsons Dis* **2017,** 3, 3.

47. Li, X.; Sundquist, J.; Sundquist, K., Subsequent risks of Parkinson disease in patients with autoimmune and related disorders: a nationwide epidemiological study from Sweden. *Neurodegener Dis* **2012,** 10, (1-4), 277-84.

48. Chang, C. C.; Lin, T. M.; Chang, Y. S.; Chen, W. S.; Sheu, J. J.; Chen, Y. H.; Chen, J. H., Autoimmune rheumatic diseases and the risk of Parkinson disease: a nationwide population-based cohort study in Taiwan. *Ann Med* **2018,** 50, (1), 83-90.

49. Yanamandra, K.; Gruden, M. A.; Casaite, V.; Meskys, R.; Forsgren, L.; Morozova-Roche, L. A., alpha-synuclein reactive antibodies as diagnostic biomarkers in blood sera of Parkinson's disease patients. *PloS one* **2011,** 6, (4), e18513.

50. Scott, K. M.; Kouli, A.; Yeoh, S. L.; Clatworthy, M. R.; Williams-Gray, C. H., A Systematic Review and Meta-Analysis of Alpha Synuclein Auto-Antibodies in Parkinson's Disease. *Frontiers in Neurology* **2018,** 9.

51. Bae, E. J.; Lee, H. J.; Rockenstein, E.; Ho, D. H.; Park, E. B.; Yang, N. Y.; Desplats, P.; Masliah, E.; Lee, S. J., Antibody-aided clearance of extracellular alpha-synuclein prevents cell-to-cell aggregate transmission. *The Journal of neuroscience : the official journal of the Society for Neuroscience* **2012,** 32, (39), 13454-69.

52. Duffy, M. F.; Collier, T. J.; Patterson, J. R.; Kemp, C. J.; Luk, K. C.; Tansey, M. G.; Paumier, K. L.; Kanaan, N. M.; Fischer, D. L.; Polinski, N. K.; Barth, O. L.; Howe, J. W.; Vaikath, N. N.; Majbour, N. K.; El-Agnaf, O. M. A.; Sortwell, C. E., Correction to: Lewy body-like alpha-synuclein inclusions trigger reactive microgliosis prior to nigral degeneration. *Journal of neuroinflammation* **2018,** 15, (1), 169.

53. Doorn, K. J.; Moors, T.; Drukarch, B.; van de Berg, W.; Lucassen, P. J.; van Dam, A. M., Microglial phenotypes and toll-like receptor 2 in the substantia nigra and hippocampus of incidental Lewy body disease cases and Parkinson's disease patients. *Acta neuropathologica communications* **2014,** 2, 90.

54. Harms, A. S.; Cao, S.; Rowse, A. L.; Thome, A. D.; Li, X.; Mangieri, L. R.; Cron, R. Q.; Shacka, J. J.; Raman, C.; Standaert, D. G., MHCII is required for alpha-synuclein-induced activation of microglia, CD4 T cell proliferation, and dopaminergic neurodegeneration. *The Journal of neuroscience : the official journal of the Society for Neuroscience* **2013,** 33, (23), 9592-600.

55. Williams, G. P.; Schonhoff, A. M.; Jurkuvenaite, A.; Thome, A. D.; Standaert, D. G.; Harms, A. S., Targeting of the class II transactivator attenuates inflammation and neurodegeneration in an alpha-synuclein model of Parkinson's disease. *Journal of neuroinflammation* **2018,** 15, (1), 244.

56. Shao, W.; Zhang, S. Z.; Tang, M.; Zhang, X. H.; Zhou, Z.; Yin, Y. Q.; Zhou, Q. B.; Huang, Y. Y.; Liu, Y. J.; Wawrousek, E.; Chen, T.; Li, S. B.; Xu, M.; Zhou, J. N.; Hu, G.; Zhou, J. W., Suppression of neuroinflammation by astrocytic dopamine

D2 receptors via alphaB-crystallin. *Nature* **2013,** 494, (7435), 90-4.

57. Yun, S. P.; Kam, T. I.; Panicker, N.; Kim, S.; Oh, Y.; Park, J. S.; Kwon, S. H.; Park, Y. J.; Karuppagounder, S. S.; Park, H.; Kim, S.; Oh, N.; Kim, N. A.; Lee, S.; Brahmachari, S.; Mao, X.; Lee, J. H.; Kumar, M.; An, D.; Kang, S. U.; Lee, Y.; Lee, K. C.; Na, D. H.; Kim, D.; Lee, S. H.; Roschke, V. V.; Liddelow, S. A.; Mari, Z.; Barres, B. A.; Dawson, V. L.; Lee, S.; Dawson, T. M.; Ko, H. S., Block of A1 astrocyte conversion by microglia is neuroprotective in models of Parkinson's disease. *Nature medicine* **2018,** 24, (7), 931-938.

58. Hinkle, J. T.; Dawson, V. L.; Dawson, T. M., The A1 astrocyte paradigm: New avenues for pharmacological intervention in neurodegeneration. *Mov Disord* **2019,** 34, (7), 959-969.

59. Guzman, J. N.; Sanchez-Padilla, J.; Chan, C. S.; Surmeier, D. J., Robust pacemaking in substantia nigra dopaminergic neurons. *The Journal of neuroscience : the official journal of the Society for Neuroscience* **2009,** 29, (35), 11011-9.

60. Gonon, F.; Bloch, B., Kinetics and geometry of the excitatory dopaminergic transmission in the rat striatum in vivo. *Adv Pharmacol* **1998,** 42, 140-4.

61. Bean, B. P., The action potential in mammalian central neurons. *Nat Rev Neurosci* **2007,** 8, (6), 451-65.

62. Guzman, J. N.; Sanchez-Padilla, J.; Wokosin, D.; Kondapalli, J.; Ilijic, E.; Schumacker, P. T.; Surmeier, D. J., Oxidant stress evoked by pacemaking in dopaminergic neurons is attenuated by DJ-1. *Nature* **2010,** 468, (7324), 696-700.

63. Puopolo, M.; Raviola, E.; Bean, B. P., Roles of subthreshold calcium current and sodium current in spontaneous firing of mouse midbrain dopamine neurons. *The Journal of neuroscience : the official journal of the Society for Neuroscience* **2007,** 27, (3), 645-56.

64. Foehring, R. C.; Zhang, X. F.; Lee, J. C.; Callaway, J. C., Endogenous calcium buffering capacity of substantia nigral dopamine neurons. *Journal of neurophysiology* **2009,** 102, (4), 2326-33.

65. Khaliq, Z. M.; Bean, B. P., Pacemaking in dopaminergic ventral tegmental area neurons: depolarizing drive from background and voltage-dependent sodium conductances. *The Journal of neuroscience : the official journal of the Society for Neuroscience* **2010,** 30, (21), 7401-13.

66. Nedergaard, S.; Flatman, J. A.; Engberg, I., Nifedipine- and omega-conotoxin-sensitive Ca2+ conductances in guinea-pig substantia nigra pars compacta neurones. *The Journal of physiology* **1993,** 466, 727-47.

67. Mercuri, N. B.; Bonci, A.; Calabresi, P.; Stratta, F.; Stefani, A.; Bernardi, G., Effects of dihydropyridine calcium antagonists on rat midbrain dopaminergic neurones. *Br J Pharmacol* **1994,** 113, (3), 831-8.

68. Chan, C. S.; Guzman, J. N.; Ilijic, E.; Mercer, J. N.; Rick, C.; Tkatch, T.; Meredith, G. E.; Surmeier, D. J., 'Rejuvenation' protects neurons in mouse models of Parkinson's disease. *Nature* **2007,** 447, (7148), 1081-6.

69. Xu, W.; Lipscombe, D., Neuronal Ca(V)1.3alpha(1) L-type channels activate at relatively hyperpolarized membrane potentials and are incompletely inhibited by

dihydropyridines. *The Journal of neuroscience : the official journal of the Society for Neuroscience* **2001,** 21, (16), 5944-51.

70. Koschak, A.; Reimer, D.; Huber, I.; Grabner, M.; Glossmann, H.; Engel, J.; Striessnig, J., alpha 1D (Cav1.3) subunits can form l-type Ca2+ channels activating at negative voltages. *The Journal of biological chemistry* **2001,** 276, (25), 22100-6.

71. Sanchez-Padilla, J.; Guzman, J. N.; Ilijic, E.; Kondapalli, J.; Galtieri, D. J.; Yang, B.; Schieber, S.; Oertel, W.; Wokosin, D.; Schumacker, P. T.; Surmeier, D. J., Mitochondrial oxidant stress in locus coeruleus is regulated by activity and nitric oxide synthase. *Nature neuroscience* **2014,** 17, (6), 832-40.

72. Exner, N.; Lutz, A. K.; Haass, C.; Winklhofer, K. F., Mitochondrial dysfunction in Parkinson's disease: molecular mechanisms and pathophysiological consequences. *EMBO J* **2012,** 31, (14), 3038-62.

73. Ritz, B.; Rhodes, S. L.; Qian, L.; Schernhammer, E.; Olsen, J. H.; Friis, S., L-type calcium channel blockers and Parkinson disease in Denmark. *Annals of neurology* **2010,** 67, (5), 600-6.

74. Marras, C.; Gruneir, A.; Rochon, P.; Wang, X.; Anderson, G.; Brotchie, J.; Bell, C. M.; Fox, S.; Austin, P. C., Dihydropyridine calcium channel blockers and the progression of parkinsonism. *Annals of neurology* **2012,** 71, (3), 362-9.

75. Ilijic, E.; Guzman, J. N.; Surmeier, D. J., The L-type channel antagonist isradipine is neuroprotective in a mouse model of Parkinson's disease. *Neurobiology of disease* **2011,** 43, (2), 364-71.

76. Investigators, P. S. G. S.-P. I., Isradipine Versus Placebo in Early Parkinson Disease: A Randomized Trial. *Ann Intern Med* **2020,** 172, (9), 591-598.

77. Herculano-Houzel, S., The human brain in numbers: a linearly scaled-up primate brain. *Front Hum Neurosci* **2009,** 3, 31.

78. Booth, H. D. E.; Hirst, W. D.; Wade-Martins, R., The Role of Astrocyte Dysfunction in Parkinson's Disease Pathogenesis. *Trends Neurosci* **2017,** 40, (6), 358-370.

79. Barres, B. A., The mystery and magic of glia: a perspective on their roles in health and disease. *Neuron* **2008,** 60, (3), 430-40.

80. Kim, J. M.; Cha, S. H.; Choi, Y. R.; Jou, I.; Joe, E. H.; Park, S. M., DJ-1 deficiency impairs glutamate uptake into astrocytes via the regulation of flotillin-1 and caveolin-1 expression. *Scientific reports* **2016,** 6, 28823.

81. Gu, X. L.; Long, C. X.; Sun, L.; Xie, C.; Lin, X.; Cai, H., Astrocytic expression of Parkinson's disease-related A53T alpha-synuclein causes neurodegeneration in mice. *Mol Brain* **2010,** 3, 12.

82. Mullett, S. J.; Hinkle, D. A., DJ-1 knock-down in astrocytes impairs astrocyte-mediated neuroprotection against rotenone. *Neurobiology of disease* **2009,** 33, (1), 28-36.

83. Solano, R. M.; Casarejos, M. J.; Menendez-Cuervo, J.; Rodriguez-Navarro, J. A.; Garcia de Yebenes, J.; Mena, M. A., Glial dysfunction in parkin null mice: effects of aging. *The Journal of neuroscience : the official journal of the Society for Neuroscience* **2008,** 28, (3), 598-611.

84. Batassini, C.; Broetto, N.; Tortorelli, L. S.; Borsoi, M.; Zanotto, C.; Galland, F.; Souza, T. M.; Leite, M. C.; Goncalves, C. A., Striatal Injury with 6-OHDA Transiently Increases Cerebrospinal GFAP and S100B. *Neural plasticity* **2015,** 2015, 387028.

85. Thannickal, T. C.; Lai, Y. Y.; Siegel, J. M., Hypocretin (orexin) cell loss in Parkinson's disease. *Brain : a journal of neurology* **2007,** 130, (Pt 6), 1586-95.

86. Sathe, K.; Maetzler, W.; Lang, J. D.; Mounsey, R. B.; Fleckenstein, C.; Martin, H. L.; Schulte, C.; Mustafa, S.; Synofzik, M.; Vukovic, Z.; Itohara, S.; Berg, D.; Teismann, P., S100B is increased in Parkinson's disease and ablation protects against MPTP-induced toxicity through the RAGE and TNF-alpha pathway. *Brain : a journal of neurology* **2012,** 135, (Pt 11), 3336-47.

87. Fardell, C.; Zettergren, A.; Ran, C.; Carmine Belin, A.; Ekman, A.; Sydow, O.; Backman, L.; Holmberg, B.; Dizdar, N.; Soderkvist, P.; Nissbrandt, H., S100B polymorphisms are associated with age of onset of Parkinson's disease. *BMC medical genetics* **2018,** 19, (1), 42.

88. Hohoff, C.; Ponath, G.; Freitag, C. M.; Kastner, F.; Krakowitzky, P.; Domschke, K.; Koelkebeck, K.; Kipp, F.; von Eiff, C.; Deckert, J.; Rothermundt, M., Risk variants in the S100B gene predict elevated S100B serum concentrations in healthy individuals. *American journal of medical genetics. Part B, Neuropsychiatric genetics : the official publication of the International Society of Psychiatric Genetics* **2010,** 153B, (1), 291-7.

89. Liu, J.; Wang, H.; Zhang, L.; Xu, Y.; Deng, W.; Zhu, H.; Qin, C., S100B transgenic

mice develop features of Parkinson's disease. *Archives of medical research* **2011,** 42, (1), 1-7.

90. Carvalho, D. Z.; Schonwald, S. V.; Schumacher-Schuh, A. F.; Braga, C. W.; Souza, D. O.; Oses, J. P.; Donis, K. C.; Rieder, C. R., Overnight S100B in Parkinson's Disease: A glimpse into sleep-related neuroinflammation. *Neuroscience letters* **2015,** 608, 57-63.

91. Hofmann, M. A.; Drury, S.; Fu, C.; Qu, W.; Taguchi, A.; Lu, Y.; Avila, C.; Kambham, N.; Bierhaus, A.; Nawroth, P.; Neurath, M. F.; Slattery, T.; Beach, D.; McClary, J.; Nagashima, M.; Morser, J.; Stern, D.; Schmidt, A. M., RAGE mediates a novel proinflammatory axis: a central cell surface receptor for S100/calgranulin polypeptides. *Cell* **1999,** 97, (7), 889-901.

92. Huttunen, H. J.; Kuja-Panula, J.; Sorci, G.; Agneletti, A. L.; Donato, R.; Rauvala, H., Coregulation of neurite outgrowth and cell survival by amphoterin and S100 proteins through receptor for advanced glycation end products (RAGE) activation. *The Journal of biological chemistry* **2000,** 275, (51), 40096-105.

93. Riuzzi, F.; Sorci, G.; Beccafico, S.; Donato, R., S100B engages RAGE or bFGF/FGFR1 in myoblasts depending on its own concentration and myoblast density. Implications for muscle regeneration. *PloS one* **2012,** 7, (1), e28700.

94. Ryczko, D.; Hanini-Daoud, M.; Condamine, S.; Breant, B. J. B.; Fougere, M.; Araya, R.; Kolta, A., S100beta-mediated astroglial control of firing and input processing in layer 5 pyramidal neurons of the mouse visual cortex. *The Journal of physiology* **2021,** 599, (2), 677-707.

95. Morquette, P.; Verdier, D.; Kadala, A.; Fethiere, J.; Philippe, A. G.; Robitaille, R.; Kolta, A., An astrocyte-dependent mechanism for neuronal rhythmogenesis. *Nature neuroscience* **2015,** 18, (6), 844-54.

96. Huntington, T. E.; Srinivasan, R., Astrocytic mitochondria in adult mouse brain slices show spontaneous calcium influx events with unique properties. *Cell Calcium* **2021,** 96, 102383.

97. Semyanov, A.; Henneberger, C.; Agarwal, A., Making sense of astrocytic calcium signals - from acquisition to interpretation. *Nat Rev Neurosci* **2020,** 21, (10), 551-564.

98. Srinivasan, R.; Huang, B. S.; Venugopal, S.; Johnston, A. D.; Chai, H.; Zeng, H.; Golshani, P.; Khakh, B. S., Ca(2+) signaling in astrocytes from Ip3r2(-/-) mice in brain slices and during startle responses in vivo. *Nature neuroscience* **2015,** 18, (5), 708-17.

99. Falkenburger, B. H.; Saridaki, T.; Dinter, E., Cellular models for Parkinson's disease. *Journal of neurochemistry* **2016,** 139 Suppl 1, 121-130.

100. Pingale, T.; Gupta, G. L., Classic and evolving animal models in Parkinson's disease. *Pharmacol Biochem Behav* **2020,** 199, 173060.

101. Park, I. H.; Arora, N.; Huo, H.; Maherali, N.; Ahfeldt, T.; Shimamura, A.; Lensch, M. W.; Cowan, C.; Hochedlinger, K.; Daley, G. Q., Disease-specific induced pluripotent stem cells. *Cell* **2008,** 134, (5), 877-86.

102. Soldner, F.; Hockemeyer, D.; Beard, C.; Gao, Q.; Bell, G. W.; Cook, E. G.; Hargus, G.; Blak, A.; Cooper, O.; Mitalipova, M.; Isacson, O.; Jaenisch, R.,

Parkinson's disease patient-derived induced pluripotent stem cells free of viral reprogramming factors. *Cell* **2009,** 136, (5), 964-77.

103. Bahmad, H.; Hadadeh, O.; Chamaa, F.; Cheaito, K.; Darwish, B.; Makkawi, A. K.; Abou-Kheir, W., Modeling Human Neurological and Neurodegenerative Diseases: From Induced Pluripotent Stem Cells to Neuronal Differentiation and Its Applications in Neurotrauma. *Frontiers in molecular neuroscience* **2017,** 10, 50.

104. Bose, A.; Petsko, G. A.; Studer, L., Induced pluripotent stem cells: a tool for modeling Parkinson’s disease. *Trends in Neurosciences* **2022,** 45, (8), 608-620.

105. Devine, M. J.; Ryten, M.; Vodicka, P.; Thomson, A. J.; Burdon, T.; Houlden, H.; Cavaleri, F.; Nagano, M.; Drummond, N. J.; Taanman, J. W.; Schapira, A. H.; Gwinn, K.; Hardy, J.; Lewis, P. A.; Kunath, T., Parkinson's disease induced pluripotent stem cells with triplication of the alpha-synuclein locus. *Nat Commun* **2011,** 2, 440.

106. Byers, B.; Cord, B.; Nguyen, H. N.; Schule, B.; Fenno, L.; Lee, P. C.; Deisseroth, K.; Langston, J. W.; Pera, R. R.; Palmer, T. D., SNCA triplication Parkinson's patient's iPSC-derived DA neurons accumulate alpha-synuclein and are susceptible to oxidative stress. *PloS one* **2011,** 6, (11), e26159.

107. Cooper, O.; Seo, H.; Andrabi, S.; Guardia-Laguarta, C.; Graziotto, J.; Sundberg, M.; McLean, J. R.; Carrillo-Reid, L.; Xie, Z.; Osborn, T.; Hargus, G.; Deleidi, M.; Lawson, T.; Bogetofte, H.; Perez-Torres, E.; Clark, L.; Moskowitz, C.; Mazzulli, J.; Chen, L.; Volpicelli-Daley, L.; Romero, N.; Jiang, H.; Uitti, R. J.; Huang, Z.; Opala, G.; Scarffe, L. A.; Dawson, V. L.; Klein, C.; Feng, J.; Ross, O. A.;

Trojanowski, J. Q.; Lee, V. M.; Marder, K.; Surmeier, D. J.; Wszolek, Z. K.; Przedborski, S.; Krainc, D.; Dawson, T. M.; Isacson, O., Pharmacological rescue of mitochondrial deficits in iPSC-derived neural cells from patients with familial Parkinson's disease. *Sci Transl Med* **2012,** 4, (141), 141ra90.

108. Nguyen, H. N.; Byers, B.; Cord, B.; Shcheglovitov, A.; Byrne, J.; Gujar, P.; Kee, K.; Schule, B.; Dolmetsch, R. E.; Langston, W.; Palmer, T. D.; Pera, R. R., LRRK2 mutant iPSC-derived DA neurons demonstrate increased susceptibility to oxidative stress. *Cell Stem Cell* **2011,** 8, (3), 267-80.

109. Jiang, H.; Ren, Y.; Yuen, E. Y.; Zhong, P.; Ghaedi, M.; Hu, Z.; Azabdaftari, G.; Nakaso, K.; Yan, Z.; Feng, J., Parkin controls dopamine utilization in human midbrain dopaminergic neurons derived from induced pluripotent stem cells. *Nat Commun* **2012,** 3, 668.

110. Vahsen, B. F.; Gray, E.; Candalija, A.; Cramb, K. M. L.; Scaber, J.; Dafinca, R.; Katsikoudi, A.; Xu, Y.; Farrimond, L.; Wade-Martins, R.; James, W. S.; Turner, M. R.; Cowley, S. A.; Talbot, K., Human iPSC co-culture model to investigate the interaction between microglia and motor neurons. *Scientific reports* **2022,** 12, (1), 12606.

111. Polymeropoulos, M. H.; Higgins, J. J.; Golbe, L. I.; Johnson, W. G.; Ide, S. E.; Di Iorio, G.; Sanges, G.; Stenroos, E. S.; Pho, L. T.; Schaffer, A. A.; Lazzarini, A. M.; Nussbaum, R. L.; Duvoisin, R. C., Mapping of a gene for Parkinson's disease to chromosome 4q21-q23. *Science (New York, N.Y.)* **1996,** 274, (5290), 1197-9.

112. Polymeropoulos, M. H.; Lavedan, C.; Leroy, E.; Ide, S. E.; Dehejia, A.; Dutra, A.;

Pike, B.; Root, H.; Rubenstein, J.; Boyer, R.; Stenroos, E. S.; Chandrasekharappa, S.; Athanassiadou, A.; Papapetropoulos, T.; Johnson, W. G.; Lazzarini, A. M.; Duvoisin, R. C.; Di Iorio, G.; Golbe, L. I.; Nussbaum, R. L., Mutation in the alpha-synuclein gene identified in families with Parkinson's disease. *Science (New York, N.Y.)* **1997,** 276, (5321), 2045-7.

113. Ungerstedt, U., 6-Hydroxy-dopamine induced degeneration of central monoamine neurons. *European journal of pharmacology* **1968,** 5, (1), 107-10.

114. Luthman, J.; Fredriksson, A.; Sundstrom, E.; Jonsson, G.; Archer, T., Selective lesion of central dopamine or noradrenaline neuron systems in the neonatal rat: motor behavior and monoamine alterations at adult stage. *Behav Brain Res* **1989,** 33, (3), 267-77.

115. Javoy, F.; Sotelo, C.; Herbet, A.; Agid, Y., Specificity of dopaminergic neuronal degeneration induced by intracerebral injection of 6-hydroxydopamine in the nigrostriatal dopamine system. *Brain Res* **1976,** 102, (2), 201-15.

116. Konnova, E. A.; Swanberg, M., Animal Models of Parkinson's Disease. In *Parkinson's Disease: Pathogenesis and Clinical Aspects*, Stoker, T. B.; Greenland, J. C., Eds. Brisbane (AU), 2018.

117. Przedborski, S.; Levivier, M.; Jiang, H.; Ferreira, M.; Jackson-Lewis, V.; Donaldson, D.; Togasaki, D. M., Dose-dependent lesions of the dopaminergic nigrostriatal pathway induced by intrastriatal injection of 6-hydroxydopamine. *Neuroscience* **1995,** 67, (3), 631-47.

118. Langston, J. W.; Ballard, P.; Tetrud, J. W.; Irwin, I., Chronic Parkinsonism in

humans due to a product of meperidine-analog synthesis. *Science (New York, N.Y.)* **1983,** 219, (4587), 979-80.

119. Langston, J. W.; Ballard, P. A., Jr., Parkinson's disease in a chemist working with 1-methyl-4-phenyl-1,2,5,6-tetrahydropyridine. *N Engl J Med* **1983,** 309, (5), 310.

120. Varastet, M.; Riche, D.; Maziere, M.; Hantraye, P., Chronic MPTP treatment reproduces in baboons the differential vulnerability of mesencephalic dopaminergic neurons observed in Parkinson's disease. *Neuroscience* **1994,** 63, (1), 47-56.

121. Ding, F.; Luan, L.; Ai, Y.; Walton, A.; Gerhardt, G. A.; Gash, D. M.; Grondin, R.; Zhang, Z., Development of a stable, early stage unilateral model of Parkinson's disease in middle-aged rhesus monkeys. *Experimental neurology* **2008,** 212, (2), 431-439.

122. Paumier, K. L.; Sukoff Rizzo, S. J.; Berger, Z.; Chen, Y.; Gonzales, C.; Kaftan, E.; Li, L.; Lotarski, S.; Monaghan, M.; Shen, W.; Stolyar, P.; Vasilyev, D.; Zaleska, M.; D. Hirst, W.; Dunlop, J., Behavioral Characterization of A53T Mice Reveals Early and Late Stage Deficits Related to Parkinson’s Disease. *PloS one* **2013,** 8, (8), e70274.

123. Chesselet, M.-F.; Richter, F.; Zhu, C.; Magen, I.; Watson, M. B.; Subramaniam, S. R., A Progressive Mouse Model of Parkinson’s Disease: The Thy1-aSyn (“Line 61”) Mice. *Neurotherapeutics : the journal of the American Society for Experimental NeuroTherapeutics* **2012,** 9, (2), 297-314.

124. Ekmark-Lewén, S.; Lindström, V.; Gumucio, A.; Ihse, E.; Behere, A.; Kahle, P.

J.; Nordström, E.; Eriksson, M.; Erlandsson, A.; Bergström, J.; Ingelsson, M., Early fine motor impairment and behavioral dysfunction in (Thy-1)-h[A30P] alpha-synuclein mice. *Brain and Behavior* **2018,** 8, (3), e00915.

125. Albert, K. V. M. H. A. U. D. A. A. M. A. A. V. V.-M. G. D. t. S. N. D. N. I. f. G. T.; Disease, M., In *Genes*, 2017; Vol. 8.

126. Huntington, T. E.; Srinivasan, R., Adeno-Associated Virus Expression of α-Synuclein as a Tool to Model Parkinson's Disease: Current Understanding and Knowledge Gaps. *Aging Dis* **2021,** 12, (4), 1120-1137.

127. Oliveras-Salvá, M.; Van der Perren, A.; Casadei, N.; Stroobants, S.; Nuber, S.; D'Hooge, R.; Van den Haute, C.; Baekelandt, V., rAAV2/7 vector-mediated overexpression of alpha-synuclein in mouse substantia nigra induces protein aggregation and progressive dose-dependent neurodegeneration. *Mol Neurodegener* **2013,** 8, (1), 44.

128. Recasens, A.; Ulusoy, A.; Kahle, P. J.; Di Monte, D. A.; Dehay, B., In vivo models of alpha-synuclein transmission and propagation. *Cell and Tissue Research* **2018,** 373, (1), 183-193.

129. Beccano-Kelly, D. A.; Volta, M.; Munsie, L. N.; Paschall, S. A.; Tatarnikov, I.; Co, K.; Chou, P.; Cao, L. P.; Bergeron, S.; Mitchell, E.; Han, H.; Melrose, H. L.; Tapia, L.; Raymond, L. A.; Farrer, M. J.; Milnerwood, A. J., LRRK2 overexpression alters glutamatergic presynaptic plasticity, striatal dopamine tone, postsynaptic signal transduction, motor activity and memory. *Hum Mol Genet* **2015,** 24, (5), 1336-49.

130. Garcia-Miralles, M.; Coomaraswamy, J.; Häbig, K.; Herzig, M. C.; Funk, N.; Gillardon, F.; Maisel, M.; Jucker, M.; Gasser, T.; Galter, D.; Biskup, S., No Dopamine Cell Loss or Changes in Cytoskeleton Function in Transgenic Mice Expressing Physiological Levels of Wild Type or G2019S Mutant LRRK2 and in Human Fibroblasts. *PloS one* **2015,** 10, (4), e0118947.

131. Li, X.; Patel, J. C.; Wang, J.; Avshalumov, M. V.; Nicholson, C.; Buxbaum, J. D.; Elder, G. A.; Rice, M. E.; Yue, Z., Enhanced striatal dopamine transmission and motor performance with LRRK2 overexpression in mice is eliminated by familial Parkinson's disease mutation G2019S. *The Journal of neuroscience : the official journal of the Society for Neuroscience* **2010,** 30, (5), 1788-97.

132. Liu, G.; Sgobio, C.; Gu, X.; Sun, L.; Lin, X.; Yu, J.; Parisiadou, L.; Xie, C.; Sastry, N.; Ding, J.; Lohr, K. M.; Miller, G. W.; Mateo, Y.; Lovinger, D. M.; Cai, H., Selective expression of Parkinson's disease-related Leucine-rich repeat kinase 2 G2019S missense mutation in midbrain dopaminergic neurons impairs dopamine release and dopaminergic gene expression. *Hum Mol Genet* **2015,** 24, (18), 5299-312.

133. Patriarchi, T.; Cho, J. R.; Merten, K.; Howe, M. W.; Marley, A.; Xiong, W. H.; Folk, R. W.; Broussard, G. J.; Liang, R.; Jang, M. J.; Zhong, H.; Dombeck, D.; von Zastrow, M.; Nimmerjahn, A.; Gradinaru, V.; Williams, J. T.; Tian, L., Ultrafast neuronal imaging of dopamine dynamics with designed genetically encoded sensors. *Science (New York, N.Y.)* **2018,** 360, (6396).

134. Li, Y.; Liu, W.; Oo, T. F.; Wang, L.; Tang, Y.; Jackson-Lewis, V.; Zhou, C.;

Geghman, K.; Bogdanov, M.; Przedborski, S.; Beal, M. F.; Burke, R. E.; Li, C., Mutant LRRK2(R1441G) BAC transgenic mice recapitulate cardinal features of Parkinson's disease. *Nature neuroscience* **2009,** 12, (7), 826-8.

135. Volpicelli-Daley, L. A.; Abdelmotilib, H.; Liu, Z.; Stoyka, L.; Daher, J. P. L.; Milnerwood, A. J.; Unni, V. K.; Hirst, W. D.; Yue, Z.; Zhao, H. T.; Fraser, K.; Kennedy, R. E.; West, A. B., G2019S-LRRK2 Expression Augments α-Synuclein Sequestration into Inclusions in Neurons. *The Journal of Neuroscience* **2016,** 36, (28), 7415-7427.

136. Lin, X.; Parisiadou, L.; Gu, X. L.; Wang, L.; Shim, H.; Sun, L.; Xie, C.; Long, C. X.; Yang, W. J.; Ding, J.; Chen, Z. Z.; Gallant, P. E.; Tao-Cheng, J. H.; Rudow, G.; Troncoso, J. C.; Liu, Z.; Li, Z.; Cai, H., Leucine-rich repeat kinase 2 regulates the progression of neuropathology induced by Parkinson's-disease-related mutant alpha-synuclein. *Neuron* **2009,** 64, (6), 807-27.

137. Barker, R. A.; Bjorklund, A.; Gash, D. M.; Whone, A.; Van Laar, A.; Kordower, J. H.; Bankiewicz, K.; Kieburtz, K.; Saarma, M.; Booms, S.; Huttunen, H. J.; Kells, A. P.; Fiandaca, M. S.; Stoessl, A. J.; Eidelberg, D.; Federoff, H.; Voutilainen, M. H.; Dexter, D. T.; Eberling, J.; Brundin, P.; Isaacs, L.; Mursaleen, L.; Bresolin, E.; Carroll, C.; Coles, A.; Fiske, B.; Matthews, H.; Lungu, C.; Wyse, R. K.; Stott, S.; Lang, A. E., GDNF and Parkinson's Disease: Where Next? A Summary from a Recent Workshop. *J Parkinsons Dis* **2020,** 10, (3), 875-891.

138. Manfredsson, F. P.; Polinski, N. K.; Subramanian, T.; Boulis, N.; Wakeman, D. R.; Mandel, R. J., The Future of GDNF in Parkinson's Disease. *Front Aging*

Neurosci **2020,** 12, 593572.

139. Serlin, Y.; Shelef, I.; Knyazer, B.; Friedman, A., Anatomy and physiology of the blood-brain barrier. *Semin Cell Dev Biol* **2015,** 38, 2-6.

140. Teleanu, D. M.; Negut, I.; Grumezescu, V.; Grumezescu, A. M.; Teleanu, R. I., Nanomaterials for Drug Delivery to the Central Nervous System. *Nanomaterials (Basel)* **2019,** 9, (3).

141. Goldsmith, M.; Abramovitz, L.; Peer, D., Precision nanomedicine in neurodegenerative diseases. *ACS Nano* **2014,** 8, (3), 1958-65.

142. Kong, S. D.; Lee, J.; Ramachandran, S.; Eliceiri, B. P.; Shubayev, V. I.; Lal, R.; Jin, S., Magnetic targeting of nanoparticles across the intact blood-brain barrier. *J Control Release* **2012,** 164, (1), 49-57.

143. Yuan, M.; Yan, T. H.; Li, J.; Xiao, Z.; Fang, Y.; Wang, Y.; Zhou, H. C.; Pellois, J. P., Superparamagnetic iron oxide-gold nanoparticles conjugated with porous coordination cages: Towards controlled drug release for non-invasive neuroregeneration. *Nanomedicine* **2021,** 35, 102392.

144. Chen, J.; Yuan, M.; Madison, C. A.; Eitan, S.; Wang, Y., Blood-brain Barrier Crossing using Magnetic Stimulated Nanoparticles. **2021**, 2021.12.23.472846.

CHAPTER II

EMERGING ROLES FOR ABERRANT ASTROCYTIC CALCIUM SIGNALS IN PARKINSON’S DISEASE*

Introduction

Astrocytes are ubiquitous cells of the central nervous system (CNS) that outnumber neurons in many brain regions [1]. These cells are important players in governing neuronal function via mechanisms such as synaptic pruning, neurotransmitter clearance, and extracellular K^+ buffering [2]. The critical role played by astrocytes in CNS function, makes it vitally important to understand the molecular mechanisms that underlie bidirectional communication between astrocytes and neurons.

Astrocytic Ca^{2+} signals are important for normal CNS function

Unlike neurons, astrocytes are not electrically excitable, which has necessitated inquiry into the molecular machinery utilized by astrocytes to exert their functional effects on neurons and neural circuits. In this regard, studies utilizing genetically encoded calcium indicators (GECIs) such as GCaMPs have shown that astrocytes

---

*Reprinted with permission from Bancroft E.A., Srinivasan R. Emerging Roles for Aberrant Astrocytic Calcium Signals in Parkinson’s Disease. *Front. Physiol*. January 2022. doi: 10.3389/fphys.2021.812212 possess a plethora of spontaneous Ca^{2+} signals *in situ* and *in vivo*. Astrocytic Ca^{2+} signals respond to a variety of pharmacological and behavioral stimuli [3], and are observed in intracellular compartments such as the soma, thick proximal branches, and fine astrocytic processes [4]. In addition, astrocytic Ca^{2+} signals occur via Ca^{2+} release from distinct subcellular organelles such as the endoplasmic reticulum (ER) [5] and mitochondria [6], as well as extracellular Ca^{2+} sources [4]. At a subcellular level, the mechanisms governing astrocytic Ca^{2+} signals in the soma are distinct from those in peripheral processes [7]. For example, Ca^{2+} signals in the soma and primary astrocytic processes occur due to metabotropic receptor activity, $InsP_3$-mediated release of Ca^{2+} from the ER and store-operated Ca^{2+} entry. On the other hand, Ca^{2+} signals in fine astrocytic processes depend on mitochondrial Ca^{2+} fluxes, ionotropic channels such as transient receptor potential (TRP) and reversal of the Na^+/Ca^{2+} exchanger, NCX. Together, these findings strongly suggest that astrocytic Ca^{2+} signals modulate a diverse array of signaling pathways not only in the astrocytes themselves, but also in the neural circuits within which they reside.

Critical roles for spontaneous astrocytic Ca^{2+} signals in CNS function are bolstered by studies showing that these signals regulate the probability of neurotransmitter release [8], long-term potentiation [9, 10], maintenance of blood brain barrier (BBB) integrity [11], neurotransmitter clearance [12, 13], and the synchronization and integration of neural activity [14-16]. Since these processes are vitally important for normal CNS function, it is likely that a disruption in spontaneous astrocytic Ca^{2+} signaling is potentially pathological. In this regard, a particularly interesting question is how aberrant astrocytic Ca^{2+} signals could contribute to neurodegeneration.

Aberrant astrocytic Ca^{2+} signaling and Parkinson's disease (PD)

Given their central role in brain function, it is not surprising that pathological alterations in astrocytes can accelerate the evolution of a variety of neurological diseases [17]. Indeed, neurodegenerative diseases such as amyotrophic lateral sclerosis (ALS), and Alzheimer's disease are characterized by distinct pathological changes in astrocytes. Examples of this include impaired glutamate uptake and death of motor neurons in ALS [18, 19] or reduced astrocyte coverage in Alzheimer's disease, which results in synaptic deficiency and early cognitive dysfunction [20]. Additionally, a recent study has shown that astrocytes derived from induced pluripotent stem cell (iPS) of PD patients with a leucine rich repeat kinase 2 (LRRK2) mutation display fragmented mitochondrial morphology, atrophic cellular morphology, altered Ca^{2+} signaling and metabolic impairment [21]. Together, these examples provide strong evidence for a central role of astrogliopathology in the evolution of neurodegenerative diseases.

Among the many known neurodegenerative disorders, PD is the second most common neurodegenerative disorder with no known cure [22]. PD is characterized by a progressive loss of substantia nigra pars compacta (SNc) dopaminergic (DA) neurons, and the onset of motor symptoms that include bradykinesia, resting tremors, postural instability, and muscle rigidity. Despite being labeled as a movement disorder, numerous non-motor symptoms are also observed during PD. These include sleep disturbances, constipation, anxiety, depression, and cognitive dysfunction [22, 23]. The complex clinical presentation of PD suggests a convergence of multiple mechanisms and cell types driving neurodegeneration. Most PD research, however, has focused on understanding pathological mechanisms that occur within the neurons themselves, without accounting for the role of astrocyte interactions with neurons, and other CNS cells during neurodegeneration. Consequently, neurocentric strategies have failed to result in the development of effective neuroprotective treatments for PD. In this context, we point to a central role for astrocytes, and more specifically, aberrant astrocytic Ca^{2+} signaling as an important contributing factor during the pathogenesis of PD.

Given the rapidly emerging importance of astrocytes in PD [24], as well as an urgent and unmet need to develop effective neuroprotective treatments, this review presents a perspective on potential mechanisms by which aberrant astrocytic Ca^{2+} signals can trigger, and possibly sustain neurodegeneration during the development of PD. We amalgamate recent independent reports to provide an evidence-based rationale for the role of aberrant astrocytic Ca^{2+} signals in pathologically altering three distinct elements of the CNS during PD, *viz.* neurons, microglia, and the blood brain barrier (BBB) (Figure 30).

Aberrant astrocytic Ca^{2+} signals can cause dysfunction in DA neurons

Protoplasmic astrocytes possess a bushy morphology with primary branches that give rise to very fine secondary branches, branchlets and leaflets [25, 26]. Fine processes from each astrocyte, can contact up to 150,000 synapses in rodents and over a million synapses in humans [27-29]. Based on the morphological relationship of astrocytic processes with neuronal synapses, spontaneous Ca^{2+} signals in astrocytic processes are optimally positioned to modulate neuronal function. In addition, the intimate morphological as well as functional relationship between astrocytes and neurons suggests that abnormal changes in Ca^{2+} signals within astrocytic processes can alter neuronal function and initiate neurodegeneration. In the sections below, we gather evidence from recent independent studies to illustrate exemplar mechanisms by which abnormal changes in astrocytic Ca^{2+} signals can trigger, and even sustain the degeneration of SNc DA neurons.

Excitatory amino acid transporter 2 (EAAT2)

Excess extracellular glutamate is a major mechanism for neurodegeneration [30, 31]. This can occur via mechanisms such as glutamate-mediated excitotoxicity [30], oxidative glutamate toxicity [32, 33], and immunoexcitotoxicity [34]. Astrocytes play a major role in neurotransmitter clearance [35] and specifically, glutamate clearance via astrocytic glutamate transporters such as EAAT2 [36]. Therefore, any reduction in astrocytic EAAT2 expression would result in abnormal levels of extracellular glutamate and neurodegeneration. Indeed, reductions in astrocytic EAAT2 expression are observed in multiple neurodegenerative diseases such as amyotrophic lateral sclerosis, Alzheimer’s disease and Huntington’s disease [37-39]. With regard to PD, two recent pieces of evidence are particularly relevant: (**i**) The targeted knockdown of EAAT2 in astrocytes causes degeneration of SNc DA neurons in a mouse model of PD [40], and (**ii**) Exposure of rodents to the PD toxin 6-hydroxydopamine (6-OHDA) causes a downregulation of EAAT2 [41].

A recent study shows that EAAT2 internalization from the surface of astrocytes increases in a Ca^{2+}-dependent manner [42]. Specifically, Ca^{2+} influx via the NCX sodium/calcium exchanger in response to increases in extracellular glutamate results in EAAT2 internalization. In a broader sense, one could infer that increased Ca^{2+} influx within astrocytes due to abnormal increases in extracellular neurotransmitters could result in EAAT2 internalization. We rationalize that a surge in striatal dopamine levels during early PD, as seen in the Thy1-α-synuclein mouse model of PD [43] can cause a downregulation of EAAT2 in striatal astrocytes. A recent study by Adermark *et al.* showed that pre-treatment of striatal brain slices with the D2 dopamine receptor agonist, sulpiride prevented synaptic depression induced by the EAAT2 blocker, TFB-TBOA [44]. These data suggest a rapid downregulation of EAAT2 function in striatal astrocytes due to an abnormal activation of striatal D2 receptors. In addition, studies have shown that synaptically released dopamine increases Ca^{2+} events in striatal astrocytes [45] and the activation of D2 receptors in ventral midbrain astrocytes causes a downregulation of EAAT2 expression [46].

When taken together, these studies point to aberrant dopamine-mediated Ca^{2+} signals in astrocytic processes as a potential mechanism for EAAT2 downregulation in astrocytes leading to excess extracellular glutamate and consequently, neurodegeneration.

Astrocytic mitochondria

Recent studies have shown that astrocytic processes contain mitochondria [6, 47, 48] and that mitochondria in fine astrocytic processes are closely associated with Ca^{2+} signals in their vicinity [48]. Interestingly, the Ca^{2+} signals associated with astrocytic mitochondria are abnormally increased in a mouse model of amyotrophic lateral sclerosis expressing a mutant form of superoxide dismutase (SOD G93A) [48], suggesting a role for abnormal mitochondrial Ca^{2+} signaling in fine astrocytic processes during neurodegeneration. In addition, we have shown that mitochondria in astrocytic processes display spontaneous Ca^{2+} influx with dual responses to neurotransmitter agonists, a dependency on ER Ca^{2+}, and the absence of functional mitochondrial uniporters (MCU) [6], suggesting that astrocytic mitochondria possess unique functional properties that optimally cater to the extensive energy needs of DA neurons. A significant proportion (~25%) of energy demands in the CNS are met by astrocytes [49], and spontaneous astrocytic mitochondrial Ca^{2+} signals derived from the endoplasmic reticulum (ER) activate mitochondrial dehydrogenases in order to generate the co-factors required for oxidative phosphorylation and ATP generation [50]. Disruption of Ca^{2+} signals in astrocytic mitochondria could therefore be a harbinger for neurodegeneration.

Given the important role of α-synuclein (α-syn) in the pathogenesis of PD, it is pertinent to discuss aberrant Ca^{2+} signals in mitochondria within astrocytic processes as it relates to α-syn pathology. Recent studies have shown that astrocytes readily take up extracellular α-syn aggregates, and that α-syn can damage astrocytic mitochondria [51], as well as alter molecular tethering between the mitochondria and ER, resulting in disrupted Ca^{2+} homeostasis [52]. Together, these reports suggest that pathological forms of α-syn can bind to astrocytic mitochondria, which could alter mitochondrial Ca^{2+} signaling in astrocytes, thereby causing a significant reduction in ATP generation and DA neuron loss. It is also important to note that astrocytes are coupled via gap junctions [53]. Therefore, pathological changes in mitochondrial Ca^{2+} signals in just a few astrocytes can affect larger populations of astrocytes within neural structures, thus magnifying the effects of aberrant astrocytic mitochondrial Ca^{2+} signaling on brain function and neurodegeneration.

Aberrant astrocytic Ca^{2+} signals can activate microglia

Microglia are classically viewed as the immune surveillance cells of the brain, with functions that include phagocytosis and synaptic pruning [54-56]. In the context of DA neuron loss in PD, microglial reactivity is a strong indicator of neuroinflammation and ongoing neuropathology. There is evidence for microglial activation in clinical PD [57-60], as well as in rodent [61-64] and non-human primate models of parkinsonism [65-68]. There are potential mechanisms by which aberrant Ca^{2+} signals in astrocytes could play a role in initiating microglial activation during PD. In the sections below, we present two potential scenarios in which aberrant changes in spontaneous astrocytic Ca^{2+}

signals could lead to abnormal crosstalk between astrocytes and microglia, thus accelerating neuronal loss in PD.

Aquaporin 4 (AQP4)

AQP4 is a tetrameric water channel, abundantly expressed in astrocytes [69, 70]. Emerging evidence suggests a role for AQP4 dysfunction in PD. Studies supporting this idea include findings that: (**i**) Humans with Lewy body pathology in the neocortex demonstrate a negative correlation between AQP4 expressing astrocytes and α-synuclein aggregates, such that astrocytes with AQP4 expression do not appear in areas with abnormal α-synuclein expression [71], (**ii**) Exposure of AQP4 knockout (KO) mice to the PD toxin, MPTP causes an increase in the susceptibility of SNc DA neurons to degeneration [72], (**iii**) AQP4 KO mice show diminished differences between ventral tegmental area (VTA) and SNc DA neurons in their susceptibility to MPTP-induced neurodegeneration [73], and (**iv**) AQP4 knockout mice display significant increases in microglial reactivity following exposure to MPTP when compared to wildtype littermates. In this case, the study also shows that the increase in microglial reactivity occurs due to secretion of neuroinflammatory molecules such as interleukin 1β (IL1β) and tumor necrosis factor α (TNFα) [74]. When taken together, these studies converge on the idea that a functional deficiency of AQP4 in astrocytes can result in microglial activation with a consequent increase in the secretion of neuroinflammatory molecules by activated microglia, in turn resulting in the loss of DA neurons.

As is the case for any channel, the ability of AQP4 to allow passage of water molecules through its pore requires precise localization at the plasma membrane. In this regard, studies show that AQP4 depends on Ca^{2+} for localization to the plasma membrane [75, 76], and that rapid translocation of AQP4 to the plasma membrane depends on Ca^{2+} signals. Furthermore, a recent study has utilized STORM-based superresolution microscopy to show that AQP4 channels cluster in very specific patterns at astrocytic endfeet [77]. Thus, there exists an intricate relationship between Ca^{2+} signaling and the normal functional localization of AQP4 in astrocytes. Based on these data, one can infer that pathological changes in spontaneous astrocytic Ca^{2+} signals will result in the mislocalization and functional deficit of astrocytic AQP4, leading to microglial activation and neuroinflammation in the brain.

Apolipoprotein E (ApoE)

An allelic variant of the ApoE gene, ApoE4 significantly increases the risk for Alzheimer's disease (AD) [78-80]. In the case of PD, a recent study created ApoE locus-targeted ApoE4 replacement mice, and utilized these mice to show that ApoE4 increases α-synuclein pathology, worsens behavioral deficits, and accelerates astrogliosis [81]. This study also showed that ApoE4 increases α-synuclein pathology in PD patients.

In the CNS, astrocytes are a major reservoir for ApoE [82, 83], and ApoE4 secretion occurs in a Ca^{2+}-dependent manner [84]. Thus, any pathological alteration in the kinetics of astrocytic Ca^{2+} signals can alter the secretion of ApoE4 from astrocytes.

Based on this rationale, increases in spontaneous astrocyte Ca^{2+} signal amplitudes as seen in reactive astrocytes [85] could increase ApoE4 secretion by astrocytes, leading to microglial activation [86, 87], increased α-synuclein uptake by microglia [88], the formation of toxic α-synuclein aggregates [89] and neurodegeneration. Although we do not yet know what may initiate aberrant Ca^{2+} signaling in astrocytes, abnormal α-synuclein uptake by astrocytes could disrupt Ca^{2+} homeostasis, and is therefore a likely candidate for triggering aberrant Ca^{2+} signals in SNc astrocytes during PD.

Aberrant astrocytic endfoot Ca^{2+} signals and BBB integrity

The BBB is an important protective barrier that allows selective passage of molecules into the brain parenchyma. Abnormal increases in BBB permeability can allow the passage of environmental toxins into the midbrain, thereby accelerating DA neuron loss. This view is supported by the epidemiological finding that pesticide exposure is associated with an increased incidence of PD in farmers [90]. In this context, a histological study of striatal brain sections from PD patients has shown abnormal extravasation of erythrocytes, as well as an increase in extravascular serum proteins such as fibrin and hemoglobin into striatal parenchyma, suggesting a loss of BBB integrity during PD [91]. Another recent study used dynamic contrast enhanced magnetic resonance imaging in 49 PD patients to show significantly higher BBB leakage in posterior white matter regions of PD patients compared to healthy controls [92]. These studies suggest that a loss of BBB integrity is likely involved in the pathogenesis of clinical PD.

The emerging evidence for a compromised BBB in PD patients motivates inquiry into whether or not astrocytes contribute to the maintenance of BBB integrity. In this regard, a recent study has utilized GLAST Cre/ERT2 mice driving the expression of the diphtheria toxin in astrocytes to ablate astrocytes in sparse regions of blood vessels. This study showed an extravasation of cadaverine from blood vessels following toxin-induced astrocyte ablation in mice [11], which strongly suggests that astrocytic endfeet do indeed play a central role in maintaining the physical integrity of the BBB.

Together, the findings described above lead to the important question of whether or not disruptions in Ca^{2+} signals in astrocytic endfeet could compromise the established dependence of tight junction proteins (TJPs) on Ca^{2+} [93, 94], thereby altering BBB integrity. Although there is currently no clear evidence for a causative role of aberrant endfoot Ca^{2+} signals in altering TJP biology in PD, the use of new imaging modalities such as multiphoton microscopes in combination with astrocyte-specific transgenic mice [95] and genetically encoded Ca^{2+} sensors in astrocytes should enable an understanding of the role of aberrant astrocytic endfoot Ca^{2+} signals in TJP and BBB function during PD.

Conclusion

In this perspective review, we discuss potential pathological mechanisms during PD in which aberrant astrocytic Ca^{2+} signals cause either neuronal dysfunction, microglial activation, or a loss of BBB integrity (Figure 30). Although we do not discuss what triggers abnormal Ca^{2+} signals in astrocytes during PD in the first place, molecules such as ApoE4 and α-synuclein likely initiate abnormal Ca^{2+} signaling in astrocytes via multiple and distinct mechanisms. It is therefore reasonable to hypothesize that once they are initiated, abnormal astrocytic Ca^{2+} signals cause further abnormalities in ApoE4 or α-synuclein, thereby setting up a vicious feedback loop between aberrant astrocytic Ca^{2+} signaling and ApoE4 or α-synuclein pathology in PD.

An additional point to note is that neurons, microglia and the BBB are also capable of directly interacting with each other, which would result in a complex network of multi-tiered pathological interactions. Based on this view, we predict that the coming decades will unravel specific mechanisms by which aberrant astrocytic Ca^{2+} signals modulate multi-tiered interactions between these seemingly distinct CNS compartments, eventually leading to neurodegeneration.

Figures

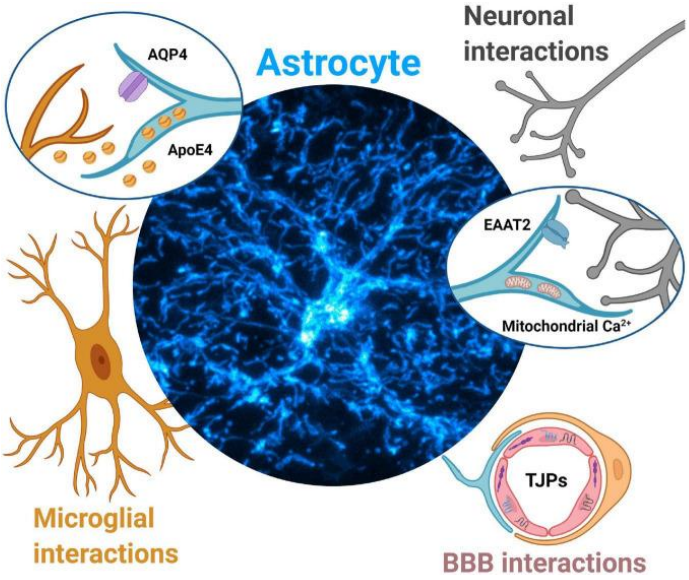

Figure 1: Aberrant astrocytic Ca^{2+} signals contribute to Parkinson's disease pathology via multiple mechanisms.

Neuronal interactions. Dopamine surges during early PD may dysregulate astrocytic Ca^{2+} signals and lead to EAAT1 internalization, leading to reduced glutamate clearance and initiation of excitotoxic cell death for dopaminergic midbrain neurons. Disruptions in astrocytic mitochondria Ca^{2+} signals (triggered from protein aggregates such as α-synuclein) lead to reduced ATP production, alteration of mitochondria-ER tethering, likely contributing to dopaminergic neurodegeneration. *Microglial interactions.* Aberrant astrocytic Ca^{2+} signals drive mislocalization of AQP4 channels in astrocytes. AQP4 deficiency in astrocytes is associated with increases in microglial activity and further secretion of inflammatory cytokines, ultimately contributing to dopaminergic neurodegeneration. Aberrant astrocytic Ca^{2+} signals may drive increased secretion of

ApoE4 which leads to microglial reactivity, increased α-synuclein pathology and eventually dopaminergic neurodegeneration. *Blood brain barrier (BBB) interactions.* Aberrant Ca^{2+} signals in astrocyte endfeet may result in altered secretion of neurotrophic factors such as GDNF, leading to dysregulation of tight junction proteins (TJPs), compromised BBB integrity, and further contribute to dopaminergic neurodegeneration.

References

1. von Bartheld, C. S.; Bahney, J.; Herculano-Houzel, S., The search for true numbers of neurons and glial cells in the human brain: A review of 150 years of cell counting. *The Journal of comparative neurology* **2016,** 524, (18), 3865-3895.
2. Verkhratsky, A.; Nedergaard, M., Physiology of Astroglia. *Physiol Rev* **2018,** 98, (1), 239-389.
3. Semyanov, A.; Henneberger, C.; Agarwal, A., Making sense of astrocytic calcium signals - from acquisition to interpretation. *Nat Rev Neurosci* **2020,** 21, (10), 551-564.
4. Srinivasan, R.; Huang, B. S.; Venugopal, S.; Johnston, A. D.; Chai, H.; Zeng, H.; Golshani, P.; Khakh, B. S., Ca(2+) signaling in astrocytes from Ip3r2(-/-) mice in brain slices and during startle responses in vivo. *Nature neuroscience* **2015,** 18, (5), 708-17.
5. Okubo, Y.; Kanemaru, K.; Suzuki, J.; Kobayashi, K.; Hirose, K.; Iino, M., Inositol 1,4,5-trisphosphate receptor type 2-independent Ca(2+) release from the

endoplasmic reticulum in astrocytes. *Glia* **2019,** 67, (1), 113-124.

6. Huntington, T. E.; Srinivasan, R., Astrocytic mitochondria in adult mouse brain slices show spontaneous calcium influx events with unique properties. *Cell Calcium* **2021,** 96, 102383.
7. Verkhratsky, A.; Semyanov, A.; Zorec, R., Physiology of Astroglial Excitability. *Function* **2020,** 1, (2).
8. Covelo, A.; Araque, A., Neuronal activity determines distinct gliotransmitter release from a single astrocyte. *eLife* **2018,** 7.
9. Shigetomi, E.; Jackson-Weaver, O.; Huckstepp, R. T.; O'Dell, T. J.; Khakh, B. S., TRPA1 channels are regulators of astrocyte basal calcium levels and long-term potentiation via constitutive D-serine release. *The Journal of neuroscience : the official journal of the Society for Neuroscience* **2013,** 33, (24), 10143-53.
10. Arizono, M.; Inavalli, V.; Panatier, A.; Pfeiffer, T.; Angibaud, J.; Levet, F.; Ter Veer, M. J. T.; Stobart, J.; Bellocchio, L.; Mikoshiba, K.; Marsicano, G.; Weber, B.; Oliet, S. H. R.; Nagerl, U. V., Structural basis of astrocytic Ca(2+) signals at tripartite synapses. *Nat Commun* **2020,** 11, (1), 1906.
11. Heithoff, B. P.; George, K. K.; Phares, A. N.; Zuidhoek, I. A.; Munoz-Ballester, C.; Robel, S., Astrocytes are necessary for blood-brain barrier maintenance in the adult mouse brain. *Glia* **2021,** 69, (2), 436-472.
12. Shigetomi, E.; Tong, X.; Kwan, K. Y.; Corey, D. P.; Khakh, B. S., TRPA1 channels regulate astrocyte resting calcium and inhibitory synapse efficacy through GAT-3. *Nature neuroscience* **2011,** 15, (1), 70-80.

13. Haustein, M. D.; Kracun, S.; Lu, X. H.; Shih, T.; Jackson-Weaver, O.; Tong, X.; Xu, J.; Yang, X. W.; O'Dell, T. J.; Marvin, J. S.; Ellisman, M. H.; Bushong, E. A.; Looger, L. L.; Khakh, B. S., Conditions and constraints for astrocyte calcium signaling in the hippocampal mossy fiber pathway. *Neuron* **2014,** 82, (2), 413-29.

14. Sasaki, T.; Ishikawa, T.; Abe, R.; Nakayama, R.; Asada, A.; Matsuki, N.; Ikegaya, Y., Astrocyte calcium signalling orchestrates neuronal synchronization in organotypic hippocampal slices. *The Journal of physiology* **2014,** 592, (13), 2771-83.

15. Pirttimaki, T. M.; Sims, R. E.; Saunders, G.; Antonio, S. A.; Codadu, N. K.; Parri, H. R., Astrocyte-Mediated Neuronal Synchronization Properties Revealed by False Gliotransmitter Release. *The Journal of neuroscience : the official journal of the Society for Neuroscience* **2017,** 37, (41), 9859-9870.

16. Deemyad, T.; Luthi, J.; Spruston, N., Astrocytes integrate and drive action potential firing in inhibitory subnetworks. *Nat Commun* **2018,** 9, (1), 4336.

17. Verkhratsky, A.; Zorec, R.; Rodriguez, J. J.; Parpura, V., Neuroglia: Functional Paralysis and Reactivity in Alzheimer's Disease and Other Neurodegenerative Pathologies. *Adv Neurobiol* **2017,** 15, 427-449.

18. Rossi, D.; Brambilla, L.; Valori, C. F.; Roncoroni, C.; Crugnola, A.; Yokota, T.; Bredesen, D. E.; Volterra, A., Focal degeneration of astrocytes in amyotrophic lateral sclerosis. *Cell Death Differ* **2008,** 15, (11), 1691-700.

19. Valori, C. F.; Brambilla, L.; Martorana, F.; Rossi, D., The multifaceted role of glial cells in amyotrophic lateral sclerosis. *Cellular and molecular life sciences : CMLS*

2014, 71, (2), 287-97.

20. Verkhratsky, A.; Zorec, R.; Rodriguez, J. J.; Parpura, V., Astroglia dynamics in ageing and Alzheimer's disease. *Curr Opin Pharmacol* **2016,** 26, 74-9.

21. Ramos-Gonzalez, P.; Mato, S.; Chara, J. C.; Verkhratsky, A.; Matute, C.; Cavaliere, F., Astrocytic atrophy as a pathological feature of Parkinson's disease with LRRK2 mutation. *NPJ Parkinsons Dis* **2021,** 7, (1), 31.

22. Poewe, W.; Seppi, K.; Tanner, C. M.; Halliday, G. M.; Brundin, P.; Volkmann, J.; Schrag, A. E.; Lang, A. E., Parkinson disease. *Nat Rev Dis Primers* **2017,** 3, 17013.

23. Schapira, A. H. V.; Chaudhuri, K. R.; Jenner, P., Non-motor features of Parkinson disease. *Nat Rev Neurosci* **2017,** 18, (7), 435-450.

24. Booth, H. D. E.; Hirst, W. D.; Wade-Martins, R., The Role of Astrocyte Dysfunction in Parkinson's Disease Pathogenesis. *Trends Neurosci* **2017,** 40, (6), 358-370.

25. Zhou, B.; Zuo, Y. X.; Jiang, R. T., Astrocyte morphology: Diversity, plasticity, and role in neurological diseases. *CNS Neurosci Ther* **2019,** 25, (6), 665-673.

26. Moye, S. L.; Diaz-Castro, B.; Gangwani, M. R.; Khakh, B. S., Visualizing Astrocyte Morphology Using Lucifer Yellow Iontophoresis. *Journal of visualized experiments : JoVE* **2019**, (151).

27. Semyanov, A.; Verkhratsky, A., Astrocytic processes: from tripartite synapses to the active milieu. *Trends Neurosci* **2021,** 44, (10), 781-792.

28. Bushong, E. A.; Martone, M. E.; Jones, Y. Z.; Ellisman, M. H., Protoplasmic astrocytes in CA1 stratum radiatum occupy separate anatomical domains. *The*

Journal of neuroscience : the official journal of the Society for Neuroscience **2002,** 22, (1), 183-92.

29. Oberheim, N. A.; Takano, T.; Han, X.; He, W.; Lin, J. H.; Wang, F.; Xu, Q.; Wyatt, J. D.; Pilcher, W.; Ojemann, J. G.; Ransom, B. R.; Goldman, S. A.; Nedergaard, M., Uniquely hominid features of adult human astrocytes. *J Neurosci* **2009,** 29, (10), 3276-87.

30. Lewerenz, J.; Maher, P., Chronic Glutamate Toxicity in Neurodegenerative Diseases-What is the Evidence? *Front Neurosci* **2015,** 9, 469.

31. Ambrosi, G.; Cerri, S.; Blandini, F., A further update on the role of excitotoxicity in the pathogenesis of Parkinson's disease. *J Neural Transm (Vienna)* **2014,** 121, (8), 849-59.

32. Wang, J.; Wang, F.; Mai, D.; Qu, S., Molecular Mechanisms of Glutamate Toxicity in Parkinson's Disease. *Front Neurosci* **2020,** 14, 585584.

33. Schubert, D.; Piasecki, D., Oxidative glutamate toxicity can be a component of the excitotoxicity cascade. *J Neurosci* **2001,** 21, (19), 7455-62.

34. Blaylock, R. L., Parkinson's disease: Microglial/macrophage-induced immunoexcitotoxicity as a central mechanism of neurodegeneration. *Surg Neurol Int* **2017,** 8, 65.

35. Eulenburg, V.; Gomeza, J., Neurotransmitter transporters expressed in glial cells as regulators of synapse function. *Brain Res Rev* **2010,** 63, (1-2), 103-12.

36. Lehre, K. P.; Danbolt, N. C., The number of glutamate transporter subtype molecules at glutamatergic synapses: chemical and stereological quantification in

young adult rat brain. *J Neurosci* **1998,** 18, (21), 8751-7.

37. Bruijn, L. I.; Becher, M. W.; Lee, M. K.; Anderson, K. L.; Jenkins, N. A.; Copeland, N. G.; Sisodia, S. S.; Rothstein, J. D.; Borchelt, D. R.; Price, D. L.; Cleveland, D. W., ALS-linked SOD1 mutant G85R mediates damage to astrocytes and promotes rapidly progressive disease with SOD1-containing inclusions. *Neuron* **1997,** 18, (2), 327-38.

38. Sharma, A.; Kazim, S. F.; Larson, C. S.; Ramakrishnan, A.; Gray, J. D.; McEwen, B. S.; Rosenberg, P. A.; Shen, L.; Pereira, A. C., Divergent roles of astrocytic versus neuronal EAAT2 deficiency on cognition and overlap with aging and Alzheimer's molecular signatures. *Proc Natl Acad Sci U S A* **2019,** 116, (43), 21800-21811.

39. Tong, X.; Ao, Y.; Faas, G. C.; Nwaobi, S. E.; Xu, J.; Haustein, M. D.; Anderson, M. A.; Mody, I.; Olsen, M. L.; Sofroniew, M. V.; Khakh, B. S., Astrocyte Kir4.1 ion channel deficits contribute to neuronal dysfunction in Huntington's disease model mice. *Nat Neurosci* **2014,** 17, (5), 694-703.

40. Zhang, Y.; Meng, X.; Jiao, Z.; Liu, Y.; Zhang, X.; Qu, S., Generation of a Novel Mouse Model of Parkinson's Disease via Targeted Knockdown of Glutamate Transporter GLT-1 in the Substantia Nigra. *ACS Chem Neurosci* **2020,** 11, (3), 406-417.

41. Chotibut, T.; Meadows, S.; Kasanga, E. A.; McInnis, T.; Cantu, M. A.; Bishop, C.; Salvatore, M. F., Ceftriaxone reduces L-dopa-induced dyskinesia severity in 6-hydroxydopamine parkinson's disease model. *Mov Disord* **2017,** 32, (11), 1547-

1556.

42. Ibanez, I.; Bartolome-Martin, D.; Piniella, D.; Gimenez, C.; Zafra, F., Activity dependent internalization of the glutamate transporter GLT-1 requires calcium entry through the NCX sodium/calcium exchanger. *Neurochem Int* **2019,** 123, 125-132.

43. Lam, H. A.; Wu, N.; Cely, I.; Kelly, R. L.; Hean, S.; Richter, F.; Magen, I.; Cepeda, C.; Ackerson, L. C.; Walwyn, W.; Masliah, E.; Chesselet, M. F.; Levine, M. S.; Maidment, N. T., Elevated tonic extracellular dopamine concentration and altered dopamine modulation of synaptic activity precede dopamine loss in the striatum of mice overexpressing human alpha-synuclein. *Journal of neuroscience research* **2011,** 89, (7), 1091-102.

44. Adermark, L.; Lagstrom, O.; Loften, A.; Licheri, V.; Havenang, A.; Loi, E. A.; Stomberg, R.; Soderpalm, B.; Domi, A.; Ericson, M., Astrocytes modulate extracellular neurotransmitter levels and excitatory neurotransmission in dorsolateral striatum via dopamine D2 receptor signaling. *Neuropsychopharmacology* **2021**.

45. Corkrum, M.; Covelo, A.; Lines, J.; Bellocchio, L.; Pisansky, M.; Loke, K.; Quintana, R.; Rothwell, P. E.; Lujan, R.; Marsicano, G.; Martin, E. D.; Thomas, M. J.; Kofuji, P.; Araque, A., Dopamine-Evoked Synaptic Regulation in the Nucleus Accumbens Requires Astrocyte Activity. *Neuron* **2020,** 105, (6), 1036-1047 e5.

46. Xin, W.; Schuebel, K. E.; Jair, K. W.; Cimbro, R.; De Biase, L. M.; Goldman, D.;

Bonci, A., Ventral midbrain astrocytes display unique physiological features and sensitivity to dopamine D2 receptor signaling. *Neuropsychopharmacology* **2019,** 44, (2), 344-355.

47. Derouiche, A.; Haseleu, J.; Korf, H. W., Fine Astrocyte Processes Contain Very Small Mitochondria: Glial Oxidative Capability May Fuel Transmitter Metabolism. *Neurochem Res* **2015,** 40, (12), 2402-13.

48. Agarwal, A.; Wu, P. H.; Hughes, E. G.; Fukaya, M.; Tischfield, M. A.; Langseth, A. J.; Wirtz, D.; Bergles, D. E., Transient Opening of the Mitochondrial Permeability Transition Pore Induces Microdomain Calcium Transients in Astrocyte Processes. *Neuron* **2017,** 93, (3), 587-605 e7.

49. van Hall, G.; Stromstad, M.; Rasmussen, P.; Jans, O.; Zaar, M.; Gam, C.; Quistorff, B.; Secher, N. H.; Nielsen, H. B., Blood lactate is an important energy source for the human brain. *J Cereb Blood Flow Metab* **2009,** 29, (6), 1121-9.

50. Cardenas, C.; Miller, R. A.; Smith, I.; Bui, T.; Molgo, J.; Muller, M.; Vais, H.; Cheung, K. H.; Yang, J.; Parker, I.; Thompson, C. B.; Birnbaum, M. J.; Hallows, K. R.; Foskett, J. K., Essential regulation of cell bioenergetics by constitutive InsP3 receptor Ca2+ transfer to mitochondria. *Cell* **2010,** 142, (2), 270-83.

51. Lindstrom, V.; Gustafsson, G.; Sanders, L. H.; Howlett, E. H.; Sigvardson, J.; Kasrayan, A.; Ingelsson, M.; Bergstrom, J.; Erlandsson, A., Extensive uptake of alpha-synuclein oligomers in astrocytes results in sustained intracellular deposits and mitochondrial damage. *Mol Cell Neurosci* **2017,** 82, 143-156.

52. Paillusson, S.; Gomez-Suaga, P.; Stoica, R.; Little, D.; Gissen, P.; Devine, M. J.;

Noble, W.; Hanger, D. P.; Miller, C. C. J., alpha-Synuclein binds to the ER-mitochondria tethering protein VAPB to disrupt Ca(2+) homeostasis and mitochondrial ATP production. *Acta Neuropathol* **2017,** 134, (1), 129-149.

53. Fujii, Y.; Maekawa, S.; Morita, M., Astrocyte calcium waves propagate proximally by gap junction and distally by extracellular diffusion of ATP released from volume-regulated anion channels. *Scientific reports* **2017,** 7, (1), 13115.

54. Li, Q.; Barres, B. A., Microglia and macrophages in brain homeostasis and disease. *Nat Rev Immunol* **2018,** 18, (4), 225-242.

55. Bohlen, C. J.; Friedman, B. A.; Dejanovic, B.; Sheng, M., Microglia in Brain Development, Homeostasis, and Neurodegeneration. *Annu Rev Genet* **2019,** 53, 263-288.

56. Bartels, T.; De Schepper, S.; Hong, S., Microglia modulate neurodegeneration in Alzheimer's and Parkinson's diseases. *Science (New York, N.Y.)* **2020,** 370, (6512), 66-69.

57. Bartels, A. L.; Willemsen, A. T.; Doorduin, J.; de Vries, E. F.; Dierckx, R. A.; Leenders, K. L., [11C]-PK11195 PET: quantification of neuroinflammation and a monitor of anti-inflammatory treatment in Parkinson's disease? *Parkinsonism & related disorders* **2010,** 16, (1), 57-9.

58. Gerhard, A.; Pavese, N.; Hotton, G.; Turkheimer, F.; Es, M.; Hammers, A.; Eggert, K.; Oertel, W.; Banati, R. B.; Brooks, D. J., In vivo imaging of microglial activation with [11C](R)-PK11195 PET in idiopathic Parkinson's disease. *Neurobiology of disease* **2006,** 21, (2), 404-12.

59. Stokholm, M. G.; Iranzo, A.; Ostergaard, K.; Serradell, M.; Otto, M.; Svendsen, K. B.; Garrido, A.; Vilas, D.; Borghammer, P.; Santamaria, J.; Moller, A.; Gaig, C.; Brooks, D. J.; Tolosa, E.; Pavese, N., Assessment of neuroinflammation in patients with idiopathic rapid-eye-movement sleep behaviour disorder: a case-control study. *Lancet Neurol* **2017,** 16, (10), 789-796.

60. McGeer, P. L.; Itagaki, S.; Boyes, B. E.; McGeer, E. G., Reactive microglia are positive for HLA-DR in the substantia nigra of Parkinson's and Alzheimer's disease brains. *Neurology* **1988,** 38, (8), 1285-91.

61. Czlonkowska, A.; Kohutnicka, M.; Kurkowska-Jastrzebska, I.; Czlonkowski, A., Microglial reaction in MPTP (1-methyl-4-phenyl-1,2,3,6-tetrahydropyridine) induced Parkinson's disease mice model. *Neurodegeneration* **1996,** 5, (2), 137-43.

62. Hoenen, C.; Gustin, A.; Birck, C.; Kirchmeyer, M.; Beaume, N.; Felten, P.; Grandbarbe, L.; Heuschling, P.; Heurtaux, T., Alpha-Synuclein Proteins Promote Pro-Inflammatory Cascades in Microglia: Stronger Effects of the A53T Mutant. *PloS one* **2016,** 11, (9), e0162717.

63. Sanchez-Guajardo, V.; Febbraro, F.; Kirik, D.; Romero-Ramos, M., Microglia acquire distinct activation profiles depending on the degree of alpha-synuclein neuropathology in a rAAV based model of Parkinson's disease. *PLoS One* **2010,** 5, (1), e8784.

64. Wu, D. C.; Jackson-Lewis, V.; Vila, M.; Tieu, K.; Teismann, P.; Vadseth, C.; Choi, D. K.; Ischiropoulos, H.; Przedborski, S., Blockade of microglial activation is neuroprotective in the 1-methyl-4-phenyl-1,2,3,6-tetrahydropyridine mouse model

of Parkinson disease. *J Neurosci* **2002,** 22, (5), 1763-71.

65. Kanaan, N. M.; Kordower, J. H.; Collier, T. J., Age and region-specific responses of microglia, but not astrocytes, suggest a role in selective vulnerability of dopamine neurons after 1-methyl-4-phenyl-1,2,3,6-tetrahydropyridine exposure in monkeys. *Glia* **2008,** 56, (11), 1199-214.

66. Barkholt, P.; Sanchez-Guajardo, V.; Kirik, D.; Romero-Ramos, M., Long-term polarization of microglia upon alpha-synuclein overexpression in nonhuman primates. *Neuroscience* **2012,** 208, 85-96.

67. Barcia, C.; Sanchez Bahillo, A.; Fernandez-Villalba, E.; Bautista, V.; Poza, Y. P. M.; Fernandez-Barreiro, A.; Hirsch, E. C.; Herrero, M. T., Evidence of active microglia in substantia nigra pars compacta of parkinsonian monkeys 1 year after MPTP exposure. *Glia* **2004,** 46, (4), 402-9.

68. McGeer, P. L.; Schwab, C.; Parent, A.; Doudet, D., Presence of reactive microglia in monkey substantia nigra years after 1-methyl-4-phenyl-1,2,3,6-tetrahydropyridine administration. *Annals of neurology* **2003,** 54, (5), 599-604.

69. Hubbard, J. A.; Hsu, M. S.; Seldin, M. M.; Binder, D. K., Expression of the Astrocyte Water Channel Aquaporin-4 in the Mouse Brain. *ASN Neuro* **2015,** 7, (5).

70. Tham, D. K.; Joshi, B.; Moukhles, H., Aquaporin-4 Cell-Surface Expression and Turnover Are Regulated by Dystroglycan, Dynamin, and the Extracellular Matrix in Astrocytes. *PloS one* **2016,** 11, (10), e0165439.

71. Hoshi, A.; Tsunoda, A.; Tada, M.; Nishizawa, M.; Ugawa, Y.; Kakita, A.,

Expression of Aquaporin 1 and Aquaporin 4 in the Temporal Neocortex of Patients with Parkinson's Disease. *Brain Pathol* **2017,** 27, (2), 160-168.

72. Fan, Y.; Kong, H.; Shi, X.; Sun, X.; Ding, J.; Wu, J.; Hu, G., Hypersensitivity of aquaporin 4-deficient mice to 1-methyl-4-phenyl-1,2,3,6-tetrahydropyrindine and astrocytic modulation. *Neurobiology of aging* **2008,** 29, (8), 1226-36.

73. Zhang, J.; Yang, B.; Sun, H.; Zhou, Y.; Liu, M.; Ding, J.; Fang, F.; Fan, Y.; Hu, G., Aquaporin-4 deficiency diminishes the differential degeneration of midbrain dopaminergic neurons in experimental Parkinson's disease. *Neurosci Lett* **2016,** 614, 7-15.

74. Sun, H.; Liang, R.; Yang, B.; Zhou, Y.; Liu, M.; Fang, F.; Ding, J.; Fan, Y.; Hu, G., Aquaporin-4 mediates communication between astrocyte and microglia: Implications of neuroinflammation in experimental Parkinson's disease. *Neuroscience* **2016,** 317, 65-75.

75. Kitchen, P.; Salman, M. M.; Halsey, A. M.; Clarke-Bland, C.; MacDonald, J. A.; Ishida, H.; Vogel, H. J.; Almutiri, S.; Logan, A.; Kreida, S.; Al-Jubair, T.; Winkel Missel, J.; Gourdon, P.; Tornroth-Horsefield, S.; Conner, M. T.; Ahmed, Z.; Conner, A. C.; Bill, R. M., Targeting Aquaporin-4 Subcellular Localization to Treat Central Nervous System Edema. *Cell* **2020,** 181, (4), 784-799 e19.

76. Salman, M. M.; Kitchen, P.; Woodroofe, M. N.; Brown, J. E.; Bill, R. M.; Conner, A. C.; Conner, M. T., Hypothermia increases aquaporin 4 (AQP4) plasma membrane abundance in human primary cortical astrocytes via a calcium/transient receptor potential vanilloid 4 (TRPV4)- and calmodulin-mediated mechanism. *Eur*

J Neurosci **2017,** 46, (9), 2542-2547.

77. Smith, A. J.; Verkman, A. S., Superresolution Imaging of Aquaporin-4 Cluster Size in Antibody-Stained Paraffin Brain Sections. *Biophys J* **2015,** 109, (12), 2511-2522.

78. Lambert, J. C.; Ibrahim-Verbaas, C. A.; Harold, D.; Naj, A. C.; Sims, R.; Bellenguez, C.; DeStafano, A. L.; Bis, J. C.; Beecham, G. W.; Grenier-Boley, B.; Russo, G.; Thorton-Wells, T. A.; Jones, N.; Smith, A. V.; Chouraki, V.; Thomas, C.; Ikram, M. A.; Zelenika, D.; Vardarajan, B. N.; Kamatani, Y.; Lin, C. F.; Gerrish, A.; Schmidt, H.; Kunkle, B.; Dunstan, M. L.; Ruiz, A.; Bihoreau, M. T.; Choi, S. H.; Reitz, C.; Pasquier, F.; Cruchaga, C.; Craig, D.; Amin, N.; Berr, C.; Lopez, O. L.; De Jager, P. L.; Deramecourt, V.; Johnston, J. A.; Evans, D.; Lovestone, S.; Letenneur, L.; Moron, F. J.; Rubinsztein, D. C.; Eiriksdottir, G.; Sleegers, K.; Goate, A. M.; Fievet, N.; Huentelman, M. W.; Gill, M.; Brown, K.; Kamboh, M. I.; Keller, L.; Barberger-Gateau, P.; McGuiness, B.; Larson, E. B.; Green, R.; Myers, A. J.; Dufouil, C.; Todd, S.; Wallon, D.; Love, S.; Rogaeva, E.; Gallacher, J.; St George-Hyslop, P.; Clarimon, J.; Lleo, A.; Bayer, A.; Tsuang, D. W.; Yu, L.; Tsolaki, M.; Bossu, P.; Spalletta, G.; Proitsi, P.; Collinge, J.; Sorbi, S.; Sanchez-Garcia, F.; Fox, N. C.; Hardy, J.; Deniz Naranjo, M. C.; Bosco, P.; Clarke, R.; Brayne, C.; Galimberti, D.; Mancuso, M.; Matthews, F.; European Alzheimer's Disease, I.; Genetic; Environmental Risk in Alzheimer's, D.; Alzheimer's Disease Genetic, C.; Cohorts for, H.; Aging Research in Genomic, E.; Moebus, S.; Mecocci, P.; Del Zompo, M.; Maier, W.; Hampel, H.; Pilotto, A.; Bullido, M.;

Panza, F.; Caffarra, P.; Nacmias, B.; Gilbert, J. R.; Mayhaus, M.; Lannefelt, L.; Hakonarson, H.; Pichler, S.; Carrasquillo, M. M.; Ingelsson, M.; Beekly, D.; Alvarez, V.; Zou, F.; Valladares, O.; Younkin, S. G.; Coto, E.; Hamilton-Nelson, K. L.; Gu, W.; Razquin, C.; Pastor, P.; Mateo, I.; Owen, M. J.; Faber, K. M.; Jonsson, P. V.; Combarros, O.; O'Donovan, M. C.; Cantwell, L. B.; Soininen, H.; Blacker, D.; Mead, S.; Mosley, T. H., Jr.; Bennett, D. A.; Harris, T. B.; Fratiglioni, L.; Holmes, C.; de Bruijn, R. F.; Passmore, P.; Montine, T. J.; Bettens, K.; Rotter, J. I.; Brice, A.; Morgan, K.; Foroud, T. M.; Kukull, W. A.; Hannequin, D.; Powell, J. F.; Nalls, M. A.; Ritchie, K.; Lunetta, K. L.; Kauwe, J. S.; Boerwinkle, E.; Riemenschneider, M.; Boada, M.; Hiltuenen, M.; Martin, E. R.; Schmidt, R.; Rujescu, D.; Wang, L. S.; Dartigues, J. F.; Mayeux, R.; Tzourio, C.; Hofman, A.; Nothen, M. M.; Graff, C.; Psaty, B. M.; Jones, L.; Haines, J. L.; Holmans, P. A.; Lathrop, M.; Pericak-Vance, M. A.; Launer, L. J.; Farrer, L. A.; van Duijn, C. M.; Van Broeckhoven, C.; Moskvina, V.; Seshadri, S.; Williams, J.; Schellenberg, G. D.; Amouyel, P., Meta-analysis of 74,046 individuals identifies 11 new susceptibility loci for Alzheimer's disease. *Nat Genet* **2013,** 45, (12), 1452-8.

79. Yamazaki, Y.; Zhao, N.; Caulfield, T. R.; Liu, C. C.; Bu, G., Apolipoprotein E and Alzheimer disease: pathobiology and targeting strategies. *Nat Rev Neurol* **2019,** 15, (9), 501-518.

80. Liu, C. C.; Liu, C. C.; Kanekiyo, T.; Xu, H.; Bu, G., Apolipoprotein E and Alzheimer disease: risk, mechanisms and therapy. *Nat Rev Neurol* **2013,** 9, (2), 106-18.

81. Zhao, N.; Attrebi, O. N.; Ren, Y.; Qiao, W.; Sonustun, B.; Martens, Y. A.; Meneses, A. D.; Li, F.; Shue, F.; Zheng, J.; Van Ingelgom, A. J.; Davis, M. D.; Kurti, A.; Knight, J. A.; Linares, C.; Chen, Y.; Delenclos, M.; Liu, C. C.; Fryer, J. D.; Asmann, Y. W.; McLean, P. J.; Dickson, D. W.; Ross, O. A.; Bu, G., APOE4 exacerbates alpha-synuclein pathology and related toxicity independent of amyloid. *Sci Transl Med* **2020,** 12, (529).

82. Sun, Y.; Wu, S.; Bu, G.; Onifade, M. K.; Patel, S. N.; LaDu, M. J.; Fagan, A. M.; Holtzman, D. M., Glial fibrillary acidic protein-apolipoprotein E (apoE) transgenic mice: astrocyte-specific expression and differing biological effects of astrocyte-secreted apoE3 and apoE4 lipoproteins. *J Neurosci* **1998,** 18, (9), 3261-72.

83. Xu, Q.; Bernardo, A.; Walker, D.; Kanegawa, T.; Mahley, R. W.; Huang, Y., Profile and regulation of apolipoprotein E (ApoE) expression in the CNS in mice with targeting of green fluorescent protein gene to the ApoE locus. *J Neurosci* **2006,** 26, (19), 4985-94.

84. Kockx, M.; Guo, D. L.; Huby, T.; Lesnik, P.; Kay, J.; Sabaretnam, T.; Jary, E.; Hill, M.; Gaus, K.; Chapman, J.; Stow, J. L.; Jessup, W.; Kritharides, L., Secretion of apolipoprotein E from macrophages occurs via a protein kinase A and calcium-dependent pathway along the microtubule network. *Circ Res* **2007,** 101, (6), 607-16.

85. Shigetomi, E.; Saito, K.; Sano, F.; Koizumi, S., Aberrant Calcium Signals in Reactive Astrocytes: A Key Process in Neurological Disorders. *International journal of molecular sciences* **2019,** 20, (4).

86. Maezawa, I.; Nivison, M.; Montine, K. S.; Maeda, N.; Montine, T. J., Neurotoxicity from innate immune response is greatest with targeted replacement of E4 allele of apolipoprotein E gene and is mediated by microglial p38MAPK. *FASEB J* **2006,** 20, (6), 797-9.

87. Vitek, M. P.; Brown, C. M.; Colton, C. A., APOE genotype-specific differences in the innate immune response. *Neurobiol Aging* **2009,** 30, (9), 1350-60.

88. Choi, I.; Zhang, Y.; Seegobin, S. P.; Pruvost, M.; Wang, Q.; Purtell, K.; Zhang, B.; Yue, Z., Microglia clear neuron-released alpha-synuclein via selective autophagy and prevent neurodegeneration. *Nat Commun* **2020,** 11, (1), 1386.

89. Davis, A. A.; Inman, C. E.; Wargel, Z. M.; Dube, U.; Freeberg, B. M.; Galluppi, A.; Haines, J. N.; Dhavale, D. D.; Miller, R.; Choudhury, F. A.; Sullivan, P. M.; Cruchaga, C.; Perlmutter, J. S.; Ulrich, J. D.; Benitez, B. A.; Kotzbauer, P. T.; Holtzman, D. M., APOE genotype regulates pathology and disease progression in synucleinopathy. *Sci Transl Med* **2020,** 12, (529).

90. Freire, C.; Koifman, S., Pesticide exposure and Parkinson's disease: epidemiological evidence of association. *Neurotoxicology* **2012,** 33, (5), 947-71.

91. Gray, M. T.; Woulfe, J. M., Striatal blood-brain barrier permeability in Parkinson's disease. *J Cereb Blood Flow Metab* **2015,** 35, (5), 747-50.

92. Al-Bachari, S.; Naish, J. H.; Parker, G. J. M.; Emsley, H. C. A.; Parkes, L. M., Blood-Brain Barrier Leakage Is Increased in Parkinson's Disease. *Front Physiol* **2020,** 11, 593026.

93. Stuart, R. O.; Sun, A.; Panichas, M.; Hebert, S. C.; Brenner, B. M.; Nigam, S. K.,

Critical role for intracellular calcium in tight junction biogenesis. *J Cell Physiol* **1994,** 159, (3), 423-33.

94. Brown, R. C.; Davis, T. P., Calcium modulation of adherens and tight junction function: a potential mechanism for blood-brain barrier disruption after stroke. *Stroke* **2002,** 33, (6), 1706-11.

95. Srinivasan, R.; Lu, T. Y.; Chai, H.; Xu, J.; Huang, B. S.; Golshani, P.; Coppola, G.; Khakh, B. S., New Transgenic Mouse Lines for Selectively Targeting Astrocytes and Studying Calcium Signals in Astrocyte Processes In Situ and In Vivo. *Neuron* **2016,** 92, (6), 1181-1195.

CHAPTER III

QUANTIFYING SPONTANEOUS CALCIUM FLUXES AND THEIR DOWNSTREAM EFFECTS IN PRIMARY MOUSE MIDBRAIN NEURONS*

Introduction

Parkinson's Disease (PD) is the second most common neurodegenerative disorder worldwide, with no known cure. Estimates suggest that PD prevalence will continue to increase and is projected to surpass 1 million diagnoses by the year 2030 in the United States alone [1]. With few effective treatments currently available to combat PD, there is a pressing need to develop more effective therapies. PD is characterized by a rapid and progressive loss of midbrain dopamine (DA) neurons [2]. The mechanisms that underlie neurodegeneration in PD are poorly understood. Evidence suggests a likely convergence of multiple mechanisms, such as oxidative stress, mitochondrial dysfunction, etc. that contribute to the initiation of apoptotic signaling cascades and eventual cell death [3].

One such convergent mechanism, glutamate-mediated excitotoxicity has been implicated in multiple neurodegenerative diseases, including PD [4]. While glutamate-mediated excitotoxicity is thought to work mainly through stimulation of NMDA

*Reprinted with permission from an open access publication Bancroft EA, Srinivasan R. Quantifying Spontaneous Ca^{2+} Fluxes and their Downstream Effects in Primary Mouse Midbrain Neurons. Journal of Visualized Experiments. September 2020. Volume 163, e61481, doi:10.3791/61481 receptors via an excessive increase in intracellular Ca^{2+} concentration and eventual initiation of apoptosis, Ca^{2+}-permeable AMPA receptors have also been implicated in the excitotoxic response [5-7]. Therefore, it is of interest to determine the contribution of AMPA receptors to glutamate-mediated apoptosis within a PD model. This can be achieved using NBQX, an AMPA and kainate blocker, which at micromolar concentrations is selective for AMAPR receptors [8]. Glutamate-mediated excitotoxicity and apoptotic signaling cascades are an ideal downstream target to measure the extent of cell death, and a potential target for therapeutic intervention. Therefore, developing a high-content method for assessing glutamate-mediated modulation of calcium activity and associated downstream signaling in primary ventral mesencephalic (VM) neurons would be valuable for screening novel treatment methods on their ability to preserve neuronal health.

Here, we have developed a protocol in which we express the genetically encoded calcium indicator (GECI), GCaMP6f, using AAV2/5 with the human synapsin (hSyn) promotor to measure the Ca^{2+} activity of mouse VM primary neurons in response to glutamate application can be measured at the physiological and molecular level. This high-content screening can be adapted for discovering pharmaceuticals or treatments that modulate Ca^{2+} activity to preserve the health of VM neurons. We propose that this primary culture model is an effective way to screen for novel PD interventions, based on their ability to preserve the health of VM neurons and mitigate the progression of PD.

Protocol

All procedures involving the use of animal subjects have been approved by the Texas A&M University Institutional Animal Care and Use Committee (25th Nov 2019; AUP# 2019-0346).

NOTE: Preparation of cell culture solutions should be done using sterile procedure in a biological safety cabinet and filtered at 0.2 µm to prevent contamination.

1. Preparation of solutions and culture medium

1.1. Prepare laminin coating solution by diluting 20 µL of 1 mg/mL laminin stock into 2 mL of sterile distilled H_2O. Prepare on the day of dissection.

1.2. Prepare 10% equine (horse) serum stop solution by adding 5 mL of ES to 45 mL of 1x Hank’s Balanced Salt Solution (HBSS). Sterile filter using a 0.2 µm filter system or syringe filter tip. Store at 4 °C.

1.3. Prepare 4% bovine serum albumin (BSA) stock solution by adding 2 g of BSA powder to 1x phosphate-buffered saline (PBS) and bringing to a final volume of 45 mL. Sterile filter using a 0.2 µm filter system or syringe filter tip. Store at 4 °C.

1.4. Prepare papain stock solution by diluting papain to 3 mg/mL in 1x HBSS. Sterile filter using a 0.2 µm filter system or syringe filter tip. Store at -20 °C.

1.5. Prepare deoxyribonuclease (DNase) solution by adding 20 mg of DNase powder to sterile H_2O and bringing to a final volume of 20 mL. Sterile filter using a 0.2 µm filter system or syringe filter tip. Store at -20 °C.

1.6. Prepare ascorbic acid stock solution by adding 352 mg of ascorbic acid to sterile distilled H_2O and bringing to a final volume of 20 mL. Heat in 37 °C bath to dissolve if necessary. Sterile filter using a 0.2 µm filter system or syringe filter tip. Store at -20 °C.

1.7. Prepare Cell Culture Medium by adding the following to 50 mL of Neurobasal medium: 500 µL of Glutamax (100x), 500 µL equine serum, 1 mL of B-27, 100 µL of ascorbic acid, 500 µL of penicillin-streptomycin, 50 µL of kanamycin and 50 µL of ampicillin. Sterile filter using a 0.2 µm filter system. Store at 4 °C.

1.8. Prepare 0.01% Triton X-100 Solution by adding 1 mL of Triton X-100 into 9 mL of 1x PBS to make a 10% solution. As Triton X-100 is viscous, pipette slowly to allow tip to fill completely. Heat in 37 °C bath to dissolve if necessary. Store at 4 °C.

1.9. To dilute 10% stock to 0.01%, perform 3 serial 1:10 dilutions. Dilute 1 mL of 10% stock into 9 mL of 1x PBS to make 1% solution. Dilute 1 mL of 1% solution into 9 mL of

1x PBS to make 0.1% solution. Dilute 1 mL of 0.1% solution into 9 mL of 1x PBS to make a 0.01% solution.

1.10. Prepare 10% and 1% normal goat serum (NGS) solution by adding 1 mL of NGS to 9 mL of 1x PBS for a 10% solution. Add 100 µL of NGS to 9.9 mL of 1x PBS to make 1% solution.

1.11. Prepare glutamate stock solution (100 mM) by adding 735 mg of L(+)-Glutamic acid to sterile distilled H_2O and bring to a final volume of 50 mL. Solubility at this concentration will be an issue. Adding small volumes (100 µL) of 1 M hydrochloric acid is sufficient to increase solubility.

1.12. Prepare NBQX stock solution (10 mM) by adding 50 mg of NBQX to sterile distilled H_2O and bring to a final volume of 13 mL.

2. Preparation of culture dishes and coverslips (Done the day before dissection)

NOTE: We have found that combining three coating agents, poly-L-lysine, poly-L-ornithine, and laminin allows for ideal cell adhesion and viability.

2.1. Place 10 35 mm Petri dishes in a biological safety cabinet. Place two circular 12 mm coverslips in each dish and fill with 70% EtOH for 10 min. Use a vacuum line to aspirate the remaining EtOH from each dish, allowing the EtOH to evaporate completely.

2.2. Pipette ~90-100 µL of 0.1% poly-L-lysine solution onto each coverslip, making sure that the entire coverslip is covered by the poly-L-lysine solution. Cover the dishes with lids and place in a 37 °C incubator for 1 h.

2.3. Aspirate remaining poly-L-lysine solution from each coverslip and rinse with sterile H_2O.

2.4. Repeat steps 2.2 – 2.3 with 0.1% poly-L-ornithine solution.

2.5. Again, repeat steps 2.2 – 2.3 with 0.01% laminin solution. Place in a 37 °C/5% CO_2 incubator until ready for cell plating.

3. Mouse embryonic dissections

NOTE: We use between 4 to 6 timed pregnant mice per culture. While much of the dissection process occurs outside of a biological safety cabinet it is still important to maintain sterile procedure. Plentiful use of 70% EtOH on surfaces near the dissection microscope and on surgical tools is ideal. A mask may also be worn during the dissection to further prevent contamination. Additionally, we use 4 separate antibiotics in the culture medium, so contamination is unlikely. However, if use of antibiotics is problematic, this dissection setup could be moved inside a sterile hood. To preserve cell viability all dissection solutions should be pre-chilled at 4 ˚C, and dissections should be completed as quickly as possible. We do not perform the dissections on ice. The method for dissection of mouse embryonic midbrain neurons is identical to previously described methods [9, 10].

3.1. Prepare a space on a bench near a dissection microscope with an absorbent pad and spray liberally with 70% EtOH.

3.2. Spray two 100 x 15 mm glass Petri dishes and one 50 x 10 mm glass Petri dish with 70% EtOH and allow EtOH to evaporate. Once evaporated, place 50 mL of sterile 1x HBSS into each 100 x 15 mm Petri dish.

3.3. Submerge surgical scissors, forceps, and microtome blade in 70% EtOH for 10 min minimum to sterilize. Place instruments on the absorbent pad to dry.

3.4. Using CO_2 followed by cervical dislocation, euthanize 2-3 month old timed pregnancy mice on embryonic day 14.

3.5. Spray the abdomen of the euthanized mice with 70% EtOH. Using forceps grab the lower abdomen and open the abdominal cavity using surgical scissors. Start cutting near where the forceps are holding the abdomen, making lateral cuts on each side until the abdominal wall can be folded back and the uterus is clearly visible.

3.6. Using surgical scissors, cut both ends of the uterine horn. Then remove the uterus and place into Petri dish with 1x HBSS.

3.7. Using straight-tip forceps carefully remove embryos from the uterus. Leave embryos in HBSS throughout this process. Using either the forceps or a microtome blade, quickly decapitate embryos by cutting near the neck. Making as level a cut as possible.

3.8. Under a dissecting microscope, move an embryo head to a dry 50 mm Petri dish and place on the ventral side. Stabilize the head with forceps by placing and penetrating near the eyes/snout. Forceps should be angled downward at ~45° to avoid penetrating the mesencephalon.

3.9. Using the forceps in the other hand, carefully remove the translucent layer of skin and skull just before the prominent ridge of the mesencephalon. Start near the midline and remove skin and skull caudally until the mesencephalon is fully exposed.

3.10. Hold the forceps perpendicular to the exposed mesencephalon with one tip between the cortex and mesencephalon and the other near the cerebellum. Press down and pinch the forceps together to remove the entire midbrain. The midbrain segment should be approximately 0.5 mm thick. Place the midbrain segment into the second Petri dish filled with fresh 1x HBSS. Repeat this process for each embryo.

3.11. Using the dissection microscope, position the brain segment with the ventral side facing up. If the meninges are still attached, carefully remove it by grabbing with the forceps and lifting up and away from the brain segment.

3.12. The brain segment should have 4 visible quadrants. Place the segment in such a manner that the two smaller quadrants are positioned superior to the two larger quadrants. There is a prominent ridge separating the superior two (small) quadrants from the inferior two (large) quadrants.

3.13. Using the forceps pinch and separate the superior quadrants from the inferior quadrants, and then discard the superior quadrants. The remaining inferior quadrants will have excess tissue laterally on the dorsal side, this tissue will look less opaque than the remaining ventral tissue. Remove the less dense dorsal tissue and discard. The remaining segment should contain both the Substantia nigra pars compacta (SNc) and the ventral tegmental area (VTA).

3.14. Using the forceps cut the remaining ventral tissue segment into 4 smaller pieces and using a 1mL wide bore pipette transfer these segments in a 15 mL conical tube with 1x HBSS. Keep the conical tube with brain segments on ice throughout the procedure.

3.15. Repeat this process for all remaining brain segments.

4. Dissociation of cells

4.1. Enzymatic digestion of cells

4.1.1. Carefully aspirate the HBSS from the 15 mL conical tube containing midbrain segments, leaving the segments at the bottom of the tube.

4.1.2. Add ~800 µL of papain solution to the tube and place in a 37 °C incubator for 7 min. Resuspend cells by flicking the tube and replace to the 37 °C incubator for an additional 7 min.

4.1.3. With a wide-bore 1 mL pipette tip remove only the midbrain segments into a 1 mL aliquot of DNase. Allow the segments to reach the bottom of the aliquot or about 1 min of exposure.

4.1.4. With a wide-bore 1 mL pipette tip remove only the midbrain segments into a 15 mL conical tube containing 2 mL of stop solution. Allow segments to settle at the bottom of the tube and repeat the rinse in an additional conical tube filled with stop solution.

4.2. Mechanical trituration of cell suspension

4.2.1. In the second stop solution rinse tube, using a wide-bore 1 mL pipette tip, pipette the cells up and down 10 times until there are no large tissue segments visible. It is important to avoid over trituration for minimal cell lysis.

4.2.2. Slowly pipette 300 µL of 4% BSA solution to the bottom of the 15 mL conical tube containing brain segments. Carefully remove the pipette tip to maintain a suspension layer. Centrifuge at 0.4 x *g* for 3 min. Then carefully aspirate the supernatant and resuspend cells in 400 µL of cell culture medium.

5. Plating the cells

NOTE: Based on experience, about 100,000 viable cells per embryo are collected. 2-3 month old timed pregnant mice typically have litter sizes of 8-10 embryos; therefore, a rough estimate for total yield of cells per timed pregnant mouse is approximately 1 million cells.

5.1. Using a hemocytometer preform a cell count and then dilute the suspension to 2,000 cells/µL using cell culture medium. Triturate briefly to mix.

5.2. Remove coverslips with laminin solution from step 2 from the incubator and aspirate the remaining laminin solution from the coated coverslips using a vacuum. Plate quickly to avoid the coverslips from drying completely. Pipette 100 µL (2.0 x 10^5 cells/coverslip) onto each coverslip and place Petri dishes into a 37 °C incubator for 1 h.

5.3. Carefully add 3 mL of cell culture medium to each dish and place back into the 37 °C incubator. Preform half medium changes 2 times per week for 2 weeks.

6. *Infection of cell culture at 14 DIV with adeno-associated viral (AAV) vectors*

6.1. For each dish prepare 1 mL of serum free DMEM medium with 1 µL of hSyn-GCaMP6f AAV (1.0 x 10^{13} titer)

6.2. Aspirate the cell culture medium from each dish and replace with 1 mL of serum free DMEM containing hSyn-GCaMP6f. Place dishes back into the 37 °C incubator for 1 h.

6.3. Aspirate the serum free medium containing AAVs and replace with 3 mL of cell culture medium. Place dishes back into the 37 °C incubator. We have found that 5-7 days of AAV infection allows for ideal levels of GCaMP expression. Continue to change medium every 2-3 days throughout this period of viral infection.

7. *Live confocal Ca^{2+} imaging between 19-21 DIV*

NOTE: As mentioned in step 6.3, imaging can be done between 5-7 days following viral infection. This is the ideal window to achieve visible expression of the fluorophore at levels which allow for detection of spontaneous Ca^{2+} activity.

7.1. Preparation of recording buffers

7.1.1. To make 1 L of HEPES recording buffer, add: 9.009 g of NaCl, 0.3728 g of KCl, 0.901 g of D-glucose, 2.381 g of HEPES, 2 mL of 1 M $CaCl_2$ stock solution, and 500 µL of 1 M $MgCl_2$ stock solution to 800 mL of sterile distilled H_2O. Bring the pH to 7.4 with NaOH. Bring to a final volume of 1 L.

7.1.2. To make 200 mL of 20 µM glutamate recording buffer, dilute 40 µL of 100 mM glutamate stock solution into 200 mL of HEPES recording buffer described above.

7.1.3. To make 200 mL of 10 µM NBQX recording buffer, dilute 200 µL of 10 mM NBQX stock solution into 200 mL of HEPES recording buffer.

7.2. Confocal imaging

7.2.1. Fill a sterile 35 mm Petri dish with 3 mL of recording buffer.

7.2.2. Remove a 35 mm Petri dish with infected cultures from the 37 °C incubator. Using fine tip forceps, carefully grab the edge of one coverslip and transfer it quickly into the Petri dish filled with recording buffer. Place the remaining coverslip in medium back into the 37 °C incubator. Transport the dish with recording buffer to the confocal microscope.

7.2.3. Start the imaging software. Proceed to next step while it initializes.

7.2.4. Start the peristaltic pump and place the line into the recording buffer. Calibrate the speed of flow to be 2 mL/min.

7.2.5. Transfer the infected coverslip from the 35 mm Petri dish into the recording bath.

7.2.6. Using the 10x water immersion objective and BF light, find the plane of focus and look for a region with a high density of neuron cell bodies. Switch to the 40x water immersion objective and using BF light refocus the sample.

7.2.7. In the “Dyes list” window within FluoView select AlexaFluor 488 and apply it.

7.2.8. AAV expression can be variable; therefore, in order to prevent overexposure and photobleaching of the fluorophores, start with low HV and laser power settings. For the AlexaFluor 488 channel, set the high voltage (HV) to 500, the gain to 1x, and offset to 0. For the 488 laser line set the power to 5%. In order to increase the effective volume imaged in the z-plane, increase the pinhole size to 300 μm. Use the “focus x2” scanning option to optimally adjust emission signals to sub-saturation levels. From here, settings can be adjusted until ideal visibility of each channel is achieved.

NOTE: To accurately capture the full range of Ca^{2+} fluxes with GCaMP, adjust the baseline HV and laser power settings in order to allow for an increase in fluorescent intensity without oversaturating the detector.

7.2.9. Once microscope settings are optimized, move the stage in order to locate a region with multiple cells displaying spontaneous changes in GCaMP6f fluorescence and focus to the desired plane for imaging.

7.2.10. Use the “Clip rect” tool to clip the imaging frame to a size that can achieve a frame interval of just under 1 second. This is necessary to set the imaging interval at 1 frame per second.

7.2.11. Set the “Interval” window to a value of 1.0 and the “Num” window to 600.

NOTE: In order to deliver different recording buffers at the desired time point (300 s), it is important to calibrate the latency of the pump to deliver the new solution to the bath. This will be dependent on the solution perfusion rate (2 mL/min) and the length of the line used to pump solution.

7.2.12. To capture a t-series movie select the “Time” option and then use the “XYt” scanning option to begin imaging.

7.2.13. Watch the imaging progress bar and move the line from the HEPES recording buffer into the 20 µM glutamate recording buffer at the appropriate time point (e.g., if the latency of the pump is calibrated to deliver solution at 60 s, move the line into the glutamate buffer at 240 frames in order to deliver glutamate at 300 s).

7.2.14. When imaging is complete, select the *Series Done* button and save the finished t-series movie. Continue to perfuse 20 µM Glutamate for an additional 5 min, so that the cultured neurons have been exposed to glutamate for a total of 10 min. Repeat this process for each coverslip to be imaged.

7.2.15. Following the additional 5 min exposure to 20 µM Glutamate, remove the coverslip from the bath and place back into the 35mm Petri dish containing recording buffer until the day of imaging is completed. When finished, proceed to step 8.

7.3. Ca^{2+} trace analysis

7.3.1. Perform image analysis in ImageJ. Install the BIO-FORMATS plugin for ImageJ, which will allow .OIB image files to open.

7.3.2. In the ImageJ toolbar, click *Analyze | Set Measurements*, and select the box for Mean gray value (MGV).

7.3.3. In ImageJ, open a t-series movie as a hyperstack.

7.3.4. Drag the slider for the movie and identify the frame with maximal glutamate response to visualize all neurons that respond to glutamate. Use the polygon tool to trace all visible neuron cell bodies, adding their ROIs to the "ROI manager" list.

7.3.5. When finished tracing and adding ROIs, select all ROIs within the *ROI Manager* window and use the *Multi measure* selection in the *more* list of options. Copy and paste these data into a spreadsheet. Complete this process for all movies to be analyzed.

7.3.6. For each ROI, convert the raw MGV data from each frame to $\Delta F/F_0$ values using the equation: $\Delta F/F_0 = [F(t) - F_0] / F_0$. Where $F(t)$ = MGV of any given frame, and F_0 = average baseline MGV of ~10 frames where no Ca^{2+} fluxes are present.

7.3.7. Using a statistical software such as OriginPro 2020, converted $\Delta F/F_0$ traces can be made into line graphs. The "Peak analyzer" function can be used (or similar function if using a different software) to measure the peak amplitude of glutamate response, latency to respond to glutamate, and area under the curve.

8. Immunostaining of cultures

NOTE: Following fixation with formalin, coverslips can be stored in 1x PBS at 4 °C until ready to be processed for immunostaining. Primary and secondary antibody incubation was done in a serial manner, as such incubation with anti-Caspase-3 primary antibody and its complementary secondary antibody preceded incubation with the anti-TH primary antibody and its complementary secondary antibody.

8.1. Immediately following glutamate exposure, place the coverslip back into its 35 mm Petri dish, aspirate the recording buffer, and add 3 mL of 10% formalin. Let sit for 40 min at room temperature (RT).

8.2. Rinse the dish 3 times with 1x PBS.

8.3. Aspirate the PBS and permeabilize cells in 1 mL of 0.01% Triton X-100 in PBS for 2 min.

8.4. Rinse the dish 3 times with 1x PBS.

8.5. Aspirate the PBS and block cells in 1 mL of 10% NGS in PBS.

8.6. Rinse the dish 3 times with 1x PBS.

8.7. Add 1 µL of rabbit anti-Caspase-3 primary antibody to 1 mL of 1% NGS in PBS (1:1000 dilution). Aspirate PBS from the dish and replace with the primary antibody solution. Place on a shaker and incubate for 1.5 h at RT.

8.8. Rinse the dish 3 times with 1x PBS.

8.9. Add 1 µL of goat anti-rabbit AlexaFluor 488 secondary antibody to 1 mL of 1% NGS in PBS (1:1000 dilution). Aspirate PBS from the dish and replace with the secondary antibody solution. Place on a shaker and incubate for 1 h at RT. Moving forward protect the samples from light.

8.10. Rinse the dish 3 times with 1x PBS.

8.11. Repeat steps 8.7 – 8.10, but using the chicken anti-TH primary antibody in step 8.7 and the goat anti-chicken AlexaFluor 594 secondary antibody in step 8.9.

8.12. Following the final PBS rinse, place 30 µL of mounting medium onto a microscope slide. Using forceps grab a coverslip from the 35 mm Petri dish and place the coverslip with the cells facing down into the mounting medium. Both coverslips will fit on a single microscope slide if placed correctly. Place in a dry, dark area and allow the mounting medium to dry overnight.

9. Confocal imaging of immunostained cultures

9.1. Confocal imaging

9.1.1. Start the imaging software. Place the sample onto the microscope stage.

9.1.2. With the microscope eyepieces, using a 20x magnification objective and epifluorescent light with a TRITC filter, focus the sample and search for a TH+ cell body.

9.1.3. Once locating a TH+ cell body, center it in the field of view and then move to the 60x magnification objective.

9.1.4. Select the AlexaFluor 488 and AlexaFluor 594 dyes in the “dye list” window.

9.1.5. As with live imaging, start with low HV, gain, offset, and laser power settings to prevent photobleaching. Use the “focus x2” scan option to assess the fluorescent intensity of each channel and adjust accordingly. As these images will later be quantified for fluorescent intensity it is necessary to keep the imaging settings consistent across all fields of view. Therefore, it is best to look at a few examples of each condition to get an idea of the range of fluorescent intensity across samples.

9.1.6. Once ideal imaging settings are determined, center the cell in the field of view and apply a 3x digital zoom. Next, select the “focus x2” scan option and move the cell of interest into the center of the field of view. Increase the digital zoom to 3x using the “zoom” slider.

9.1.7. Using the focus knob, find the plane of focus with the brightest fluorescence and capture a single plane XY image. Save the image to finish.

9.1.8. Switch back to the 20x magnification objective to search for another TH+ cell. Repeat this process until the desired number of cells have been sampled from each condition.

9.2. Image analysis

9.2.1. In the ImageJ toolbar, click *Analyze | Set Measurements*, and select the boxes for Area, Integrated density, and Mean gray value.

9.2.2. Open an image as a hyperstack with each channel separated by dragging and dropping into the ImageJ toolbar or selecting the image via the file menu.

9.2.3. Use the TH channel (594 nm) to draw ROIs around the cell body. Using the polygon tracing tool in ImageJ, closely trace the outer edge of the cell body. Where the distance between the cell membrane and cell nucleus is the smallest, trace a straight line through the cytosol to the edge of the nucleus and then closely follow the outline of the nucleus in order to exclude it. Then trace a straight line back to the external membrane, bordering the initial line as closely as possible, and continue to follow the outline of the cell body until the ROI is complete.

9.2.4. Using the keyboard shortcut “T” or using the toolbar menu path *Analyze* | *Tools* | *ROI Manager*, open the ROI manager and add the ROI that was just drawn to the list.

9.2.5. Select the window of the caspase-3 channel (488 nm), and then select the added ROI in the “ROI Manager” list.

9.2.6. In the *ROI Manager* window, select the *Measure* button. The results window will appear with the measurements set previously. Copy these to a spreadsheet and repeat this process for each cell.

Representative results

Following initial culturing of cells, we treated VM culture dishes at 14 DIV with 1 µL of AAV hSyn-GCaMP6f and allowed for 5 days of viral expression. On the day of imaging HEPES recording buffer was prepared fresh. We used two conditions; in one condition 20 µM glutamate was applied for 10 min, while in the other condition 5 min of

10 µM NBQX application preceded a 10 min co-application of 10 µM NBQX + 20 µM glutamate. In both conditions, we observed heterogenous and spontaneous changes in GCaMP6f fluorescence, which indicate spontaneous Ca^{2+} fluxes, as shown in the representative traces (Figure 1A,B, Supplemental Movie 1-2). Application of 20 µM glutamate generated a robust and sustained Ca^{2+} response in both spontaneously active and quiescent neurons (Figure 1A, Supplemental Movie 1). Application of 10 µM NBQX reduced spontaneous activity, and partially blocked the glutamate response (Figure 1B, Supplemental Movie 2). The extent to which glutamate application stimulated a Ca^{2+} response in each condition was quantified using area under the curve, peak amplitude, and latency to respond. Both area under the curve and peak amplitude were similar for both the glutamate and NBQX + glutamate treated conditions (Figure 1C), while latency to response was significantly increased in the NBQX + glutamate condition (Figure 2A,B)**.** In addition to quantifying the Ca^{2+} response to glutamate treatment, we fixed and stained samples with an anti-caspase-3 antibody as a measure of glutamate-mediated apoptosis. We observed a range of caspase-3 activation across the conditions (Figure 3A,B). Caspase-3 activation was quantified by measuring area and mean caspase-3 intensity. When compared to untreated control cells, the average area of cells with caspase-3 activation under glutamate and NBQX + glutamate conditions trended towards significance (Figure 3B). Mean caspase-3 intensity was significantly higher in the glutamate and NBQX + glutamate conditions as compared to untreated controls (Figure 3B). Together, these results demonstrate a high-content framework in which apoptosis of neurons can be measured by quantifying Ca^{2+} responses to

excitotoxic agents and followed up with an analysis of downstream apoptotic events such as caspase-3 activation in the same set of cultures.

Discussion

We describe a long-term primary ventral mesencephalic (VM) cell culture system for high-content analysis of glutamate-mediated apoptosis in neurons. Studies have employed primary midbrain dopaminergic cultures to elucidate excitotoxic mechanisms in the context of PD models [11, 12]. In this study, we employ a combinatorial approach using GECIs to measure Ca^{2+} activity and further associate this activity with downstream molecular changes, such as initiation of apoptotic signaling cascades [4]. The method has multiple advantages to other similar cell culture systems. As we have particular interest in excitotoxicity within the context of Parkinson's disease, using primary VM cell cultures is ideal. By using different field relocation techniques, such as gridded coverslips or a motorized XY microscope stage combined with TH immunostaining, we can directly study the cell type specific effects of glutamate-mediated apoptosis in DA neurons. Additionally, the 3-week cell culture model allows for neurons to develop their full, mature molecular profile, reflecting adult DA neurons [9]. Previous methods have mainly focused on molecular changes following glutamate-mediated excitotoxicity [13, 14]. The model is unique in its ability to correlate acute changes in neuronal physiology with downstream molecular events in identified cell types. One limitation of the primary culture model is that the dissection technique captures the entire ventral midbrain, including DA and GABAergic neurons as well as neurons from the SNc and VTA. Evidence now suggests that DA neurons of the SNc have selective vulnerability to calcium and eventual cell death compared to DA neurons of the neighboring VTA [15]. Unfortunately, differentiating SNc from VTA neurons in embryonic cultures has proven difficult with few anatomical landmarks to define these structures in the embryonic brain.

We demonstrate that the primary culture technique allows for quantification of heterogenous spontaneous Ca^{2+} activity (**Figure 1**). Therefore, this is an ideal cell culture system model to study tonically active cells, such as pacemaking dopaminergic neurons of the midbrain, neocortical neurons, and GABAergic neurons of the suprachiasmatic nucleus (SCN)[16, 17]. In most applications, Ca^{2+} imaging does not achieve the same temporal resolution as electrophysiology. Therefore, it is likely that a single Ca^{2+} event is analogous to a burst of neuronal action potentials. This can be interpreted to mean that Ca^{2+} imaging allows for relatively accurate measures of abnormal bursting activity in pacemaking cells and is therefore appropriate for a high content screen of Ca^{2+-}mediated excitotoxic cell death.

To achieve and maintain spontaneous Ca^{2+} activity, it is important to address two key points in the protocol. First is the plating density of the cells following dissection. For primary VM neurons, previous studies have used around 100,000 cells/cm^2 [9, 10]. We have adapted the protocol to plate a density of 200,000 cells/cm^2, which creates a heterogenous range of spontaneous activity and increases the number of dopaminergic VM neurons present on each coverslip. Since different pacemaking neurons have distinct firing properties [16], the plating density needs to be customized to the cell type being studied and optimized in order to achieve ideal levels of spontaneous activity. Second is the incubation time following viral infection of AAVs. Like plating density, this will be dependent on the specific context of the research question and type of AAV being used. For the specific AAV, 5 days of incubation following viral infection is ideal to achieve the desired protein expression levels, which allows for dynamic changes in GCaMP fluorescence in order to record Ca^{2+} activity. Many factors determine how quickly and efficiently an AAV will express its cargo, much of which is outside the scope of this method, but briefly, it is important to consider promoter activity and the rate at which the cargo protein matures and folds.

Another advantage of the method is that it allows for considerable flexibility in format, expression vectors, use of imaging equipment, and the range of scientific questions that can be addressed. In addition, the method enables inquiry into a wide range of specific questions that surround glutamate-mediated excitotoxicity in PD, and other models of nervous system dysfunction. For example, glutamate-mediated excitotoxicity involves multiple receptors and signaling cascades [5]. By using the method, and as demonstrated with the AMPAR blocker, NBQX in **Figure 1**, it is possible to dissect out specific components of the excitotoxic glutamate response at a physiological and molecular level. Conceivably, a similar approach using inhibitors of second messenger systems could be used to determine their contribution to excitotoxicity. Additionally, the AAVs used here could be adapted to express genetically coded calcium indicators (GECIs) with cell-specific promoters or AAV-expressed optogenetic sensors could be used to measure other parameters such as neurotransmitter release.

Apart from primary embryonic dissections and confocal imaging, much of the protocol uses basic laboratory skills that do not require specialized training. Therefore, the limitations to the model include the difficulty of the embryonic dissection technique, the length of time the cells must be cultured to reach maturity, and access to a confocal microscope, or similar imaging apparatus. The many benefits and flexibility of the method outweighs these limitations, making this an ideal model to study the role glutamate-mediated excitotoxicity in nervous system disorders. Finally, this model could be an effective tool to screen novel compounds for anti-apoptotic effects and their ability to preserve DA neuron health.

Figures

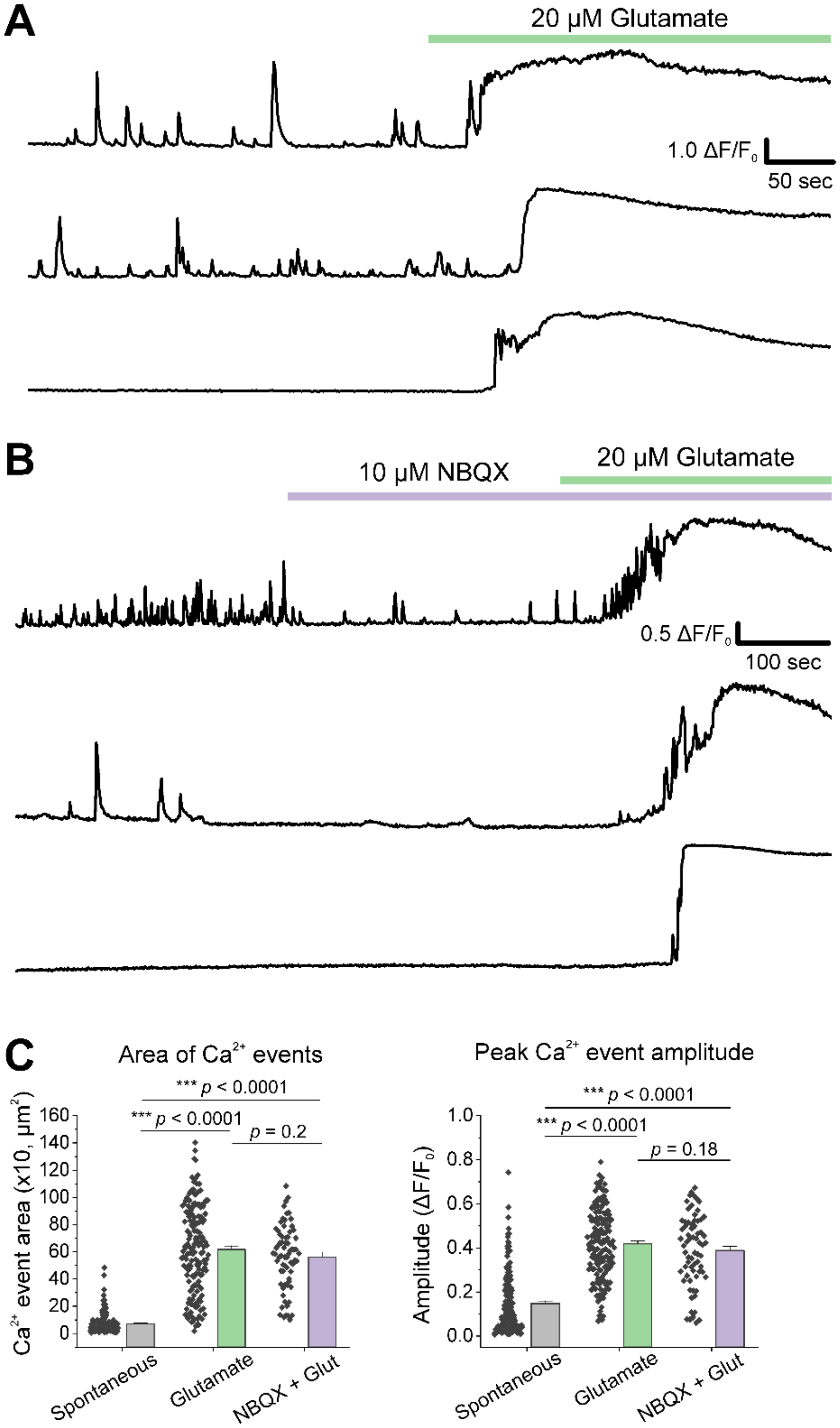
A
20 μM Glutamate
1.0 ΔF/F₀
50 sec
B
10 μM NBQX
20 μM Glutamate
0.5 ΔF/F₀
100 sec
C
Area of Ca²⁺ events
*** p < 0.0001
*** p < 0.0001
p = 0.2
Ca²⁺ event area (x10, μm²)
160
140
120
100
80
60
40
20
0
Spontaneous
Glutamate
NBQX + Glut
Peak Ca²⁺ event amplitude
*** p < 0.0001
*** p < 0.0001
p = 0.18
Amplitude (ΔF/F₀)
1.0
0.8
0.6
0.4
0.2
0.0
Spontaneous
Glutamate
NBQX + Glut

Figure 2: Cultured ventral mesencephalic neurons display spontaneous Ca^{2+} activity and are robustly stimulated by glutamate application.
(**A**) Representative traces of spontaneous Ca^{2+} activity in VM neurons and their response to 20 µM Glutamate application. (**B**) Representative traces of spontaneous Ca^{2+} activity in VM neurons and their response to 10 µM NBQX + 20 µM Glutamate application. (**C**) Population data showing area under the curve and peak amplitude of Ca^{2+} traces.

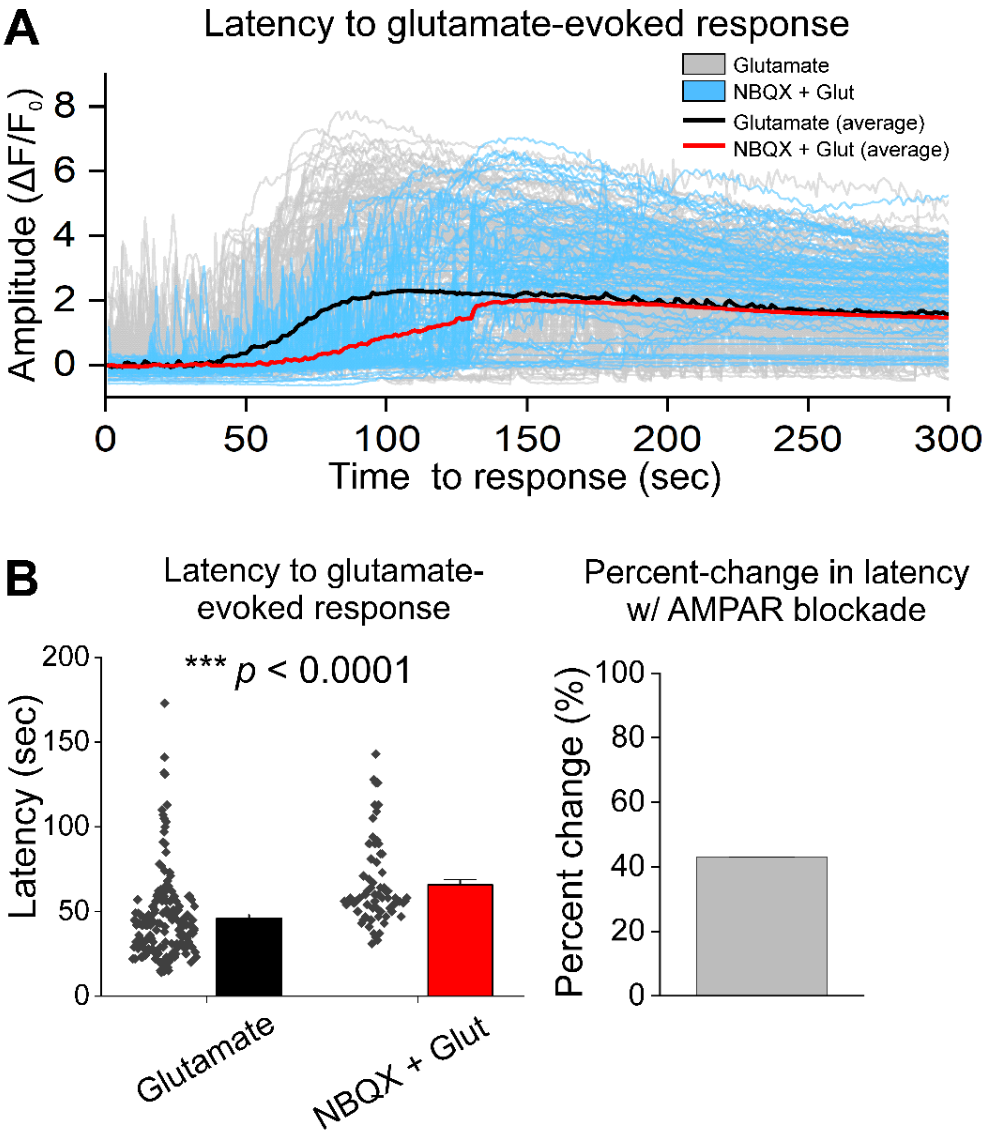

Figure 3: AMPAR blockade with NBQX delays response to glutamate application in cultured ventral mesencephalic neurons.

(**A**) Representative Ca^{2+} traces of glutamate (gray) and NBQX + glutamate (blue) evoked responses. Average Ca^{2+} traces of glutamate (black) and NBQX + glutamate (red) are shown overlaid. (**B**) Population data showing latency to response for glutamate and NBQX + glutamate evoked responses. Percent change between glutamate and NBQX + glutamate conditions is displayed in the right panel.

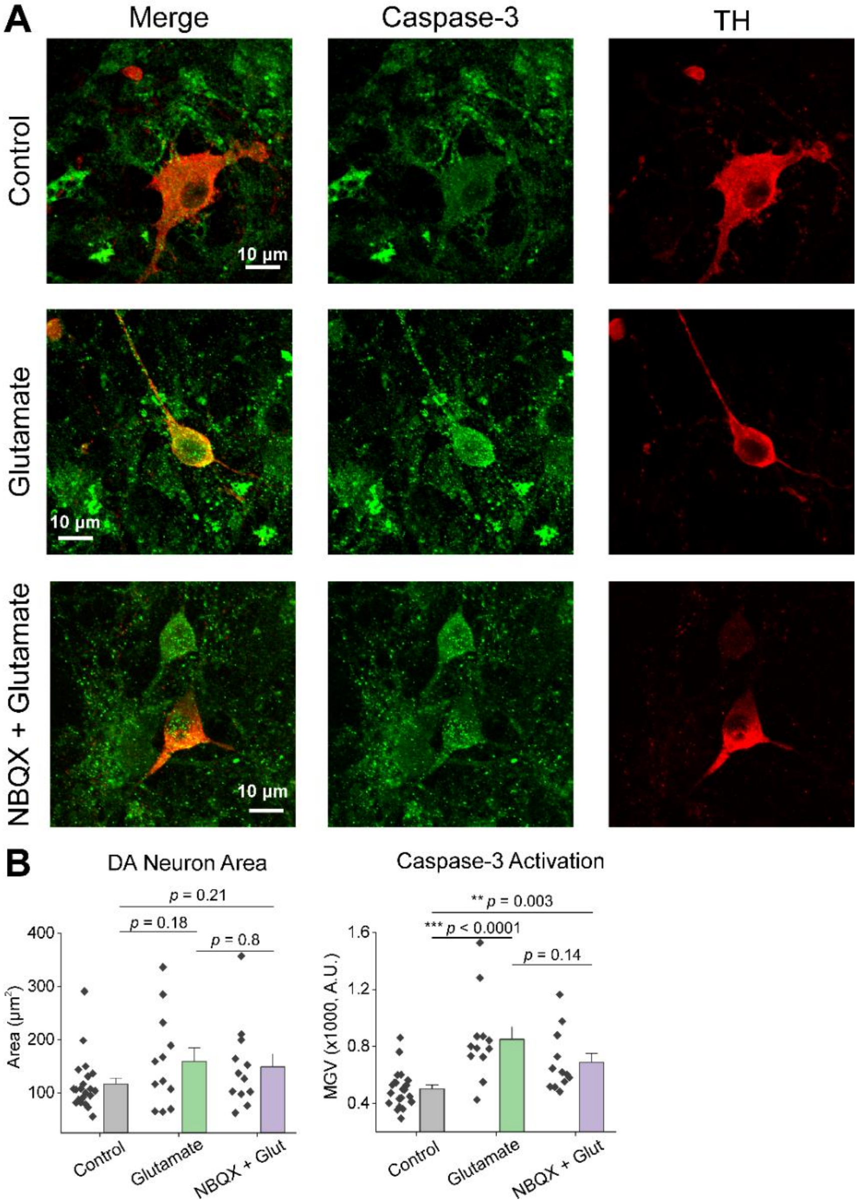

Figure 4: Glutamate application increases caspase-3 expression in tyrosine hydroxylase (TH) positive ventral mesencephalic neurons.

(**A**) Representative confocal images of VM cultures immunostained for caspase-3 (green) and TH (red), scale bar = 10 µm. (**B**) Population data showing DA neuron area and mean gray value of caspase-3 expression in each condition.

References

1. Marras, C.; Beck, J. C.; Bower, J. H.; Roberts, E.; Ritz, B.; Ross, G. W.; Abbott, R. D.; Savica, R.; Van Den Eeden, S. K.; Willis, A. W.; Tanner, C. M.; Parkinson's Foundation, P. G., Prevalence of Parkinson's disease across North America. *NPJ Parkinsons Dis* **2018,** 4, 21.
2. Poewe, W.; Seppi, K.; Tanner, C. M.; Halliday, G. M.; Brundin, P.; Volkmann, J.; Schrag, A. E.; Lang, A. E., Parkinson disease. *Nat Rev Dis Primers* **2017,** 3, 17013.
3. Mehta, A.; Prabhakar, M.; Kumar, P.; Deshmukh, R.; Sharma, P. L., Excitotoxicity: bridge to various triggers in neurodegenerative disorders. *European journal of pharmacology* **2013,** 698, (1-3), 6-18.
4. Ambrosi, G.; Cerri, S.; Blandini, F., A further update on the role of excitotoxicity in the pathogenesis of Parkinson's disease. *J Neural Transm (Vienna)* **2014,** 121, (8), 849-59.
5. Dong, X. X.; Wang, Y.; Qin, Z. H., Molecular mechanisms of excitotoxicity and their relevance to pathogenesis of neurodegenerative diseases. *Acta pharmacologica Sinica* **2009,** 30, (4), 379-87.
6. Vieira, M.; Fernandes, J.; Burgeiro, A.; Thomas, G. M.; Huganir, R. L.; Duarte, C. B.; Carvalho, A. L.; Santos, A. E., Excitotoxicity through Ca2+-permeable AMPA

receptors requires Ca2+-dependent JNK activation. *Neurobiology of disease* **2010,** 40, (3), 645-55.

7. Sebe, J. Y.; Cho, S.; Sheets, L.; Rutherford, M. A.; von Gersdorff, H.; Raible, D. W., Ca(2+)-Permeable AMPARs Mediate Glutamatergic Transmission and Excitotoxic Damage at the Hair Cell Ribbon Synapse. *The Journal of neuroscience : the official journal of the Society for Neuroscience* **2017,** 37, (25), 6162-6175.
8. Brickley, S. G.; Farrant, M.; Swanson, G. T.; Cull-Candy, S. G., CNQX increases GABA-mediated synaptic transmission in the cerebellum by an AMPA/kainate receptor-independent mechanism. *Neuropharmacology* **2001,** 41, (6), 730-6.
9. Srinivasan, R.; Henley, B. M.; Henderson, B. J.; Indersmitten, T.; Cohen, B. N.; Kim, C. H.; McKinney, S.; Deshpande, P.; Xiao, C.; Lester, H. A., Smoking-Relevant Nicotine Concentration Attenuates the Unfolded Protein Response in Dopaminergic Neurons. *The Journal of neuroscience : the official journal of the Society for Neuroscience* **2016,** 36, (1), 65-79.
10. Henley, B. M.; Cohen, B. N.; Kim, C. H.; Gold, H. D.; Srinivasan, R.; McKinney, S.; Deshpande, P.; Lester, H. A., Reliable Identification of Living Dopaminergic Neurons in Midbrain Cultures Using RNA Sequencing and TH-promoter-driven eGFP Expression. *Jove-J Vis Exp* **2017**, (120).
11. Douhou, A.; Troadec, J. D.; Ruberg, M.; Raisman-Vozari, R.; Michel, P. P., Survival promotion of mesencephalic dopaminergic neurons by depolarizing concentrations of K+ requires concurrent inactivation of NMDA or AMPA/kainate receptors. *Journal of neurochemistry* **2001,** 78, (1), 163-74.

12. Lavaur, J.; Le Nogue, D.; Lemaire, M.; Pype, J.; Farjot, G.; Hirsch, E. C.; Michel, P. P., The noble gas xenon provides protection and trophic stimulation to midbrain dopamine neurons. *Journal of neurochemistry* **2017,** 142, (1), 14-28.

13. Kritis, A. A.; Stamoula, E. G.; Paniskaki, K. A.; Vavilis, T. D., Researching glutamate - induced cytotoxicity in different cell lines: a comparative/collective analysis/study. *Frontiers in cellular neuroscience* **2015,** 9, 91.

14. Gupta, K.; Hardingham, G. E.; Chandran, S., NMDA receptor-dependent glutamate excitotoxicity in human embryonic stem cell-derived neurons. *Neuroscience letters* **2013,** 543, 95-100.

15. Surmeier, D. J.; Obeso, J. A.; Halliday, G. M., Selective neuronal vulnerability in Parkinson disease. *Nat Rev Neurosci* **2017,** 18, (2), 101-113.

16. Ramirez, J. M.; Tryba, A. K.; Pena, F., Pacemaker neurons and neuronal networks: an integrative view. *Curr Opin Neurobiol* **2004,** 14, (6), 665-674.

17. Guzman, J. N.; Sanchez-Padilla, J.; Chan, C. S.; Surmeier, D. J., Robust pacemaking in substantia nigra dopaminergic neurons. *The Journal of neuroscience : the official journal of the Society for Neuroscience* **2009,** 29, (35), 11011-9.

CHAPTER IV

EXTRACELLULAR S100B INHIBITS A-TYPE VOLTAGE-GATED POTASSIUM CURRENTS AND INCREASE L-TYPE VOLTAGE-GATED CALCIUM CHANNEL ACTIVITY IN DOPAMINERGIC NEURONS*

Introduction

Parkinson's disease (PD) is the second most common neurodegenerative disorder, projected to reach pandemic proportions by 2040 [1]. Understanding the mechanisms by which dopaminergic (DA) neurons degenerate in PD is therefore vital for developing effective disease-modifying treatments that slow down or even stop the progressive loss of DA neurons

Interestingly, patients with PD display increased levels of S100B in their cerebrospinal fluid and serum [2, 3], as well as significantly higher S100B expression in the substantia nigra pars compacta (SNc) [2]. Several lines of evidence show that apart from being merely associated with PD, upregulated S100B can also actively contribute to the degeneration of DA neurons. Specifically, studies show that: (**i**) A single nucleotide polymorphism, rs9722, which is associated with increased levels of serum S100B results in an elevated risk for early onset PD [4, 5], (**ii**) Ablation of S100B in

*Reprinted with permission from Bancroft E.A., et al. Extracellular S100B inhibits A-type voltage-gated potassium currents and increases L-type voltage-gated calcium channel activity in dopaminergic neurons. Glia. August 2022. Online ahead of print. doi:10.1021/acsanm.1c02665 mice protects against MPTP-induced DA loss [2], (**iii**) Mice overexpressing S100B develop parkinsonian features [2, 6], and (**iv**) Overnight S100B elevation correlates with increased PD severity and sleep disruption [7]. Taken together, these reports clearly converge on the idea that abnormal levels of S100B in the SNc could trigger the degeneration of DA neurons in PD patients.

During PD, midbrain astrocytes become reactive and demonstrate a pathological increase in the expression levels of astrocyte-specific proteins such as glial fibrillary acid protein (GFAP) [8, 9] and S100B [2]. Among the many proteins that are upregulated in reactive astrocytes, S100B is of particular interest in the context of PD because of its potential to initiate pathological processes in DA neurons during early stage PD. Indeed, extracellular S100B has been shown to alter neuronal activity in multiple brain regions [10, 11], and extracellularly secreted S100B from astrocytes accelerates neurodegeneration by engaging receptor for advanced glycation endproducts (RAGE)-mediated pro-inflammatory pathways in astrocytes and microglia [12-14]. In addition to signaling through RAGE receptors, S100B and the S100 family of proteins interact intracellularly with several ion channels and receptors expressed in neurons, and these interactions result in significant biological effects such as increased neurotropism or the modulation of neuronal excitability [15]. The documented effects of S100B on neurons point to S100B as an active participant in modulating neuronal function during health and disease.

In this study, we test the hypothesis that an abnormal increase in extracellular S100B, secreted by midbrain astrocytes alters the activity of SNc DA neurons by interacting with ion channels expressed on the surface of these neurons. Using primary co-cultures of mouse midbrain neurons and astrocytes, we show that exposure of midbrain cultures to picomolar concentrations of S100B specifically alters the activity of tyrosine hydroxylase expressing (TH^+) DA neurons by mechanisms that include: (**i**) Increasing intrinsic neuronal firing via an inhibition of A-type voltage-gated potassium channels (VGKCs), and (**ii**) Increasing the frequency of spontaneous Ca^{2+} fluxes via L-type voltage-gated calcium channels (VGCCs). Since a large body of evidence now suggests that VGKCs, VGCCs and astrocytes play central roles in the development of PD [16-26], our results have important implications for understanding how extracellular S100B secreted by midbrain astrocytes can alter the function of voltage-gated channels expressed in DA neurons, thereby resulting in early PD.

Materials and Methods

Mice

All experimental procedures with mice were approved by the Texas A&M University Institutional Animal Care and Use Committee (IACUC), animal use protocol numbers 2017-0053 and 2019-0346. Adult (3-4 month) male and female C57BL/6 wildtype mice and embryos (ED14) from timed-pregnant female C57BL/6 mice were obtained from the Texas A&M Institute for Genomic Medicine (TIGM). Pregnant mice were group housed in a temperature controlled environment on a 12:12 h light:dark cycle with food and water available *ad libitum*.

Stereotaxic cranial injections

AAV 2/5 GfaABC$_1$D-Lck-GCaMP6f was stereotaxically injected into the SNc of adult (3-4 month) mice using previously described methods (Srinivasan et al., 2015; Srinivasan, Lu, et al., 2016). Briefly, each mouse was unilaterally injected with 1 µl of AAV 2/5 GfaABC1D-Lck-GCaMP6f (10^{13} genome copies/ml) (Vector Builder, Chicago, IL) with a beveled glass injection pipette using a motorized Pump 11 Pico Plus Elite pump (Harvard Apparatus), attached to a stereotaxic frame (Kopf Instruments). AAVs were injected into the SNC at a rate of 500 nl/min. Coordinates for SNc injections were 3.0 mm posterior to bregma, 1.5 mm lateral to midline, and 4.2 mm ventral to the pial surface. For all stereotaxic surgeries, mice were anesthetized using isoflurane dispensed through a SomnoSuite Low Flow Anesthesia System (Kent Scientific).

Immunostaining of mouse brain sections and DA cultures

Three to four-month old male and female mice were transcardially perfused with phosphate-buffered saline (PBS, ThermoFisher, Waltham, MA, USA) followed by 10% Formalin/PBS (VWR, Radnor, PA, USA). Brains were postfixed in 10% Formalin/PBS for 24-48 h at 4°C, then moved to 30% sucrose (Sigma-Aldrich, St. Louis, MO, USA) in

PBS for dehydration. Brains were sectioned in the coronal plane to obtain midbrain sections with 40 μm thickness using a sliding microtome (SM2010 R, Leica, Nussloch, Germany). Midbrain sections were permeabilized in 0.5% Triton X-100 (Sigma-Aldrich) in PBS, and blocked in 10% normal goat serum (NGS, Abcam, Cambridge, UK) in PBS. Primary antibodies used were rabbit polyclonal anti-S100B (1:1000, Abcam) and chicken polyclonal anti-TH (1:1000, Abcam), mouse monocolonal anti-NeuN (1:1000, Abcam), rabbit polyclonal anti-GFP (1:1000, Abcam). Secondary antibodies used were goat polyclonal anti-rabbit Alexa Fluor 488 (1:1000, Abcam), goat polyclonal anti-chicken Alexa Fluor 594 (1:1000, Abcam), and goat polyclonal anti-mouse Alexa Fluor 405 (1:1000, Abcam). Antibodies were incubated in a 1% NGS/PBS solution. For each midbrain subregion, 2 fields of view (FOV) from 2-3 sections per mouse (3 mice total per brain region) were used to quantify wrapping of neuronal somata in the SNc, ventral tegmental area (VTA) and substantia nigra pars reticulata (SNr) by S100B-containing astrocytic processes.

DA cultures were fixed by placing coverslips in 10% Formaldehyde/PBS for 40 min. Cultures were permeabilized in 0.01% Triton X-100/PBS and blocked in 10% NGS/PBS solution. Antibodies used in sections were also used in cultures, with the addition of mouse polyclonal anti-NeuN (1:1000, Abcam) and goat polyclonal anti-mouse Alexa Fluor 405 (1:1000, Abcam). Imaging was performed using a confocal microscope (Fluoview 1200, Olympus, Tokyo, Japan) with a 60X and 1.35 numerical aperture (NA) oil-immersion objective (Olympus).

Primary mouse midbrain neuron and astrocyte co-cultures

For co-culturing primary mouse midbrain neurons and astrocytes, neurobasal medium, DMEM + GlutaMAX medium, GlutaMAX supplement, B-27, equine serum, and penicillin-streptomycin were purchased from ThermoFisher. Deoxyribonuclease I (DNase), poly-L-lysine, poly-L-ornithine, laminin, ascorbic acid, kanamycin, and ampicillin were purchased from Sigma-Aldrich. Corning 35 mm uncoated plastic cell culture dishes were purchased from VWR, 12 mm circular cover glass No. 1 was purchased from Phenix Research Products (Candler, NC, USA). Papain was purchased from Worthington Biomedical Corporation (Lakewood, NJ, USA).

Detailed methods to co-culture primary mouse DA neuron and astrocytes have been previously described [27-29]. Briefly, cultures were obtained from embryonic day (ED14) mouse embryos of mixed sexes. Timed-pregnant mice (obtained from Texas A&M Institute for Genomic Medicine) were sacrificed via cervical dislocation and embryos were removed. Embryos were decapitated and ventral midbrain was dissected using previously described methods [27, 28]. Following dissection, cells were digested in papain for 15 min at 37°C, then cells were separated using DNase treatment and mechanical trituration in a stop solution of 10% equine serum in PBS. Cells were plated at a density between 200,000-300,000 cells per cover glass on 12 mm circular cover glasses triple coated with poly-L-lysine, poly-L-ornithine and laminin. After plating, cells were placed in an incubator at 37°C with 5% CO_2 for 1 h, followed by addition of 3 ml of neurobasal media supplemented with GlutaMAX, B-27, equine serum, ascorbic acid and containing penicillin-streptomycin, kanamycin, and ampicillin. Culture medium was exchanged at 3 d intervals and all primary mouse midbrain neuron-astrocyte co-cultures were maintained for at least 3 weeks before performing experiments.

Adeno-associated virus (AAV) vectors

To confirm that S100B containing processes enveloping neurons in the SNc were astrocytic, we utilized AAV 2/5 GfaABC1D-Lck-GCaMP6 obtained as a gift from Baljit Khakh deposited to Addgene (Watertown, MA, USA)

To perform electrophysiology and image spontaneous Ca^{2+} fluxes in visually identified DA neurons from primary mouse midbrain co-cultures, we utilized adeno-associated viruses (AAVs) that reliably report TH^{+} DA neurons (either AAV 2/5 TH-GFP or AAV 2/5 TH-tdTomato). AAV 2/5 TH-GFP and AAV 2/5 TH-tdTomato were packaged by Vector Builder (Chicago, IL). The targeting plasmid for packaging AAV 2/5 TH-tdTomato was cloned from a pAAV-mouse THp-eGFP plasmid obtained as a gift from Dr. Viviana Gradinaru (California Institute of Technology, Pasadena, CA). The eGFP cassette in the pAAV-mouse THp-eGFP plasmid was replaced with tdTomato between restriction sites Not1 and BamH1. Spontaneous Ca^{2+} fluxes in midbrain neurons were recorded using either AAV 2/5 hSyn-GCaMP6f or AAV 2/5 hSyn-RCaMP, both of which were purchased from Addgene.

All AAV infections were performed at 14 days in vitro (DIV), as previously described [27]. For AAV infections, the culture medium was removed and 1 ml of serum-free DMEM + GlutaMAX medium containing ~1 x 10^{10} genome copies of each AAV was added to each dish and allowed to incubate at 37°C with 5% CO_2 for 1 h. Serum-free medium containing AAVs was then removed and replaced with 3 ml of neurobasal medium supplemented with equine serum, B27 and GlutaMAX. Electrophysiological measurements and imaging experiments were performed on day 5 following infection with appropriate AAVs.

Electrophysiology

Whole cell recordings in both current and voltage-clamp mode were performed on cultured mouse midbrain neurons. Whole-cell current clamp was used to measure action potential (AP) frequency while whole-cell voltage-clamp was used to measure the fast inactivating (I_A) and non-inactivating (I_K) voltage-gated potassium currents. All recordings were performed using a Multiclamp 700B amplifier, Digidata 1400A interface and pClamp 10 software (Molecular Devices, San Jose, CA). All recordings utilized the extracellular gas-free recording buffer described below for Ca^{2+} imaging with the addition of AP5 (50 µM, Hello Bio, Princeton, NJ), NBQX (10 µM, Hello Bio), and Bicuculline (10 µM, Hello Bio) to measure intrinsic action potentials in cultured mouse midbrain neurons. Voltage-clamp experiments measuring I_A and I_K potassium currents also utilized tetrodotoxin (TTX, 0.3 µM). For electrophysiology and Ca^{2+} imaging experiments, monomeric recombinant human S100B peptide was obtained from Sino Biological (cat # 10181-H07E; Wayne, PA). To denature S100B peptide, recombinant S100B was boiled at 100°C for 1 h. Extracellular recording buffers were bath perfused and solution exchanges were performed using a gravity-based feed delivery system with a perfusion rate of 2 ml/min. In all physiology experiments (electrophysiology and Ca^{2+} imaging), multiple bath applications of S100B were performed on the same cultures with a minimum 10 min washout period between applications. We did not observe any differences in the effect of S100B between the first and last applications. The internal pipette solution for both current and voltage-clamp recordings contained (in mM): 136 K-gluconate, 10 HEPES, 0.1 EGTA, 4 Mg-ATP, 0.1 GTP, 25 NaCl, 2 $MgCl_2$, pH 7.2 with KOH, 290-300 mOsm. Patch pipettes were pulled from glass capillary tubing (KG-33, 1.5 mm outer diameter, King Precision Glass, Claremont, CA) using a Flaming/Brown P-87 pipette puller (Sutter Instrument, Novato, CA) with resistance between 6-12 MΩ, and were fire polished prior to use.

To isolate I_A currents in neurons, two voltage-step protocols were sequentially employed in whole-cell mode. The first protocol was used to record total voltage-gated potassium channel (VGKC) currents and consisted of a 100 ms prepulse (max conductance) at -90 mV followed by a 250 ms step at increasingly depolarized potentials (from -100 to 50 mV, 10 mV steps) (Supplementary Fig. 1A). The second protocol was used to inhibit I_A currents in order to specifically isolate I_K. For this protocol, the patched neuron was subjected to a 100 ms prepulse at +50 mV, followed by 250 ms steps at increasingly depolarized potentials (from -100 to +50 mV, 10 mV steps) (Supplementary Fig. 1B). In order to specifically visualize and measure I_A in TH^+ and TH^- midbrain neurons, current traces from the second protocol were subtracted from the first protocol using Clampfit 11.1 (Molecular Devices) (Supplementary Fig. 1C).

Imaging of spontaneous Ca^{2+} fluxes in cultured midbrain neurons

The protocol for imaging spontaneous Ca^{2+} fluxes in primary cultures of mouse midbrain neurons has been previously published {Bancroft, 2020 #1951}. Briefly, cultures were placed in a gas free recording buffer containing (mM): 154 NaCl, 5 KCl, 2 $CaCl_2$, 0.5 $MgCl_2$, 5 D-glucose, 10 HEPES, pH adjusted to 7.4 with NaOH (all purchased from Sigma-Aldrich). Imaging was performed using a confocal microscope (Fluoview 1200, Olympus) with a 40X, 0.8 NA water-immersion objective (Olympus). We used a 488-nm laser line to excite GCaMP6f and eGFP, and a 569-nm laser line for tdTomato and RCaMP. The imaging frame was clipped to allow for a sampling rate of 1 frame per sec. For all experiments, spontaneous activity was imaged for 300 s, followed by peptide/drug application. Recording buffers were bath perfused using a peristaltic pump at a rate of 2 ml/min. For each field of view imaged, a corresponding z-stack of both GCaMP6f and TH-tdTomato expression was captured and co-localization was used to identify TH^+ cells. Diltiazem was purchased from Tocris (Minneapolis, MN), Mibefradil and 4-aminopyridine (4-AP) were purchased from Sigma-Aldrich, and cyclopiazonic acid (CPA) was purchased from Abcam.

Image processing and data analyses

Image processing was performed using ImageJ v1.52e (NIH, Rockville, MD, USA). To quantify astrocyte wrapping of neuronal somata from immunostained mouse midbrain sections, z-stacks of TH, NeuN and corresponding S100B labeled midbrain sections were converted to projection images using the maximum intensity projection tool in ImageJ. TH and NeuN expressing neuronal somata were traced using the polygon tool. Neuronal somata regions of interest (ROIs) were manually demarcated in this way were applied to the S100B maximum intensity projection image, followed by clearing of all S100B signals outside of the neuronal soma ROI. Then, the S100B signal from maximum intensity projections were manually thresholded to capture all S100B-labeled astrocytic processes within the neuronal ROI. A separate ROI for S100B labeled astrocytic processes within the neuronal somata ROI was created in this way, and ROI areas as well as mean gray values were separately measured for both neuronal somata and for S100B-containing astrocytic processes within the neuronal somata ROI. Astrocyte wrapping around each neuronal somata was derived as a percentage by dividing the neuronal ROI area by the S100B ROI area and multiplying by 100. This analysis was performed for neurons and astrocytes in the SNc, VTA and SNr.

For analysis of Ca^{2+} fluxes in TH^+ and TH^- neurons from primary mouse midbrain co-cultures, time stacks (t-stacks) obtained from confocal imaging of live midbrain neurons were used to create maximum intensity projections and adjusted to increase brightness in order to visualize all active neuronal somata in a field of view. Somata displaying spontaneous Ca^{2+} fluxes were individually traced with the polygon tool and added to the ROI manager. The ROIs were used to extract neuronal Ca^{2+} flux traces from t-stacks, and only somata with one or more spontaneous Ca^{2+} flux events were selected for analysis. Mean gray values from Ca^{2+} flux event traces were converted to ΔF/F values using a 10 s period with no Ca^{2+} flux events to obtain baseline fluorescence (F). For each XY time-series movie analyzed, a corresponding z-stack image of both hSyn-GCaMP6f/hSyn-RCaMP and TH-tdTomato/TH-GFP expression was used to create red and green fluorescence co-localized max intensity projection images. Images obtained in this way were merged, and co-localization of GCaMP6f/RCaMP with tdTomato/GFP was used to definitively identify TH^{+} neurons, while cells displaying GCaMP6f/RCaMP labeling without tdTomato/GFP were identified as TH^{-} neurons. All neuronal Ca^{2+} flux traces obtained using the above procedures were manually analyzed with MiniAnalysis v6.0.7 (Synaptosoft, Fort Lee, NJ, USA) to detect and quantify Ca^{2+} flux frequency (events/min) and amplitude (ΔF/F). Area under the curve (AUC) measurements were quantified using Origin 2019 v9.6 (OriginLab, Northampton, Massachusetts, USA). Traces were plotted as line graphs and the integrate tool in the gadgets menu of Origin 2019 was applied to each trace. The baseline was held constant for all traces and area under the curve was measured for individual time segments of each trace as follows: Spontaneous (0-300 secs), 4-AP (300-600 secs), 4-AP + diltiazem (900-1200 secs). All analysis of electrophysiological data, including subtraction of VGKC traces was performed using Clampfit 11.1 (Molecular Devices). Action potentials from electrophysiological recordings were quantified using the event detection function in MiniAnalysis (Synaptosoft).

Statistical analyses

All statistical analyses were performed using Origin 2019 v9.6 Data presented are mean ± SEM. For each data set, normality was first determined in Origin using the Shapiro-Wilk test. Normally distributed data were analyzed via two-sample t-tests or paired sample t-tests when appropriate. Non-normally distributed data were analyzed with Mann-Whitney or paired sample Wilcoxon-signed rank test for between group differences. Data were considered to be significantly different at $p < 0.05$. For statistical analysis of differences in VGKC current amplitudes, current amplitudes of control versus S100B exposed cells were subjected to mixed-design ANOVA analysis, followed by a *post hoc* Bonferroni test to statistically compare differences in current amplitude at specific voltages. The exact statistical test used and sample sizes are described for each experiment in the figure legends. Exact *p* values comparing datasets are shown in each of the figures.

Results

Wrapping of S100B-containing astrocytic processes around SNc DA neurons is significantly increased only in male mice

The foundational premise of this study is based on testing the hypothesis that extracellular S100B, secreted by astrocytes can alter the activity of DA neurons in the SNc. Therefore, we first assessed the extent to which S100B containing astrocytic processes envelop TH^+ and TH^- neurons in the SNc, VTA, and SNr of adult male and female mice.

To do this, midbrain sections of 3 – 4 month old adult male and female mice were immunostained for TH, S100B, and NeuN, then imaged and quantified (Figure 17A-D). Surprisingly, we found that TH^+ SNc neurons in only male mice showed a significant ~1.69 fold increase in wrapping of S100B containing astrocytic processes compared to TH^+ neurons in the VTA and TH^- neurons in the SNC, VTA, and SNr (SNc TH^+: 26.26 ± 1.76 μm^2, SNc TH^-: 15.54 ± 2.71 μm^2, VTA TH^+: 15.49 ± 1.40 μm^2, VTA TH^-: 15.52 ± 1.54 μm^2, SNr TH^-: 19.46 ± 1.57 μm^2). (Figure 17D). By contrast, female mice demonstrated largely similar astrocytic wrapping of TH^+ and TH^- neurons in the SNc, VTA, and SNr (SNc TH^+: 19.85 ± 1.28 μm^2, SNc TH^-: 15.73 ± 1.36 μm^2, VTA TH^+: 15.69 ± 1.08 μm^2, VTA TH^-: 15.08 ± 1.77 μm^2, SNr TH^-: 18.19 ± 1.75 μm^2) (Fig. 17D). In addition, astrocytic wrapping of TH^+ SNc neurons in male mice was significantly ~1.32 fold higher than in female mice (Figure. 17D). To definitively confirm that the cells wrapping around TH^+ neurons in the SNc are astrocytes, we injected the midbrain of adult male mice with an AAV expressing Lck-GCaMP6f under transcriptional control of the well established astrocyte specific promoter, GfaABC1D. Following 2 weeks of expression, brains were extracted, sectioned, and fixed with 10% formalin and then immunostained with an anti-GFP and anti-TH antibody to visualize

GCaMP6f expression in relation to DA neuron somata. As shown in Figure 17E, GCaMP6f was robustly expressed in astrocytic processes that wrap around TH^+ neuronal somata.

These data reveal a striking region- and sex-specific difference in the extent to which S100B containing astrocytic processes envelop midbrain neurons. Specifically, we show that astrocytic wrapping of neuronal somata in the midbrain is specific to SNc DA neurons only in male mice. Thus, S100B secreted from astrocytes could potentially exert robust functional effects on SNc DA neurons of male mice.

Acute exposure to extracellular S100B specifically inhibits voltage-gated A-type potassium currents in TH^+ but not in TH^- neurons

Our finding that S100B-containing astrocytic processes display robust wrapping around the SNc DA neurons of adult male mice suggests that small increases in secreted S100B from astrocytes could alter the activity of DA neurons. To test this hypothesis, we used cultured primary mouse midbrain neurons and determined if acute extracellular exposure to picomolar concentrations of extracellular S100B peptide alters DA neuron activity.

Since VGKCs are known to play a central role in regulating the frequency of action potentials in neurons [19, 20, 22-24], we first assessed the effect of extracellular S100B on VGKC currents in TH^+ DA neurons. As described previously [27, 29-31], primary mouse ventral midbrain neurons were cultured from ED14 embryos and maintained for ~21 DIV prior to experiments (Figure 18A). Immunostaining of ~3-week old midbrain cultures showed NeuN$^+$ neurons that were either TH$^+$ or TH$^-$, along with primary midbrain astrocytes expressing S100B (Figure 18B). To visually identify live TH$^+$ neurons, mouse midbrain-astrocyte co-cultures were infected with AAV 2/5 TH-GFP 5 days prior to performing electrophysiological recordings. This procedure enabled an unambiguous identification of TH$^+$ and TH$^-$ neurons in live mouse midbrain cultures (Figure. 18C). Fast inactivating A-type (I_A), and non-inactivating (I_K) voltage-gated potassium currents were measured using whole-cell voltage clamp recording protocols, as described in methods (Figure 25). All recordings were acquired in the presence of AP5, DNQX, bicuculline and TTX in order to synaptically isolate neurons, and block action potentials.

In the case of fast inactivating I_A currents, at depolarizing potentials of -40 to +50 mV, TH$^+$ neurons showed significantly smaller current amplitudes than TH$^-$ neurons (Figure 18D & E). In addition, TH$^+$ neurons showed a linear I-V relationship at all recorded potentials, which was in contrast to TH$^-$ neurons that displayed inward rectification at strongly depolarizing potentials between +20 to +50 mV (Figure 18E). Five min bath exposure to 50 pM S100B peptide significantly decreased I_A by ~1.75-fold at +50 mV in TH$^+$ neurons (Control: 633.17 ± 132.84 pA, S100B: 361.77 ± 89.55 pA) (Figure 18E & F). By contrast, following acute exposure to extracellular S100B, TH$^-$ neurons did not show any change I_A (Control: 922.76 ± 134.10 pA, S100B: 857.310 ± 139.20 pA) (Figure 18E & F).

In the case of non-inactivating voltage-gated potassium currents (I_K), both TH^+ and TH^+ neurons showed very similar I-V profiles, with outward rectification at strongly depolarizing voltages (Figure 19A-C). Bath exposure to 50 pM S100B peptide had no effect on I_K in either TH^+ or TH^- neurons (Control TH^+: 1600.34 ± 143.99, S100B TH^+: 1529.07 ± 186.15, Control TH^-: 2047.56 ± 201.12, S100B TH^-: 1978.74 ± 206.81) (Figure 19B & C). Taken together, these data show that extracellular S100B inhibits only I_A but not I_K in TH^+ DA neurons, with no effect on either I_A or I_K in TH^- midbrain neurons.

Acute exposure to extracellular S100B increases the frequency of intrinsic APs in TH^+ neurons

Fast inactivating I_A plays a central role in governing the frequency of APs in pacemaking neurons, such that inhibition of I_A increases the frequency of APs [32-34]. Having found that extracellular S100B inhibits I_A only in TH^+ DA neurons, we next asked if extracellular S100B exposure also alters the frequency of intrinsic firing in cultured midbrain DA neurons. As shown in Figure 18C, TH^+ and TH^- neurons were visually identified based on the presence or absence of TH-GFP expression as a reporter for TH^+ neurons, and spontaneous APs were recorded using whole-cell current clamp (Figure 20A). To measure intrinsic firing of midbrain neurons, all recordings were acquired in the presence of synaptic blockers, AP5, DNQX and bicuculline.

We found that in the absence of S100B, TH^+ neurons showed an average intrinsic AP frequency of 0.6 ± 0.07 Hz, while TH^- neurons showed a significantly higher intrinsic AP frequency of 1.9 ± 0.33 Hz (Figure 20A & B). As rationalized, bath exposure to 50 pM extracellular S100B significantly increased AP frequency in TH^+ neurons by 2.1-fold (from 0.6 ± 0.07 Hz to 1.28 ± 0.14 Hz), while significantly decreasing AP frequency by 1.4-fold in TH^- neurons (from 1.9 ± 0.33 Hz to 1.34 ± 0.19) (Figure 20B). These data show that in TH^+ DA neurons, extracellular S100B specifically increased intrinsic AP frequency, likely via the inhibition of I_A.

Cultured mouse midbrain TH^+ and TH^- neurons demonstrate spontaneous Ca^{2+} fluxes that require L-type VGCCs

Multiple studies indicate that dysfunctional Ca^{2+} influx via L-type VGCCs contributes to DA neuron loss and the development of PD [18, 35-40]. Based on these observations, we rationalized that S100B-mediated inhibition of I_A could depolarize TH^+ neurons, thereby increasing L-type VGCC activity in TH^+ DA neurons.

We have previously shown that neurons in primary mouse midbrain cultures demonstrate robust spontaneous Ca^{2+} fluxes that are strongly inhibited by the L-type VGCC inhibitor, diltiazem, however, these prior studies did not differentiate between TH^+ and TH^- neurons [27, 31]. Therefore, we first conducted a series of experiments to specifically characterize spontaneous Ca^{2+} fluxes in TH^+ and TH^- neurons. Primary mouse midbrain cultures were infected with AAV 2/5 hSyn-GCaMP6f and AAV 2/5

TH-tdTomato, which enabled the measurement of spontaneous Ca^{2+} fluxes in midbrain neurons, along with the ability to distinguish between TH^+ and TH^- neurons (Figure 26A & B). We found that TH^- cells displayed a ~2-fold higher spontaneous Ca^{2+} flux frequency than TH^+ neurons as well as a ~2-fold higher amplitude in spontaneous Ca^{2+} flux events when compared to TH^+ neurons (TH^+ frequency: 2.19 ± 0.19 events/min, TH^- frequency: 4.61 ± 0.27 events/min, TH^+ amplitude: 0.19 ± 0.02 $\Delta F/F$, TH^- amplitude: 0.55 ± 0.04 $\Delta F/F$) (Figure 26C & D and supplementary movie 1). Furthermore, spontaneous Ca^{2+} fluxes in both TH^+ and TH^- neurons depended on extracellular, but not intracellular Ca^{2+} stores (Figure 27 and supplementary movie 2 & 3), and spontaneous Ca^{2+} flux events in both TH^+ and TH^- neurons were almost completely inhibited by the L-type VGCC blocker diltiazem (TH^+ spontaneous: 3.14 ± 0.47 events/min , TH^+ diltiazem: 0.55 ± 0.12 events/min, TH^- spontaneous: 2.04 ± 0.28 events/min, TH^- diltiazem: 0.8 ± 0.21 events/min) (Figure 28A and supplementary movie 4), but only partially inhibited by the T-type VGCC blocker, mibefradil (TH^+ spontaneous: 7.10 ± 0.44 events/min , TH^+ mibefradil: 5.90 ± 0.44 events/min, TH^- spontaneous: 6.75 ± 0.47 events/min, TH^- mibefradil: 5.38 ± 0.51 events/min) (Figure 28B and supplementary movie 5).

Taken together, these data show that the vast majority of spontaneous Ca^{2+} flux events in both TH^+ and TH^- neurons occur due to the activity of L-type VGCCs with some contribution from T-type VGCCs and depend on extracellular Ca^{2+} stores, and that TH^- neurons display more robust and frequent Ca^{2+} fluxes than TH^+ neurons.

Acute exposure to extracellular S100B increases spontaneous Ca^{2+} fluxes only in TH^+ DA neurons

Having observed that TH^+ and TH^- neurons display robust L-type VGCC-mediated spontaneous Ca^{2+} fluxes, we next sought to determine if exposure to extracellular S100B alters these spontaneous Ca^{2+} fluxes in TH^+ and TH^- neurons. To do this, midbrain cultures were bath perfused with 50 pM of S100B peptide, and spontaneous Ca^{2+} flux frequencies and amplitudes in TH^+ and TH^- neurons were measured. S100B application caused a significant 2-fold increase in the frequency of Ca^{2+} fluxes in TH^+ neurons, but not in TH^- neurons (TH^+ spontaneous: 2.19 ± 0.19 events/min, TH^+ S100B: 3.25 ± 0.22 events/min, TH^- spontaneous: 4.61 ± 0.27 events/min, TH^- S100B: 4.59 ± 0.30 events/min) (Figure 21, Supplementary movie 1). The ability of extracellular S100B to specifically increase Ca^{2+} flux frequency only in TH^+ neurons was also observed when data were plotted as average Ca^{2+} flux frequencies across multiple independent weeks of midbrain cultures (TH^+ spontaneous: 2.17 ± 0.30 events/min, TH^+ S100B: 3.28 ± 0.34 events/min, TH^- spontaneous: 4.45 ± 0.45 events/min, TH^- S100B: 4.37 ± 0.62 events/min) (Figure 21B), which rules out a skewing of the data as a result of a few individual midbrain cultures with abnormal S100B responses. As an additional control, bath application of denatured S100B peptide did not alter Ca^{2+} flux frequency in TH^+ neurons (TH^+ spontaneous: 5.13 ± 1.31 events/min, TH^+ dS100B: 4.93 ± 1.57 events/min, TH^- spontaneous: 9.88 ± 2.65

events/min, TH$^-$ dS100B: 9.00 ± 3.21 events/min) (Figure 29), thus confirming the necessity for properly folded S100B to mediate this effect.

S100B caused a small statistically significant decrease in the amplitude of VGCC mediated Ca^{2+} fluxes in TH$^+$ neurons (TH$^+$ spontaneous: 0.19 ± 0.02 ΔF/F, TH$^+$ S100B: 0.17 ± 0.02 ΔF/F) (Figure 21C). However, we did not observe a S100B induced change in amplitude when these data were plotted as average amplitudes obtained from multiple cells in the same culture (Ind. cultures, Figure 21C). By contrast, TH$^-$ neurons did not demonstrate a S100B induced change in amplitude when the data were plotted from individual cells or individual cultures (TH$^-$ spontaneous: 0.55 ± 0.04 ΔF/F, TH$^-$ S100B: 0.57 ± 0.04 ΔF/F) (Figure 21C). It should be noted that we observed a very small, statistically significant reduction in Ca^{2+} flux amplitudes for TH$^+$ neurons only when the data were plotted as an average of amplitudes from individual neurons and not across independent DA cultures (Figure 21C). These data show that S100B specifically increases the frequency of Ca^{2+} fluxes only in TH$^+$ midbrain neurons with no effect on TH$^-$ neurons.

Acute exposure to extracellular S100B increases spontaneous Ca^{2+} fluxes in TH$^+$ DA neurons via L-type, but not T-type VGCCs

We next assessed the extent to which S100B requires L-type and T-type VGCCs for increasing Ca^{2+} flux frequency in TH$^+$ neurons. Ca^{2+} fluxes in midbrain neurons were recorded following bath application of 50 pM S100B, and a subsequent co-application of

50 pM S100B with 100 μM diltiazem (Figure 22A). As shown in our prior experiment (Figure 21), acute application of S100B once again significantly increased Ca^{2+} flux frequency in TH^{+} neurons, but not TH^{-} neurons and did not alter the amplitude of Ca^{2+} fluxes in either TH^{+} or TH^{-} neurons (Figure 22B & C). Co-exposure of midbrain cultures to 50 pM S100B + 100 μM diltiazem completely inhibited the S100B-mediated increase of Ca^{2+} fluxes in TH^{+} neurons, with no effect on Ca^{2+} flux amplitude for the few remaining Ca^{2+} events (TH^{+} spontaneous: 4.68 ± 0.43 events/min, TH^{+} S100B: 5.32 ± 0.36 events/min, TH^{+} S100B + diltiazem: 2.42 ± 0.33 events/min, TH^{-} spontaneous: 5.75 ± 0.51 events/min, TH^{-} S100B: 5.49 ± 0.48 events/min, TH^{-} S100B + diltiazem: 2.61 ± 0.31 events/min) (Figure 22A-C, Supplementary movie 4). To further confirm blockade of L-type VGCCs inhibits the S100B-mediated increase in Ca^{2+} fluxes in TH^{+} neurons, we reversed the order of drug applications in the experiment described above (Figure 22D-F). We observed that L-type VGCC blockade with 100 μM diltiazem prior to S100B application completely abolished the S100B-mediated increase in Ca^{2+} fluxes in TH^{+} neurons (TH^{+} spontaneous: 3.14 ± 0.47 events/min, TH^{+} diltiazem: 0.55 ± 0.12 events/min, TH^{+} S100B + diltiazem: 0.24 ± 0.07 events/min, TH^{-} spontaneous: 2.04 ± 0.28 events/min, TH^{-} diltiazem: 0.8 ± 0.21 events/min, TH^{-} S100B + diltiazem: 0.26 ± 0.16 events/min) (Figure 22D-F). These results confirm that that S100B increases Ca^{2+} flux frequency in TH^{+} neurons via L-Type VGCCs.

To determine if T-type VGCCs are involved in S100B-mediated increases in the Ca^{2+} flux frequency of TH^{+} DA neurons, spontaneous Ca^{2+} fluxes were recorded in aCSF, then treated for 15 min with the T-type VGCC antagonist, mibefradil. Ca^{2+} fluxes in TH$^-$ and TH$^+$ DA neurons were then recorded in the presence of 1 μM mibefradil + 50 pM S100B (Figure 23A). We found that mibefradil significantly reduced Ca^{2+} flux frequency in both TH$^+$ and TH$^-$ neurons (TH$^+$ spontaneous: 7.10 ± 0.44 events/min, TH$^+$ mibefradil: 5.89 ± 0.44 events/min, TH$^-$ spontaneous: 6.75 ± 0.47 events/min, TH$^-$ mibefradil: 5.38 ± 0.51 events/min) (Figure 23B & C). However, co-application of S100B with mibefradil was unable to inhibit S100B-mediated increases in Ca^{2+} flux frequency in TH$^+$ DA neurons (TH$^+$ S100B + mibefradil: 6.57 ± 0.38 events/min), (Figure 23B, Supplementary movie 5). In the case of TH$^-$ neurons, we observed significant reductions in Ca^{2+} flux frequency following exposure to either mibefradil alone or co-exposure of mibefradil with S100B (TH$^-$ S100B + mibefradil: 5.03 ± 0.44 events/min) (Figure 23C) In addition, none of the recording conditions altered Ca^{2+} flux amplitudes in TH$^+$ and TH$^-$ neurons (TH$^+$ spontaneous: 0.44 ± 0.07 ΔF/F, TH$^+$ mibefradil: 0.42 ± 0.06 ΔF/F, TH$^+$ S100B + mibefradil: 0.37 ± 0.05 ΔF/F, TH$^-$ spontaneous: 0.40 ± 0.05 ΔF/F, TH$^-$ mibefradil: 0.45 ± 0.07 ΔF/F, TH$^-$ S100B + mibefradil: 0.42 ± 0.07 ΔF/F) (Figure 23B & C). When taken together, these results show that the effect of S100B-mediated increases in Ca^{2+} flux frequency in TH$^+$ neurons does not depend on T-type VGCCs but requires L-type VGCCs.

Inhibition of A-type VGKCs is sufficient for increasing intrinsic APs and Ca^{2+} flux frequency in TH$^+$ neurons

Our results thus far show that acute extracellular exposure to S100B specifically inhibits I_A only in TH^+ DA neurons, and this is accompanied by an increase the frequency of L-type VGCC-mediated Ca^{2+} fluxes. Based on these data, we rationalized that S100B-mediated inhibition of I_A in TH^+ neurons underlies the increase in L-type VGCC activity. To directly test this hypothesis, we asked if inhibiting I_A in TH^+ neurons with 4-AP, which is a known inhibitor of A-type potassium currents [41-43], mimics the observed S100B-mediated increase in intrinsic AP and Ca^{2+} flux frequency. Based on the established fact that I_A governs AP frequency in neurons [41-43], we measured the effect of 100 µM 4-AP on intrinsic AP firing in synaptically isolated TH^+ and TH^- neurons in the presence of AP5, DNQX, and bicuculline. Bath application of 100 µM 4-AP significantly increased AP firing frequency in TH^+ and TH^- neurons by ~1.8 fold (TH^+ spontaneous: 0.56 ± 0.08 Hz, TH^+ 4-AP: 1.07 ± 0.14 Hz, TH^- spontaneous: 1.07 ± 0.11 Hz, TH^- 4-AP: 1.71 ± 0.18 Hz) (Figure 24A & B).

In order to assess the effect of 4-AP mediated inhibition of I_A on L-type VGCC activity, we recorded Ca^{2+} signals in TH^+ and TH^- neurons following bath application of 100 µM 4-AP, and a subsequent co-application of 100 µM 4-AP and 100 µM of the L-type VGCC blocker diltiazem (Figure 24C). AUC was used as a measure of changes in Ca^{2+} fluxes following the application of 4-AP, and 4-AP + diltiazem. We found that 100 µM 4-AP significantly increased Ca^{2+} fluxes by ~1.85 fold in TH^+ neurons, while co-application of 4-AP with 100 µM diltiazem completely inhibited this increase in Ca^{2+} fluxes (Spontaneous: 42.90 ± 5.00 ΔF/F x sec, 4-AP: 78.10 ± 7.11 ΔF/F x sec, 4-AP + diltiazem: 21.81 ± 2.97 ΔF/F x sec) (Figure 24C &D). Similarly, 100 µM 4-AP significantly increased Ca^{2+} fluxes in TH^- neurons by ~1.75 fold, while co-application of 4-AP with 100 µM diltiazem completely inhibited this increase in Ca^{2+} fluxes (Spontaneous: 48.44 ± 4.52 ΔF/F x sec, 4-AP: 83.65 ± 5.12 ΔF/F x sec, 4-AP + diltiazem: 21.80 ± 3.87 ΔF/F x sec) (Figure 24C & D). These data correlate well with the observed 100 µM 4-AP-induced increase in intrinsic AP frequency in TH^+ and TH^- neurons. Taken together, these data provide clear evidence for the role of VGKC-mediated I_A currents in regulating L-type VGCC activity specifically in TH^+ DA neurons.

Discussion

Developing effective neuroprotective therapies for PD requires an understanding of mechanisms by which abnormal astrocyte-neuron signaling in the midbrain could lead to a loss of SNc DA neurons. In this context, S100B, a ubiquitously expressed astrocytic protein, is particularly interesting because multiple reports in PD patients and animal models suggest that this protein plays an active role in the degeneration of SNc DA neurons [2-7]. Here, we utilize primary cultures of mouse midbrain neurons to show that acute extracellular exposure to picomolar concentrations of S100B alters the activity of A-type VGKCs, and consequently, Ca^{2+} fluxes via L-type VGCCs only in TH^+ DA neurons. Taken together, our findings provide a novel mechanistic basis for understanding how an abnormal increase in extracellularly secreted S100B by midbrain astrocytes during early stages of PD could specifically alter DA neuron function, thereby predisposing the midbrain to neurodegeneration.

We show a striking sex difference whereby S100B-containing astrocytic processes envelop DA neuronal somata in the SNc of only male but not female mice (Figure 17). This finding is significant because of two reasons: (**i**) Our reported sex difference correlates with the well established two-fold increased risk for clinical PD in males compared with females [44], (**ii**) Astrocytic coverage of neuropil is a critical determinant in modulating the excitability of neurons via mechanisms such as the secretion of astrocyte-derived factors, the clearance of neurotransmitters, and extracellular K^+ buffering [45]. Thus, the observed morphological differences in interaction of astrocytic processes with SNc DA neurons, in combination with an increased S100B density in the SNc when compared to the VTA suggest that any abnormal increase in astrocytic secretion of S100B into extracellular milieu of the SNc could significantly alter the functionality of SNc DA neurons with relatively little effect on DA neurons within the VTA. In addition, the average concentration of S100B levels in the CSF of PD patients is ~3.1 μg/l [2], and ~70 to 80% of S100B in the CSF is due to secretion from the brain and not from serum [2, 46]. These values lead us to estimate that extracellular S100B concentrations in the SNc during PD are likely in the range of 50 – 100 pM. Therefore, this study utilizes a PD-relevant extracellular concentration of 50 pM S100B to assess alterations in midbrain DA neuron function.

Recent studies demonstrate that secreted S100B can buffer extracellular Ca^{2+}, thereby altering the function of Ca^{2+} sensitive K^+ channels in pacemaking neurons [10, 11]. In addition, a study using the mollusk as an animal model has shown that extracellular S100B alters potassium currents thereby increasing electrical discharge in the central nervous system [47]. Inspired by these data, we asked if extracellular S100B exposure alters the function of VGKCs and intrinsic APs in cultured midbrain neurons. Experiments revealed that 50 pM S100B specifically inhibited A-type voltage-gated potassium currents (I_A) in TH^+, but not TH^- neurons (Figure 18). Mechanistically, the inhibition of I_A by S100B is not likely to involve Ca^{2+} buffering because picomolar concentrations of S100B cannot buffer extracellular Ca^{2+} to the extent of altering ion channel function. Therefore, the ability of S100B to inhibit I_A likely involves a direct interaction between S100B and VGKCs. The specific inhibition of I_A only in TH^+ neurons suggests that TH^+ and TH^- neurons differ in their VGKC composition. In line with this rationale, we show that TH^+ and TH^- neurons display significant qualitative and quantitative differences in baseline I-V relationships for fast inactivating I_A (Figure 18E). Although we do not yet know the identity of VGKC subtypes that are inhibited by extracellular S100B in TH^+ DA neurons, studies have shown that the vast majority of fast inactivating I_A in SNc DA neurons require the Kv4.3 subtype [22, 33, 48]. Based on these reports, we infer that extracellular S100B likely inhibits Kv4.3 channels in cultured TH^+ DA neurons.

We show that extracellular S100B causes a 2-fold increase in intrinsic AP frequency in TH^+, and not in TH^- neurons (Figure 20). This finding is in line with established roles for A-type VGKCs in regulating AP frequency [32-34, 49]. Therefore, inhibition of I_A by S100B is expected to cause an increase in AP frequency, which would result in the observed potentiating effect of S100B on intrinsic APs in TH^+ neurons. Paradoxically, TH^- neurons showed a decrease intrinsic AP frequency following exposure to extracellular S100B (Figure 20B). Since extracellular S100B does not affect either I_A or I_K in TH^- neurons, our data suggest that S100B-mediated inhibition of intrinsic APs in TH^- neurons likely occurs via a mechanism that is independent of VGKCs.

Our data suggest that the ability of extracellular S100B to specifically increase L-type VGCC Ca^{2+} fluxes only in TH^+ and not TH^- neurons (Figures 21 & 22) lies downstream of S100B-mediated inhibition of I_A in TH^+ neurons. This conclusion is strongly supported by the finding that 4-AP-mediated inhibition of I_A in midbrain neurons causes a significant increase in intrinsic firing frequency and spontaneous Ca^{2+} fluxes in TH^+ neurons (Figure 24). The idea that I_A inhibition causes an increase in L-type VGCC activity in TH^+ DA neurons is novel. Although a previous study has shown that inhibition of L-type VGCCs does not affect intrinsic firing in DA neurons [50] to our knowledge, the data presented in this study are the first to show that an inhibition of I_A in TH^+ DA neurons increases the frequency of Ca^{2+} fluxes through L-type VGCCs. This idea is also supported by the finding that spontaneous L-type VGCC-mediated Ca^{2+} flux frequencies are significantly higher in TH^- neurons when compared to TH^+ cells (Figure 26D), which correlates quite well with the 2-fold higher intrinsic AP frequency in TH- neurons when compared to TH^+ neurons (Figure 20). Furthermore, it is notable that extracellular S100B did not alter the activity of T-type VGCCs in TH^+ neurons

(Figure 23), which suggests that VGKCs and L-type VGCCs in TH$^+$ DA neurons are specifically and functionally coupled.

In summary, this study uncovers a novel mechanism in which extracellular S100B specifically inhibits fast inactivating A-type VGKCs in TH$^+$ DA neurons, thereby increasing intrinsic neuronal firing, which in turn causes an increase in the frequency of Ca^{2+} fluxes via L-type VGCCs. In this study, we do not consider the local release of S100B onto neurons from astrocytes, however a recent study has used optogenetic stimulation for local release of endogenous astrocytic S100B, which results in altered activity of pyramidal neurons in the visual cortex [11]. In addition, the release of S100B from astrocytes could activate RAGE receptors expressed on astrocytes, resulting in altered gliotransmission and cytokine release [12-14]. Given the important role of L-type VGCC dysfunction in PD [18, 35-40], these findings are relevant to understanding how extracellular S100B alters DA neuron function, thereby initiating neurodegenerative processes during early PD. Furthermore, our finding that the interaction between extracellular S100B and VGKCs is specific to TH$^+$ DA neurons provides a potential avenue for discovering novel neuroprotective PD drugs that specifically disrupt S100B-VGKC interactions in DA neurons. Important questions include whether or not an acute interaction between extracellular S100B and VGKCs in TH$^+$ DA neurons leads to PD, and whether the sex-specific association of S100B with SNc DA neurons only in male mice can partially explain observed sex differences in clinical PD. In this regard, future work will focus on assessing the *in vivo* effects of extracellularly secreted astrocytic S100B on SNc DA function, neuronal loss and PD-related behavioral deficits.

Figures

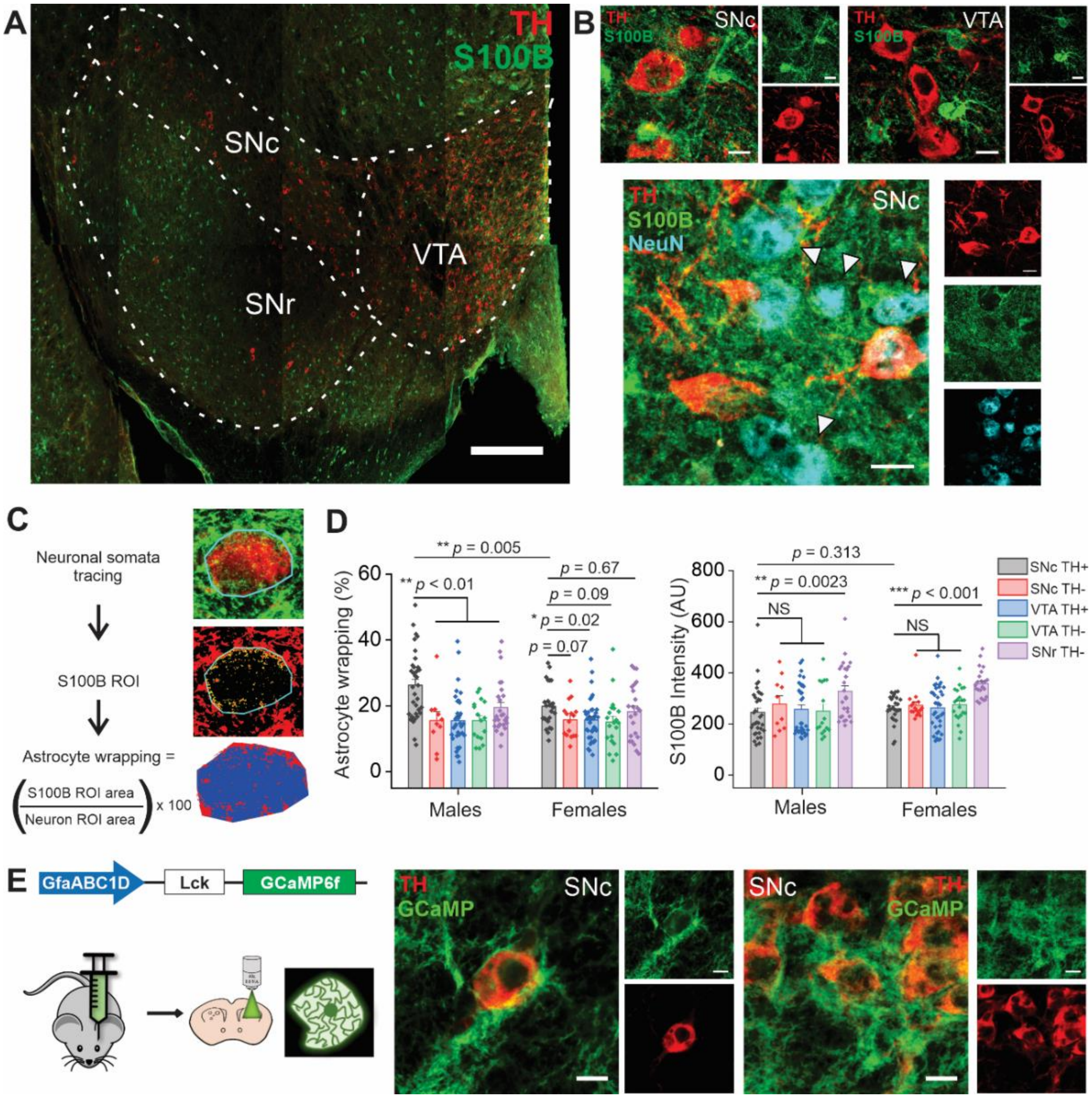

Figure 5: Wrapping of S100B-containing astrocytic processes around SNc DA neurons is significantly increased only in male mice.
(A) A representative confocal mosaic of a mouse midbrain section immunostained for S100B (green) and TH (red), scale bar = 300 µm. Subregions of the midbrain are indicated with dotted lines (SNc = substantia nigra pars compacta; VTA = ventral tegmental area; SNr = substantia nigra pars reticulata) **(B)** Representative high magnification confocal images of S100B and TH expression in the SNc (top left) and

VTA (top right), NeuN expression in the SNc is shown in the lower panel with white arrows denoting TH- neurons, scale bar = 10 μm. **(C)** Schematic of astrocyte wrapping analysis, described in detail in the methods section. **(D)** Graphs showing astrocyte wrapping of neuronal somata (left panel) and S100B expression intensity (right panel) across specific midbrain subregions in male and female mice. n = 8 midbrain sections from 3 male and 3 female mice. All errors are SEM; p values are based on two sample t-tests except for SNc TH^+, VTA TH^+, and SNc TH^+, SNr TH^- comparisons which are Mann-Whitney tests. **(E)** Schematic for genetically expressing membrane bound GCaMP6f in astrocytes using AAV 2/5 $GfaABC_1D$-Lck-GCaMP6f, including representative confocal images of astrocyte processes enveloping TH^+ neurons in the SNc.

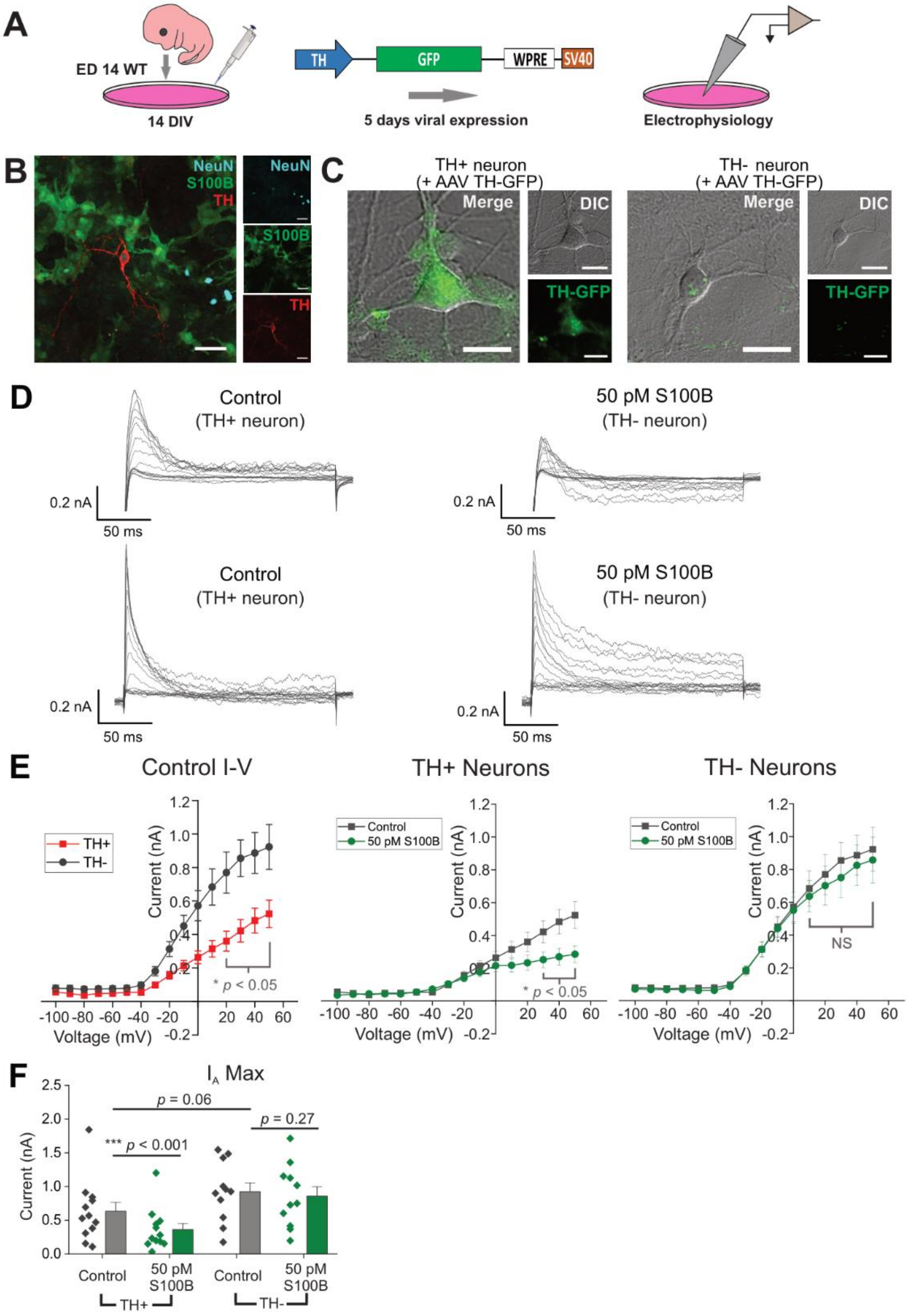
A
ED 14 WT
14 DIV
TH
GFP
WPRE
SV40
5 days viral expression
Electrophysiology
B
NeuN
S100B
TH
C
TH+ neuron
(+ AAV TH-GFP)
TH- neuron
(+ AAV TH-GFP)
Merge
DIC
TH-GFP
D
Control
(TH+ neuron)
50 pM S100B
(TH- neuron)
0.2 nA
50 ms
E
Control I-V
TH+ Neurons
TH- Neurons
TH+
TH-
Control
50 pM S100B
Current (nA)
Voltage (mV)
* p < 0.05
NS
F
I_A Max
Current (nA)
p = 0.06
*** p < 0.001
p = 0.27
Control
50 pM S100B
TH+
TH-

Figure 6: Acute exposure to S100B specifically inhibits A-type voltage-gated potassium currents (I_A) in TH^+ neurons.
(A) Schematic for measuring spontaneous action potentials and ionic currents in primary mouse midbrain neuron cultures using AAV 2/5 TH-GFP virus. **(B)** Representative image of a formalin-fixed primary mouse midbrain culture stained for NeuN, S100B and TH; scale bar = 50 μm. **(C)** Representative images of TH-GFP expression in TH^+ and TH^- neurons. **(D)** Representative traces of subtracted I_A from TH^+ and TH^- neurons with (right) and without (left) 50 pM S100B. **(E)** Left panel, I-V curves of TH^+ and TH^- neurons in regular aCSF. Right panels, average I-V curves from TH^+ and TH^- neurons with and without S100B. **(F)** Comparison of max I_A from the most depolarizing stimulation step in TH^+ and TH^- neurons. n = 12 for TH^+ neurons and 11 for TH^- neurons from 3 independent weeks of culture. All errors are SEM; p values for I-V curves are based on mixed-design ANOVA with post-hoc Bonferroni correction; p values for max I_A Wilcoxon signed rank tests are used for TH^+ control, TH^+ S100B, paired sample t-tests for TH^- control, TH^- S100B, and Mann-Whitney tests for TH^+ control, TH^- control.

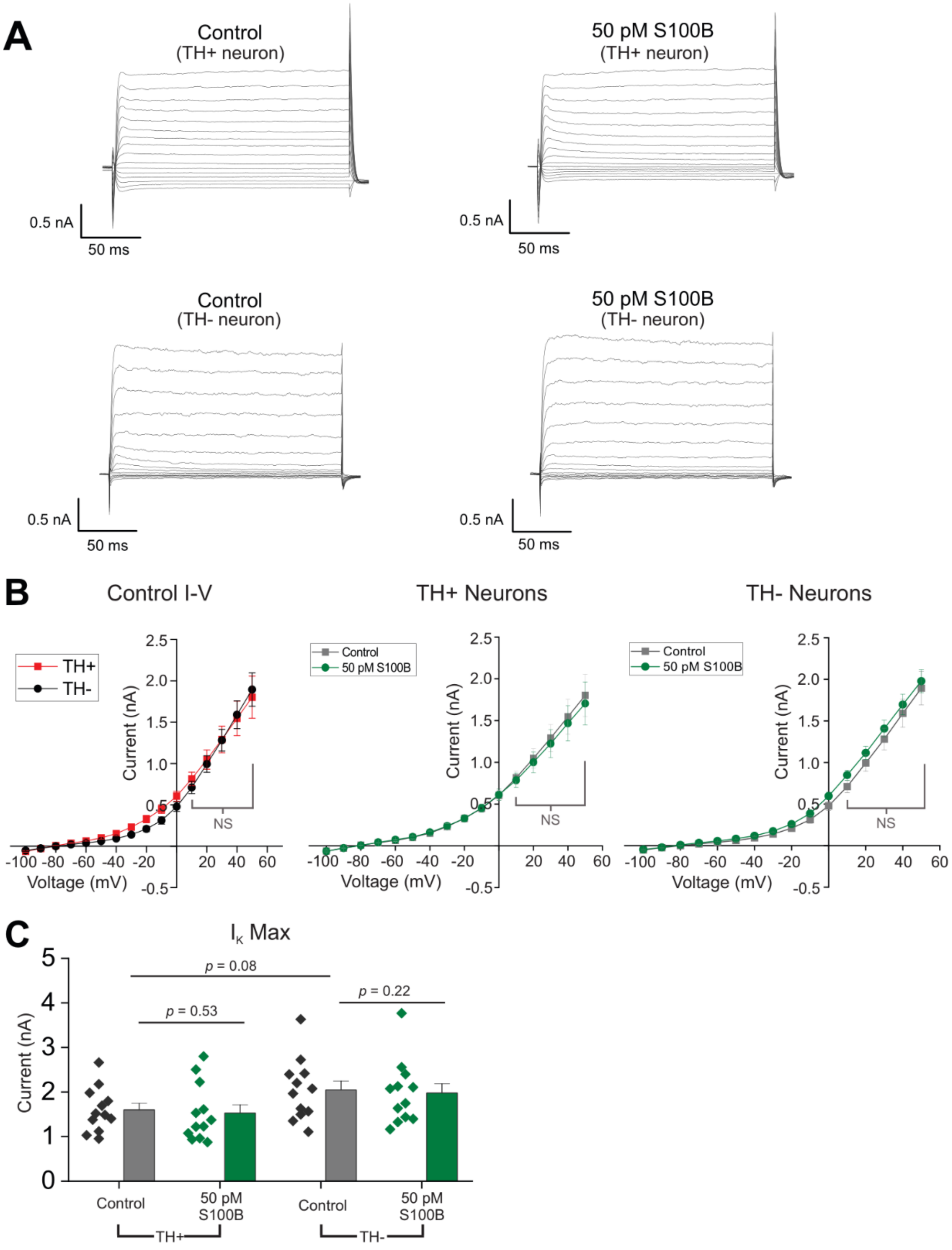

Figure 7: Acute S100B exposure does not inhibit non-inactivating voltage-gated potassium currents (I_K) in midbrain neurons.

(A) Representative traces of I_K from TH$^+$ and TH$^-$ neurons with (right) and without (left) 50 pM S100B. **(B)** Left panel, I-V curves of TH$^+$ and TH$^-$ neurons in regular aCSF.

Right panels, average I-V curves from TH^+ and TH^- neurons with and without S100B. **(C)** Comparison of max I_K from the most depolarizing stimulation step in TH^+ and TH^- neurons. n = 11 for TH^+ neurons and 12 for TH^- neurons from 3 independent weeks of culture. All errors are SEM; p values for I-V curves are based on mixed-design ANOVA with post-hoc Bonferroni correction; p values for max I_K are based on paired sample t-tests for TH^+ control, TH^+ S100B and TH^- control, TH^- S100B, and two sample t-tests for TH^+ control, TH^- control.

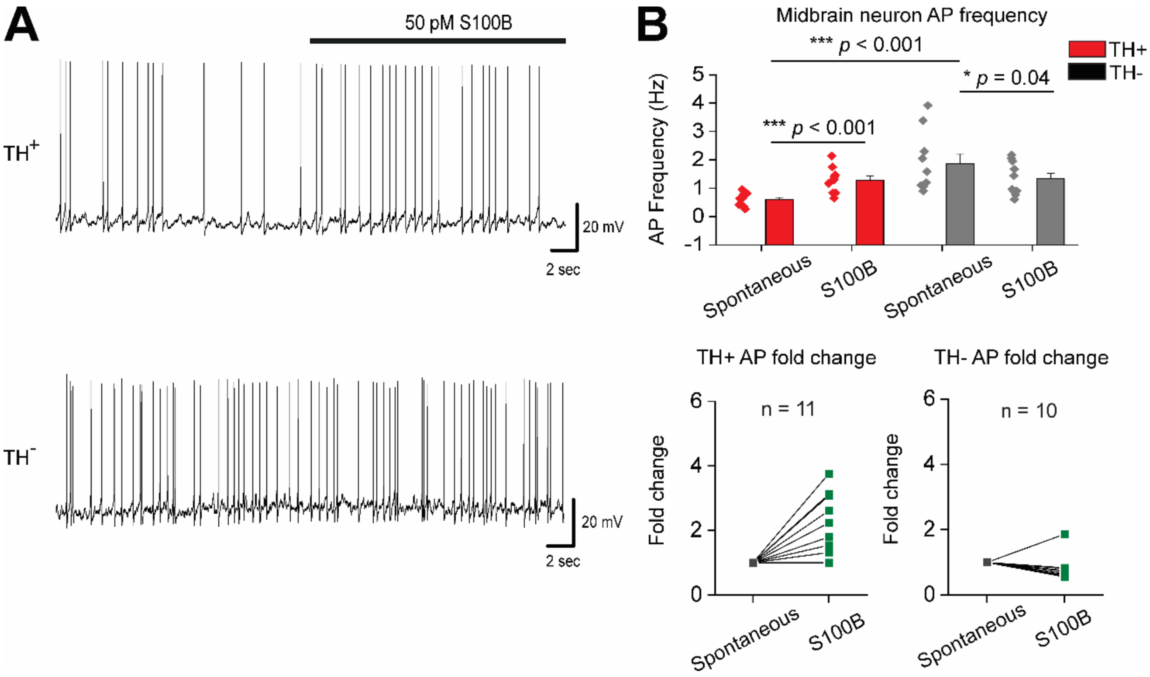

Figure 8: Acute S100B exposure increases intrinsic AP frequency in TH^+ neurons. **(A)** Representative traces of AP recordings from TH^+ and TH^- neurons with acute application of 50 pM S100B. **(B)** Average AP frequency of TH^+ and TH^- neurons with and without S100B; fold change for each TH^+ and TH^- neuron is shown in the graphs below. n = 11 for TH^+ neurons and 10 for TH^- neurons from 3 independent weeks of culture. All errors are SEM; p values for AP frequency are based on paired sample t-tests for TH^+ spontaneous, TH^+ S100B, Wilcoxon signed rank tests for TH^- spontaneous, TH^- S100B, and Mann-Whitney tests for TH^+ spontaneous, TH^- control.

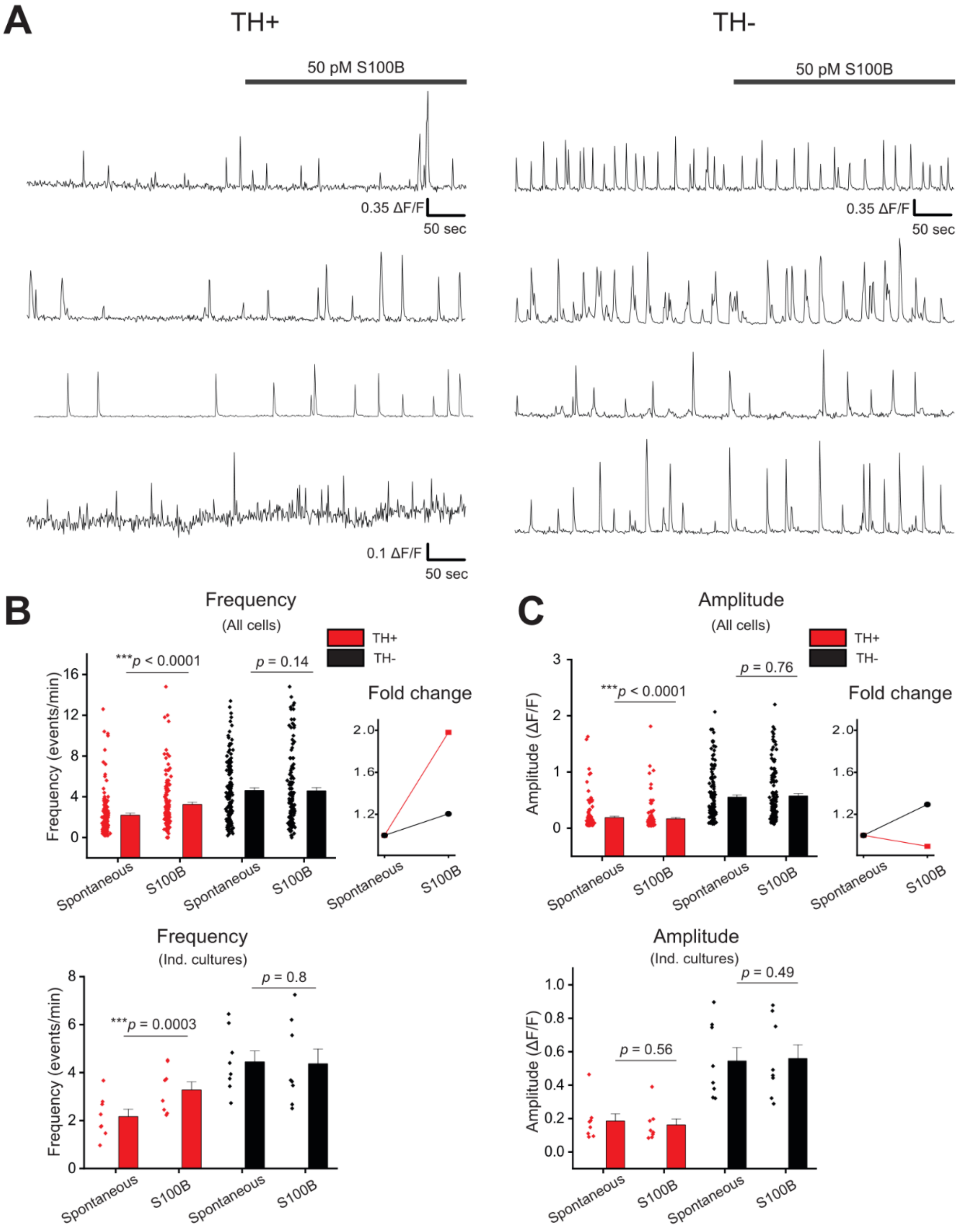

Figure 9: Acute exposure of primary midbrain cultures to S100B peptide increases spontaneous Ca^{2+} flux frequency only in TH^+ neurons.

(A) Multiple representative traces of spontaneous Ca^{2+} fluxes in TH^{+} and TH^{-} neurons with acute bath application of 50 pM S100B peptide are shown. **(B)** A graph with average frequency of Ca^{2+} flux events from individual TH^{+} (red) and TH^{-} (black) neurons with and without S100B peptide is shown. The line graph on the right shows the average fold change of Ca^{2+} flux frequency for TH^{+} and TH^{-} cells following S100B application. The graph below shows the average frequency of TH^{+} and TH^{-} neurons binned by week of culture. **(C)** A graph with average amplitude of Ca^{2+} events from individual TH^{+} (red) and TH^{-} (black) neurons with and without S100B peptide. The line graph on the right shows the average fold change of Ca^{2+} flux amplitude for TH^{+} and TH^{-} cells following S100B application. The graph below shows the average amplitude of TH^{+} and TH^{-} neurons binned by individual culture. n = 137 for TH^{+} neurons and 134 for TH^{-} neurons from 8 independent cultures. All errors are SEM; p values for all cells are based on Wilcoxon signed rank tests for TH^{+} spontaneous, TH^{+} S100B and TH^{-} spontaneous, TH^{-} S100B and Mann-Whitney tests for TH^{+} spontaneous, TH^{-} spontaneous; p values for individual cultures are based on paired sample t-tests for TH^{+} spontaneous, TH^{+} S100B and TH^{-} spontaneous, TH^{-} S100B, and two sample t-tests for TH^{+} spontaneous, TH^{-} spontaneous.

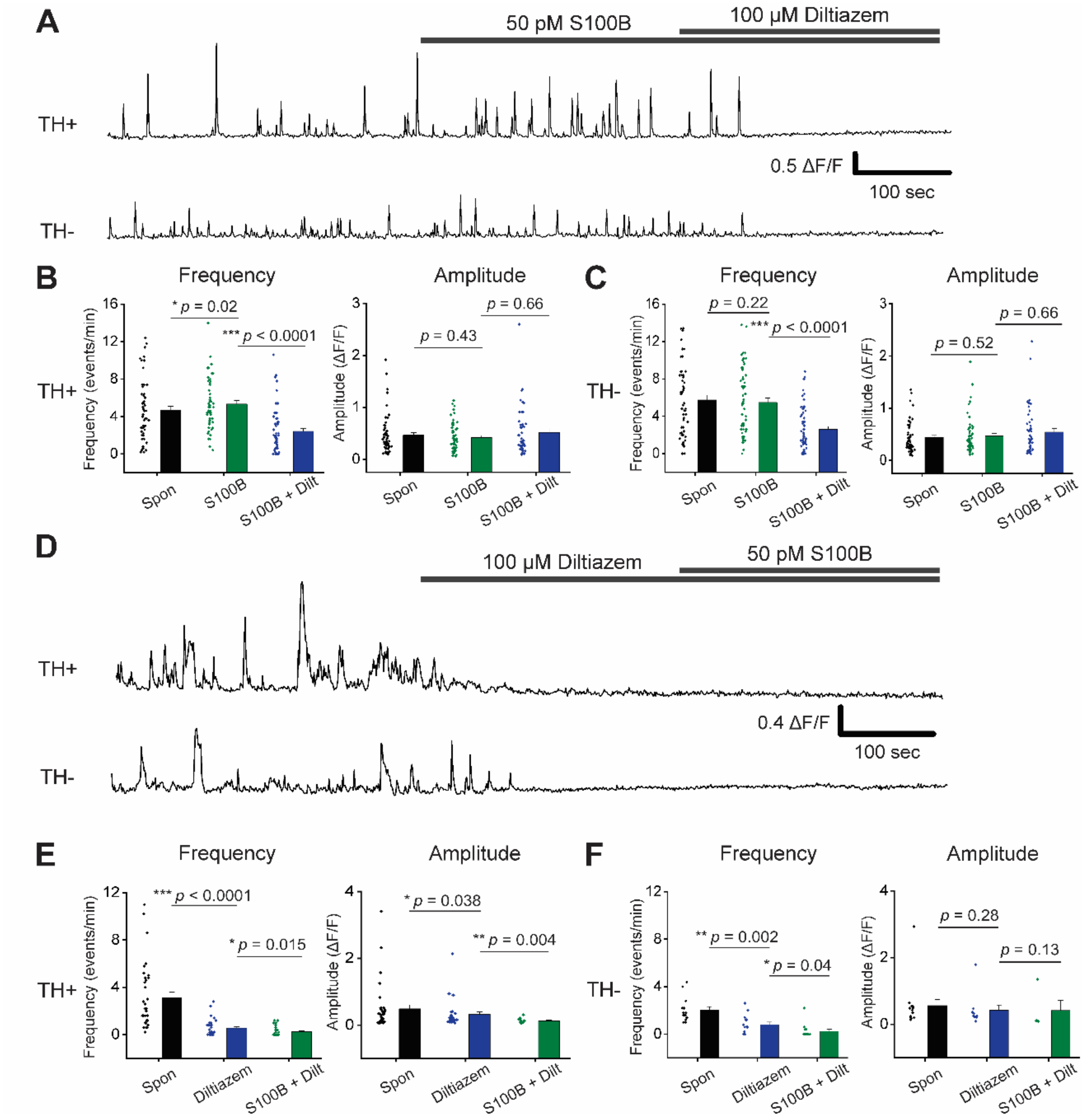

Figure 10: Extracellular S100B mediated increase in spontaneous Ca^{2+} fluxes in TH^{+} DA neurons require active L-type VGCCs.

(A) Representative traces of spontaneous Ca^{2+} fluxes in a TH^{+} and TH^{-} neuron with bath application of S100B, followed by co-application of S100B with diltiazem. **(B)** Graphs show average Ca^{2+} flux frequency and amplitude of TH^{+} neurons without any drug (black) with bath applied S100B (green), and co-applied S100B + diltiazem (blue). **(C)** Graphs show average Ca^{2+} flux frequency and amplitude of TH^{-} neurons without drug (black) with bath applied S100B (green), and co-applied S100B + diltiazem (blue). n = 55 for TH^{+} neurons and 57 for TH^{-} neurons from 4 independent weeks of culture. All errors are SEM; p values for frequency and amplitude are based on Wilcoxon signed rank tests for all cases in panels B and C. **(D)** Representative traces of spontaneous Ca^{2+} fluxes in a TH^{+} and TH^{-} neuron with bath application of diltiazem, followed by co-application of diltiazem with S100B. **(E)** Graphs show average Ca^{2+} flux frequency and amplitude of TH^{+} neurons without any drug (black) with bath applied diltiazem (blue), and co-applied diltiazem + S100B (green). **(F)** Graphs show average Ca^{2+} flux frequency and amplitude of TH^{-} neurons without any drug (black) with bath applied diltiazem (blue), and co-applied diltiazem + S100B (green). n = 34 for TH^{+} neurons and 18 for TH^{-} neurons from 4 independent weeks of culture. All errors are SEM; p values for frequency and amplitude are based on Wilcoxon signed rank tests for all cases in panels E and F.

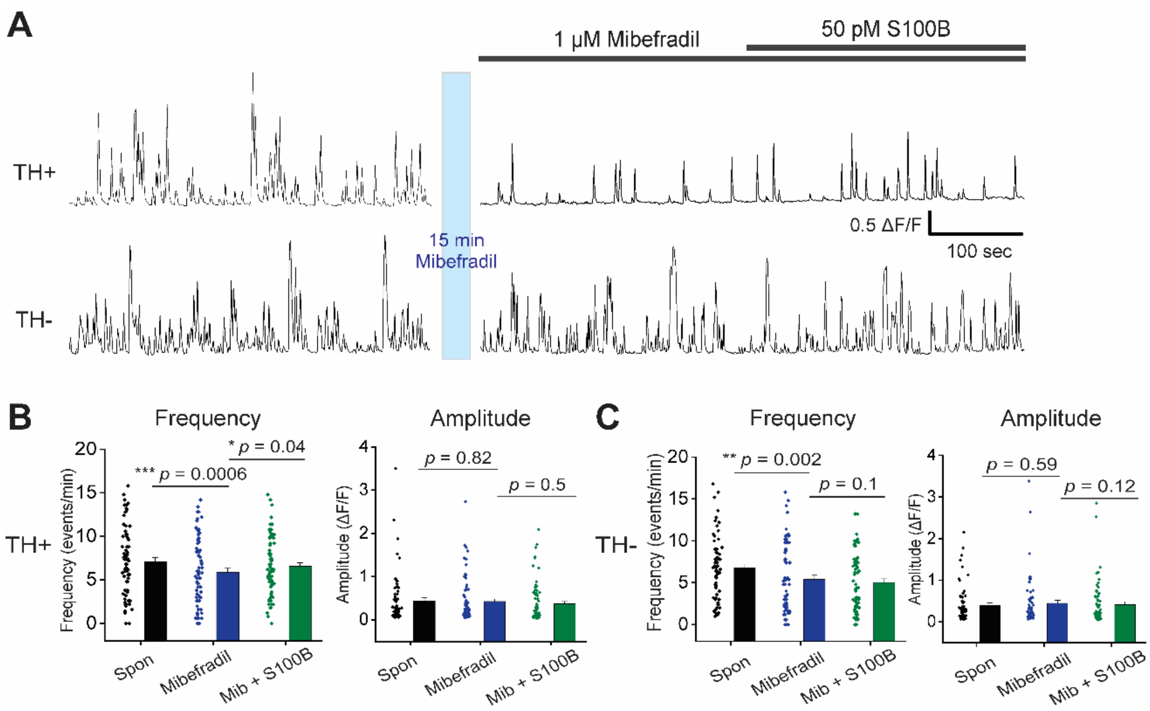

Figure 11: Extracellular S100B mediated increase in spontaneous Ca^{2+} fluxes in TH^{+} DA neurons does not require active T-type VGCCs.
(A) Representative traces of spontaneous Ca^{2+} fluxes in a TH^{+} and TH^{-} neuron after 15 min incubation with 1 μM mibefradil, followed by co-application of S100B with mibefradil. **(B)** Graphs show average Ca^{2+} flux frequency and amplitude of TH^{+} neurons without any drug (black) with bath applied mibefradil (blue), and co-applied S100B + mibefradil (green). **(C)** Graphs show average Ca^{2+} flux frequency and amplitude of TH^{-} neurons without drug (black) with bath applied mibefradil (blue), and co-applied S100B + mibefradil (green). n = 75 for TH^{+} neurons and 66 for TH^{-} neurons from 4 independent weeks of culture. All errors are SEM; p values for frequency and amplitude are based on Wilcoxon signed rank tests for all cases in panels B and C.

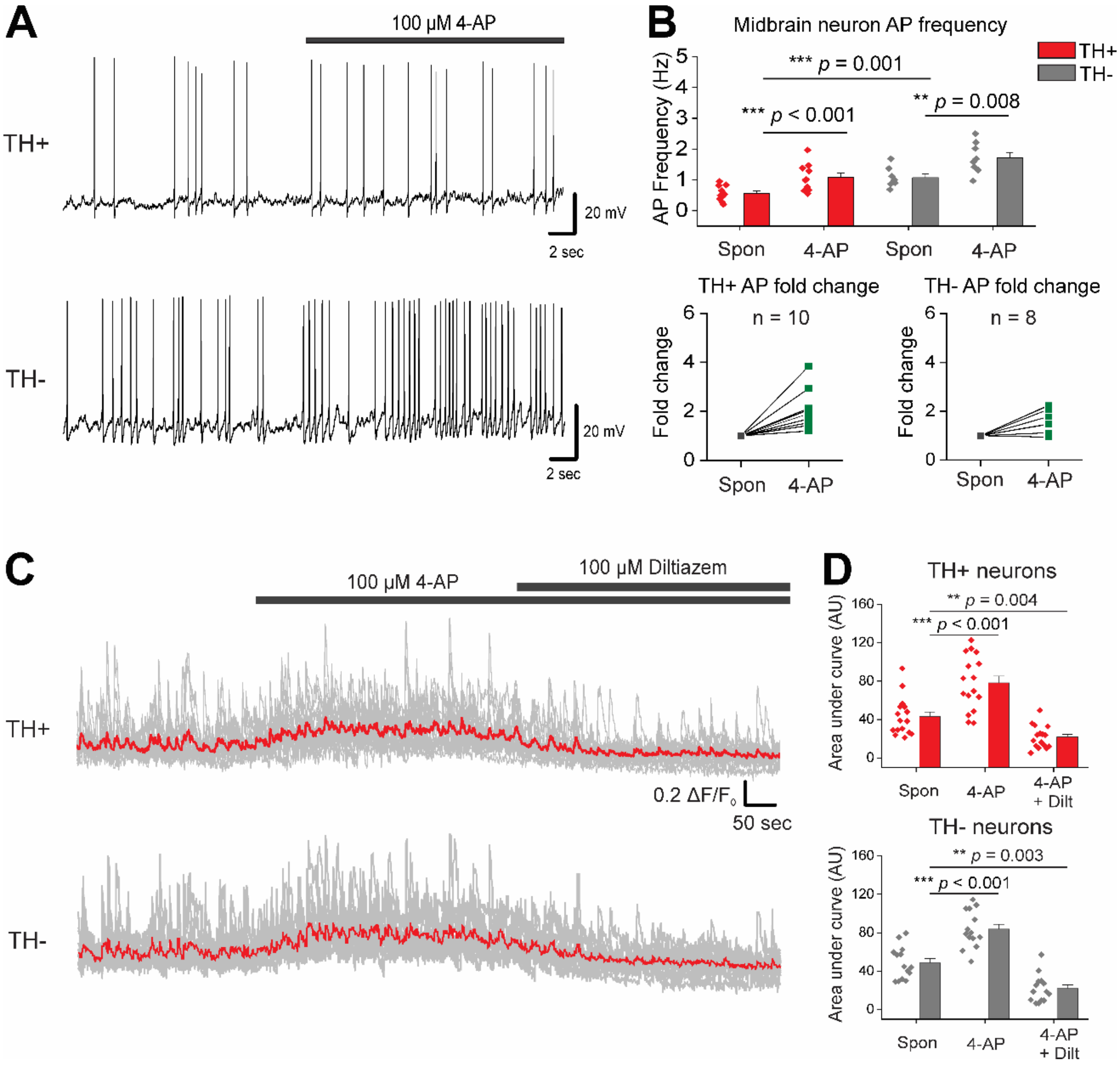

Figure 12: The A-type VGKC inhibitor, 4-AP mimics S100B-mediated increases in intrinsic APs and L-type VGCC-mediated Ca^{2+} flux frequencies in midbrain neurons.

(A) Representative traces of AP recordings from TH$^+$ and TH$^-$ neurons with acute application of 100 µM 4-AP. **(B)** Average AP frequency of TH$^+$ and TH$^-$ neurons with and without 4-AP; fold change for each TH$^+$ and TH$^-$ neuron is shown in the graphs below. n = 10 for TH$^+$ neurons and 9 for TH$^-$ neurons from 2 independent weeks of culture. All errors are SEM; p values are based on paired sample t-tests for TH$^+$ spontaneous, TH$^+$ 4-AP and TH$^-$ spontaneous, TH$^-$ 4-AP or two sample t-tests for TH$^+$ spontaneous, TH$^-$ spontaneous. **(C)** Representative Ca^{2+} traces of TH$^+$ and TH$^-$ neurons with bath application of 4-AP, followed by co-application of 4-AP + diltiazem, the red line represents the average Ca^{2+} activity from all neurons of that cell type. **(D)** Graphs of average area under the curve with bath application of 4-AP, followed by co-application of 4-AP + diltiazem. n = 16 for TH^+ neurons and 14 for TH^- neurons from 2 independent weeks of culture. All errors are SEM; p values for TH^+ neurons are based on Wilcoxon signed rank tests, and paired sample t-tests for TH^- neurons.

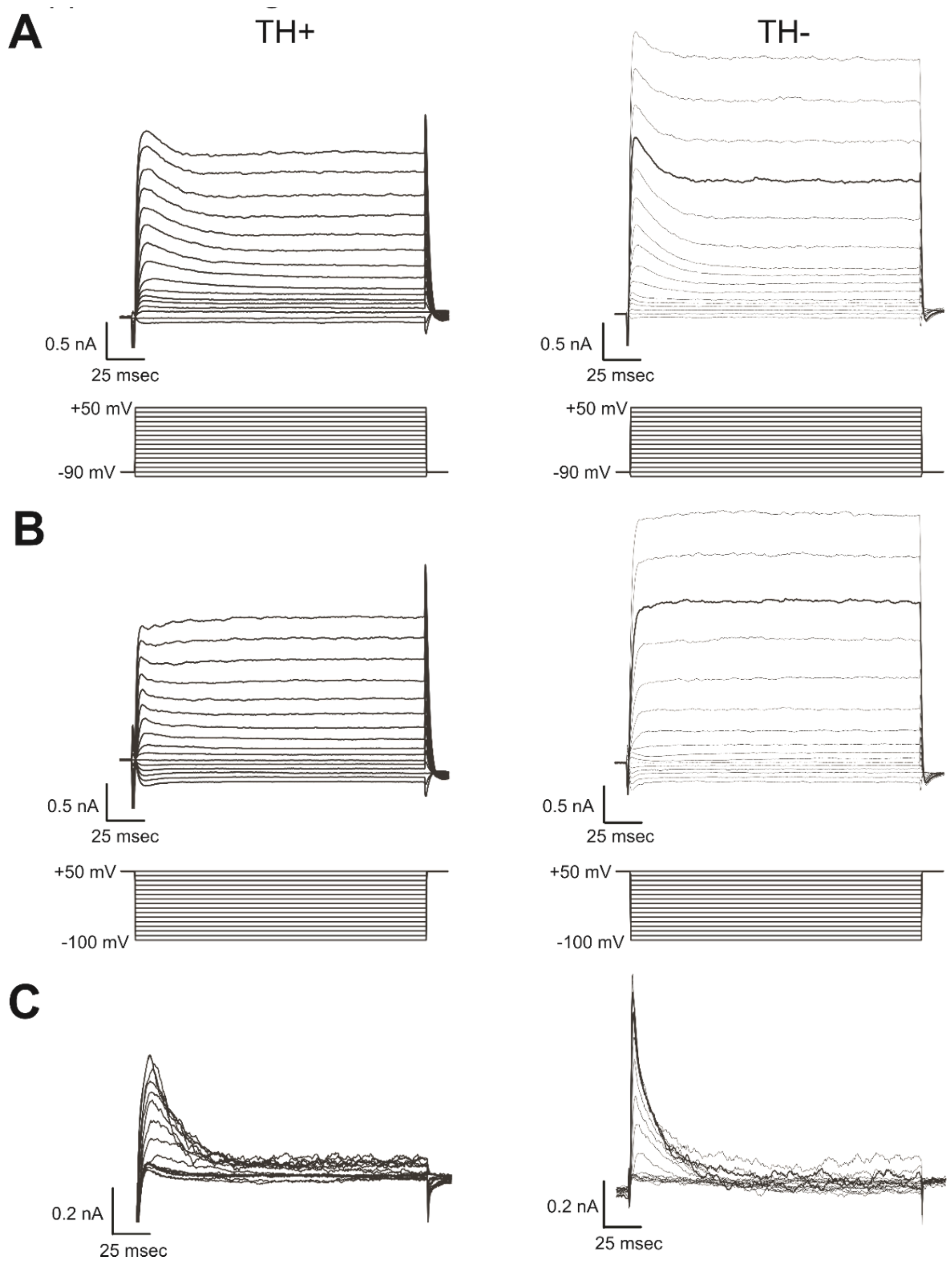

Figure 13: Stimulation protocols for electrical isolation of A-type potassium current (I_A).

(A) Representative current traces from TH^+ and TH^- neurons using a stimulation protocol consisting of a 100 ms prepulse (max conductance) at -90 mV followed by a 250 ms step at increasingly depolarized potentials (-100 to 50 mV, 10 mV steps) **(B)** Representative current traces from TH^+ and TH^- neurons using a stimulation protocol consisting of a 100 ms prepulse at +50 mV (to remove I_A contribution) followed by a 250 ms step at increasingly depolarized potentials (-100 to 50 mV, 10 mV steps) **(C)** Representative currents traces of subtracted I_A from TH^+ and TH^- neurons; traces were generated from subtracting the traces in (B) from the traces in (A).

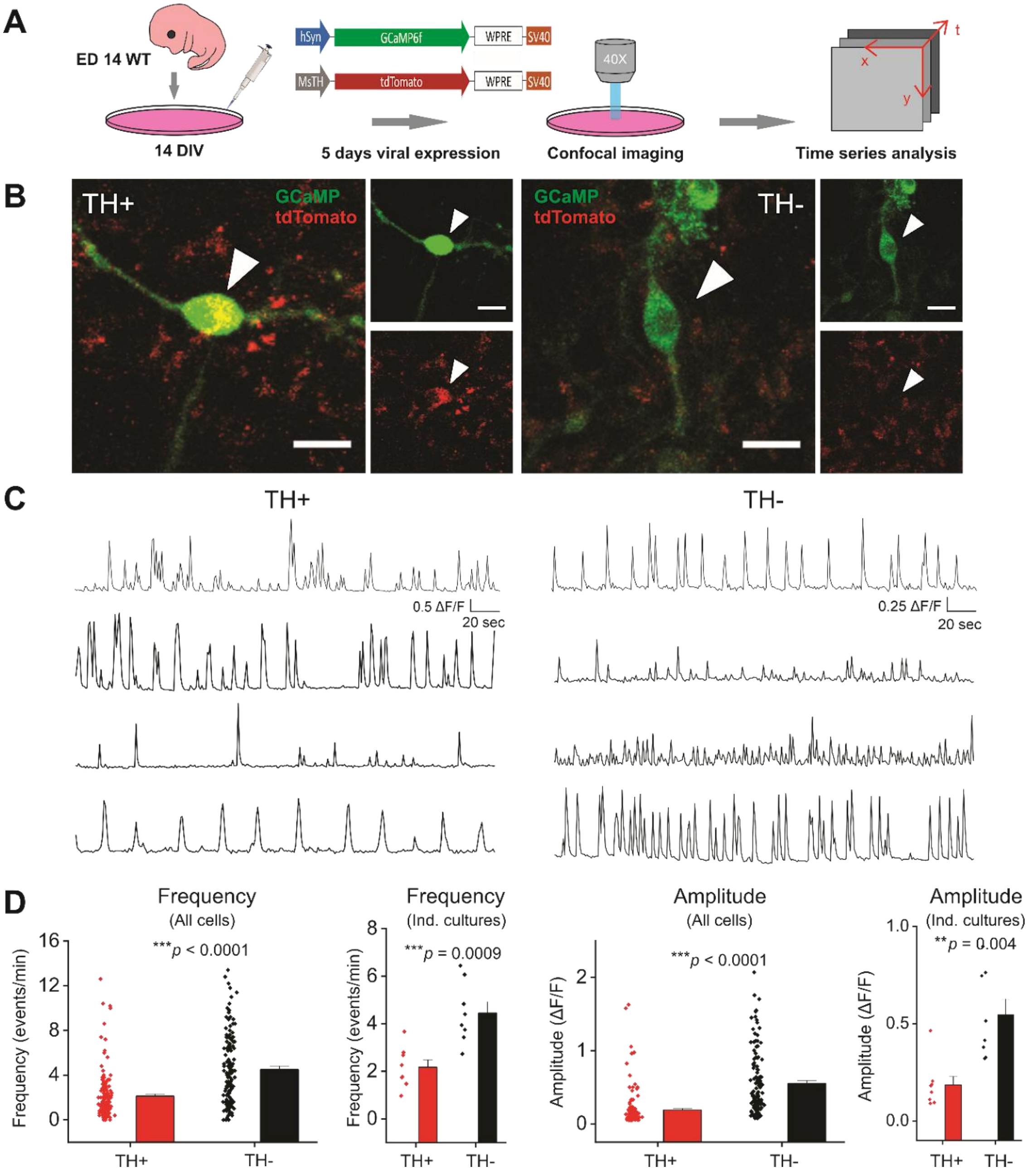

Figure 14: Cultured mouse primary TH$^+$ and TH$^-$ neurons differ with regard to spontaneous Ca^{2+} flux kinetics.

(A) Schematic for measuring spontaneous Ca^{2+} fluxes in primary mouse midbrain neuron cultures using AAV 2/5 hSyn-GCaMP6f and AAV 2/5 TH-tdTomato viruses. **(B)** Representative confocal images of live primary mouse midbrain cultures are shown. Arrowheads point to an example of a TH$^+$ neuron with hSyn-GCaMP6f (green) and TH-tdTomato (red) expression and an example of a TH$^-$ neuron with hSyn-GCaMP6f expression, but no expression of TH-tdTomato; scale bar = 20 μm. **(C)** Multiple representative traces of spontaneous Ca^{2+} fluxes in TH^{+} and TH^{-} neurons showing the heterogenous nature of spontaneous Ca^{2+} flux events in cultured TH^{+} and TH^{-} neurons. **(D)** Average frequency and amplitude of Ca^{2+} flux events from individual TH^{+} and TH^{-} neurons. Graphs are presented as the entire dataset of individual cells (All cells) and also binned by independent weeks of culture (Ind. cultures). n = 137 for TH^{+} neurons and 134 for TH^{-} neurons from 8 independent weeks of culture. All errors are SEM; p values are based on Mann-Whitney tests.

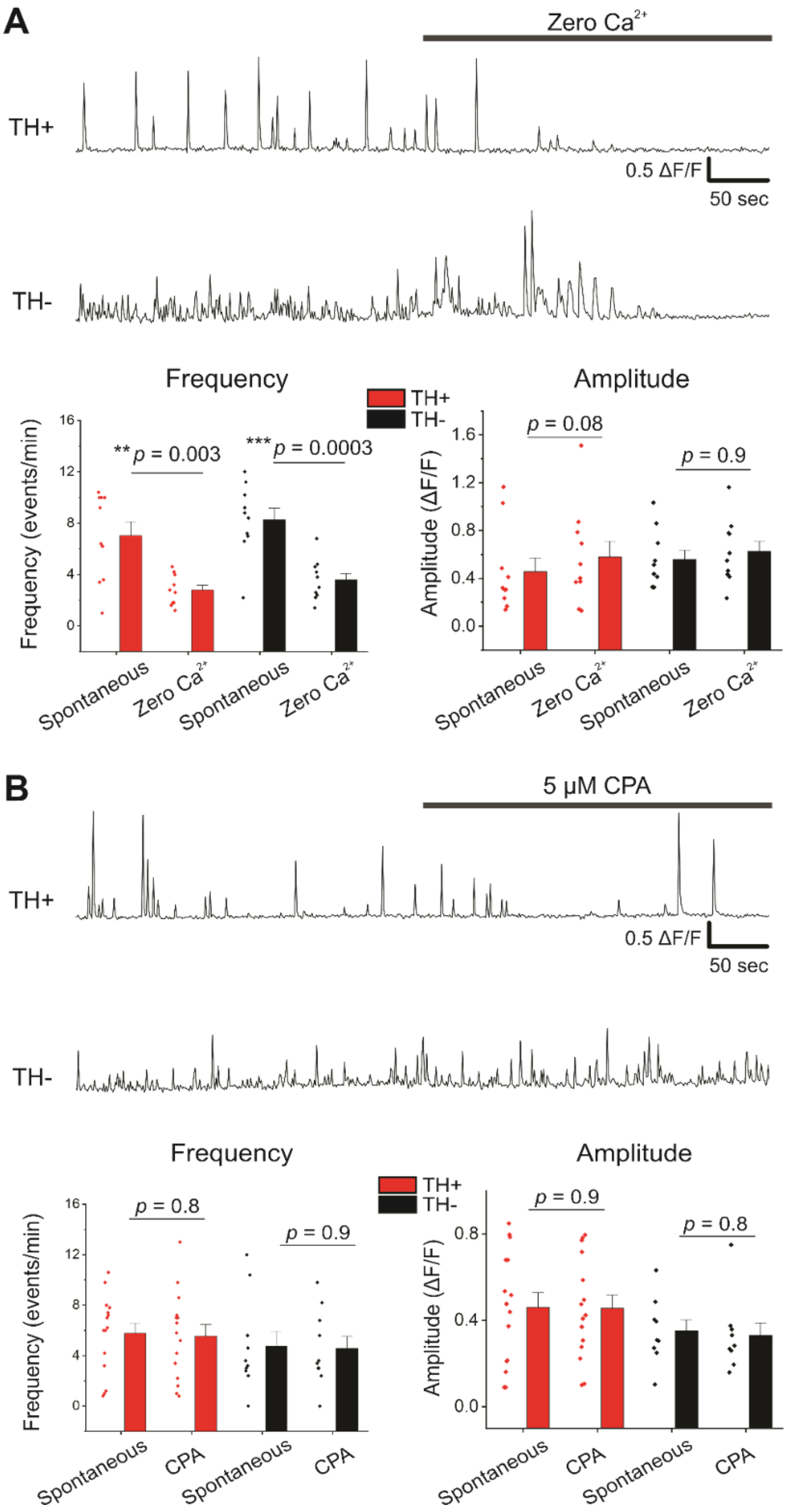
A
Zero Ca2+
TH+
0.5 ΔF/F
50 sec
TH-
Frequency
TH+
TH-
Frequency (events/min)
16
12
8
4
0
** p = 0.003
*** p = 0.0003
Spontaneous
Zero Ca2+
Spontaneous
Zero Ca2+
Amplitude
Amplitude (ΔF/F)
1.6
1.2
0.8
0.4
0.0
p = 0.08
p = 0.9
Spontaneous
Zero Ca2+
Spontaneous
Zero Ca2+
B
5 μM CPA
TH+
0.5 ΔF/F
50 sec
TH-
Frequency
TH+
TH-
Frequency (events/min)
16
12
8
4
0
p = 0.8
p = 0.9
Spontaneous
CPA
Spontaneous
CPA
Amplitude
Amplitude (ΔF/F)
0.8
0.4
0.0
p = 0.9
p = 0.8
Spontaneous
CPA
Spontaneous
CPA

Figure 15: Spontaneous Ca^{2+} fluxes in cultured mouse midbrain neurons depend on extracellular Ca^{2+}.

(A) Representative traces of spontaneous Ca^{2+} fluxes in a TH^{+} and TH^{-} neuron with bath applied zero Ca^{2+} aCSF. The graphs below show average Ca^{2+} flux frequency and amplitude for TH^{+} (red) and TH^{-} (black) neurons with and without zero Ca^{2+} aCSF **(B)** Representative traces of spontaneous Ca^{2+} fluxes in a TH^{+} and TH^{-} neuron with bath applied 5 μM CPA. The graphs below show average Ca^{2+} flux frequency and amplitude for TH^{+} (red) and TH^{-} (black) neurons with and without 5 μM CPA. For zero Ca^{2+} aCSF experiments, n = 10 for TH^{+} neurons and 15 for TH^{-} neurons from 3 independent weeks of culture. For CPA experiments, n = 15 for TH^{+} neurons and 10 for TH^{-} neurons from 3 independent weeks of culture. All errors are SEM; p values for frequency are based on paired sample t tests and Wilcoxon signed ranked tests for amplitudes of TH^{+} spon, TH^{+} zero Ca^{2+} and TH^{-} spon, TH^{-} CPA.

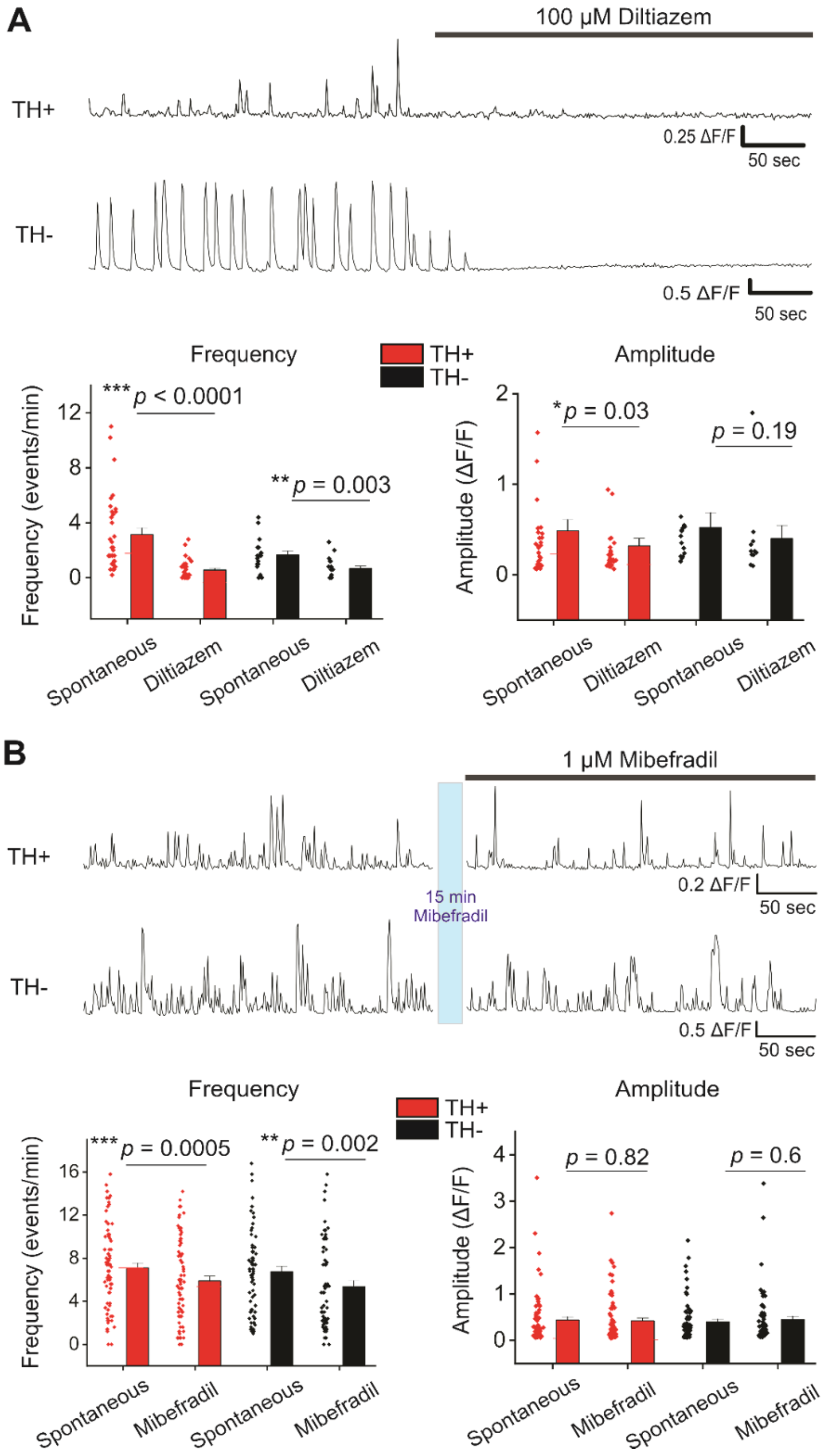
A
100 μM Diltiazem
TH+
0.25 ΔF/F
50 sec
TH-
0.5 ΔF/F
50 sec
Frequency
TH+
TH-
Frequency (events/min)
***p < 0.0001
**p = 0.003
12
8
4
0
Spontaneous
Diltiazem
Spontaneous
Diltiazem
Amplitude
Amplitude (ΔF/F)
*p = 0.03
p = 0.19
2
1
0
Spontaneous
Diltiazem
Spontaneous
Diltiazem
B
1 μM Mibefradil
TH+
15 min Mibefradil
0.2 ΔF/F
50 sec
TH-
0.5 ΔF/F
50 sec
Frequency
TH+
TH-
Frequency (events/min)
***p = 0.0005
**p = 0.002
16
12
8
4
0
Spontaneous
Mibefradil
Spontaneous
Mibefradil
Amplitude
Amplitude (ΔF/F)
p = 0.82
p = 0.6
4
3
2
1
0
Spontaneous
Mibefradil
Spontaneous
Mibefradil

Figure 16: Spontaneous Ca^{2+} fluxes in cultured mouse midbrain neurons largely require L-type VGCCs.
(A) Representative traces of spontaneous Ca^{2+} fluxes in a TH^{+} and TH^{-} neuron with bath applied 100 µM diltiazem. The graphs below show average Ca^{2+} flux frequency and amplitude of TH^{+} (red) and TH^{-} (black) neurons with and without diltiazem **(B)** Representative traces of spontaneous Ca^{2+} fluxes in a TH^{+} and TH^{-} neuron following 15 min bath application of 1 µM mibefradil. The graphs below show average Ca^{2+} flux frequency and amplitude of TH^{+} (red) and TH^{-} (black) neurons with and without mibefradil. For diltiazem experiments, n = 34 for TH^{+} neurons and 18 for TH^{-} neurons from 4 independent weeks of culture. For mibefradil experiments, n = 75 for TH^{+} neurons and 66 for TH^{-} neurons from 4 independent weeks of culture. All errors are SEM; p values are based on Wilcoxon signed rank test.

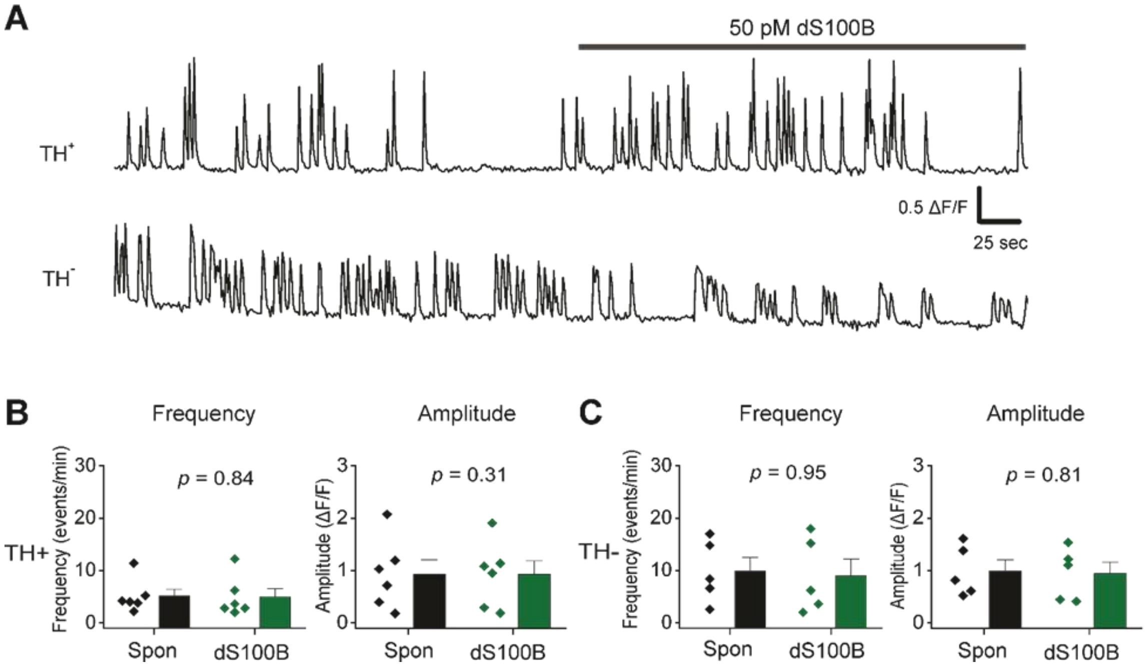

Figure 17: Acute exposure of primary midbrain cultures to denatured S100B peptide has no effect on spontaneous Ca^{2+} flux frequency in TH^{+} neurons.
(A) Representative traces of spontaneous Ca^{2+} fluxes in a TH^{+} and TH^{-} neuron with acute bath application of 50 pM denatured S100B peptide are shown. **(B)** Average frequency and amplitude of Ca^{2+} flux events prior to and during application of denatured S100B for TH^{+} neurons. **(C)** Average frequency and amplitude of Ca^{2+} flux events prior to and during application of denatured S100B for TH^{-} neurons. n = 6 for TH^{+} neurons and 4 for TH^{-} neurons. All errors are SEM; p values are based on Mann-Whitney tests.

References

1. Dorsey, E. R.; Bloem, B. R., The Parkinson Pandemic-A Call to Action. *JAMA Neurol* **2018,** 75, (1), 9-10.
2. Sathe, K.; Maetzler, W.; Lang, J. D.; Mounsey, R. B.; Fleckenstein, C.; Martin, H. L.; Schulte, C.; Mustafa, S.; Synofzik, M.; Vukovic, Z.; Itohara, S.; Berg, D.; Teismann, P., S100B is increased in Parkinson's disease and ablation protects against MPTP-induced toxicity through the RAGE and TNF-alpha pathway. *Brain : a journal of neurology* **2012,** 135, (Pt 11), 3336-47.
3. Schaf, D. V.; Tort, A. B.; Fricke, D.; Schestatsky, P.; Portela, L. V.; Souza, D. O.; Rieder, C. R., S100B and NSE serum levels in patients with Parkinson's disease. *Parkinsonism & related disorders* **2005,** 11, (1), 39-43.
4. Fardell, C.; Zettergren, A.; Ran, C.; Carmine Belin, A.; Ekman, A.; Sydow, O.; Backman, L.; Holmberg, B.; Dizdar, N.; Soderkvist, P.; Nissbrandt, H., S100B polymorphisms are associated with age of onset of Parkinson's disease. *BMC medical genetics* **2018,** 19, (1), 42.
5. Hohoff, C.; Ponath, G.; Freitag, C. M.; Kastner, F.; Krakowitzky, P.; Domschke, K.; Koelkebeck, K.; Kipp, F.; von Eiff, C.; Deckert, J.; Rothermundt, M., Risk variants in the S100B gene predict elevated S100B serum concentrations in healthy individuals. *American journal of medical genetics. Part B, Neuropsychiatric genetics : the official publication of the International Society of Psychiatric Genetics* **2010,** 153B, (1), 291-7.

6. Liu, J.; Wang, H.; Zhang, L.; Xu, Y.; Deng, W.; Zhu, H.; Qin, C., S100B transgenic mice develop features of Parkinson's disease. *Archives of medical research* **2011,** 42, (1), 1-7.

7. Carvalho, D. Z.; Schonwald, S. V.; Schumacher-Schuh, A. F.; Braga, C. W.; Souza, D. O.; Oses, J. P.; Donis, K. C.; Rieder, C. R., Overnight S100B in Parkinson's Disease: A glimpse into sleep-related neuroinflammation. *Neuroscience letters* **2015,** 608, 57-63.

8. Batassini, C.; Broetto, N.; Tortorelli, L. S.; Borsoi, M.; Zanotto, C.; Galland, F.; Souza, T. M.; Leite, M. C.; Goncalves, C. A., Striatal Injury with 6-OHDA Transiently Increases Cerebrospinal GFAP and S100B. *Neural plasticity* **2015,** 2015, 387028.

9. Thannickal, T. C.; Lai, Y. Y.; Siegel, J. M., Hypocretin (orexin) cell loss in Parkinson's disease. *Brain : a journal of neurology* **2007,** 130, (Pt 6), 1586-95.

10. Morquette, P.; Verdier, D.; Kadala, A.; Fethiere, J.; Philippe, A. G.; Robitaille, R.; Kolta, A., An astrocyte-dependent mechanism for neuronal rhythmogenesis. *Nature neuroscience* **2015,** 18, (6), 844-54.

11. Ryczko, D.; Hanini-Daoud, M.; Condamine, S.; Breant, B. J. B.; Fougere, M.; Araya, R.; Kolta, A., S100beta-mediated astroglial control of firing and input processing in layer 5 pyramidal neurons of the mouse visual cortex. *The Journal of physiology* **2021,** 599, (2), 677-707.

12. Hofmann, M. A.; Drury, S.; Fu, C.; Qu, W.; Taguchi, A.; Lu, Y.; Avila, C.; Kambham, N.; Bierhaus, A.; Nawroth, P.; Neurath, M. F.; Slattery, T.; Beach, D.;

McClary, J.; Nagashima, M.; Morser, J.; Stern, D.; Schmidt, A. M., RAGE mediates a novel proinflammatory axis: a central cell surface receptor for S100/calgranulin polypeptides. *Cell* **1999,** 97, (7), 889-901.

13. Huttunen, H. J.; Kuja-Panula, J.; Sorci, G.; Agneletti, A. L.; Donato, R.; Rauvala, H., Coregulation of neurite outgrowth and cell survival by amphoterin and S100 proteins through receptor for advanced glycation end products (RAGE) activation. *The Journal of biological chemistry* **2000,** 275, (51), 40096-105.

14. Riuzzi, F.; Sorci, G.; Beccafico, S.; Donato, R., S100B engages RAGE or bFGF/FGFR1 in myoblasts depending on its own concentration and myoblast density. Implications for muscle regeneration. *PloS one* **2012,** 7, (1), e28700.

15. Hermann, A.; Donato, R.; Weiger, T. M.; Chazin, W. J., S100 calcium binding proteins and ion channels. *Front Pharmacol* **2012,** 3, 67.

16. Booth, H. D. E.; Hirst, W. D.; Wade-Martins, R., The Role of Astrocyte Dysfunction in Parkinson's Disease Pathogenesis. *Trends Neurosci* **2017,** 40, (6), 358-370.

17. Gomez, J. A.; Perkins, J. M.; Beaudoin, G. M.; Cook, N. B.; Quraishi, S. A.; Szoeke, E. A.; Thangamani, K.; Tschumi, C. W.; Wanat, M. J.; Maroof, A. M.; Beckstead, M. J.; Rosenberg, P. A.; Paladini, C. A., Ventral tegmental area astrocytes orchestrate avoidance and approach behavior. *Nature Communications* **2019,** 10, (1), 1455.

18. Ilijic, E.; Guzman, J. N.; Surmeier, D. J., The L-type channel antagonist isradipine is neuroprotective in a mouse model of Parkinson's disease. *Neurobiology of*

disease **2011,** 43, (2), 364-71.

19. Iyer, R.; Ungless, M. A.; Faisal, A. A., Calcium-activated SK channels control firing regularity by modulating sodium channel availability in midbrain dopamine neurons. *Scientific reports* **2017,** 7, (1), 5248.

20. Koyama, S.; Appel, S. B., A-type K+ current of dopamine and GABA neurons in the ventral tegmental area. *Journal of neurophysiology* **2006,** 96, (2), 544-54.

21. Lang, C.; Campbell, K. R.; Ryan, B. J.; Carling, P.; Attar, M.; Vowles, J.; Perestenko, O. V.; Bowden, R.; Baig, F.; Kasten, M.; Hu, M. T.; Cowley, S. A.; Webber, C.; Wade-Martins, R., Single-Cell Sequencing of iPSC-Dopamine Neurons Reconstructs Disease Progression and Identifies HDAC4 as a Regulator of Parkinson Cell Phenotypes. *Cell Stem Cell* **2019,** 24, (1), 93-106 e6.

22. Liss, B.; Franz, O.; Sewing, S.; Bruns, R.; Neuhoff, H.; Roeper, J., Tuning pacemaker frequency of individual dopaminergic neurons by Kv4.3L and KChip3.1 transcription. *EMBO J* **2001,** 20, (20), 5715-24.

23. Martel, P.; Leo, D.; Fulton, S.; Berard, M.; Trudeau, L. E., Role of Kv1 potassium channels in regulating dopamine release and presynaptic D2 receptor function. *PloS one* **2011,** 6, (5), e20402.

24. Noh, W.; Pak, S.; Choi, G.; Yang, S.; Yang, S., Transient Potassium Channels: Therapeutic Targets for Brain Disorders. *Frontiers in cellular neuroscience* **2019,** 13, 265.

25. Olson, P. A.; Tkatch, T.; Hernandez-Lopez, S.; Ulrich, S.; Ilijic, E.; Mugnaini, E.; Zhang, H.; Bezprozvanny, I.; Surmeier, D. J., G-protein-coupled receptor

modulation of striatal CaV1.3 L-type Ca2+ channels is dependent on a Shank-binding domain. *The Journal of neuroscience : the official journal of the Society for Neuroscience* **2005,** 25, (5), 1050-62.

26. Sun, H.; Jiang, M.; Fu, X.; Cai, Q.; Zhang, J.; Yin, Y.; Guo, J.; Yu, L.; Jiang, Y.; Liu, Y.; Feng, L.; Nie, Z.; Fang, J.; Jin, L., Mesencephalic astrocyte-derived neurotrophic factor reduces cell apoptosis via upregulating HSP70 in SHSY-5Y cells. *Transl Neurodegener* **2017,** 6, 12.

27. Bancroft, E. A.; Srinivasan, R., Quantifying Spontaneous Ca2+ Fluxes and their Downstream Effects in Primary Mouse Midbrain Neurons. *Journal of visualized experiments : JoVE* **2020**, (163).

28. Henley, B. M.; Cohen, B. N.; Kim, C. H.; Gold, H. D.; Srinivasan, R.; McKinney, S.; Deshpande, P.; Lester, H. A., Reliable Identification of Living Dopaminergic Neurons in Midbrain Cultures Using RNA Sequencing and TH-promoter-driven eGFP Expression. *Journal of visualized experiments : JoVE* **2017**, (120).

29. Zarate, S. M.; Pandey, G.; Chilukuri, S.; Garcia, J. A.; Cude, B.; Storey, S.; Salem, N. A.; Bancroft, E. A.; Hook, M.; Srinivasan, R., Cytisine is neuroprotective in female but not male 6-hydroxydopamine lesioned parkinsonian mice and acts in combination with 17-beta-estradiol to inhibit apoptotic endoplasmic reticulum stress in dopaminergic neurons. *Journal of neurochemistry* **2021,** 157, (3), 710-726.

30. Srinivasan, R.; Henley, B. M.; Henderson, B. J.; Indersmitten, T.; Cohen, B. N.; Kim, C. H.; McKinney, S.; Deshpande, P.; Xiao, C.; Lester, H. A., Smoking-

Relevant Nicotine Concentration Attenuates the Unfolded Protein Response in Dopaminergic Neurons. *The Journal of neuroscience : the official journal of the Society for Neuroscience* **2016,** 36, (1), 65-79.

31. Yuan, M.; Bancroft, E. A.; Chen, J.; Srinivasan, R.; Wang, Y., Magnetic Fields and Magnetically Stimulated Gold-Coated Superparamagnetic Iron Oxide Nanoparticles Differentially Modulate L-Type Voltage-Gated Calcium Channel Activity in Midbrain Neurons. *ACS Applied Nano Materials* **2022**.

32. Amendola, J.; Woodhouse, A.; Martin-Eauclaire, M. F.; Goaillard, J. M., Ca(2)(+)/cAMP-sensitive covariation of I(A) and I(H) voltage dependences tunes rebound firing in dopaminergic neurons. *The Journal of neuroscience : the official journal of the Society for Neuroscience* **2012,** 32, (6), 2166-81.

33. Haddjeri-Hopkins, A.; Tapia, M.; Ramirez-Franco, J.; Tell, F.; Marqueze-Pouey, B.; Amalric, M.; Goaillard, J. M., Refining the Identity and Role of Kv4 Channels in Mouse Substantia Nigra Dopaminergic Neurons. *eNeuro* **2021,** 8, (4).

34. Tarfa, R. A.; Evans, R. C.; Khaliq, Z. M., Enhanced Sensitivity to Hyperpolarizing Inhibition in Mesoaccumbal Relative to Nigrostriatal Dopamine Neuron Subpopulations. *The Journal of neuroscience : the official journal of the Society for Neuroscience* **2017,** 37, (12), 3311-3330.

35. Branch, S. Y.; Sharma, R.; Beckstead, M. J., Aging decreases L-type calcium channel currents and pacemaker firing fidelity in substantia nigra dopamine neurons. *The Journal of neuroscience : the official journal of the Society for Neuroscience* **2014,** 34, (28), 9310-8.

36. Kang, S.; Cooper, G.; Dunne, S. F.; Dusel, B.; Luan, C. H.; Surmeier, D. J.; Silverman, R. B., CaV1.3-selective L-type calcium channel antagonists as potential new therapeutics for Parkinson's disease. *Nat Commun* **2012,** 3, 1146.

37. Singh, A.; Verma, P.; Balaji, G.; Samantaray, S.; Mohanakumar, K. P., Nimodipine, an L-type calcium channel blocker attenuates mitochondrial dysfunctions to protect against 1-methyl-4-phenyl-1,2,3,6-tetrahydropyridine-induced Parkinsonism in mice. *Neurochem Int* **2016,** 99, 221-232.

38. Verma, A.; Ravindranath, V., CaV1.3 L-Type Calcium Channels Increase the Vulnerability of Substantia Nigra Dopaminergic Neurons in MPTP Mouse Model of Parkinson's Disease. *Front Aging Neurosci* **2019,** 11, 382.

39. Wang, Q. M.; Xu, Y. Y.; Liu, S.; Ma, Z. G., Isradipine attenuates MPTP-induced dopamine neuron degeneration by inhibiting up-regulation of L-type calcium channels and iron accumulation in the substantia nigra of mice. *Oncotarget* **2017,** 8, (29), 47284-47295.

40. Wang, R.; Ma, Z.; Wang, J.; Xie, J., L-type Cav1.2 calcium channel is involved in 6-hydroxydopamine-induced neurotoxicity in rats. *Neurotox Res* **2012,** 21, (3), 266-70.

41. Bourdeau, M. L.; Morin, F.; Laurent, C. E.; Azzi, M.; Lacaille, J. C., Kv4.3-mediated A-type K+ currents underlie rhythmic activity in hippocampal interneurons. *The Journal of neuroscience : the official journal of the Society for Neuroscience* **2007,** 27, (8), 1942-53.

42. Mei, Y. A.; Wu, M. M.; Huan, C. L.; Sun, J. T.; Zhou, H. Q.; Zhang, Z. H., 4-

aminopyridine, a specific blocker of K(+) channels, inhibited inward Na(+) current in rat cerebellar granule cells. *Brain Res* **2000,** 873, (1), 46-53.

43. Williams, S. B.; Hablitz, J. J., Differential modulation of repetitive firing and synchronous network activity in neocortical interneurons by inhibition of A-type K(+) channels and Ih. *Frontiers in cellular neuroscience* **2015,** 9, 89.

44. Baldereschi, M.; Di Carlo, A.; Rocca, W. A.; Vanni, P.; Maggi, S.; Perissinotto, E.; Grigoletto, F.; Amaducci, L.; Inzitari, D., Parkinson's disease and parkinsonism in a longitudinal study: two-fold higher incidence in men. ILSA Working Group. Italian Longitudinal Study on Aging. *Neurology* **2000,** 55, (9), 1358-63.

45. Verhoog, Q. P.; Holtman, L.; Aronica, E.; van Vliet, E. A., Astrocytes as Guardians of Neuronal Excitability: Mechanisms Underlying Epileptogenesis. *Front Neurol* **2020,** 11, 591690.

46. Begcevic, I.; Brinc, D.; Drabovich, A. P.; Batruch, I.; Diamandis, E. P., Identification of brain-enriched proteins in the cerebrospinal fluid proteome by LC-MS/MS profiling and mining of the Human Protein Atlas. *Clinical proteomics* **2016,** 13, 11.

47. Kubista, H.; Donato, R.; Hermann, A., S100 calcium binding protein affects neuronal electrical discharge activity by modulation of potassium currents. *Neuroscience* **1999,** 90, (2), 493-508.

48. Hahn, J.; Tse, T. E.; Levitan, E. S., Long-term K+ channel-mediated dampening of dopamine neuron excitability by the antipsychotic drug haloperidol. *The Journal of neuroscience : the official journal of the Society for Neuroscience* **2003,**

23, (34), 10859-66.

49. Putzier, I.; Kullmann, P. H.; Horn, J. P.; Levitan, E. S., Dopamine neuron responses depend exponentially on pacemaker interval. *Journal of neurophysiology* **2009,** 101, (2), 926-33.

50. Guzman, J. N.; Sanchez-Padilla, J.; Chan, C. S.; Surmeier, D. J., Robust pacemaking in substantia nigra dopaminergic neurons. *The Journal of neuroscience : the official journal of the Society for Neuroscience* **2009,** 29, (35), 11011-9.

CHAPTER V

MACROPHAGE MIGRATION INHIBITORY FACTOR ALTERS FUNCTIONAL PROPERTIES OF CA1 HIPPOCAMPAL NEURONS IN BRAIN SLICES*

Introduction

Traumatic brain injury (TBI) is a frequently occurring injury with an annual incidence rate in the U.S. of greater than 1.7 million people. Approximately 5.3 million people in the U.S. live with TBI associated disability, resulting in an estimated annual economic burden of $48 billion [1]. Adolescent males, young children and the elderly, represent a large majority of TBI cases [1] although all demographics are affected. Treatments for TBI have thus far been lacking and all clinical trials have failed. Therefore, it is imperative to develop a better mechanistic understanding of TBI, so that therapeutic targets can be identified, and TBI-associated impairments can be improved.

A TBI results in two phases of injury; the primary injury being mechanical impact to the brain, while the secondary injury involves an early and often prolonged immune response. TBIs are highly variable and the primary injury can be mild sub-concussive, concussive or penetrating, each with a different degree of injury-related severity, and each impacting different areas of the brain with different angular and rotational forces. Despite this variability, there are some relatively homogeneous features of TBI pathology,

---

*Reprinted with permission from Bancroft E.A., et al. Macrophage Migration Inhibitory Factor Alters Functional Properties of CA1 Hippocampal Neurons in Mouse Brain Slices. Int J Mol Sci. December 2019. doi: 10.3390/ijms21010276 including the rapid induction of an immune response and a neuroinflammatory response to injury.

The initial TBI-induced immune response is a non-specific innate response, which occurs rapidly after a TBI. In some cases, the initial innate immune response can precede an antigen-specific adaptive immune response. The innate immune response to TBI involves a sequela of events including the release of damage associated molecular patterns (DAMPs) and pathogen associated molecular patterns (PAMPs) [2]. These signaling molecules interact with pattern recognition receptors (PRRs) such as toll-like receptors (TLRs), and nucleotide-binding oligomerization domain-like (NOD) receptors (NLRs) expressed on neurons, astrocytes, microglia, and central nervous system (CNS)-infiltrating macrophages [3-5]. In many cases, the net effect of this receptor interaction is the production and subsequent release of cytokines and chemokines. Binding of DAMPs and/or PAMPs to PRRs triggers a cellular signaling response involving multiple kinases, including NFκB kinase. NFκB levels are elevated following TBI and is associated with increases in numerous other cytokines (e.g. IL-6, TNF-a) as part of the progression of the innate inflammatory response [6].

Among the milieu of elevated inflammatory proteins after a CNS injury is the cytokine, macrophage migration inhibitory factor (MIF) [7-9]. MIF is elevated after a TBI and the extent of this elevation is proportional with the prognosis of TBI, such that more severe injuries are associated with higher levels of MIF [7]. MIF is a secreted immunoregulatory cytokine that stimulates the inflammatory response, plays a role in responding to pathogens, and contributes to other immune or autoimmune events [10].

MIF is highly expressed in multiple brain regions, including cortex, hypothalamus, hippocampus, cerebellum, and pons [11]. Most MIF within the CNS is thought to be synthesized locally, as high levels of MIF mRNA have been detected in both astrocyte and neuronal cell bodies [12]. Thus, MIF may be an important protein to examine as both a prognostic indicator of TBI, and, for direct trophic and/or functional effects in the brain.

Some of the functions of MIF in the immune system and brain have been previously explored. In an innate immune response, MIF binds to the CD74 receptor complex, along with co-stimulatory factor CD-44, initiating downstream signaling cascades and facilitating the immune response [10, 13-25]. The MIF/CD74 signaling complex is also conserved in microglia and astrocytes. In microglia, MIF/CD74 interaction inhibits microglial activation and leads to decreased levels of pro-inflammatory cytokines such as IFN-γ [26]. Conversely, in astrocytes, MIF/CD74 interaction facilitates astrocyte reactivity, stimulates pro-inflammatory cytokine production and increases NFκB levels [22, 27, 28]. In addition to these immunomodulatory roles, recent studies support the ability of MIF to modulate trophic functions in the CNS. MIF has been shown to directly bind and inhibit serine protease HTRA1 activity on FGF8 in astrocytes, which prevents the enzymatic breakdown of FGF8 and facilitates astrocyte migration [29]. Furthermore, 48 h of MIF exposure stimulated axonal growth [30], consistent with a trophic potential shared by numerous other cytokines and chemokines [31, 32].

Numerous cytokines that have been shown to exhibit trophic functions, have also been found to directly modulate neuronal functioning, including synaptic plasticity and long-term potentiation of hippocampal neurons [31, 32]. Consistent with this notion, MIF has been shown to inhibit Angiotensin II-elicited increases in neuronal firing via interactions with the intracellular domain of AngII [33]. Moreover, evidence suggests that MIF might modulate the activity of neurons via glial cells or directly modulate the firing frequency of neurons [30]. One recent study observed increased firing frequency in dorsal root ganglion (DRG) cells following acute bath application of MIF peptide [30]. Since acute MIF application is sufficient to modulate neuronal excitability in the peripheral nervous system (PNS), similar mechanisms may exist in the CNS. Based on this rationale, we sought to determine if MIF can modulate hippocampal neuronal function. MIF was microinjected into the hippocampus and Ca^{2+} responses in CA1 pyramidal neurons from live mouse brain hippocampal slices expressing GCaMP6f were assessed. The results supported rejection of the null hypothesis and demonstrated that *in vivo* microinjection of MIF alters CA1 pyramidal neuron function.

Results

MIF alters baseline Ca^{2+} event frequency in CA1 pyramidal neurons

The effect of MIF exposure on Ca^{2+} signals was assessed in CA1 pyramidal neuron soma, in acute mouse brain slices. Mice were stereotaxically injected with a genetically encoded calcium indicator, GCaMP6f, into the CA1 region of the hippocampus and co-injected with either saline or 200 ng of recombinant MIF peptide (rMIF). Two weeks later, 300 µm thick live hippocampal slices were obtained and imaged for Ca^{2+} events in CA1 pyramidal neurons. Robust GCaMP6f expression was observed in CA1 pyramidal neuron soma, and their apical dendrites in stratum radiatum in both saline and MIF-injected animals [Figure 31A, 31B]. To optimize conditions for observing Ca^{2+} activity in CA1 pyramidal neurons, hippocampal slices were perfused with Mg^{2+} free extracellular solution and 10 uM bicuculline. While the incidence of baseline activity under these conditions was similar in saline and MIF-treated mice (2 of 21 slices for saline, 2 out of 26 slices for MIF), Ca^{2+} signal kinetics were altered in MIF-injected mice. Specifically, MIF-treated animals displayed a significantly higher frequency of Ca^{2+} events when compared to saline controls (Mann-Whitney test, $p = 0.035$, $n = 4$ mice per condition and 2 to 3 slices per mouse, per condition) [Figure 31C]. However, the amplitude and half-width of Ca^{2+} events in MIF–injected mice was not significantly different from controls (Mann-Whitney test, $p = 0.26$ for amplitude and $p = 0.38$ for half width) [Figure 31D, 31E]. These data are summarized in Table 1, and suggest exposure to MIF increases the frequency of baseline calcium activity in CA1 pyramidal neurons of adult mice.

MIF does not significantly alter NMDA + D-serine evoked response in CA1 layer neuronal somata

Since induction of basal activity required conditions (0 Mg^{2+} and bicuculline) that enhance NMDA channel activity, we sought to assess the effect of MIF on NMDA channel function in hippocampal CA1 pyramidal neurons. Pharmacologically-evoked

Ca^{2+} responses with bath application of NMDA + D-serine were measured in hippocampal CA1 pyramidal neurons from both saline and MIF-exposed mice, and the response amplitude, half-width, and rise time was quantified. NMDA + D-serine elicited a single robust Ca^{2+} response in both conditions. Responses were sustained and longer than baseline activity Ca^{2+} events [Figure 32A, 32B]. For regions of interest (ROIs) located in the CA1 layer of the hippocampus, the amplitude, half-width, and rise time of NMDA + D-serine-evoked Ca^{2+} responses were not significantly different between groups (Mann-Whitney test,, $p = 0.63$ for amplitude; $p = 0.38$ for half width; $p = 0.15$ for rise time; $n = 2$ to 3 slices from each mouse in both conditions) [Figure 32C]. These data suggest that MIF had no significant effect on the Ca^{2+} responses to NMDA + D-serine in the CA1 cell layer.

NMDA + D-serine response in apical dendrites of CA1 neurons is altered by MIF

Distinct subtypes of NMDA receptors are expressed in the pyramidal neuron cell bodies and apical dendritic processes of hippocampal neurons, located within stratum radiatum [34]. GCaMP6f expression was observed throughout these apical dendrites in CA1 stratum radiatum in saline and MIF-treated mice [Figure 33A, 33B]. To determine if MIF alters kinetics of NMDA + D-serine responses, specifically in the stratum radiatum processes, we analyzed Ca^{2+} responses in this subregion. For ROIs located in the stratum radiatum, MIF had no significant effect on the amplitude of Ca^{2+} responses, but MIF significantly increased both half-width and rise time, of Ca^{2+} responses, compared to saline controls (Mann-Whitney test, $p = 0.14$ for amplitude; $p = 0.04$ for half width; $p = 0.02$ for rise time). These data, summarized in Table 2, demonstrate a prolonged Ca^{2+} response in CA1 stratum radiatum, following NMDA + D-serine application in MIF-treated animals, when compared to saline controls. This finding suggests that MIF specifically alters the kinetics of NMDA receptor function in CA1 pyramidal cell apical dendrites, without an effect on the NMDA kinetics of CA1 pyramidal neuron somata.

Discussion

A direct effect of MIF on hippocampal neuronal function has not been previously explored. In this study, we demonstrate for the first time, that MIF alters baseline functional properties of hippocampal CA1 pyramidal neurons [Figure 31], and changes the kinetics of pharmacologically evoked NMDA responses in the apical dendrites of these neurons [Figure 33]. MIF is known to involved in several inflammatory and trophic responses, via its role in modulating signaling mechanisms that are regulated by TLR4, p53 and CD74 signaling [10, 13-25]. While there is evidence showing the involvement of MIF in inflammatory pathways, as well as evidence for MIF effects on peripheral neurons, this is the first study to show that MIF influences cortical neurons. These findings have widespread implications for a range of neurological and neuropathological functions.

Considering that MIF is elevated relatively soon after a TBI, it is possible that MIF might be directly involved in single-cell and circuit-level alterations observed following a brain insult. We found that a single *in vivo* injection of 200 ng recombinant MIF was sufficient to induce long lasting (~2-weeks) effects on neuronal activity. A single exposure of the mouse hippocampus to exogenous MIF led to significant increases in the baseline frequency of Ca^{2+} events in mouse CA1 layer pyramidal neurons as late as two weeks after exposure (Figure 31 and Table 2). This suggests the possibility that injury-induced increases in MIF secretion by astrocytes and neurons, may be sufficient to initiate processes that induce long-term changes in neuronal function. Interestingly, MIF increased Ca^{2+} event frequency with no effects on the amplitude and half-width of baseline Ca^{2+} events [Figure 31], suggesting that MIF specifically triggers a change in the membrane excitability of CA1 pyramidal neurons. Since biophysical properties of Kv1 voltage-gated potassium channels in macrophages can be modified by activation or suppression of immune components [35], and because MIF is an important immune mediator [10], our study is consistent with the notion that alterations in immune signaling can affect neuronal excitability and/or function. Another study shows that MIF increases firing frequency of dorsal root ganglion by almost 3-fold, within ~3 min, further supporting the role of early and direct interactions between MIF and Kv channels [30]. Considering that neuronal insults such as TBI increase seizure susceptibility, it is enticing to speculate that changes in MIF-induced baseline excitability of hippocampal neurons, via an interaction with Kv channels, might directly promote epileptogenic activity in the hippocampus. Future studies will assess the epileptogenic effects of stimulating and blocking MIF signaling.

MIF modulates NMDA kinetics, another excitatory component of hippocampal neurons that has been implicated in hyperexcitability following brain insults such as TBI. Although NMDA + D-serine-evoked Ca^{2+} responses in CA1 pyramidal neuron cell bodies only displayed a trend towards an increase in half-width and rise time, [Figure 32 and Table 3], NMDA + D-serine significantly increased the amplitude, half width, and rise time of Ca^{2+} responses in the apical dendrites of these CA1 pyramidal cells [Figure 33 and Table 3]. Since increases in half-width and rise time reached significance in these apical dendrites, but not the CA1 somata, it appears that stratum radiatum processes are more vulnerable to MIF-associated changes in NMDA function. In models of epileptogenesis, including brain insult models, a major contributor to epileptiform activity is ectopic mossy fiber sprouting from the granule cells of the dentate gyrus to hippocampal pyramidal cells. This aberrant sprouting is, at least in part, dependent on NMDA activity [36, 37]. Although we have examined apical dendrites in stratum radiatum of CA1 and not CA3, the data from the current study showing a direct influence of MIF on NMDA activity, suggests a mediation of NMDA function in hippocampal pyramidal neurons. It is possible that MIF induces alteration to the stoichiometric composition and / or subcellular localization of NMDA receptors. Since specific subtypes of NMDA receptors display completely different biophysical properties and desensitization kinetics [38, 39], one may observe a differential response in neuronal soma versus processes. Future studies will dissect out these possibilities by assessing NMDA trafficking and assembly, and if these effects arise from extracellularly secreted astrocytic, neuronal, or other sources of MIF.

The finding that a single microinjection of MIF is sufficient to modulate the kinetics of both, baseline Ca^{2+} activity and pharmacologically-evoked Ca^{2+} responses in CA1 layer somata and their apical dendrites, respectively, suggests that MIF can modulate more than one functional property of pyramidal neurons. Since this is a novel modulatory role, little is known about the mechanism by which MIF drives the observed effects on Ca^{2+} signaling in hippocampal neurons. Another unanswered question, is whether or not the introduction of recombinant MIF stimulates or inhibits the production of endogenous MIF. Therefore, the acute/chronic nature of MIF exposure using this method is unknown. While it is possible that MIF is driving these effects indirectly via astrocytes, the time course of response is suggestive of a sustained effect on neurons, even at 2-weeks after MIF was microinjected into the hippocampus. Subsequent studies will further investigate acute effects of MIF exposure on neurons, as well as direct interactions with extracellular membrane proteins, including NMDA expressed on hippocampal neurons.

Materials and Methods

Mice

Mouse care and experimental procedures were approved by the Texas A&M University Institutional Animal Care and Use Committee. Adult (2-3 month) male C57BL/6 wildtype mice were used. Mice were group housed with food and water available ad libitum and kept in a temperature-controlled environment with a 12:12 h light:dark cycle.

Experimental groups

This study uses two experimental groups of mice. Control mice were injected with 0.9% saline vehicle into the CA1 region of the hippocampus, while experimental mice were injected with 200ng recombinant MIF peptide in 0.9% saline into the CA1 region of the hippocampus. Additionally, both control and MIF-injected mice recived an injection of AAV.Syn.GCaMP6f.WPRE.SV40 into the hippocampus in order to detect calcium events. Only one surgery per animal was performed with both injections (Saline + AAV or MIF + AAV) being made simultaneously.

Stereotaxic microinjections for in situ hippocampal neuron imaging

All surgical procedures were done under general anesthesia using isoflurane (induction 5%, maintenance 1-2.5% vol/vol) as previously reported [40, 41]. Anesthesia was monitored continuously and adjusted as needed. Following induction, mice were placed in a stereotaxic frame (David Kopf Instruments) with their head fixed via blunt ear bars and their nose placed in a nose cone which delivers the anesthetic (Kent Scientific). The surgical incision site was sterilized by three cleanings with 10% povidone iodine and 70% ethanol. Skin incisions were made and then followed by craniotomies of 2-3mm above the right parietal cortex using a small steel burr (Fine Science Tools) powered by a high-speed drill (K.1070; Foredom). Saline (0.9%) was applied to the drilling site to reduce heat, and to keep the incision from drying out. Unilateral AAV + MIF-, or saline-injections were performed using the stereotaxic apparatus described above to guide the placement of beveled glass pipettes (World Precision Instruments) into the right hippocampus (2 mm posterior to bregma, 1.5 mm lateral to midline, and 1.6 mm from the pial surface). 1.5 µl pAAV.Syn.GCaMP6f.WPRE.SV40 (titer of 1 x 10^{13} gc/ml, Addgene) plus 200 ng of saline, or human MIF peptide (Sino Biological) were injected using a syringe pump (PicoPump11; Harvard Apparatus). Following injection, glass pipettes were left in place for 10 min, and then gradually withdrawn. Surgical wounds were closed with single external 5-0 nylon sutures. After surgery animals were allowed to recover in a cage placed on a low-voltage heating pad. No analgesics were used. Mice were sacrificed at 14 d after surgery for imaging.

Brain slice preparation and confocal Ca^{2+} Imaging

Brain slice imaging was performed as previously reported [40, 41]. Adult mouse brain coronal slices were cut at 300 µm thickness using a vibratome (Microslicer dtk-

1000). Slicing solution contained (mM): 194 Sucrose, 30 NaCl, 4.5 KCl, 1.2 NaH_2PO_4, 26 $NaHCO_3$, 10 D-glucose, 1 $MgCl_2$, saturated with 95% O_2 and 5% CO_2. Slices were incubated in an artificial cerebrospinal fluid recording solution (aCSF) for 30 min at 34°C, then moved to a room temperature for imaging. aCSF solution contained (mM): 126 NaCl, 2.5 KCl, 1.24 NaH_2PO_4, 1.3 $MgCl_2$, 2.4 $CaCl_2$, 26 $NaHCO_3$, 10 D-glucose. Imaging was performed using a commercially available confocal microscope (Fluoview 1000, Olympus) with a 40X water-immersion objective with a numerical aperture of 0.8. We used the 488-nm line of a krypton-argon laser to excite GCaMP6f. For imaging Ca^{2+} signals, slices were focused to a plane where cell bodies of CA1 pyramidal neurons and their processes were clearly demarcated. The imaging frame was clipped in order to achieve a 1 frame per second (fps) sampling rate. For all experiments baseline activity was measured in a zero Mg^{2+} aCSF + 10 μM Bicuculline (Abcam) recording buffer for 300 seconds, then followed by bath application of 300 μM NMDA (Sigma) + 100 μM D-serine (Alfa Asar) for 300 sec. Solutions and drugs were bath perfused at 2 ml/min using a peristaltic pump.

Data Analysis

Image analysis was performed using ImageJ v1.52e (NIH). Ca^{2+} events were analyzed using MiniAnalysis v6.0.7 (Synaptosoft). Image time series (t-series) files were adjusted to increase brightness in order to visualize all neuronal somata. Three square ROIs (75 μm x 75 μm) were drawn in both the CA1 cell layer and stratum radiatum in such a way that the ROIs were equidistant and did not overlap. t-series were then closed and reopened with default brightness/contrast. Mean gray value of each ROI for all image frames was extracted and then converted to $\Delta F/F$ values. Baseline F was determined from 10 sec periods without transients/events. For baseline event analysis ROIs were drawn around individual cells, and only cells with one or more Ca^{2+} events in the absence of NMDA + D-serine application were selected. For Ca^{2+} event analysis, frequency was measured as the total number of Ca^{2+} events divided by the recording time, and expressed as events/min. Amplitude was measured as the magnitude of change in fluorescence ($\Delta F/F$) from baseline to event peak. Rise time was measured as the time in seconds for an individual Ca^{2+} event to reach its peak amplitude from baseline. Half-width was measured as the time for an individual Ca^{2+} event to reach 50% of its peak amplitude from baseline.

Statistical analyses

All data and statistical analyses were performed using Origin 2019 (ver. 9.6). Data presented are mean ± s.e.m. For each data set, normality was first determined in Origin using the Shapiro-Wilk test. Non-normally distributed data were analyzed via Mann-Whitney tests. Data was considered to be significantly different at $p < 0.05$. For each analysis performed exact p-values are reported.

Figures

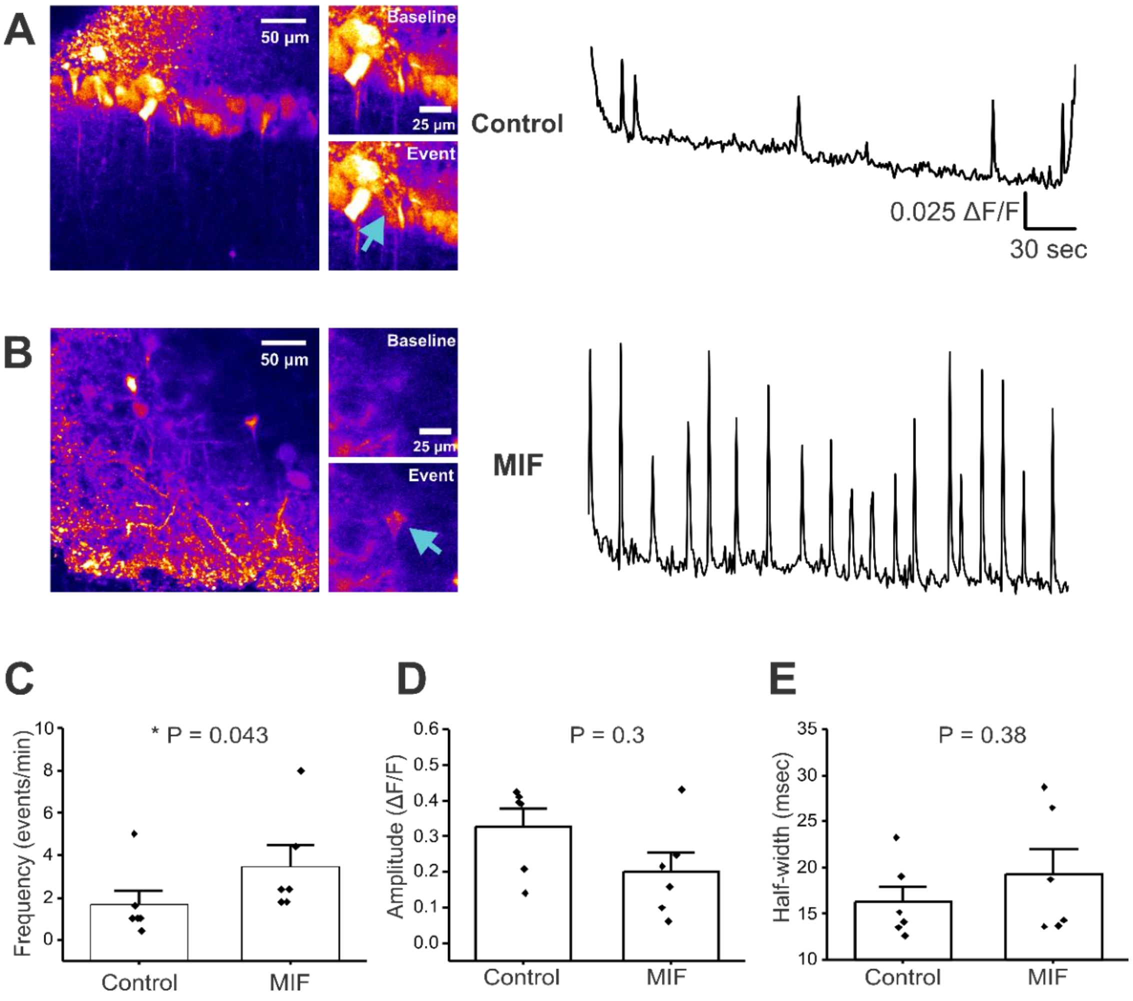

Figure 18: Baseline Activity in CA1 neuronal somata of hippocampal brain slices. All experiments were conducted in aCSF with 0 Mg^{2+} and 10 µM Bicuculline. **(A)** Left, representative image of GCaMP expression in control mouse hippocampal brain slice, with insets just before and during a Ca^{2+} event. Right, representative trace of baseline activity from a CA1 pyramidal neuron cell body (denoted by blue arrow). **(B)** Left, representative image of GCaMP expression in MIF-treated mouse hippocampal brain slice, with insets just before and during a calcium event. Right, representative trace from a CA1 pyramidal neuron cell body (denoted by blue arrow). **(C-E)** Average data of spontaneous events from 2 to 3 slices per condition, in 4 control mice and in 4 MIF-treated mice. Left, frequency (events/min). Middle, Amplitude (ΔF/F). Right, Half-width (msec).

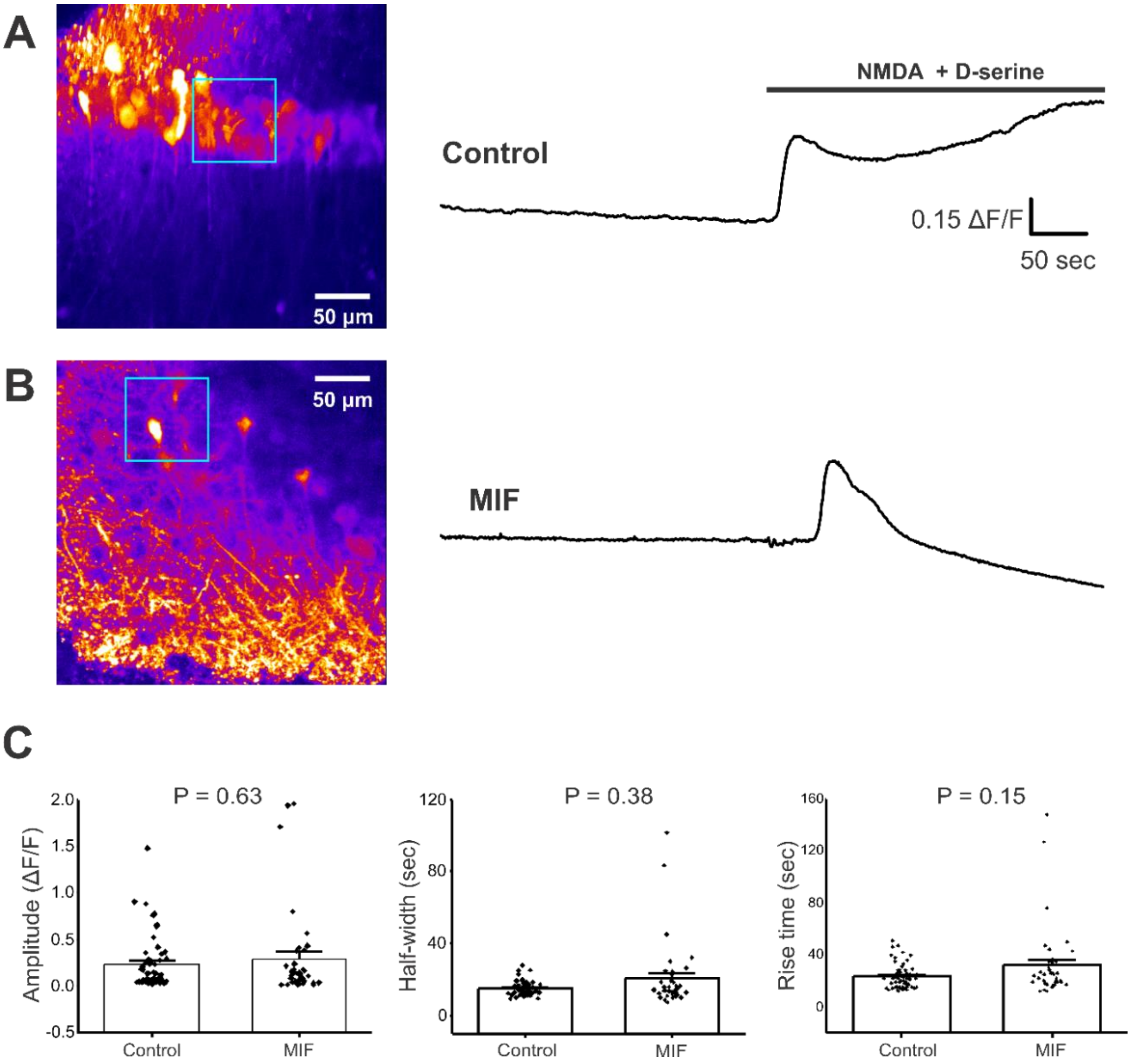

Figure 19: NMDA + D-serine response in CA1 neuronal somata of hippocampal brain slices.

All experiments were conducted in aCSF with 0 Mg^{2+} and 10 μM Bicuculline**. (A)** Left, Representative image of GCaMP expression in the CA1 layer of hippocampal brain slices from control mice (blue square represents ROI). Right, representative trace from ROI, with and without NMDA + D-serine application. **(B)** Left, Representative image of GCaMP expression in the CA1 layer of hippocampal brain slices from MIF mice (blue square represents ROI). Right, representative trace from ROI with and without NMDA + D-serine application. **(C)** Average amplitude, half-width and rise time data of NMDA + D-serine response from 2 to 4 slices each, from 8 control mice and 4 MIF-treated mice.

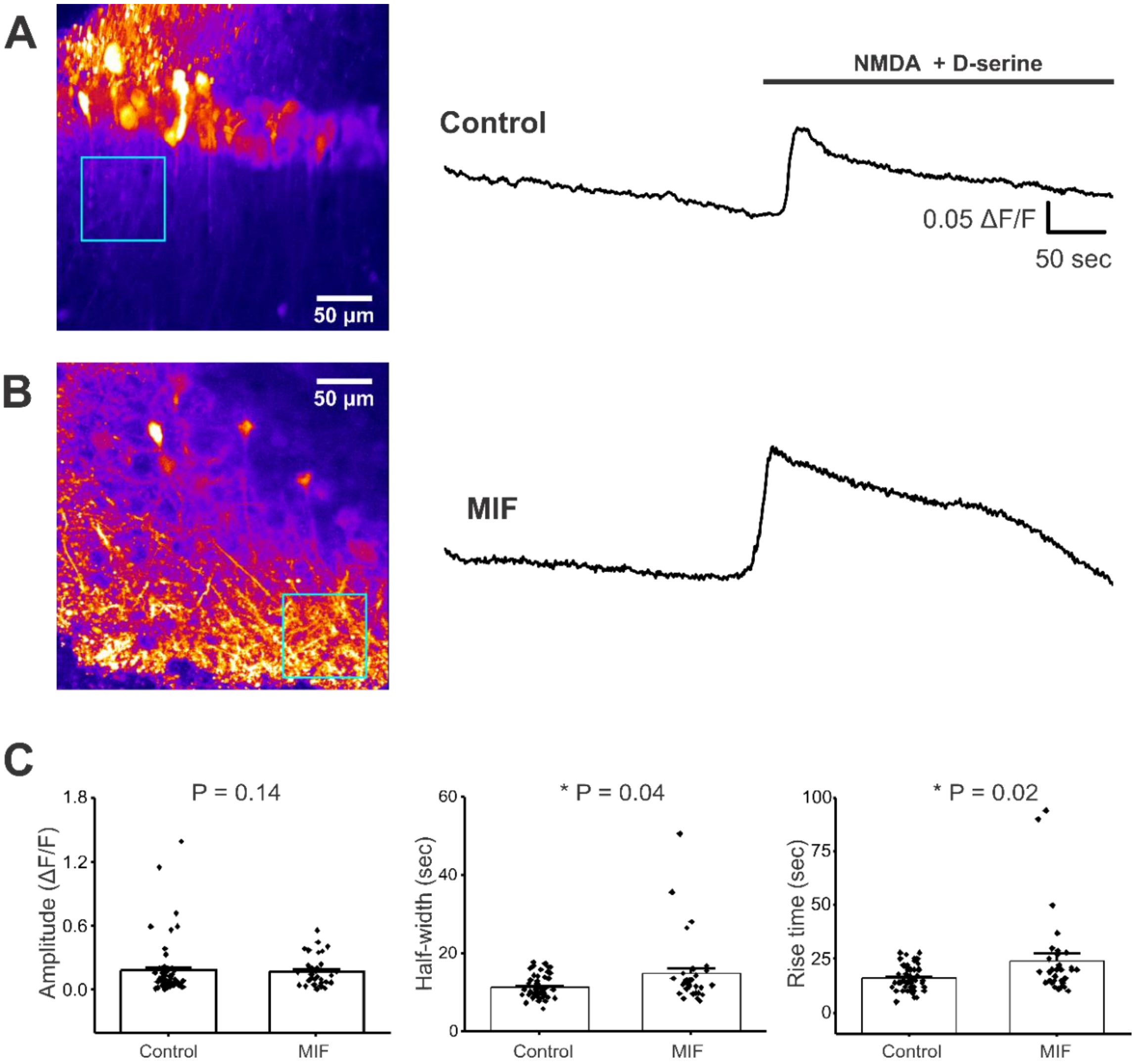

Figure 20: NMDA + D-serine response in CA1 stratum radiatum neuronal processes of hippocampal brain slices.

All experiments were conducted in aCSF with 0 Mg^{2+} and 10 µM Bicuculline**.** **(A)** Left, Representative image of GCaMP expression in the stratum radiatum of hippocampal brain slices from control mice (blue square represents ROI). Right, representative trace from ROI, with and without NMDA + D-serine application. **(B)** Left, Representative image of GCaMP expression in the stratum radiatum of hippocampal brain slices from MIF-treated mice (blue square represents ROI Right, representative trace from ROI, with and without NMDA + D-serine application. **(C)** Average amplitude, half-width and rise time data of NMDA + D-serine response from 2 to 4 slices each, from 8 control mice and 4 MIF-treated mice.

Tables

Table 1: Summary of spontaneous activity

Condition	% of slices w/ baseline activity	Mean Frequency	Mean Amplitude	Mean Half-width
Control	10	1.667 ± 0.68	0.328 ± 0.05	16.274 ± 1.67
MIF	8	**3.467 ± 0.99 ***	0.215 ± 0.05	19.250 ± 2.77

Values presented as Mean ± SEM
* denotes significance at P < 0.05

Table 2: Summary of NMDA responses

		Mean Amplitude		Mean Half-width		Mean Rise time	
Condition	% of slices responded	CA1 cell layer	Stratum Radiatum	CA1 cell layer	Stratum Radiatum	CA1 cell layer	Stratum Radiatum
Control	55	0.231 ± 0.04	0.180 ± 0.18	14.962 ± 0.53	11.370 ± 0.39	23.333 ± 1.29	16.211 ± 0.74
MIF	50	0.289 ± 0.08	0.177 ± 0.02	20.445 ± 2.98	**14.786 ± 1.52 ***	31.974 ± 4.48	**24.303 ± 3.36 ***

Values presented as Mean ± SEM
* denotes significance at P < 0.05

References

1. Faul, M.; Xu, L.; Wald, M. M.; Coronado, V.; Dellinger, A. M., Traumatic brain injury in the United States: national estimates of prevalence and incidence, 2002–2006. *Injury Prevention* **2010,** 16, (Suppl 1), A268.
2. Bianchi, M. E., DAMPs, PAMPs and alarmins: all we need to know about danger. *Journal of leukocyte biology* **2007,** 81, (1), 1-5.
3. Tang, S.-C.; Arumugam, T. V.; Xu, X.; Cheng, A.; Mughal, M. R.; Jo, D. G.; Lathia, J. D.; Siler, D. A.; Chigurupati, S.; Ouyang, X.; Magnus, T.; Camandola, S.; Mattson, M. P., Pivotal role for neuronal Toll-like receptors in ischemic brain injury and functional deficits. *Proceedings of the National Academy of Sciences of the United States of America* **2007,** 104, (34), 13798-13803.
4. Bowman, C. C.; Rasley, A.; Tranguch, S. L.; Marriott, I., Cultured astrocytes express toll-like receptors for bacterial products. *Glia* **2003,** 43, (3), 281-91.
5. Olson, J. K.; Miller, S. D., Microglia initiate central nervous system innate and adaptive immune responses through multiple TLRs. *Journal of immunology (Baltimore, Md. : 1950)* **2004,** 173, (6), 3916-24.
6. Hang, C. H.; Shi, J. X.; Li, J. S.; Wu, W.; Yin, H. X., Concomitant upregulation of nuclear factor-kB activity, proinflammatory cytokines and ICAM-1 in the injured brain after cortical contusion trauma in a rat model. *Neurology India* **2005,** 53, (3), 312-7.
7. Yang, D. B.; Yu, W. H.; Dong, X. Q.; Zhang, Z. Y.; Du, Q.; Zhu, Q.; Che, Z. H.;

Wang, H.; Shen, Y. F.; Jiang, L., Serum macrophage migration inhibitory factor concentrations correlate with prognosis of traumatic brain injury. *Clinica chimica acta; international journal of clinical chemistry* **2017,** 469, 99-104.

8. Wang, C. W.; Ma, P. J.; Wang, Y. Y.; Yang, M.; Su, L. L.; Wang, S.; Liu, Y. X.; Yuan, B.; Zhao, J. H., Serum level of macrophage migration inhibitory factor predicts severity and prognosis in patients with ischemic stroke. *Cytokine* **2019,** 115, 8-12.

9. Li, Y. S.; Chen, W.; Liu, S.; Zhang, Y. Y.; Li, X. H., Serum macrophage migration inhibitory factor levels are associated with infarct volumes and long-term outcomes in patients with acute ischemic stroke. *The International journal of neuroscience* **2017,** 127, (6), 539-546.

10. Jankauskas, S. S.; Wong, D. W. L.; Bucala, R.; Djudjaj, S.; Boor, P., Evolving complexity of MIF signaling. *Cellular signalling* **2019,** 57, 76-88.

11. Bacher, M.; Meinhardt, A.; Lan, H. Y.; Dhabhar, F. S.; Mu, W.; Metz, C. N.; Chesney, J. A.; Gemsa, D.; Donnelly, T.; Atkins, R. C.; Bucala, R., MIF expression in the rat brain: implications for neuronal function. *Molecular medicine (Cambridge, Mass.)* **1998,** 4, (4), 217-30.

12. Ogata, A.; Nishihira, J.; Suzuki, T.; Nagashima, K.; Tashiro, K., Identification of macrophage migration inhibitory factor mRNA expression in neural cells of the rat brain by in situ hybridization. *Neuroscience letters* **1998,** 246, (3), 173-7.

13. Leng, L.; Metz, C. N.; Fang, Y.; Xu, J.; Donnelly, S.; Baugh, J.; Delohery, T.; Chen, Y.; Mitchell, R. A.; Bucala, R., MIF signal transduction initiated by binding

to CD74. *The Journal of experimental medicine* **2003,** 197, (11), 1467-76.

14. Shi, X.; Leng, L.; Wang, T.; Wang, W.; Du, X.; Li, J.; McDonald, C.; Chen, Z.; Murphy, J. W.; Lolis, E.; Noble, P.; Knudson, W.; Bucala, R., CD44 is the signaling component of the macrophage migration inhibitory factor-CD74 receptor complex. *Immunity* **2006,** 25, (4), 595-606.

15. Bernhagen, J.; Krohn, R.; Lue, H.; Gregory, J. L.; Zernecke, A.; Koenen, R. R.; Dewor, M.; Georgiev, I.; Schober, A.; Leng, L.; Kooistra, T.; Fingerle-Rowson, G.; Ghezzi, P.; Kleemann, R.; McColl, S. R.; Bucala, R.; Hickey, M. J.; Weber, C., MIF is a noncognate ligand of CXC chemokine receptors in inflammatory and atherogenic cell recruitment. *Nature medicine* **2007,** 13, (5), 587-96.

16. Heber-Katz, E.; Schwartz, R. H.; Matis, L. A.; Hannum, C.; Fairwell, T.; Appella, E.; Hansburg, D., Contribution of antigen-presenting cell major histocompatibility complex gene products to the specificity of antigen-induced T cell activation. *The Journal of experimental medicine* **1982,** 155, (4), 1086-99.

17. Maier, M.; Wutzler, S.; Bauer, M.; Trendafilov, P.; Henrich, D.; Marzi, I., Altered gene expression patterns in dendritic cells after severe trauma: implications for systemic inflammation and organ injury. *Shock (Augusta, Ga.)* **2008,** 30, (4), 344-51.

18. Huttl, S.; Helfrich, F.; Mentrup, T.; Held, S.; Fukumori, A.; Steiner, H.; Saftig, P.; Fluhrer, R.; Schroder, B., Substrate determinants of signal peptide peptidase-like 2a (SPPL2a)-mediated intramembrane proteolysis of the invariant chain CD74. *The Biochemical journal* **2016,** 473, (10), 1405-22.

19. Huttl, S.; Klasener, K.; Schweizer, M.; Schneppenheim, J.; Oberg, H. H.; Kabelitz, D.; Reth, M.; Saftig, P.; Schroder, B., Processing of CD74 by the Intramembrane Protease SPPL2a Is Critical for B Cell Receptor Signaling in Transitional B Cells. *Journal of immunology (Baltimore, Md. : 1950)* **2015,** 195, (4), 1548-63.

20. Karin, M.; Ben-Neriah, Y., Phosphorylation meets ubiquitination: the control of NF-[kappa]B activity. *Annual review of immunology* **2000,** 18, 621-63.

21. Lawrence, T., The nuclear factor NF-kappaB pathway in inflammation. *Cold Spring Harbor perspectives in biology* **2009,** 1, (6), a001651.

22. Su, Y.; Wang, Y.; Zhou, Y.; Zhu, Z.; Zhang, Q.; Zhang, X.; Wang, W.; Gu, X.; Guo, A.; Wang, Y., Macrophage migration inhibitory factor activates inflammatory responses of astrocytes through interaction with CD74 receptor. *Oncotarget* **2017,** 8, (2), 2719-2730.

23. Mitchell, R. A.; Metz, C. N.; Peng, T.; Bucala, R., Sustained mitogen-activated protein kinase (MAPK) and cytoplasmic phospholipase A2 activation by macrophage migration inhibitory factor (MIF). Regulatory role in cell proliferation and glucocorticoid action. *The Journal of biological chemistry* **1999,** 274, (25), 18100-6.

24. Mitchell, R. A.; Liao, H.; Chesney, J.; Fingerle-Rowson, G.; Baugh, J.; David, J.; Bucala, R., Macrophage migration inhibitory factor (MIF) sustains macrophage proinflammatory function by inhibiting p53: regulatory role in the innate immune response. *Proceedings of the National Academy of Sciences of the United States of America* **2002,** 99, (1), 345-50.

25. Roger, T.; David, J.; Glauser, M. P.; Calandra, T., MIF regulates innate immune responses through modulation of Toll-like receptor 4. *Nature* **2001,** 414, (6866), 920-4.

26. Ghoochani, A.; Schwarz, M. A.; Yakubov, E.; Engelhorn, T.; Doerfler, A.; Buchfelder, M.; Bucala, R.; Savaskan, N. E.; Eyüpoglu, I. Y., MIF-CD74 signaling impedes microglial M1 polarization and facilitates brain tumorigenesis. *Oncogene* **2016,** 35, 6246.

27. Zhou, Y.; Guo, W.; Zhu, Z.; Hu, Y.; Wang, Y.; Zhang, X.; Wang, W.; Du, N.; Song, T.; Yang, K.; Guan, Z.; Wang, Y.; Guo, A., Macrophage migration inhibitory factor facilitates production of CCL5 in astrocytes following rat spinal cord injury. *Journal of neuroinflammation* **2018,** 15, (1), 253.

28. Zhang, Y.; Zhou, Y.; Chen, S.; Hu, Y.; Zhu, Z.; Wang, Y.; Du, N.; Song, T.; Yang, Y.; Guo, A.; Wang, Y., Macrophage migration inhibitory factor facilitates prostaglandin E2 production of astrocytes to tune inflammatory milieu following spinal cord injury. *Journal of neuroinflammation* **2019,** 16, (1), 85.

29. Fex Svenningsen, A.; Loring, S.; Sorensen, A. L.; Huynh, H. U. B.; Hjaeresen, S.; Martin, N.; Moeller, J. B.; Elkjaer, M. L.; Holmskov, U.; Illes, Z.; Andersson, M.; Nielsen, S. B.; Benedikz, E., Macrophage migration inhibitory factor (MIF) modulates trophic signaling through interaction with serine protease HTRA1. *Cellular and molecular life sciences : CMLS* **2017,** 74, (24), 4561-4572.

30. Alexander, J. K.; Cox, G. M.; Tian, J. B.; Zha, A. M.; Wei, P.; Kigerl, K. A.; Reddy, M. K.; Dagia, N. M.; Sielecki, T.; Zhu, M. X.; Satoskar, A. R.; McTigue,

D. M.; Whitacre, C. C.; Popovich, P. G., Macrophage migration inhibitory factor (MIF) is essential for inflammatory and neuropathic pain and enhances pain in response to stress. *Experimental neurology* **2012,** 236, (2), 351-62.

31. Plata-Salaman, C. R.; ffrench-Mullen, J. M., Interleukin-1 beta inhibits Ca2+ channel currents in hippocampal neurons through protein kinase C. *European journal of pharmacology* **1994,** 266, (1), 1-10.

32. Murray, C. A.; Lynch, M. A., Evidence that increased hippocampal expression of the cytokine interleukin-1 beta is a common trigger for age- and stress-induced impairments in long-term potentiation. *The Journal of neuroscience : the official journal of the Society for Neuroscience* **1998,** 18, (8), 2974-81.

33. Sun, C.; Li, H.; Leng, L.; Raizada, M. K.; Bucala, R.; Sumners, C., Macrophage migration inhibitory factor: an intracellular inhibitor of angiotensin II-induced increases in neuronal activity. *The Journal of neuroscience : the official journal of the Society for Neuroscience* **2004,** 24, (44), 9944-52.

34. Racca, C.; Stephenson, F. A.; Streit, P.; Roberts, J. D.; Somogyi, P., NMDA receptor content of synapses in stratum radiatum of the hippocampal CA1 area. *The Journal of neuroscience : the official journal of the Society for Neuroscience* **2000,** 20, (7), 2512-22.

35. Villalonga, N.; David, M.; Bielanska, J.; Vicente, R.; Comes, N.; Valenzuela, C.; Felipe, A., Immunomodulation of voltage-dependent K+ channels in macrophages: molecular and biophysical consequences. *J Gen Physiol* **2010,** 135, (2), 135-47.

36. Okazaki, M. M.; Evenson, D. A.; Nadler, J. V., Hippocampal mossy fiber sprouting and synapse formation after status epilepticus in rats: visualization after retrograde transport of biocytin. *The Journal of comparative neurology* **1995,** 352, (4), 515-34.

37. Sutula, T.; Koch, J.; Golarai, G.; Watanabe, Y.; McNamara, J. O., NMDA receptor dependence of kindling and mossy fiber sprouting: evidence that the NMDA receptor regulates patterning of hippocampal circuits in the adult brain. *The Journal of neuroscience : the official journal of the Society for Neuroscience* **1996,** 16, (22), 7398-406.

38. Iacobucci, G. J.; Popescu, G. K., NMDA receptors: linking physiological output to biophysical operation. *Nat Rev Neurosci* **2017,** 18, (4), 236-249.

39. Vicini, S.; Wang, J. F.; Li, J. H.; Zhu, W. J.; Wang, Y. H.; Luo, J. H.; Wolfe, B. B.; Grayson, D. R., Functional and pharmacological differences between recombinant N-methyl-D-aspartate receptors. *Journal of neurophysiology* **1998,** 79, (2), 555-66.

40. Srinivasan, R.; Huang, B. S.; Venugopal, S.; Johnston, A. D.; Chai, H.; Zeng, H.; Golshani, P.; Khakh, B. S., Ca(2+) signaling in astrocytes from Ip3r2(-/-) mice in brain slices and during startle responses in vivo. *Nature neuroscience* **2015,** 18, (5), 708-17.

41. Srinivasan, R.; Henley, B. M.; Henderson, B. J.; Indersmitten, T.; Cohen, B. N.; Kim, C. H.; McKinney, S.; Deshpande, P.; Xiao, C.; Lester, H. A., Smoking-Relevant Nicotine Concentration Attenuates the Unfolded Protein Response in

Dopaminergic Neurons. *The Journal of neuroscience : the official journal of the Society for Neuroscience* **2016,** 36, (1), 65-79.

CHAPTER VI

MAGNETIC FIELDS AND MAGNETICALLY STIMULATED GOLD-COATED SUPERPARAMAGNETIC IRON OXIDE NANOPARTICLES DIFFERENTIALLY MODULATE L-TYPE VOLTAGE-GATED CALCIUM CHANNEL ACTIVITY IN MIDBRAIN NEURONS*

Introduction

Parkinson's disease (PD) is the second most common neurodegenerative disease [1], characterized by a progressive loss of midbrain substantia nigra pars compacta (SNc) dopaminergic (DA) neurons [2, 3]. Unfortunately, current therapies for PD such as treatment with levodopa or deep brain stimulation are merely symptomatic and lose efficacy over time [4]. As a consequence, novel strategies focused on regulating pacemaking activity in SNc DA neurons, thereby either slowing DA neuron loss, or modulating basal ganglia circuitry are an attractive therapeutic avenue for PD [5]. Among these strategies, pulsed magnetic stimulation (MS) has gained attention as a non-invasive brain stimulation strategy. Pulsed MS promotes neuronal survival [6],

*Reprinted with permission from Yuan M., Bancroft E.A., et al. Magnetic fields and magnetically stimulated gold-coated superparamagnetic iron oxide nanoparticles differentially modulate L-type voltage-gated calcium channel activity in midbrain neurons. ACS Applied Nano Materials. January 2022. doi:10.1021/acsanm.1c02665 stimulates neuronal differentiation [5, 7], regulates intracellular Ca^{2+} flux [8] and induces membrane depolarization [9]. However, off-target effects and poor localization of brain pulsed MS results in severe side effects such as epileptic seizures [10]. In addition, the interactions between magnetic fields and subcellular biological elements using MS alone may not be strong enough to selectively regulate neuronal activity [11, 12]. Static MS (SMS) has the potential to mitigate these side effects, and can be combined with magnetic nanoparticles (NPs) in order to translate magnetic fields into highly localized mechanical forces at the cell membrane or within the cytoplasm [12]. In this regard, recent reports show that superparamagnetic iron oxide (SPIO) NPs under SMS can trigger Ca^{2+} fluxes by activating N type mechanosensitive Ca^{2+} channels in cortical neuron networks [13, 14], and opening mechano-sensitive Ca^{2+} permeable ion channels (PIEZO2 and TRPV4) in primary dorsal root ganglion neurons [15].

In this context, an unexplored question is whether or not SMS stimulation combined with SPIO NPs can affect the activity of L-type voltage-gated Ca^{2+} channels (VGCCs) in midbrain neurons, which is an important neuroprotective target for PD [16]. Since uncoated SPIO NPs with SMS stimulation may cause toxicity [17, 18], and are likely to aggregate [19-21], we recently developed gold coated SPIO (Au-SPIO) core-shell NPs [22-25], which could improve the stability of SPIO NPs and protect them from reacting with biological media.[26, 27] We showed that Au-SPIO NPs displayed improved biocompatibility, cellular uptake and surface functionality, promoted growth and differentiation of neuronal PC-12 cells [23], and facilitated targeted drug delivery [28, 29]. Besides, Au-SPIO NPs with size of 20 nm possess strong potential for efficient blood brain barrier crossing [30-35]. It is also reported that Au NPs with similar size and surface parameters had a blood half-life of around 30 h and that the clearance of Au NPs occurs via the reticuloendothelial system in spleen and lymph nodes [36]. A prior study has shown that on attaching to cell membrane, negative surface charges on NPs affect membrane polarization, thereby regulating VGCC activity [37]. In contrast, another study has reported that when compared to a negligible polarization effect of negative and neutral states, the uptake of positively charged Au NPs into cells causes membrane depolarization of different cell types, leading to an increase in Ca^{2+} flux [38]. However, the effect of negatively charged Au-SPIO NPs on L-type VGCC-mediated Ca^{2+} fluxes in native midbrain neurons in the presence or absence of MS is completely unknown.

In this study, we prepared Au-SPIO NPs via a seed growth method using hydroxylamine hydrochloride as the reducing agent and modified the surface of Au-SPIO NPs by Cy3 fluorescence dye to explore their interaction with midbrain DA neurons (Figure 8). We compared the effects of either SMS alone or SMS with Au-SPIO NPs (SMS-Au-SPIO) on Ca^{2+} activity in midbrain neurons. Using these Au-SPIO NPs, we showed that exposure of cultured primary mouse midbrain neurons to either SMS through a Halbach array applicator or SMS-Au-SPIO altered L-type VGCC-mediated spontaneous Ca^{2+} fluxes in midbrain neurons (Figure 8). We suggest that this may be an important upstream event that explains the ability of SMS or SMS-Au-SPIO NPs to alter intracellular Ca^{2+} concentrations in midbrain neurons, thereby exerting neuroprotective effects in preclinical animal models of PD.

Experimental Section

Preparation of fluorescence tagged Au-SPIO NPs

Au-SPIO core-shell NPs were synthesized using the seed growth method according to our previously reported work [23]. First, SPIO core seeds were synthesized using a co-precipitation method [23] and synthesized SPIO seeds (60 mM) were diluted to 1.5 mM using deionized (DI) water. The diluted solution was mixed with sodium citrate (0.1 M) using an equal volume ratio (5.5 ml SPIO: 5.5 ml sodium citrate), and stirred for 10 min to allow for exchange of OH^- absorbed at the surface of SPIO seeds with citrate ligands. This solution was further diluted with 89 ml DI water before adding 0.5 ml of $HAuCl_4$ solution (1%). The pH value of this solution was checked and adjusted between 8-10 using NaOH solution (0.1M), followed by the addition of 0.6 ml of $NH_2OH*HCl$ (0.2 M) into the solution to reduce Au^{3+} and form Au shell at the surface of SPIO seeds within 5 minutes. This process was repeated by adding 0.5 ml of $HAuCl_4$ solution (1%) and 0.2 ml of $NH_2OH*HCl$ (0.2 M) sequentially to form a thicker Au shell. The whole reaction was performed at room temperature. Synthesized Au-SPIO NPs were then separated using a magnet, washed with DI water 3 times, and finally dispersed in 7.5 ml of DI water. All the chemicals used in this step were obtained from Sigma-Aldrich (St. Louis, MO).

To visualize an interaction between Au-SPIO NPs and midbrain neurons using confocal microscopy, it is necessary to use Cy3 dye for the fluorescence conjugation of

Au-SPIO NPs, which do not autofluoresce [39]. To do this, ~100 uL of Cy3-PEG-SH solution (PG2-S3TH-2k, Nanocs Inc.) at a concentration of 1 mg/ml was added to 1 ml of Au-SPIO solution at a concentration of 1.2747 mg/ml. After Cy3 conjugation, the resulting solution was mixed for 24 hours, centrifuged, washed using DI water 3 times, and finally redispersed in 1 ml DI water to remove the unbounded Cy3-PEG-SH.

Material characterization

To reveal the morphology of Au-SPIO NPs, transmission electron microscopy (TEM) was performed using a FEI Tecnai G2 F20 S-Twin Field-Emission Scanning Transmission Electron Microscope (operating voltage: 200 kV). To confirm the existence of Au on SPIO, the light absorption spectrum was recorded at room temperature using a SHIMADZU UV-2450 spectrophotometer (Shimadzu Corp.) Zeta potential and hydrodynamic diameter were measured by dynamic light scattering using a Zetasizer apparatus (Malvern Instruments). The results were obtained from triplicate experiments.

Culturing primary embryonic mouse midbrain neurons

Reagents used to culture primary embryonic mouse DA neurons included neurobasal medium, DMEM + GlutaMAX medium, GlutaMAX supplement, B-27, equine serum, and penicillin-streptomycin purchased from ThermoFisher (Waltham, MA, USA), as well as Deoxyribonuclease I (DNase), poly-L-lysine, poly-L-ornithine, laminin, ascorbic acid, kanamycin, and ampicillin purchased from Sigma-Aldrich (St. Louis, MO, USA). Papain was purchased from Worthington Biomedical Corporation (Lakewood, NJ, USA). Corning 35 mm uncoated plastic cell culture dishes were purchased from VWR (Radnor, PA, USA), 12 mm circular cover glass No. 1 was purchased from Phenix Research Products (Candler, NC, USA).

Detailed methods to culture primary embryonic mouse DA neurons have been previously described [40-42]. Briefly, cultures were obtained from embryonic day (ED14) mouse embryos of both sexes. Timed-pregnant mice (Texas A&M Institute for Genomic Medicine) were sacrificed by cervical dislocation and embryos were removed. Embryos were then decapitated, and the ventral midbrain was dissected using methods previously described [40-42]. Cells were then digested in papain for 15 min at 37°C. Next, cells were separated using DNase treatment and mechanical trituration in a stop solution of 10 % equine serum in Hank's balanced salt solution (HBSS, Sigma-Aldrich). Cells were plated on 12 mm cover glass triple coated with poly-L-lysine, poly-L-orinithine, and laminin at a density of 200,000 cells per cover glass. Following plating, cells were incubated at 37°C with 5% CO_2 for 1 h, followed by the addition of neurobasal media supplemented with GlutaMax, B-27, equine serum, ascorbic acid and containing penicillin-streptomycin, kanamycin, ampicillin. Culture medium was exchanged at 3 d intervals and all primary cultures were allowed to mature for 3 weeks before experiments were performed. All experiments performed in this study were replicated on 3-4 independent midbrain cultures.

Adeno-associated viral (AAV) vectors

To image spontaneous Ca^{2+} activity in primary midbrain neurons, we employed the adeno-associated virus AAV 2/5 hSyn-GCaMP6f purchased from Addgene (Cat # 100837-AAV, RRID: Addgene_100837). AAV infections were performed at 14 days in vitro (DIV), as previously described {Bancroft, 2020}. Briefly, culture medium was removed and 1 ml of serum-free DMEM + GlutaMAX medium containing 1 ul of Syn-GCaMP6f (titer = 1 x 10^{13} genome copies/ml) was added to each dish and allowed to incubate at 37°C with 5% CO_2 for 1 h. Next, the serum-free medium containing AAVs was removed and replaced with 3 ml of supplemented neurobasal medium. Imaging was performed 5 d following AAV infection.

Confocal imaging of spontaneous Ca^{2+} fluxes in cultured midbrain neurons

The protocol used for imaging spontaneous Ca^{2+} fluxes in primary midbrain neurons has been previously described.[4] Briefly, cultures were placed in a gas free recording buffer containing (mM): 154 NaCl, 5 KCl, 2 $CaCl_2$, 0.5 $MgCl_2$, 5 D-glucose, 10 HEPES, pH adjusted to 7.4 with NaOH (all purchased from Sigma-Aldrich). Imaging was performed using a confocal microscope (Fluoview 1200, Olympus, Tokyo, Japan) with a 40X, 0.8 NA water-immersion objective (Olympus). We used a 488-nm line of an Argon laser to excite GCaMP6f. The imaging frame was clipped to allow for an image sampling rate of 1 frame per sec (FPS). For all experiments, spontaneous Ca^{2+} was recorded for 300 s, and for L-type VGCC blocking experiments followed by 300 s of drug application. L-type VGCCs were blocked using diltiazem (100 μM) which has shown efficient and specific blocking of L-type VGCCs [43-45]. In the future, we will consider dihydropyridine drugs such as nifedipine as an alternative. Recording buffers were bath perfused using a peristaltic pump set at a rate of 2 ml/min. Diltiazem was purchased from Tocris (Minneapolis, MN). To quantify the exponential decay of blockade by diltiazem, Ca^{2+} traces were fitted to an exponential equation. Latency to blockade was determined for each condition by recording the time (in seconds) at which the last discernable (> 0.1 $\Delta F/F_0$) Ca^{2+} event occurred for each neuron. Average latencies for each condition were then compared. For all imaging experiments, statistical tests and *p* values are reported in the figures and figure legends.

Immunostaining of primary midbrain cultures

Immediately following imaging, cultures were placed in 10% formalin for 40 min. Cultures were permeabilized in 0.01% Triton X-100/PBS and blocked in 10% normal goat serum (NGS)/PBS solution. Antibodies used included chicken polyclonal anti-TH (1:1000, Abcam) and rabbit polyclonal anti-cleaved caspase-3 (1:1000, Cell Signaling Technologies, Danvers, MA). Imaging was performed using a confocal microscope (Fluoview 1200, Olympus) with a 60X, 1.35 NA oil-immersion objective (Olympus).

Evaluation of PSD for spontaneous Ca^{2+} flux signals

The power spectral density (PSD) of a calcium flux signal x(t) can be expressed as the average of the Fourier transform magnitude squared, over a large time interval.

$$S_x(f) = \lim_{T\to\infty} E\left\{\frac{1}{2T}\left|\int_{-T}^{T} x(t)e^{-j2\pi f t}dt\right|^2\right\}$$

In Matlab, a function called periodogram was used, which directly gave the results of PSD.

Evaluation of synchronization of spontaneous Ca^{2+} fluxes using GFS

Global field synchronization (GFS) can estimate functional connectivity of brain processes. Here we use this method to quantify the synchronization level of the neuron Ca^{2+} flux in a frequency-dependent manner. To determine the GFS values, Ca^{2+} fluxes for each neuron recorded within individual fields of view were transformed into frequency domains using Fast Fourier Transform (FFT), which allows for comparison of Ca^{2+} flux amplitudes and phase at each frequency [46]. FFT-transformed signals at each frequency were then visualized as a cloud of points in a complex plane, yielding two eigenvalue. The GFS (0-1) was defined as [47]:

$$GFS(f) = \frac{|E(f)_1 - E(f)_2|}{E(f)_1 + E(f)_2}$$

where $E(f)_1$ and $E(f)_2$ are two eigenvalues obtained from principal-component analysis at a given frequency f. High GFS values in a given frequency indicate that a large part of the recorded calcium activity at that frequency is phase locked, which can be interpreted as increased overall functional connectivity. Low GFS values indicate that no preferential phase could be determined. GFS=1 indicates the complete synchronization of Ca^{2+} flux amplitudes and phase, while GFS=0 indicates asynchronous Ca^{2+} fluxes. The Matlab code and functions for calculating the GFS value are in SI.

Results and Discussion

SMS enhances the intracellular delivery of Au-SPIO NPs into primary cultured mouse DA neurons

Midbrain DA neurons were isolated from the ventral mesencephalon (VM) of mouse embryonic day 14 (E14) embryos and mechanically dissociated [40]. Dissociated cells were further cultured for 2 weeks prior to treatment with 20 μg/ml of Au-SPIO NPs. To apply SMS, primary mouse midbrain cultures were placed inside a magnetic applicator composed of 8 * N52 NdFeB magnetic cubes (0.5 inch) arranged in a Halbach-like array for 30 min (Figure 9A). Inside the applicator, a constant magnetic field gradient of -36.19 T/m was estimated along the radial direction (Figure 9B). Au-SPIO NPs were synthesized using hydroxylamine hydrochloride to form an Au layer at SPIO core according to a previously reported method [23, 48]. As shown in Figure 9A, TEM images of Au-SPIO NPs displayed quasi-spherical shapes and an average diameter of 20 ± 4 nm, while uncoated SPIO NPs displayed an average diameter of 13 ± 3 nm (Figure 13). The formation of an Au shell on SPIO was confirmed by a UV-Vis light absorbance spectrum (Figure 14), which exhibited the characteristic light absorbance peak of Au shell at 523 nm [22]. Zeta potential and hydrodynamic diameter results

(Table 1) further showed that fresh Au-SPIO NPs possessed a negative zeta potential of -44.2 ± 0.7 mV and a hydrodynamic diameter of 23.5 ± 0.1 nm. While one month-old Au-SPIO NPs had a negative zeta potential of -42.3 ± 1.6 mV and a hydrodynamic diameter of 23.6 ± 0.2 nm. The nearly unchanged zeta potential and hydrodynamic diameter indicated their high stability in aqueous solution because of a strong electrostatic repulsive force. Our previous work also demonstrated no decrease of the characteristic absorbance peak for up to 21 days, suggesting that Au-SPIO NPs are stable in cell culture medium [22]. It has been reported that Au coating affects the superparamagnetic property of SPIO and causes a slight reduction of magnetization from 59.6 to 54.3 emu/g [48]. This can be attributed to the obstructed rotation of SPIO NPs by Au coating. To verify the magnetic properties of Au-SPIO NPs, we also tested their magnetic behavior using an external magnetic field. As shown in Figure 15, Au-SPIO NPs exhibited fast movement towards magnetic field within 5 seconds, confirming the magnetic response of Au-SPIO NPs. To visualize an interaction between Au-SPIO NPs and midbrain neurons using confocal microscopy, Au-SPIO NPs were tagged with Cy3 dye (Nanocs, cat # PG2-S3TH-2k, red), and midbrain neurons were stained with antibodies against NeuN (Abcam, cat # ab104224) and tyrosine hydroxylase (TH) (Abcam, cat # ab76442). As shown with confocal z-stacks in Figure 10A, in the absence of SMS, a few negatively charged Au-SPIO NPs were internalized into the cytosol of midbrain neurons (average intracellular fluorescence = 932 A.U.), while SMS caused a significant increase in internalization of Au-SPIO NPs into midbrain neurons (average intracellular fluorescence = 2676 A.U.). To further demonstrate Cy3 tagged Au-SPIO

NPs were truly internalized into the neuronal cytosol, Figure 10B shows a single optical plane image of Au-SPIO and SMS-Au-SPIO from example cells in panel A. No significant difference was observed in the size of midbrain neurons between groups, suggesting that neither SMS nor Au-SPIO NPs caused osmotic swelling of neurons. Our previous work has demonstrated that Au-SPIO NPs can be absorbed by neuron-like cells through endocytic pathway [23]. One of the possible mechanism to enhance internalization of Au-SPIO NPs into midbrain neurons via SMS is to promote endocytic uptake of NPs by overcoming the membrane deformation cost using SMS [49]. To further confirm this hypothesis, detailed experimental protocols can be designed to study different cellular uptake mechanisms, which will be explored in the future.

SMS-Au-SPIO regulates Ca^{2+} fluxes in midbrain neurons via L-type VGCCs

A previous study has shown that negatively charged Au-SPIO NPs adhere to hippocampal neuronal membranes and modulate the excitability of these cells [37], however, the underlying mechanisms are unclear. We therefore sought to determine differences in midbrain neuron activity following either exposure to Au-SPIO alone or co-exposure to Au-SPIO with SMS. We rationalized that since SMS causes negatively charged Au-SPIO NPs to penetrate the cytoplasm of neurons (Figure 10), this will likely modulate spontaneous midbrain neuron Ca^{2+} fluxes in a manner that is distinct from exposure to Au-SPIO NPs without SMS.

To quantify spontaneous Ca^{2+} fluxes in cultured mouse midbrain neurons, we followed a previously published protocol [40]. Briefly, we used an AAV expressing the genetically encoded Ca^{2+} indicator, GCaMP6f, driven by a neuron-specific human synapsin promoter (hSyn) (AAV 2/5 hSyn-GCaMP6f). Two-week-old primary mouse midbrain neuron cultures were infected with 1 x 10^9 genome copies of AAV 2/5 hSyn-GCaMP6f per 35 mm dish and cultured for 5 additional days. Cells were then cultured for 24 h with exposure to 20 μg/ml Au-SPIO NPs. This concentration did not induce the toxicity of neuron-like cells in our previous study [23, 24]. Before imaging, the cells were placed in the magnetic applicator for 30 min for both SMS and SMS-Au-SPIO groups. As shown in Figure 11A-B, in all cases, we observed robust spontaneous neuronal Ca^{2+} fluxes, but each treatment condition caused a distinct alteration in spontaneous Ca^{2+} flux activity. Specifically, when compared to untreated control cultures (average frequency = 8.7 events/min, average amplitude = 1.05 $\Delta F/F_0$, average half-width = 17.71 msec), SMS alone reduced the frequency (4.0 events/min) and half-width (15.36 msec) of Ca^{2+} fluxes, while Au-SPIO NPs alone reduced the frequency (4.9 events/min) but increased the amplitude (1.6 $\Delta F/F_0$) and half-width (19.96 msec) of Ca^{2+} fluxes. Co-exposure to SMS-Au-SPIO reduced Ca^{2+} flux frequency (5.9 events/min) with no effect on half-width or amplitude.

We next asked if these spontaneous Ca^{2+} fluxes were caused by L-type VGCCs. Neuronal cultures were bath perfused with 100 μM diltiazem, which is a specific inhibitor of L-type VGCCs [43-45]. Ca^{2+} fluxes in the presence of diltiazem were then imaged using confocal microscope and analyzed. We first fit the Ca^{2+} event traces following diltiazem exposure for each of the four conditions (Control, SMS, Au-SPIO, SMS-Au-SPIO) to exponential fits. We found that SMS, Au-SPIO and SMS-Au-SPIO decreased decay rates by approximately 40% when compared to untreated control cells (Figure 16). Having found a substantial difference in decay rates with each of the three manipulations, we then analyzed latency to complete blockade by diltiazem as reported in the Experimental Section.

As shown in Figure 8A-B, diltiazem almost completely inhibited spontaneous Ca^{2+} fluxes in untreated control cultures (spontaneous = 6.3 events/min, diltiazem = 1.2 events/min), suggesting that the spontaneous Ca^{2+} fluxes in these midbrain neurons were predominantly caused by L-type VGCCs. Interestingly, when compared to control (78.7 s), the blockade by diltiazem was significantly delayed by both Au-SPIO NPs (127.1 s) and SMS-Au-SPIO (178.8 s), but not with SMS (88.8 s) exposure alone. One mechanism that could contribute to delayed blockade by diltiazem is a change in the activity of L-type VGCCs due to changes in the resting membrane potential of midbrain neurons, caused by negatively charged Au-SPIO NPs. Interestingly SMS did not alter the amplitude but altered the frequency of Ca^{2+} fluxes. The effect of SMS on ion channel properties and voltage gating are complex and difficult to interpret per se. The observed absence of delay following L type VGCC blockade, despite changes in Ca^{2+} flux frequency, could be explained by the idea that channel open times are regulated distinctly from voltage sensing and desensitization. Indeed, a recent study has shown that magnetic fields alter the kinetics of voltage gated sodium and potassium channels via possible effect on sialic acid glycosylation motifs on these channels [50]. This suggests that the mechanism of voltage sensing is dependent on SMS, while the influx of ions through VGCCs is regulated by mechanisms that do not depend on SMS. Additionally, in our recent work [51], we have proved that the activity of L-type VGCC in DA neuron did not depend on the calcium release from the endoplasmic reticulum. We have also shown that the activity of L-type VGCC mainly depends on extracellular Ca^{2+} level, rather than the intracellular Ca^{2+} store.

Note that Figure 8A contains representative $\Delta F/F_0$ Ca^{2+} traces for each condition, including a gray bar labeled “100 uM Diltiazem” to denote when diltiazem was added. In Figure 8B, for graphs representing population data, each dot for each condition represents the value of a single cell. The wide distribution of data for each condition is because of inherent variability that is observed in native co-cultures of astrocyte-midbrain neurons [40, 41].

To gain more insight into how the activity of L-type VGCCs was altered by the different treatment conditions, we utilized FFT as a method to transform the Ca^{2+} flux from time domain to frequency domain. We then obtained the PSD for Ca^{2+} fluxes in each midbrain neuron. Thus, PSD would reflect changes in amplitude of the Ca^{2+} fluxes at each discreet frequency. We analyzed PSD of spontaneous Ca^{2+} fluxes before (Figure 9A) and after (Figure 9B) diltiazem application. As shown in Figure 9A, PSD analysis of untreated control cultures showed that there were significant differences in Ca^{2+} flux amplitude within the lower range of frequencies (<0.1 Hz, corresponding to 0.6 – 6 events/min). Compared to controls, SMS decreased while Au-SPIO NPs increased Ca^{2+} flux amplitudes at lower frequencies <0.1 Hz. Interestingly, SMS-Au-SPIO did not affect Ca^{2+} flux amplitude at lower frequencies, however, after diltiazem application (Figure 9B), both SMS and SMS-Au-SPIO decreased the amplitude of Ca^{2+} fluxes. In addition, Au-SPIO alone did not affect the amplitude of Ca^{2+} fluxes in midbrain neurons. These data confirm that SMS-Au-SPIO regulates L-type VGCC activity, but the underlying mechanism is unclear. One possibility is that the Au-SPIO NPs without SMS are adhered to the extracellular surface of the neuronal plasma membrane, as shown in Figure 10. This can modulate membrane potential and alter spontaneous Ca^{2+} fluxes (Figure 10) [37]. However, since SMS causes internalization of negatively charged Au-SPIO NPs into the cytosol of midbrain neurons (Figure 10), this would also alter membrane potential and delay diltiazem-mediated blockade of Ca^{2+} activity (Figure 10). This hypothesis is based on our recent observation that SMS-Au-SPIO NPs hyperpolarize the membrane potential of PC-12 cells, while Au-SPIO NPs alone depolarize the membrane potential of PC-12 cells [52], which is possibly due to cellular mobility change of Au-SPIO NPs under SMS. Importantly, PC-12 cells possess several properties that are similar to midbrain DA neurons, including expression of tyrosine hydroxylase and the synthesis of dopamine [53]. Therefore, we believe that Au-SPIO NPs in the presence of SMS will similarly cause a hyperpolarization of the resting membrane potential and membrane resistance of DA neurons.

It is interesting to note that although SMS alone reduced the excitability of neurons in lower frequencies (<0.1 Hz), SMS did not affect the latency to diltiazem-mediated L-type VGCC blockade. Since lower frequencies of Ca^{2+} activity would correspond to a sparse population of active VGCCs in a neuron, this would allow SMS to manipulate the amplitude of VGCC mediated Ca^{2+} influx more efficiently. Future study will be performed to further explore how SMS-Au-SPIO affects the change in membrane resistance of midbrain DA neurons.

SMS-Au-SPIO alters midbrain neuron synchronization

As midbrain neurons establish synapses via axonal growth [54], synchronous neuronal Ca^{2+} fluxes between them play an important role in regulating these processes [55-58]. Excessive synchronization of electroencephalography signals has been observed in PD patients between their motor cortex and basal ganglia [59]. However, it is unclear if neighboring DA neuron synchronization in the midbrain is associated with PD pathology, and how this is related with L-type VGCC activity. Based on these studies, we sought to determine the extent to which SMS-Au-SPIO NPs can modulate the synchronization of Ca^{2+} fluxes in midbrain neurons. To do this, we first conducted a synchronization analysis of neighboring midbrain neurons using GFS to quantify multiple Ca^{2+} fluxes in an interdependent single system from large sets of midbrain neurons. GFS is more efficient and accurate [46, 60] in comparison to the conventional approach [55] which is mainly done manually by counting the percentage of cells that display simultaneous Ca^{2+} fluxes (GFS=1 indicates the complete synchronization of Ca^{2+} flux amplitudes and phase, while GFS=0 indicates asynchronous Ca^{2+} fluxes.). GFS analysis of all three groups (SMS, Au-SPIO, and SMS-Au-SPIO) showed that before applying diltiazem, SMS-Au-SPIO and Au-SPIO did not affect synchronization, while

SMS slightly increased synchronization (Figure 11A). Additional post-diltiazem experiments showed that all three groups maintained similar synchronicity as untreated control cells (Figure 11B). These data suggest that the SMS-induced Ca^{2+} synchronization is mainly gated by L-type VGCC in midbrain neurons, and such an effect can be reversed by adding Au-SPIO NPs.

SMS-Au-SPIO does not induce DA neuron apoptosis in cultured mouse midbrain neurons

Since dysregulated Ca^{2+} fluxes play an important role in the pathogenesis of neurodegeneration in PD, we sought to determine the effect of SMS and SMS-Au-SPIO NPs on apoptotic signaling in cultured DA neurons. For this purpose, we used TH as a DA neuron marker, and an antibody against cleaved caspase-3 (Cell Signaling, cat # 9661S) as a marker for apoptosis. We found that, when compared to control (699.4 A.U.), SMS (1206.1 A.U.) alone significantly increased while SMS-Au-SPIO (530.9 A.U.) decreased the levels of cleaved caspase-3 in DA neurons. In addition, Au-SPIO (563.3 A.U.) alone did not result in an obvious increase in cleaved caspase-3 (Figure 12). Taken together with the synchronization results, these findings suggest that SMS likely induces caspase-3 activation and initiates apoptosis by increasing the synchronization of neuronal Ca^{2+} fluxes. Furthermore, it is likely that the addition of Au-SPIO interrupts the mechanism by which SMS increases Ca^{2+} flux synchronicity, consequently preventing caspase-3 activation and apoptosis.

Conclusions

In summary, we demonstrate that SMS and SMS-Au-SPIO can regulate spontaneous Ca^{2+} fluxes in midbrain neurons via the modulation of L-type VGCC activity. We first explored the interaction between Au-SPIO and DA neurons and found that SMS could significantly enhance the intracellular delivery of negatively charged Au-SPIO NPs to DA neurons. We then revealed a significant reduction in the frequency of spontaneous Ca^{2+} fluxes in midbrain neurons exposed to SMS, Au-SPIO, or the combination of SMS-Au-SPIO, suggesting that SMS and Au-SPIO when used in combination or alone are capable of regulating spontaneous Ca^{2+} fluxes in midbrain neurons. The delayed L-type VGCCs blockade by SMS-Au-SPIO suggests that SMS-Au-SPIO treatment modulates Ca^{2+} fluxes by altering the L-type VGCC activity, which is further demonstrated by PSD calculation. GFS analysis and an evaluation of apoptosis with cleaved caspase-3 suggest that SMS-induced synchronization of Ca^{2+} flux may initiate apoptosis, while combining SMS with Au-SPIO NPs reduces the apoptosis. Taken together, these results suggest that combining SMS with Au-SPIO NPs may be an effective neuroprotective strategy for PD. They further suggest that neuroprotection by SMS-Au-SPIOs likely occurs via a regulation of L-type VGCC activity, and a consequent attenuation of apoptotic signaling cascades. SMS-Au-SPIO could also serve as a potential tool for targeted delivery of therapeutic agents to specific brain regions, and the localized modulation of Ca^{2+} flux activity. These results also provide important insights on how SMS-Au-SPIO modulate spontaneous Ca^{2+} fluxes and the associated downstream cellular processes in midbrain neurons. Future studies will explore the effect of NP surface charge, pH, and other parameters on the cellular uptake of NPs, as well as their ability to electrically tune the activity of native midbrain neurons with and without SMS. Additional experiments will be performed to explore how long it takes to reach the maximum accumulation of Au-SPIO in DA neurons. We will also dissect the relationship between L-type VGCC activity, Ca^{2+} flux synchronization and apoptotic signaling. In future studies, *in vivo* experiments will be performed to verify toxicity, biodistribution and pharmacokinetic behavior of SMS-Au-SPIO, as well as targeted delivery of therapeutic agents to specific brain regions. We will also explore if SMS-Au-SPIO-induced alterations in spontaneous Ca^{2+} activity affects dopamine release and thus PD therapeutics.

Figures

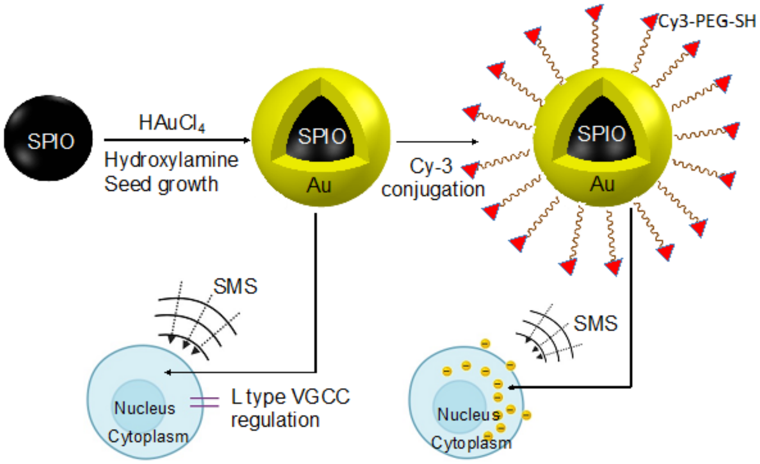

Figure 21: The SPIO NPs were coated with gold by the seed growth process using hydroxylamine as reducing agent.
On one side, Au-SPIO NPs in combination with SMS were used to regulate L type VGCC. On the other side, Au-SPIO NPs were functionalized with Cy3-PEG-SH as fluorescence dye to explore their interaction with midbrain DA neurons under the effect of SMS treatment.

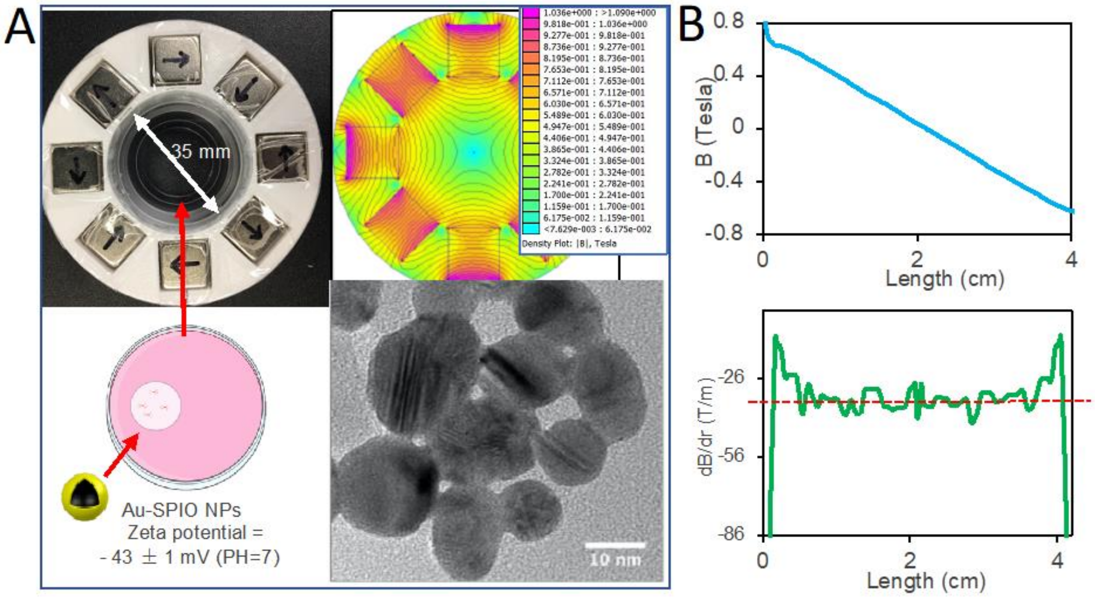

Figure 22: Properties of SMS and SMS-Au-SPIO treatment and their interaction with cultured DA neurons.

(A) Top: the setup (left) and the finite element modeling (right) of the static magnetic applicator using N52 magnets; Bottom: 35 mm petri dish showing how cells in the coverslip (white circle) are positioned during SMS stimulation and the zeta potential of Au-SPIO NPs as treatment in cell culture medium (left); and a TEM image of Au-SPIO NPs (right). **(B)** Top: Finite element modeling (FEM) result of the flux density inside the magnetic applicator; Bottom: the gradient dB/dr (T/m) along the radial direction. The red dotted line indicates an estimated average value of dB/dr =-36.19 T/m.

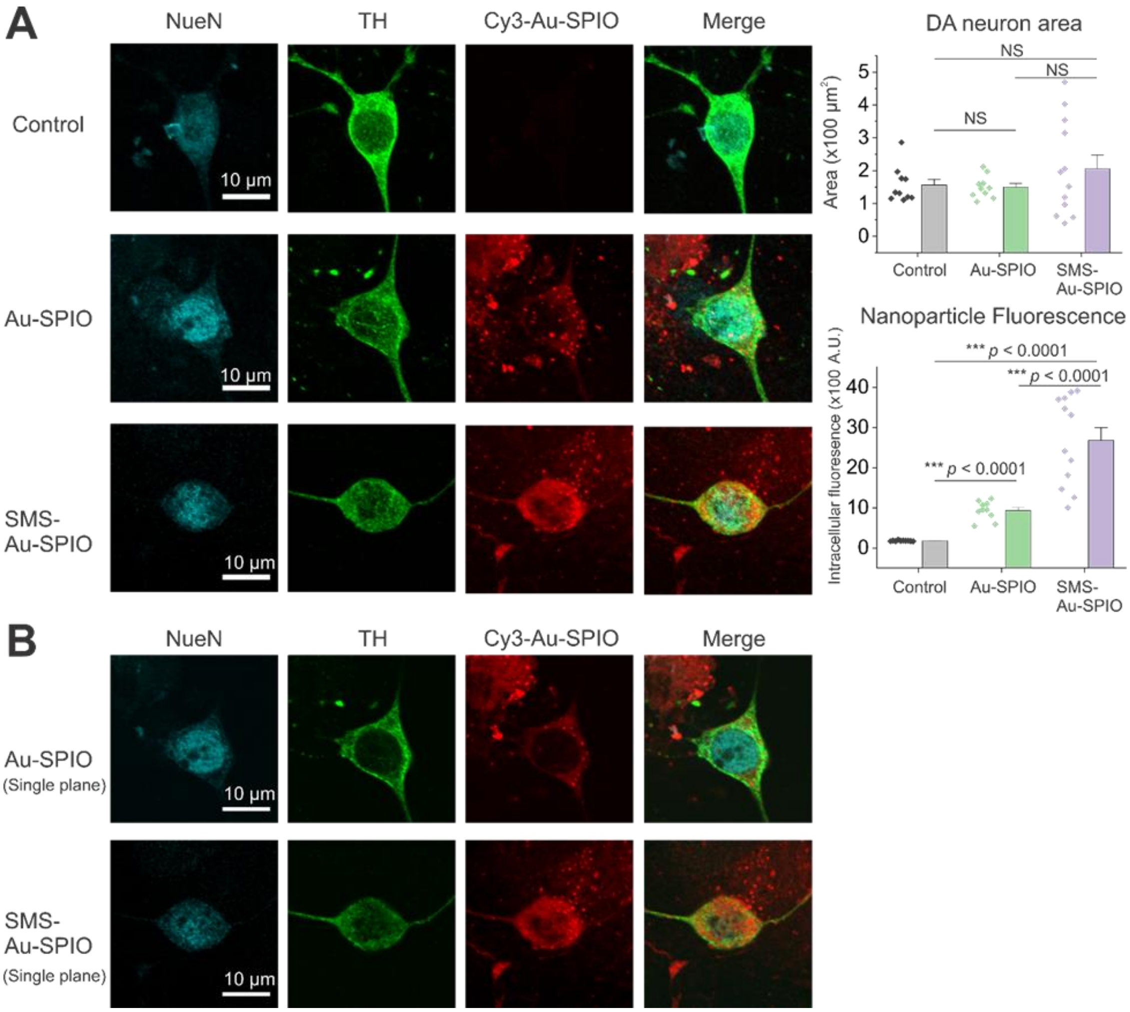

Figure 23: Interaction between SMS-Au-SPIO and cultured DA neurons.
(A) Left; representative confocal z-stacks at 60X magnification of NeuN, TH, Cy3 tagged Au-SPIO expression, and merged images (NeuN, TH and Cy3) in cultured primary midbrain neurons. Scale bar, 10 μm. Right: summary data of DA neuron area and mean Cy3 fluorescence intensity. **(B)** Single optical plane images for the Au-SPIO

and SMS-Au-SPIO conditions from z-stacks in panel A. Scale bar, 10 µm. All experiments were performed on 2 independent cultures. n = 10 control neurons, 10 Au-SPIO neurons, 12 SMS-Au-SPIO neurons. Error bars are ± SEM and p values are indicated for all graphs, based on two sample t-test for normally distributed data and Mann-Whitney test for non-normally distributed data. *p* < 0.05 was considered statistically significant. NS = not significant.

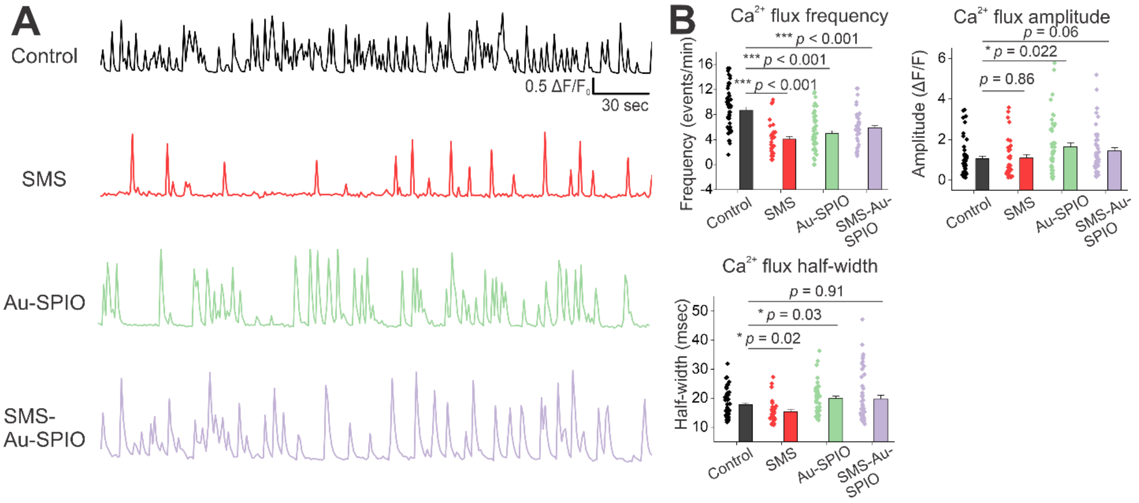

Figure 24: SMS and SMS-Au-SPIO alter spontaneous Ca^{2+} activity in cultured primary midbrain neurons.

(A) Representative ΔF/F0 traces of spontaneous Ca^{2+} in primary midbrain neurons from each experimental condition. **(B)** Summary data of spontaneous Ca^{2+} flux frequency, amplitude, and half-width. All experiments were performed on 4 independent cultures. n = 50 control neurons, 33 SMS neurons, 50 Au-SPIO neurons, and 48 SMS-Au-SPIO neurons. Error bars are SEM and p values are reported in all graphs, based on Mann-Whitney tests for non-normally distributed data, or two-sample t-tests for normally distributed data.

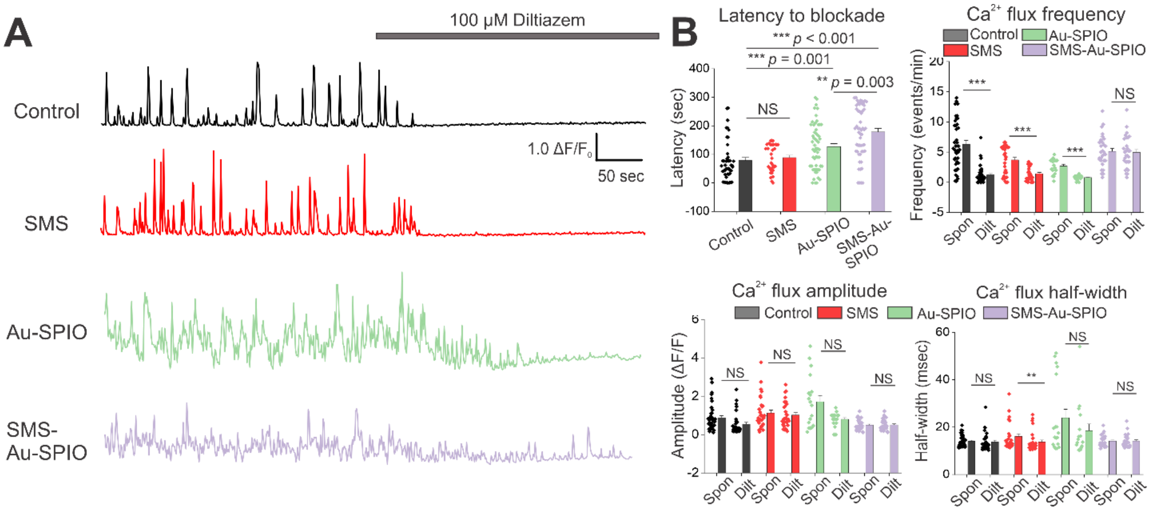

Figure 25: SMS and SMS-Au-SPIO alter Ca^{2+} activity via L-type VGCCs in cultured primary midbrain neurons.

(A) Representative $\Delta F/F_0$ traces of primary midbrain neurons with L-type VGCC blocker diltiazem applied from 300 to 600 s following imaging of spontaneous events in the first 300 s as indicated by the gray bar. **(B)** Summary data including latency to L-type VGCC blockade, Ca^{2+} flux frequency, amplitude, and half-width prior to and during diltiazem application. All experiments were performed on 3 independent cultures. n = 46 control neurons, 33 SMS neurons, 57 Au-SPIO neurons, and 56 SMS-Au-SPIO neurons. Error bars are ± SEM and p values are indicated for all graphs, based on two sample t-test for normally distributed data, Mann-Whitney test for non-normally distributed data, and paired-sample Wilcoxon-Sign rank test for paired measures. $P < 0.05$ is considered statistically significant. * = $p > 0.05$, ** = $p > 0.01$, *** = $p > 0.001$. NS = not significant.

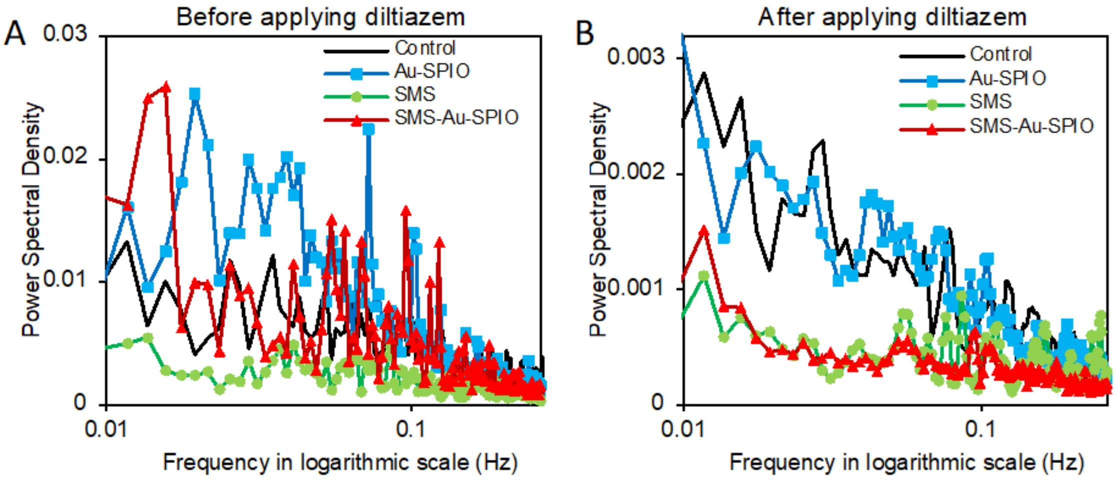

Figure 26: Differential effects of SMS and SMS-Au-SPIO on regulating Ca^{2+} flux amplitudes gated by L-type VGCC at lower frequencies < 0.1 Hz.
The PSD of spontaneous Ca^{2+} flux **(A)** before and **(B)** after the diltiazem application.

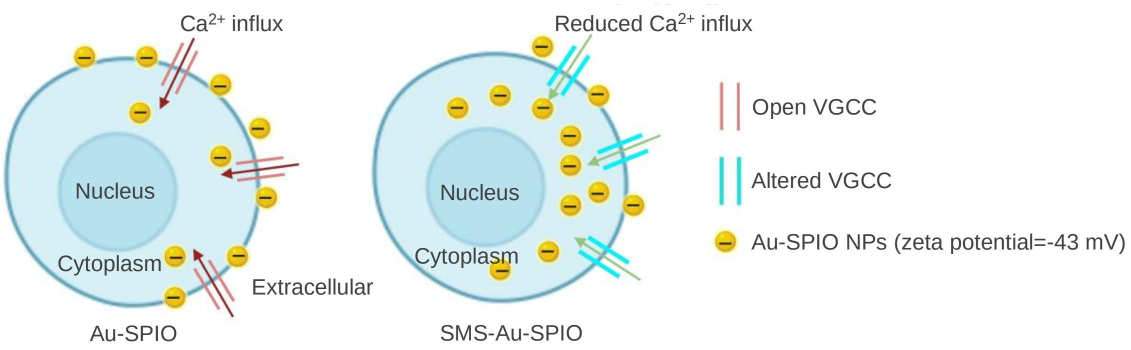

Figure 27: Schematic illustration of SMS-Au-SPIO regulating L-type VGCC activity.

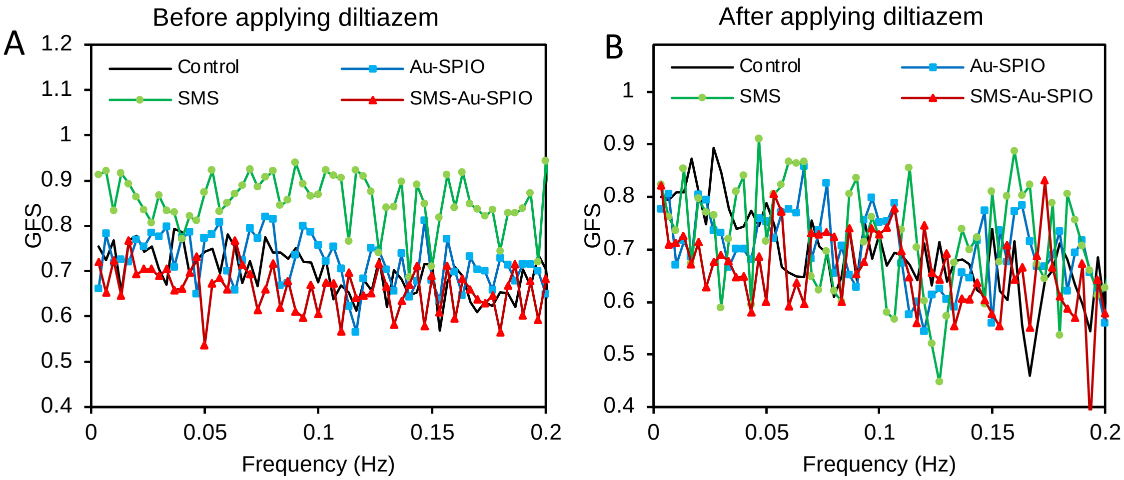

Figure 28: The effect of SMS and SMS-SPIO-Au on synchronicity of Ca^{2+} fluxes in midbrain neurons before and after diltiazem application.
GFS value **(A)** before and **(B)** after diltiazem application. A GFS value between 0 and 1 reflects the level of synchronization of Ca^{2+} fluxes between two neurons, where GFS = 1 indicates the full synchronization of Ca^{2+} fluxes and GFS = 0 indicates no synchronization.

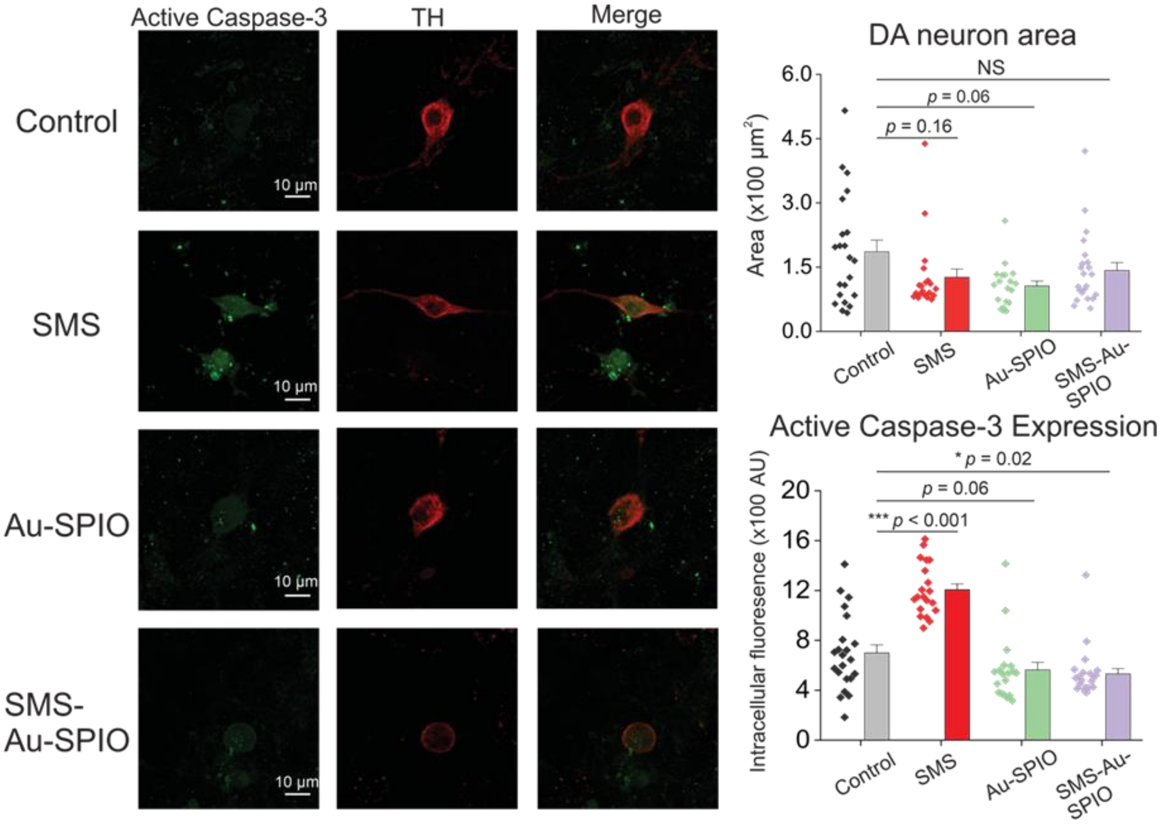

Figure 29: Caspase-3 cleavage in midbrain DA neurons is induced by SMS but not by SMS-Au-SPIO.
Left, representative confocal images at 60X magnification of cleaved caspase-3 and TH expression (DA neuron marker) in cultured primary midbrain neurons. Scale bar, 10 µm; Right, summary data of DA neuron area (top) and active caspase-3 expression (bottom). All experiments were performed on 3 independent cultures. n=22 control neurons, 20 SMS neurons, 19 Au-SPIO neurons, 29 SMS-Au-SPIO neurons. Error bars are ± SEM. p values are indicated for all graphs and are based on two sample t-test for normally distributed data and Mann-Whitney test for non-normally distributed data. $p < 0.05$ is considered statistically significant. NS = not significant.

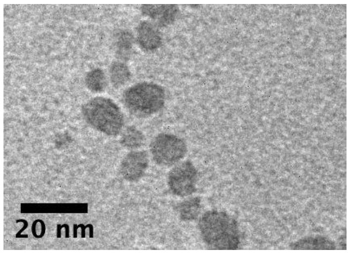

Figure 30: TEM of SPIO NPs before coating of Au. (average diameter: 13 ± 3 nm measured from at least 50 NPs)

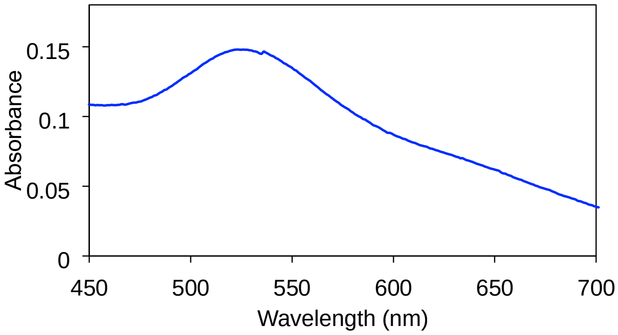

Figure 31: UV–vis absorption spectra of SPIO-Au NPs in DI water with the characteristic Au surface plasmon peak at 523 nm.

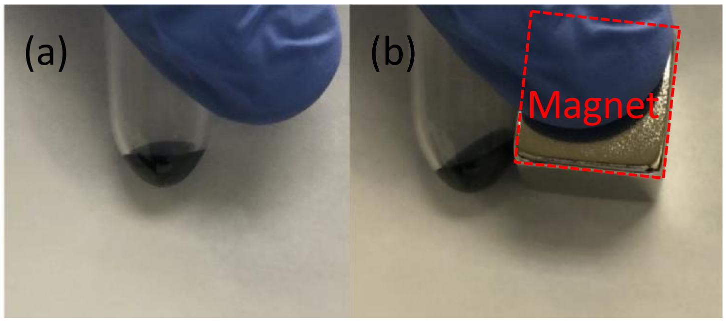

Figure 32: Magnetic properties of Au-SPIO. (a) before and (b) after the application of magnet for 5 seconds, showing the accumulation and movement of Au-SPIO NPs towards the magnetic field direction.

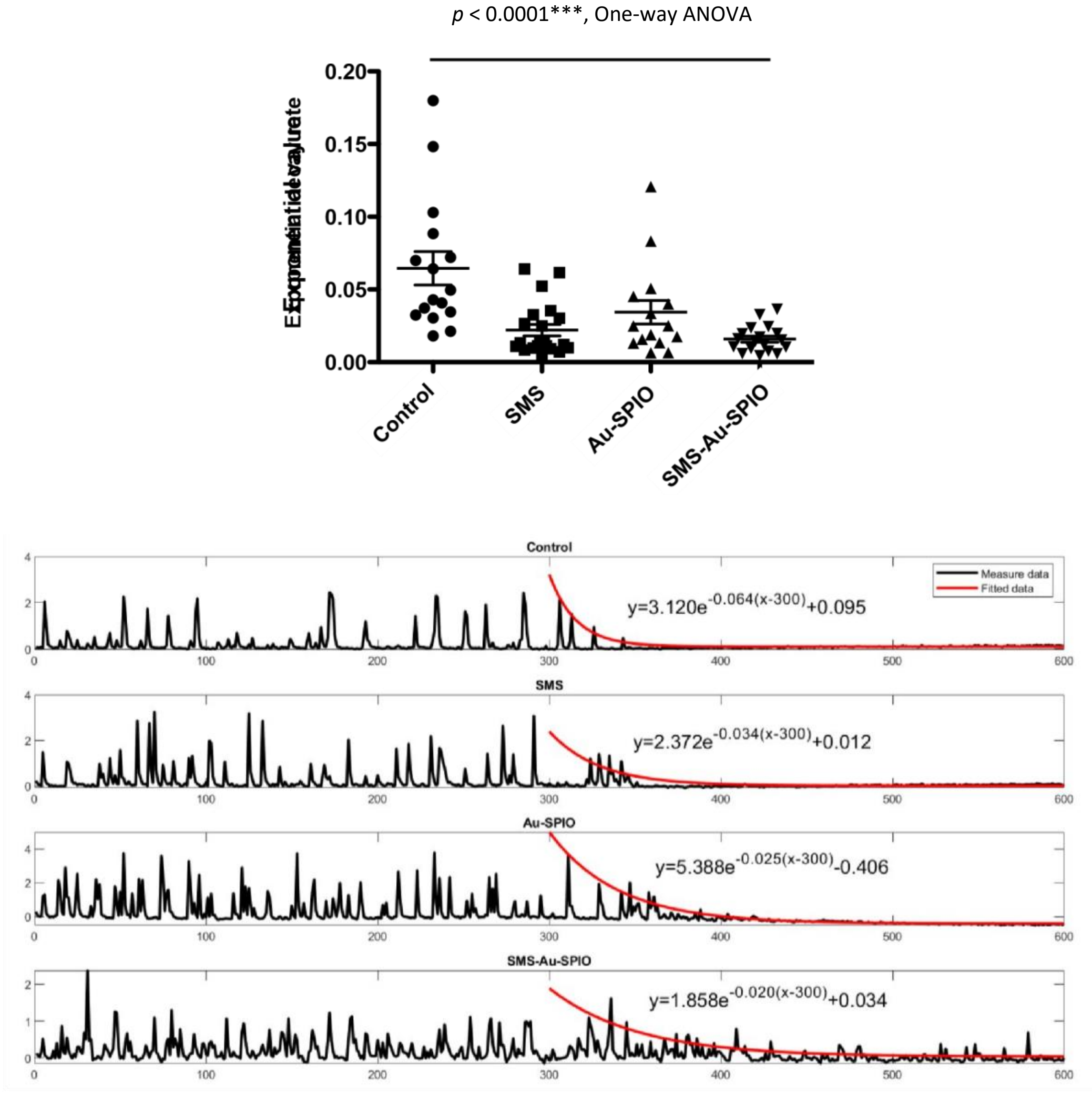

Figure 33: Exponential decay rates and fitting of example traces of calcium events in the presence of diltiazem for control, SMS, Au-SPIO, SMS-Au-SPIO groups.

Tables

Table 3: Zeta potential and hydrodynamic diameter measurement of SPIO-Au NPs from triplicated experiments.

	Fresh SPIO-Au NPs	1 month-old SPIO-Au NPs (after 1 month of synthesis)
Zeta potential (mV)	23.5 ± 0.1	23.6 ± 0.2
Hydrodynamic diameter (nm)	-44.2 ± 0.7	-42.3 ± 1.6

References

1. Surmeier, D. J.; Obeso, J. A.; Halliday, G. M., Selective neuronal vulnerability in Parkinson disease. *Nat Rev Neurosci* **2017,** 18, (2), 101-113.
2. Surmeier, D. J.; Guzman, J. N.; Sanchez-Padilla, J.; Schumacker, P. T., The role of calcium and mitochondrial oxidant stress in the loss of substantia nigra pars compacta dopaminergic neurons in Parkinson's disease. *Neuroscience* **2011,** 198, 221-31.
3. Surmeier, D. J., Calcium, ageing, and neuronal vulnerability in Parkinson's disease. *Lancet Neurol* **2007,** 6, (10), 933-8.
4. Mead, B. P.; Kim, N.; Miller, G. W.; Hodges, D.; Mastorakos, P.; Klibanov, A. L.; Mandell, J. W.; Hirsh, J.; Suk, J. S.; Hanes, J.; Price, R. J., Novel Focused

Ultrasound Gene Therapy Approach Noninvasively Restores Dopaminergic Neuron Function in a Rat Parkinson's Disease Model. *Nano Lett* **2017,** 17, (6), 3533-3542.

5. Cantello, R.; Tarletti, R.; Civardi, C., Transcranial magnetic stimulation and Parkinson's disease. *Brain Res Brain Res Rev* **2002,** 38, (3), 309-27.
6. Oda, T.; Koike, T., Magnetic field exposure saves rat cerebellar granule neurons from apoptosis in vitro. *Neuroscience letters* **2004,** 365, (2), 83-6.
7. Chervyakov, A. V.; Chernyavsky, A. Y.; Sinitsyn, D. O.; Piradov, M. A., Possible Mechanisms Underlying the Therapeutic Effects of Transcranial Magnetic Stimulation. *Front Hum Neurosci* **2015,** 9, 303.
8. Li, Y.; Yan, X.; Liu, J.; Li, L.; Hu, X.; Sun, H.; Tian, J., Pulsed electromagnetic field enhances brain-derived neurotrophic factor expression through L-type voltage-gated calcium channel- and Erk-dependent signaling pathways in neonatal rat dorsal root ganglion neurons. *Neurochem Int* **2014,** 75, 96-104.
9. Ma, J.; Zhang, Z.; Su, Y.; Kang, L.; Geng, D.; Wang, Y.; Luan, F.; Wang, M.; Cui, H., Magnetic stimulation modulates structural synaptic plasticity and regulates BDNF-TrkB signal pathway in cultured hippocampal neurons. *Neurochem Int* **2013,** 62, (1), 84-91.
10. Durmaz, O.; Ates, M. A.; Senol, M. G., Repetitive Transcranial Magnetic Stimulation (rTMS)-Induced Trigeminal Autonomic Cephalalgia. *Noro Psikiyatr Ars* **2015,** 52, (3), 309-311.
11. Wang, N.; Butler, J. P.; Ingber, D. E., Mechanotransduction across the cell surface

and through the cytoskeleton. *Science (New York, N.Y.)* **1993,** 260, (5111), 1124-7.

12. Hughes, S.; McBain, S.; Dobson, J.; El Haj, A. J., Selective activation of mechanosensitive ion channels using magnetic particles. *J R Soc Interface* **2008,** 5, (25), 855-63.
13. Tay, A.; Kunze, A.; Murray, C.; Di Carlo, D., Induction of Calcium Influx in Cortical Neural Networks by Nanomagnetic Forces. *ACS Nano* **2016,** 10, (2), 2331-41.
14. Tay, A.; Di Carlo, D., Magnetic Nanoparticle-Based Mechanical Stimulation for Restoration of Mechano-Sensitive Ion Channel Equilibrium in Neural Networks. *Nano Lett* **2017,** 17, (2), 886-892.
15. Tay, A.; Sohrabi, A.; Poole, K.; Seidlits, S.; Di Carlo, D., A 3D Magnetic Hyaluronic Acid Hydrogel for Magnetomechanical Neuromodulation of Primary Dorsal Root Ganglion Neurons. *Adv Mater* **2018**, e1800927.
16. Ortner, N. J., Voltage-Gated Ca(2+) Channels in Dopaminergic Substantia Nigra Neurons: Therapeutic Targets for Neuroprotection in Parkinson's Disease? *Front Synaptic Neurosci* **2021,** 13, 636103.
17. Mahmoudi, M.; Hofmann, H.; Rothen-Rutishauser, B.; Petri-Fink, A., Assessing the in vitro and in vivo toxicity of superparamagnetic iron oxide nanoparticles. *Chem Rev* **2012,** 112, (4), 2323-38.
18. Yarjanli, Z.; Ghaedi, K.; Esmaeili, A.; Rahgozar, S.; Zarrabi, A., Iron oxide nanoparticles may damage to the neural tissue through iron accumulation,

oxidative stress, and protein aggregation. *BMC Neurosci* **2017,** 18, (1), 51.

19. Cheng, Y.; Morshed, R. A.; Auffinger, B.; Tobias, A. L.; Lesniak, M. S., Multifunctional nanoparticles for brain tumor imaging and therapy. *Adv Drug Deliv Rev* **2014,** 66, 42-57.

20. Nam, S. Y.; Ricles, L. M.; Suggs, L. J.; Emelianov, S. Y., Imaging strategies for tissue engineering applications. *Tissue Eng Part B Rev* **2015,** 21, (1), 88-102.

21. Kumar, C. S.; Mohammad, F., Magnetic nanomaterials for hyperthermia-based therapy and controlled drug delivery. *Adv Drug Deliv Rev* **2011,** 63, (9), 789-808.

22. Yuan, M.; Wang, Y.; Qin, Y. X., SPIO-Au core-shell nanoparticles for promoting osteogenic differentiation of MC3T3-E1 cells: Concentration-dependence study. *J Biomed Mater Res A* **2017,** 105, (12), 3350-3359.

23. Yuan, M.; Wang, Y.; Qin, Y. X., Promoting neuroregeneration by applying dynamic magnetic fields to a novel nanomedicine: Superparamagnetic iron oxide (SPIO)-gold nanoparticles bounded with nerve growth factor (NGF). *Nanomedicine* **2018,** 14, (4), 1337-1347.

24. Yuan, M.; Wang, Y.; Qin, Y. X., Engineered nanomedicine for neuroregeneration: light emitting diode-mediated superparamagnetic iron oxide-gold core-shell nanoparticles functionalized by nerve growth factor. *Nanomedicine* **2019,** 21, 102052.

25. Yuan, M.; Wang, Y.; Hwang, D.; Longtin, J. P., Thermocouple-tip-exposing temperature assessment technique for evaluating photothermal conversion efficiency of plasmonic nanoparticles at low laser power density. *Rev Sci Instrum*

2019, 90, (9), 094902.

26. Lu, A. H.; Salabas, E. L.; Schuth, F., Magnetic nanoparticles: synthesis, protection, functionalization, and application. *Angew Chem Int Ed Engl* **2007,** 46, (8), 1222-44.

27. Laurent, S.; Forge, D.; Port, M.; Roch, A.; Robic, C.; Vander Elst, L.; Muller, R. N., Magnetic iron oxide nanoparticles: synthesis, stabilization, vectorization, physicochemical characterizations, and biological applications. *Chem Rev* **2008,** 108, (6), 2064-110.

28. Yuan, M.; Yan, T. H.; Li, J.; Xiao, Z.; Fang, Y.; Wang, Y.; Zhou, H. C.; Pellois, J. P., Superparamagnetic iron oxide-gold nanoparticles conjugated with porous coordination cages: Towards controlled drug release for non-invasive neuroregeneration. *Nanomedicine* **2021,** 35, 102392.

29. Chen, J.; Wang, Y., Personalized dynamic transport of magnetic nanorobots inside the brain vasculature. *Nanotechnology* **2020,** 31, (49), 495706.

30. Geng, F.; Xing, J. Z.; Chen, J.; Yang, R.; Hao, Y.; Song, K.; Kong, B., Pegylated glucose gold nanoparticles for improved in-vivo bio-distribution and enhanced radiotherapy on cervical cancer. *J Biomed Nanotechnol* **2014,** 10, (7), 1205-16.

31. Kong, S. D.; Lee, J.; Ramachandran, S.; Eliceiri, B. P.; Shubayev, V. I.; Lal, R.; Jin, S., Magnetic targeting of nanoparticles across the intact blood-brain barrier. *J Control Release* **2012,** 164, (1), 49-57.

32. Lasagna-Reeves, C.; Gonzalez-Romero, D.; Barria, M. A.; Olmedo, I.; Clos, A.; Sadagopa Ramanujam, V. M.; Urayama, A.; Vergara, L.; Kogan, M. J.; Soto, C.,

Bioaccumulation and toxicity of gold nanoparticles after repeated administration in mice. *Biochem Biophys Res Commun* **2010,** 393, (4), 649-55.

33. Shilo, M.; Motiei, M.; Hana, P.; Popovtzer, R., Transport of nanoparticles through the blood-brain barrier for imaging and therapeutic applications. *Nanoscale* **2014,** 6, (4), 2146-52.

34. Bondarenko, O.; Saarma, M., Neurotrophic Factors in Parkinson's Disease: Clinical Trials, Open Challenges and Nanoparticle-Mediated Delivery to the Brain. *Frontiers in cellular neuroscience* **2021,** 15, 682597.

35. Chen, J.; Yuan, M.; Madison, C. A.; Eitan, S.; Wang, Y., Blood-brain Barrier Crossing using Magnetic Stimulated Nanoparticles. **2021**, 2021.12.23.472846.

36. Perrault, S. D.; Walkey, C.; Jennings, T.; Fischer, H. C.; Chan, W. C., Mediating tumor targeting efficiency of nanoparticles through design. *Nano Lett* **2009,** 9, (5), 1909-15.

37. Dante, S.; Petrelli, A.; Petrini, E. M.; Marotta, R.; Maccione, A.; Alabastri, A.; Quarta, A.; De Donato, F.; Ravasenga, T.; Sathya, A.; Cingolani, R.; Proietti Zaccaria, R.; Berdondini, L.; Barberis, A.; Pellegrino, T., Selective Targeting of Neurons with Inorganic Nanoparticles: Revealing the Crucial Role of Nanoparticle Surface Charge. *ACS Nano* **2017,** 11, (7), 6630-6640.

38. Arvizo, R. R.; Miranda, O. R.; Thompson, M. A.; Pabelick, C. M.; Bhattacharya, R.; Robertson, J. D.; Rotello, V. M.; Prakash, Y. S.; Mukherjee, P., Effect of nanoparticle surface charge at the plasma membrane and beyond. *Nano Lett* **2010,** 10, (7), 2543-8.

39. Gaiduk, A.; Ruijgrok, P. V.; Yorulmaz, M.; Orrit, M., Making gold nanoparticles fluorescent for simultaneous absorption and fluorescence detection on the single particle level. *Phys Chem Chem Phys* **2011,** 13, (1), 149-53.

40. Bancroft, E. A.; Srinivasan, R., Quantifying Spontaneous Ca2+ Fluxes and their Downstream Effects in Primary Mouse Midbrain Neurons. *Journal of visualized experiments : JoVE* **2020**, (163).

41. Zarate, S. M.; Pandey, G.; Chilukuri, S.; Garcia, J. A.; Cude, B.; Storey, S.; Salem, N. A.; Bancroft, E. A.; Hook, M.; Srinivasan, R., Cytisine is neuroprotective in female but not male 6-hydroxydopamine lesioned parkinsonian mice and acts in combination with 17-beta-estradiol to inhibit apoptotic endoplasmic reticulum stress in dopaminergic neurons. *Journal of neurochemistry* **2021,** 157, (3), 710-726.

42. Henley, B. M.; Cohen, B. N.; Kim, C. H.; Gold, H. D.; Srinivasan, R.; McKinney, S.; Deshpande, P.; Lester, H. A., Reliable Identification of Living Dopaminergic Neurons in Midbrain Cultures Using RNA Sequencing and TH-promoter-driven eGFP Expression. *Journal of visualized experiments : JoVE* **2017**, (120).

43. Davenport, B.; Li, Y.; Heizer, J. W.; Schmitz, C.; Perraud, A. L., Signature Channels of Excitability no More: L-Type Channels in Immune Cells. *Frontiers in immunology* **2015,** 6, 375.

44. Laryushkin, D. P.; Maiorov, S. A.; Zinchenko, V. P.; Gaidin, S. G.; Kosenkov, A. M., Role of L-Type Voltage-Gated Calcium Channels in Epileptiform Activity of Neurons. *International journal of molecular sciences* **2021,** 22, (19).

45. Tang, L.; Gamal El-Din, T. M.; Lenaeus, M. J.; Zheng, N.; Catterall, W. A., Structural Basis for Diltiazem Block of a Voltage-Gated Ca(2+) Channel. *Molecular pharmacology* **2019,** 96, (4), 485-492.

46. Achermann, P.; Rusterholz, T.; Durr, R.; Konig, T.; Tarokh, L., Global field synchronization reveals rapid eye movement sleep as most synchronized brain state in the human EEG. *R Soc Open Sci* **2016,** 3, (10), 160201.

47. Koenig, T.; Lehmann, D.; Saito, N.; Kuginuki, T.; Kinoshita, T.; Koukkou, M., Decreased functional connectivity of EEG theta-frequency activity in first-episode, neuroleptic-naïve patients with schizophrenia: preliminary results. *Schizophrenia research* **2001,** 50, (1-2), 55-60.

48. Zhang, S.; Qi, Y.; Yang, H.; Gong, M.; Zhang, D.; Zou, L., Optimization of the composition of bimetallic core/shell Fe2O3/Au nanoparticles for MRI/CT dual-mode imaging. *Journal of Nanoparticle Research* **2013,** 15, (11), 2023.

49. Li, J.; Sun, J.; Chen, T.; Li, X., Towards a better understanding of the effects of the magnetic nanoparticles size and magnetic field on cellular endocytosis. *Journal of Physics D: Applied Physics* **2020,** 53, (17), 175401.

50. Zheng, Y.; Dou, J. R.; Gao, Y.; Dong, L.; Li, G., Effects of 15 Hz square wave magnetic fields on the voltage-gated sodium and potassium channels in prefrontal cortex pyramidal neurons. *Int J Radiat Biol* **2017,** 93, (4), 449-455.

51. Bancroft, E. A.; Pandey, G.; Zarate, S. M.; Srinivasan, R., Extracellular S100B alters spontaneous Ca²⁺ fluxes in dopaminergic neurons via L-type voltage gated calcium channels: Implications for Parkinson’s disease. **2021,**

2021.02.24.432751.

52. Georgas, E. Y., M.; Wang, Y.; Qin, Y.-X., Remote Regulation of Activities and Action Potential by Dynamic Magnetic Field Stimulated Superparamegnetic Iron Oxide Gold Core Shell Nanoparticles. In *Cellular and Molecular Bioengineering Congerence (2022 CMBE)*, Indian Wells, CA, USA, 2022.

53. Bai, Q.; He, J.; Qiu, J.; Wang, Y.; Wang, S.; Xiu, Y.; Yu, C., Rotenone induces KATP channel opening in PC12 cells in association with the expression of tyrosine hydroxylase. *Oncol Rep* **2012,** 28, (4), 1376-84.

54. Brignani, S.; Pasterkamp, R. J., Neuronal Subset-Specific Migration and Axonal Wiring Mechanisms in the Developing Midbrain Dopamine System. *Front Neuroanat* **2017,** 11, 55.

55. Voigt, T.; Baier, H.; Dolabela de Lima, A., Synchronization of neuronal activity promotes survival of individual rat neocortical neurons in early development. *The European journal of neuroscience* **1997,** 9, (5), 990-9.

56. Hardingham, G. E.; Fukunaga, Y.; Bading, H., Extrasynaptic NMDARs oppose synaptic NMDARs by triggering CREB shut-off and cell death pathways. *Nature neuroscience* **2002,** 5, (5), 405-14.

57. Martin, H. G.; Wang, Y. T., Blocking the deadly effects of the NMDA receptor in stroke. *Cell* **2010,** 140, (2), 174-6.

58. Hardingham, G. E.; Bading, H., The Yin and Yang of NMDA receptor signalling. *Trends Neurosci* **2003,** 26, (2), 81-9.

59. Lee, S.; Liu, A.; Wang, Z. J.; McKeown, M. J., Abnormal Phase Coupling in

Parkinson's Disease and Normalization Effects of Subthreshold Vestibular Stimulation. *Front Hum Neurosci* **2019,** 13, 118.

60. Jalili, M.; Barzegaran, E.; Knyazeva, M. G., Synchronization of EEG: bivariate and multivariate measures. *IEEE transactions on neural systems and rehabilitation engineering : a publication of the IEEE Engineering in Medicine and Biology Society* **2014,** 22, (2), 212-21.

CHAPTER VII

CONCLUSIONS

PD is a complex multi-system disease involving various cell types and with few effective treatments available to patients. While the neurocentric approach to PD research has given us much insight into intrinsic mechanisms by which neurons die in the context of PD, it has led to few effective clinical treatments. Understanding the interaction between cell types, particularly neuron-astrocyte interactions, in PD is crucial for better understanding the nature of DA neurodegeneration and will hopefully provide novel therapeutic targets and strategies to combat PD. Recent efforts have shifted in this direction as studies now implicate multiple CNS cell types such as, microglia and astrocytes, as contributors to PD pathology [1, 2]. The nature of astrocyte-neuron interaction in PD has been challenging to study, however, the development of new tools and strategies to measure different aspects of glial biology has afforded the field the ability to examine this relationship in more intricate detail. One major advance is the availability of genetically encoded calcium indicators (GECIs) which give us the ability to measure Ca^{2+} dynamics in real time and allow for cell specific expression within the CNS [3, 4]. Paired with the advancement of optical imaging techniques such as multi-photon microscopy, miniscopes, and fiber photometry we now have the ability to measure *in vivo* Ca^{2+} dynamics in real time in awake, freely moving animals [5, 6].

Additionally, the challenge of drug-delivery of novel therapeutics to the brain has been a major roadblock for advancing PD treatments. The difficulty of drug-delivery to the brain is, in part, due to the high selectivity of the BBB [7, 8]. As such, it is crucial to generate non-invasive strategies to deliver therapeutics across the BBB via “hijacking” of existing machinery or by completely novel mechanisms. One likely candidate to overcome the selectivity of the BBB is the use of nanoparticles as a vehicle system for therapeutic molecules such as proteins, AAVs, or other genetic materials. These nanoparticles can be specifically engineered with physical properties that allow for passage through the BBB via existing machinery for active transport [8]. While this emerging drug-delivery technology is promising there are still many limitations and will require future efforts to characterize the efficacy and safety of nanoparticle-based drug-delivery systems.

In this dissertation, I combine the use of GECIs with *in vitro* and *in vivo* models of PD and TBI to study the nature of astrocyte-neuron interactions in the context of these pathologies. Specifically, I discovered a sex-based increase in the wrapping as S100B+ astrocytic processes in the SNc of male mice and that extracellular S100B directly modulates DA neuron physiology via an interaction with voltage-gated ion channels. Similarly, treatment with another secretable astrocytic protein, MIF, following TBI directly modulates the activity of CA1 hippocampal neurons and increases sensitivity to glutamatergic agonists. In addition, I have characterized the effects of gold-coated superparamagnetic iron oxide nanoparticles, a novel drug delivery system, on DA neuron physiology. In this conclusion, I will briefly discuss implications of these findings and present future directions for studying astrocytic modulation of neuronal physiology in PD and the use of nanoparticles as a drug-delivery system for treatment of neurodegenerative disease.

Modulation of DA physiology by secretable CNS cell factors

The concept of astrocytic modulation of neuronal communication is not new, specifically considering the tripartite synapse and regulation of synaptic function [9-11]. Nevertheless, it is important to consider novel mechanisms by which astrocytes influence neuronal activity and function. Emerging evidence continues to support the idea that astrocytes are actively involved in cell-cell communication within the CNS via secretory mechanisms [12, 13]. A range of molecules have been identified to be actively secreted by astrocytes including ATP, D-serine, glutamate, and brain-derived neurotrophic factor (BDNF), some of which contribute to subsequent changes in neuronal function [14, 15]. Recent studies have begun to uncover the plethora of molecules which are present in the astrocyte secretome, with approximately 6000 protein groups being identified [13, 16]. Paired with increasing evidence, including the work done in Chapter IV and VI of this dissertation, that secreted astrocytic proteins can directly modulate neuronal activity via interactions with plasma membrane proteins such as ion-channels and other types of receptors [17-20], it is important to understand how these astrocyte signaling mechanisms contribute to CNS physiology in health and disease. In this context, the primary midbrain astrocyte-neuron co-cultures developed and characterized in chapters II-IV will be a useful tool for determining extracellular effects of astrocytic secretory molecules on DA neuron physiology. In the case of DA neurons and S100B, discussed in Chapter IV, it is important to further study how S100B-mediated changes VGC activity and action potential frequencies in DA neurons contributes to neurodegenerative processes. Future work will need to further assess the relationship of VGKC and VGCC activity in DA neurons and the *in vivo* effects of extracellular S100B on SNc DA physiology, neuronal loss, and PD-related behavioral deficits.

Novel-drug delivery mechanisms for neuroprotective PD therapeutics

Much of the past work on improving non-invasive systemic drug delivery to the brain has been focused on disrupting the integrity of the BBB thereby increasing its passive permeability [7, 8]. As one can imagine, this approach is problematic as it is non-selective and, while increasing brain distribution of the intended drug, allows for unfettered access of other potentially harmful molecules. In addition to BBB permeability issues, pharmacokinetic issues exist with systemic administration of therapeutics for treatment of brain diseases, mainly their rapid elimination from the body prior to reaching the brain [7, 8]. NPs are quickly emerging as a likely candidate for specific brain-targeted drug-delivery. NPs can be specifically functionalized with appropriate molecules or surface charge to reduce elimination and promote active trans- or endocytosis through BBB epithelial cells [8, 21-23]. However, one major concern relates to the toxicity of these NPs to biological tissues, as many are made from metals. While SPIO NPs have been approved by the FDA for certain diagnostic and therapeutic use, many studies suggest there are still concerns over toxicity [24-26]. In addition to concerns over acute toxicity, since many of these functionalized NPs have surface charge, it is important to consider their effect on neuronal membrane potential which is discussed in more detail in Chapter III. In the case of PD and specifically for the pacemaking DA neurons of the midbrain, the modulation of neuronal membrane potential and firing frequency by the surface charge of NPs can exert a direct effect on their function regardless of any packaged or caged molecules. To this end, the primary midbrain astrocyte-neuron co-cultures used in Chapter II-IV would be a great tool for screening acute effects of novel NPs on DA neuron physiology. As long-term changes in neuronal excitability can lead to significant changes to their genome and proteome [27-29], it is important to consider how prolonged treatment using a NP based delivery method may alter neuronal physiology and function.

In addition, given the shortcomings of currently available animal models of PD, there is a need for the development of more comprehensive models that more closely resemble clinical PD phenotypes. Newer animal models of PD have used novel genetic manipulations in an attempt to resemble PD pathology more closely, however these are still problematic for distinct reasons. A recent study has generated a novel α-synuclein based transgenic mouse model which expresses a α-synuclein fragment previously implicated in PD pathogenesis [30]. While this model displays progressive neurodegeneration and development of motor deficits, accumulation of α-synuclein, loss of striatal synapses, and the loss of SNc DA neurons, these changes are not fully established until 9 months of age. One potential strategy that does not require reinventing the wheel would be to combine and adapt currently available models in an attempt to recreate the constellation of PD phenotypes. For example, lower dose 6-OHDA injections to the striatum combined with protein overexpression could address two pitfalls of these independent models. First, lower doses of 6-OHDA will drive neurodegeneration but at a much slower rate than conventionally used doses. Second, simultaneous overexpression of proteins such as α-synuclein or S100B will address the lack of protein aggregation and Lewy body formation seen in toxin models of PD. While this approach may reflect the clinical phenotypes of PD more closely, one main limitation remains, a much more rapid loss of DA neurons than what occurs in clinical PD. Finally, primary midbrain culture models, like the one characterized in Chapter II-IV, are an excellent tool to study discrete mechanisms involved in cell-cell communication in the context of PD. Further screening of the astrocyte secretome for molecules that directly modulate DA neuron physiology is of particular interest and could lead to the discovery of novel therapeutic targets in the future.

References

1. Poewe, W.; Seppi, K.; Tanner, C. M.; Halliday, G. M.; Brundin, P.; Volkmann, J.; Schrag, A. E.; Lang, A. E., Parkinson disease. *Nat Rev Dis Primers* **2017,** 3, 17013.
2. Teismann, P.; Schulz, J. B., Cellular pathology of Parkinson's disease: astrocytes,

microglia and inflammation. *Cell Tissue Res* **2004,** 318, (1), 149-61.

3. Lohr, C.; Beiersdorfer, A.; Fischer, T.; Hirnet, D.; Rotermund, N.; Sauer, J.; Schulz, K.; Gee, C. E., Using genetically encoded calcium indicators to study astrocyte physiology: A field guide. *Frontiers in Cellular Neuroscience* **2021,** 15.
4. Oh, J.; Lee, C.; Kaang, B. K., Imaging and analysis of genetically encoded calcium indicators linking neural circuits and behaviors. *Korean J Physiol Pharmacol* **2019,** 23, (4), 237-249.
5. Flusberg, B. A.; Nimmerjahn, A.; Cocker, E. D.; Mukamel, E. A.; Barretto, R. P.; Ko, T. H.; Burns, L. D.; Jung, J. C.; Schnitzer, M. J., High-speed, miniaturized fluorescence microscopy in freely moving mice. *Nat Methods* **2008,** 5, (11), 935-8.
6. Sych, Y.; Chernysheva, M.; Sumanovski, L. T.; Helmchen, F., High-density multi-fiber photometry for studying large-scale brain circuit dynamics. *Nat Methods* **2019,** 16, (6), 553-560.
7. Rawal, S. U.; Patel, B. M.; Patel, M. M., New Drug Delivery Systems Developed for Brain Targeting. *Drugs* **2022,** 82, (7), 749-792.
8. Teleanu, D. M.; Negut, I.; Grumezescu, V.; Grumezescu, A. M.; Teleanu, R. I., Nanomaterials for Drug Delivery to the Central Nervous System. *Nanomaterials (Basel)* **2019,** 9, (3).
9. Araque, A.; Parpura, V.; Sanzgiri, R. P.; Haydon, P. G., Tripartite synapses: glia, the unacknowledged partner. *Trends Neurosci* **1999,** 22, (5), 208-15.
10. Araque, A.; Sanzgiri, R. P.; Parpura, V.; Haydon, P. G., Astrocyte-induced

modulation of synaptic transmission. *Can J Physiol Pharmacol* **1999,** 77, (9), 699-706.

11. Newman, E. A.; Zahs, K. R., Modulation of neuronal activity by glial cells in the retina. *J Neurosci* **1998,** 18, (11), 4022-8.

12. Vardjan, N.; Parpura, V.; Verkhratsky, A.; Zorec, R., Gliocrine System: Astroglia as Secretory Cells of the CNS. *Adv Exp Med Biol* **2019,** 1175, 93-115.

13. Verkhratsky, A.; Matteoli, M.; Parpura, V.; Mothet, J. P.; Zorec, R., Astrocytes as secretory cells of the central nervous system: idiosyncrasies of vesicular secretion. *EMBO J* **2016,** 35, (3), 239-57.

14. Gucek, A.; Jorgacevski, J.; Singh, P.; Geisler, C.; Lisjak, M.; Vardjan, N.; Kreft, M.; Egner, A.; Zorec, R., Dominant negative SNARE peptides stabilize the fusion pore in a narrow, release-unproductive state. *Cell Mol Life Sci* **2016,** 73, (19), 3719-31.

15. Jha, M. K.; Kim, J. H.; Song, G. J.; Lee, W. H.; Lee, I. K.; Lee, H. W.; An, S. S. A.; Kim, S.; Suk, K., Functional dissection of astrocyte-secreted proteins: Implications in brain health and diseases. *Prog Neurobiol* **2018,** 162, 37-69.

16. Han, D.; Jin, J.; Woo, J.; Min, H.; Kim, Y., Proteomic analysis of mouse astrocytes and their secretome by a combination of FASP and StageTip-based, high pH, reversed-phase fractionation. *Proteomics* **2014,** 14, (13-14), 1604-9.

17. Bancroft, E. A.; De La Mora, M.; Pandey, G.; Zarate, S. M.; Srinivasan, R., Extracellular S100B inhibits A-type voltage-gated potassium currents and increases L-type voltage-gated calcium channel activity in dopaminergic neurons.

Glia **2022**.

18. Bancroft, E.; Srinivasan, R.; Shapiro, L. A., Macrophage Migration Inhibitory Factor Alters Functional Properties of CA1 Hippocampal Neurons in Mouse Brain Slices. *Int J Mol Sci* **2019,** 21, (1).

19. Morquette, P.; Verdier, D.; Kadala, A.; Fethiere, J.; Philippe, A. G.; Robitaille, R.; Kolta, A., An astrocyte-dependent mechanism for neuronal rhythmogenesis. *Nat Neurosci* **2015,** 18, (6), 844-54.

20. Ryczko, D.; Hanini-Daoud, M.; Condamine, S.; Breant, B. J. B.; Fougere, M.; Araya, R.; Kolta, A., S100beta-mediated astroglial control of firing and input processing in layer 5 pyramidal neurons of the mouse visual cortex. *J Physiol* **2021,** 599, (2), 677-707.

21. Tosi, G.; Costantino, L.; Ruozi, B.; Forni, F.; Vandelli, M. A., Polymeric nanoparticles for the drug delivery to the central nervous system. *Expert Opin Drug Deliv* **2008,** 5, (2), 155-74.

22. Shi, N.; Pardridge, W. M., Noninvasive gene targeting to the brain. *Proc Natl Acad Sci U S A* **2000,** 97, (13), 7567-72.

23. Goldsmith, M.; Abramovitz, L.; Peer, D., Precision nanomedicine in neurodegenerative diseases. *ACS Nano* **2014,** 8, (3), 1958-65.

24. Jeng, H. A.; Swanson, J., Toxicity of metal oxide nanoparticles in mammalian cells. *J Environ Sci Health A Tox Hazard Subst Environ Eng* **2006,** 41, (12), 2699-711.

25. Veranth, J. M.; Kaser, E. G.; Veranth, M. M.; Koch, M.; Yost, G. S., Cytokine

responses of human lung cells (BEAS-2B) treated with micron-sized and nanoparticles of metal oxides compared to soil dusts. *Part Fibre Toxicol* **2007,** 4, 2.

26. Hafeli, U. O.; Riffle, J. S.; Harris-Shekhawat, L.; Carmichael-Baranauskas, A.; Mark, F.; Dailey, J. P.; Bardenstein, D., Cell uptake and in vitro toxicity of magnetic nanoparticles suitable for drug delivery. *Mol Pharm* **2009,** 6, (5), 1417-28.

27. Lin, W. H.; Gunay, C.; Marley, R.; Prinz, A. A.; Baines, R. A., Activity-dependent alternative splicing increases persistent sodium current and promotes seizure. *J Neurosci* **2012,** 32, (21), 7267-77.

28. Boulting, G. L.; Durresi, E.; Ataman, B.; Sherman, M. A.; Mei, K.; Harmin, D. A.; Carter, A. C.; Hochbaum, D. R.; Granger, A. J.; Engreitz, J. M.; Hrvatin, S.; Blanchard, M. R.; Yang, M. G.; Griffith, E. C.; Greenberg, M. E., Activity-dependent regulome of human GABAergic neurons reveals new patterns of gene regulation and neurological disease heritability. *Nat Neurosci* **2021,** 24, (3), 437-448.

29. Lee, P. R.; Fields, R. D., Activity-Dependent Gene Expression in Neurons. *Neuroscientist* **2021,** 27, (4), 355-366.

30. Tian, Y.; He, M.; Pan, L.; Yuan, X.; Xiong, M.; Meng, L.; Yao, Z.; Yu, Z.; Ye, K.; Zhang, Z., Transgenic Mice Expressing Human alpha-Synuclein 1-103 Fragment as a Novel Model of Parkinson's Disease. *Front Aging Neurosci* **2021,** 13, 760781.